

**The Design of a Functionally Graded Composite for Service in High Temperature Lead and Lead-Bismuth Cooled Nuclear Reactors**

by

Michael Philip Short

Dual B.S., Nuclear Science and Eng. & Materials Science and Eng. (2005)  
Massachusetts Institute of Technology  
and  
M.S., Materials Science & Engineering (2010)  
Massachusetts Institute of Technology

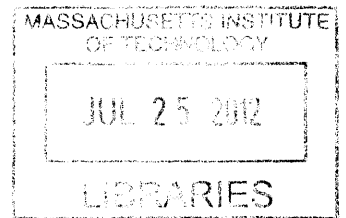
Submitted to the Department of Nuclear Science and Engineering  
in partial fulfillment of the requirements for the degree of  
Doctor of Philosophy in Nuclear Science and Engineering

at the

Massachusetts Institute of Technology

August 2010


**ARCHIVES**




©2010 Massachusetts Institute of Technology. All rights reserved.

Author .....  
Department of Nuclear Science and Engineering  
August 25, 2010

Certified by .....  
Ronald G. Ballinger  
Professor, Nuclear Science and Engineering  
and Materials Science and Engineering  
Thesis Supervisor

Certified by .....  
  
Assistant Professor, Nuclear Science and Engineering  
Thesis Reader

Certified by .....  
Hannu Hänninen  
Professor, Engineering Design and Production  
Aalto University, School of Science and Technology  
Thesis Reader

Accepted by .....  
  
Mujid S. Kazimi  
TEPCO Professor of Nuclear Engineering  
Chair, Department Committee on Graduate Students



# The Design of a Functionally Graded Composite for Service in High Temperature Lead and Lead-Bismuth Cooled Nuclear Reactors

by

Michael Philip Short

Submitted to the Department of Nuclear Science and Engineering  
on August 25, 2010, in partial fulfillment of the  
requirements for the degree of  
Doctor of Philosophy in Nuclear Science and Engineering

## Abstract

A material that resists lead-bismuth eutectic (LBE) attack and retains its strength at 700°C would be an enabling technology for LBE-cooled reactors. No single alloy currently exists that can economically meet the required performance criteria of high strength and corrosion resistance. A Functionally Graded Composite (FGC) was created with layers engineered to perform these functions. F91 was chosen as the structural layer of the composite for its strength and radiation resistance. Fe-12Cr-2Si, an alloy developed from previous work in the Fe-Cr-Si system, was chosen as the corrosion-resistant cladding layer because of its chemical similarity to F91 and its superior corrosion resistance in both oxidizing and reducing environments.

Fe-12Cr-2Si experienced minimal corrosion due to its self-passivation in oxidizing and reducing environments. Extrapolated corrosion rates are below one micron per year at 700°C. Corrosion of F91 was faster, but predictable and manageable. Diffusion studies showed that 17 microns of the cladding layer will be diffusionally diluted during the three year life of fuel cladding. 33 microns must be accounted for during the sixty year life of coolant piping.

5 cm coolant piping and 6.35 mm fuel cladding were produced on a commercial scale by weld-overlaying Fe-12Cr-2Si onto F91 billets and co-extruding them, followed by pilgering. An ASME certified weld was performed followed by the prescribed quench-and-tempering heat treatment for F91. A minimal heat affected zone was observed, demonstrating field weldability. Finally, corrosion tests were performed on the fabricated FGC at 700°C after completely breaching the cladding in a small area to induce galvanic corrosion at the interface. None was observed.

This FGC has significant impacts on LBE reactor design. The increases in outlet temperature and coolant velocity allow a large increase in power density, leading to either a smaller core for the same power rating or more power output for the same size core. This FGC represents an enabling technology for LBE cooled fast reactors.

Thesis Supervisor: Ronald G. Ballinger  
Title: Professor, Nuclear Science and Engineering  
and Materials Science and Engineering

Thesis Reader: Bilge Yildiz  
Title: Assistant Professor, Nuclear Science and Engineering

Thesis Reader: Hannu Hänninen  
Title: Professor, Engineering Design and Production  
Aalto University, School of Science and Technology

## Acknowledgments

First and foremost, I wish to thank Professor Ron Ballinger for being my advisor throughout my undergraduate and graduate studies for nearly a decade. Professor Ballinger was my TA for my first class at MIT, and ever since he has provided a tremendous amount of insight, support, expertise and camaraderie over the past years, and for that I am eternally grateful. Almost all of my lab experience and some of my morals were acquired under Professor Ballinger's guidance. Thank you for being a wonderful advisor and for helping me when I needed it the most.

I also wish to acknowledge the professors and students who have provided me with the most guidance and insight through my studies about nuclear materials. First comes Heather MacLean, who was my mentor when I was an undergraduate. She helped me through my first years ever working in a lab, and her patience in training and helping me is part of why I still enjoy this work so much. Next is Jeongyoun Lim, from whom I inherited the lead-bismuth alloy project. I wouldn't have had a project to work on if it weren't for her tireless hours in the lab, and her helping me get my footing in the project while she was a postdoc.

I wish to acknowledge all the helpful discussions, explanations, and comments on my thesis from Professor Neil Todreas and Professor Bilge Yildiz of MIT, and from Professor Hannu Hänninen of Aalto University in Finland. Your guidance kept me on the right track, helping me to accomplish this work efficiently, to make numerous connections around the world, and to extract all the value and insight from my data that I may not have seen on my own. Special thanks go to Professor Hänninen, who signed on to be my thesis reader not long before the thesis was due, providing me with expert advice and a different outlook on my thesis that I hadn't considered. It's true what they say: sometimes help comes from the most unexpected places.

Thanks are also due to Professor Sam Allen, who I've known since I arrived at MIT as an undergraduate nine years ago. When I took a blacksmithing and metallurgy class co-taught by him, I had no idea that it would lead me to a career studying metals. I originally wanted to be an electrical engineer, but blacksmithing and other

metalwork sparked my interest far more.

Thanks also go to Toby Bashaw of MIT, and to JD Smith of MassArt, for teaching me most of what I know about working hands-on with metals. The intuition I gained by working on real projects with them helped me to intuitively understand complex microstructural processes by seeing and feeling their effects on larger pieces of metal. Books are one thing, but their knowledge combined with real experience is the most effective teaching tool there is.

Because of the uniquely commercial aspect of this project, I wish to acknowledge the vendors who were more than accomodating fitting a smaller research project with unfamiliar materials into already busy commercial schedules. I wish to specifically thank the following people and companies who helped make this project a commercial success: Ron Erhard at Deep Hole Specialists in Chagrin Falls, OH, Gaylord Smith and Rick Corn at Special Metals in Huntington, WV, Clem Templeton at Braeburn Alloy Steel in Lower Burrell, PA, Jon Salkin and Mike Myers at Arc Applications in York, PA, George Lincoln at Metalwerks PMD, Inc. in Aliquippa, PA, Joe Runkel at Bodycote, Inc. in Andover, MA, Steve Wood and Terry Goheen at H. C. Starck in Coldwater, MI, Frank Turner at Electrode Engineering in Harrington, TN, and Ken Newlen and Venkat Ishwar at Haynes International in Arcadia, LA.

I want to thank a few international collaborators who have expressed much interest in this project, notably Marc Vankeerberghen of SCK-CEN in Belgium, Il Soon Hwang of Seoul National University in Korea, and the organizers of the Bodycote 2009 Paper Prize Competition held in Köln, Germany. Receiving this much attention from all over the world is what got me really excited about this project, and made me change my intended career path from the world of business back into academia, so that I could continue this work.

The Uhlig corrosion lab provided me with an excellent working environment, full of interesting and dynamic people who aren't afraid to be politically incorrect in order to get the job done and have a good time. I specifically want to thank Julian Benz, Mike Dunlevy, Jon Gibbs, Joe Huble, Fanny Mas, Tim Lucas, Jeff Hixon, Kevin Miu, Jane Diecker, and Dave Rigual for being great colleagues, sounding boards for

ideas, and friends. Thanks are due to my nine UROPs over the past five years for their help on the project: Brian Baum, Sean Morton, Yunzhi Wang, Katie Chang, Faisal Amir, Ballin Smith, Sara Ferry, Jay Seman and Patrick Hoymak. I especially want to thank Sara and Sean for going in-depth enough to provide much useful data and analysis, which helped make this project a real success.

I wish to say thank you to my family for their undying support throughout all phases of my life. Jonathan, Mom and Dad, thank you for being there, whether I had a serious problem to solve or just wanted someone to talk to.

Finally, I want to say thank you to my wife, Marina. Marrying you has shown me that there are some things in life where you need to plunge in head first, hold nothing back, and give it your all. I used to be worried about being stuck in a marriage, never wanting to be tied down to anything. Being with you showed me that you can't be stuck in something you enjoy so much, that I feel privileged to be part of our relationship. I love you, sweetie. This work is dedicated to you.





# Contents

<b>1</b>	<b>Introduction</b>	<b>39</b>
1.1	The Need for Gen. IV Reactors . . . . .	39
1.1.1	Summary of the Goals of the Gen. IV Reactor Program . . . . .	41
1.1.2	Comparison of the Proposed Coolants for the Gen. IV Program . . . . .	44
1.1.3	The Case for Liquid Lead and LBE as a Reactor Coolant . . . . .	48
1.1.4	Material Compatibility Issues with Lead and LBE . . . . .	50
1.1.5	One Solution - A Functionally Graded Composite (FGC) . . . . .	52
1.1.6	General System Description . . . . .	53
1.2	Research Objectives and Thesis Goals . . . . .	54
1.2.1	Performance Requirements of the FGC . . . . .	54
1.2.2	Impact of Success of the FGC . . . . .	56
1.3	Outline . . . . .	58
<b>2</b>	<b>Background</b>	<b>61</b>
2.1	Characteristics of Liquid Metal Corrosion . . . . .	61
2.1.1	Thermodynamic Basis for Liquid Metal Attack by Lead and LBE . . . . .	62
2.1.1.1	Oxidizing Environments . . . . .	63
2.1.1.2	Reducing Environments . . . . .	65
2.1.2	Mechanisms of Corrosion in Liquid Lead and LBE . . . . .	69
2.1.3	Kinetics of Corrosion in Lead and LBE . . . . .	77
2.1.3.1	Static Corrosion . . . . .	77
2.1.3.2	Flow Assisted Corrosion . . . . .	80
2.2	Prevention of Liquid Metal Corrosion . . . . .	83

2.2.1	Passivation of Alloys in Lead and LBE by Oxide Formation . . . . .	83
2.2.2	Methods for Prevention of Lead and LBE Corrosion . . . . .	88
2.2.2.1	Oxygen Control . . . . .	88
2.2.2.2	Oxide Layer Engineering . . . . .	91
2.2.2.3	Other Methods . . . . .	93
2.3	Selection of FGC Layer Alloys . . . . .	95
2.3.1	Requirements for Materials in a Lead- or LBE-Cooled Gen. IV Reactor . . . . .	95
2.3.2	Previous Work in the Fe-Cr-Si System . . . . .	99
2.3.3	Selection of FGC Layers . . . . .	103
2.3.3.1	Structural Layer . . . . .	103
2.3.3.2	Cladding Layer . . . . .	110
2.3.4	FGC Success Criteria . . . . .	113
2.4	Selection of Composite Dimensions and Processing Steps . . . . .	114
2.4.1	Thermal-Hydraulic Constraints . . . . .	114
2.4.2	Reactor Physics Considerations . . . . .	115
2.4.3	Strength Constraints . . . . .	116
2.4.4	Corrosion & Diffusion Constraints . . . . .	116
2.4.5	Selection of Dimensions . . . . .	117
2.4.6	Selection of Processing Steps . . . . .	118
2.4.7	Notes on Selection of Dimensions and Processing Steps . . . . .	120
<b>3</b>	<b>Experimental Methods</b>	<b>121</b>
3.1	Material Procurement and Initial Testing . . . . .	121
3.1.1	Material Procurement . . . . .	121
3.1.2	Initial Testing . . . . .	121
3.2	Static LBE Corrosion Testing . . . . .	122
3.2.1	Experimental System Description . . . . .	123
3.2.2	Sample Preparation, Experimental Procedures and Test Matrix	126
3.2.3	Analysis Procedures . . . . .	131

3.2.3.1	Post-Experimental Sample Preparation . . . . .	131
3.2.3.2	Optical Microscopy . . . . .	131
3.2.3.3	SEM and EDX Analysis . . . . .	132
3.2.3.4	XPS Surface Analysis . . . . .	132
3.2.3.5	SIMS Depth Profiles . . . . .	133
3.3	Diffusion Studies . . . . .	133
3.3.1	Experimental System Description . . . . .	134
3.3.2	Sample Preparation, Experimental Procedures and Test Matrix	134
3.3.3	Analysis Procedures . . . . .	135
3.3.3.1	Post-Experimental Sample Preparation . . . . .	135
3.3.3.2	Optical Microscopy . . . . .	136
3.3.3.3	Electron Microprobe Analyzer (EMPA) Concentra- tion Profiles . . . . .	136
3.3.3.4	Micro- and Nanohardness Profiles . . . . .	137
3.4	Commercial Feasibility Study . . . . .	138
3.4.1	Material Procurement . . . . .	138
3.4.2	Material Processing Procedures . . . . .	139
3.4.2.1	Initial Machining of Alloy F91 Billets . . . . .	141
3.4.2.2	Weld Wire Fabrication . . . . .	142
3.4.2.3	Weld Overlay . . . . .	142
3.4.2.4	Co-Extrusion . . . . .	144
3.4.2.5	Pilgering and Tube Drawing . . . . .	145
3.4.3	Testing Procedures and Analysis Techniques . . . . .	146
3.4.3.1	Post-Experimental Sample Preparation . . . . .	147
3.4.3.2	Optical Microscopy . . . . .	147
3.4.3.3	Microhardness Testing . . . . .	147
3.5	Auxiliary Tests . . . . .	147
3.5.1	Initial Welding Study . . . . .	148
3.5.1.1	Experimental Procedure . . . . .	148
3.5.1.2	Post-Experimental Sample Preparation . . . . .	148

3.5.1.3	Optical Microscopy . . . . .	148
3.5.2	Commercially Certified FGC Welding Study . . . . .	149
3.5.2.1	Sample Procurement . . . . .	149
3.5.2.2	Post-Experimental Sample Preparation . . . . .	150
3.5.2.3	Optical Microscopy . . . . .	150
3.5.2.4	Microhardness Profiles . . . . .	151
3.5.3	Composite Breach Corrosion Study . . . . .	152
3.5.3.1	Experimental System Description . . . . .	152
3.5.3.2	Sample Preparation & Experimental Procedure . . . . .	152
3.5.3.3	Post-Experimental Sample Preparation . . . . .	152
3.5.3.4	Optical Microscopy . . . . .	153
3.5.3.5	SEM and EDX Analysis . . . . .	153
3.6	Descriptions of Analysis Methods . . . . .	153
3.6.1	Sample Preparation . . . . .	153
3.6.2	Sample Etching . . . . .	154
3.6.3	Optical Microscopy . . . . .	155
3.6.4	SEM and EDX . . . . .	155
3.6.5	EMPA Concentration Profiling . . . . .	157
3.6.6	Micro- and Nanohardness Analysis . . . . .	158
3.6.7	XPS Surface Analysis . . . . .	159
3.6.8	SIMS Depth Profiling . . . . .	160
<b>4</b>	<b>Results</b>	<b>161</b>
4.1	Initial Testing . . . . .	161
4.1.1	Optical Microscopy . . . . .	161
4.1.2	Microhardness Tests . . . . .	162
4.2	Static LBE Test Results . . . . .	163
4.2.1	Results for F91 . . . . .	164
4.2.1.1	Optical Microscopy . . . . .	164
4.2.1.2	SEM and EDX Analysis . . . . .	168

4.2.2	Results for Fe-12Cr-2Si . . . . .	173
4.2.2.1	Optical Microscopy . . . . .	173
4.2.2.2	SEM and EDX Analysis . . . . .	173
4.2.2.3	XPS Surface Analysis . . . . .	177
4.2.2.4	SIMS Concentration Depth Profiles . . . . .	192
4.3	Diffusion Study Results . . . . .	201
4.3.1	Optical Microscopy . . . . .	201
4.3.1.1	Control Samples . . . . .	201
4.3.1.2	700°C & 750°C Aged Samples . . . . .	203
4.3.1.3	800°C Aged Samples . . . . .	205
4.3.2	EMPA Concentration Profiles . . . . .	207
4.3.3	Micro- and Nanohardness Profiles . . . . .	212
4.4	Commercial Feasibility Results . . . . .	217
4.4.1	Weld Wire Fabrication . . . . .	217
4.4.2	Weld Overlaying . . . . .	218
4.4.3	Extrusion . . . . .	222
4.4.4	Pilgering . . . . .	225
4.4.5	Tube Drawing for Fuel Cladding . . . . .	225
4.5	Auxiliary Studies . . . . .	225
4.5.1	Initial Welding Study . . . . .	225
4.5.1.1	Optical Microscopy . . . . .	225
4.5.2	Commercially Certified FGC Welding Study . . . . .	227
4.5.2.1	Optical Microscopy . . . . .	227
4.5.2.2	Microhardness Profiles . . . . .	231
4.5.3	Composite Breach Corrosion Study . . . . .	231
4.5.3.1	Optical Microscopy . . . . .	231
4.5.3.2	SEM Analysis . . . . .	234
<b>5</b>	<b>Discussion</b>	<b>237</b>
5.1	Corrosion Resistance of the FGC . . . . .	238

5.1.1	Performance of the Fe-12Cr-2Si Cladding Layer . . . . .	239
5.1.1.1	Oxidizing Environments . . . . .	240
5.1.1.2	Reducing Environments . . . . .	243
5.1.2	Performance of the F91 Base Layer . . . . .	244
5.1.3	Performance of the FGC in the Event of Total Cladding Breach	247
5.2	Diffusional Stability of the FGC . . . . .	247
5.2.1	Calculated Diffusion Coefficients . . . . .	248
5.2.1.1	Silicon Diffusion in F91 . . . . .	248
5.2.1.2	Silicon Diffusion in Fe-12Cr-2Si . . . . .	251
5.2.2	Extrapolations to the End-of-Life for a Typical LBE-Cooled Reactor at 700°C . . . . .	252
5.2.2.1	Diffusion Characteristics . . . . .	252
5.2.2.2	Corrosion Resistance . . . . .	253
5.2.2.3	Physical Properties . . . . .	254
5.2.2.4	Radiation Embrittlement and Radiation Induced Mi- gration . . . . .	254
5.3	Commercial Feasibility of Producing this FGC . . . . .	255
5.3.1	Feasibility of Each Processing Step . . . . .	255
5.3.2	Effects of Processing on the Performance of the FGC . . . . .	257
5.3.3	Effects of Each Processing Step on the Next Step . . . . .	257
5.4	Reactor Performance Gains and Economic Implications of Using this FGC . . . . .	258
5.4.1	Performance Gains . . . . .	258
5.4.2	Economic Gains . . . . .	261
<b>6</b>	<b>Conclusion &amp; Future Work</b>	<b>265</b>
6.1	Key Result & Contributions . . . . .	265
6.1.1	Key Results . . . . .	266
6.1.2	Key Contributions . . . . .	266
6.2	Overall Conclusions . . . . .	267

6.3 Overall Summary of Experimental Results . . . . .	268
6.4 Future Work . . . . .	271
<b>Bibliography</b>	<b>275</b>
<b>A Code for Calculation of Resource Depletion</b>	<b>293</b>
<b>B Extrusion Report from H. C. Starck</b>	<b>295</b>
<b>C ASME-Certified Welding Report from Artisan Industries</b>	<b>301</b>
<b>D C Code and Input File Used to Calculate Silicon Diffusion Constants in Alloy F91</b>	<b>305</b>





# List of Figures

2-1	Pourbaix diagrams for pure Fe and pure Cr showing oxide stability zones in water as functions of pH and potential. Diagrams were generated using the HSC chemistry software package, version 5.1, by Outokumpu, Inc. Analogous regions exist for these metals in LBE. Zones where the pure metal is stable in LBE are subject to corrosion via dissolution. . . . .	62
2-2	Ellingham diagram for metal/metal oxide systems found in this study [1]. Oxides are stable above each solid line, and metals are stable below each solid line. Oxygen concentrations and corresponding hydrogen to water vapor ratios are shown with dotted lines. . . . .	64
2-3	Examples of diffusion coefficients for metals and oxygen in relevant metals and oxides. Data are plotted over cited temperature ranges given in Table 2.1. Markers for metals are solid, while those for oxides are hollow. Note how much lower diffusion coefficients are for chromium and silicon oxides. . . . .	67
2-4	Relevant phase diagrams for stainless steels in liquid LBE [2, 3, 4, 5]. The most important features to note on these phase diagrams are the stability lines between the liquid phase and the two phase region on the high-Pb or the high-Bi side of each binary phase diagram. . . . .	68
2-5	Iron-oxygen binary phase diagram, showing magnetite to wüstite phase change at 570°C [6]. Areas of wüstite stability are shaded. . . . .	70

2-6	Diagram showing how passive layer breaching would lead to accelerated anodic dissolution. The zones beneath the oxide have been depleted in passivating metals, leading to accelerated dissolution and liquid metal attack. The deepest part of the crevice lacks sufficient oxygen to passivate, and is attacked by liquid metal dissolution. . . . .	73
2-7	Solubilities of Cr and Ni in liquid lead, LBE and bismuth as functions of temperature [7]. These were derived from the binary phase diagrams for each combination of metals. . . . .	77
2-8	Diagram of how mass transport works in a flowing liquid metal loop, such as in the LFR. Solubilities increase as a function of temperature, so materials dissolve more in the hot leg. When the solubility drops in the cold leg, these materials drop out of solution. This cycle causes faster dissolution in the hot leg and crud buildup in the cold leg. (Photo courtesy of INL [8]) . . . . .	78
2-9	MatCalc simulations of oxygen diffusion in $\alpha$ -Fe immersed in 700°C oxygen-rich LBE for one hour, with and without a 2 $\mu$ m thick layer of chromium oxide. The thin chromium oxide layer acts as a very effective barrier to oxygen diffusion due to the low diffusivity of oxygen through chromia. The initial oxygen concentration of the $\alpha$ -Fe was assumed to be zero, and diffusion coefficients were assumed to be independent of concentration. The formation of oxide phases was also not considered in this simulation. . . . .	80
2-10	Regimes of flow assisted corrosion, showing mass loss rate vs. coolant velocity [9] . . . . .	81
2-11	Example potential-current curves for Fe and Cr in sulfuric acid, demonstrating how and at what potentials passivation drastically lowers the corrosion rate [10]. Data to the left of the graph represent lower corrosion currents. The regions of each curve where the corrosion current suddenly drops between voltages of -0.4 V and 1.2 V represent regions of passivation. . . . .	83

2-12	Example curve of passive corrosion rate versus time [11]. Formation of the passive layer is marked by fast formation, immediately followed by a sharp decrease in corrosion current density due to protection of the underlying metal by the passivating oxide. . . . .	85
2-13	Schematic of all possible oxide layers formed upon exposure of an Fe-Cr alloy to an oxygenated environment [12]. Not all of these oxides will form on every Fe-Cr alloy. The lower the oxygen concentration, the less likely it is that Fe <sub>2</sub> O <sub>3</sub> and FeO will form. . . . .	86
2-14	Diagram showing the stability of wüstite as functions of temperature and chromium content [12]. Note that the lowest wüstite stability temperature increases with added chromium. . . . .	87
2-15	Example oxide layer thicknesses versus time for Fe-Cr and Fe-Cr-Si alloys. Note that the Fe-Cr alloys continue to grow oxide layers, while the Fe-Cr-Si alloys' oxide thicknesses decrease over time after initial growth. [7] . . . . .	88
2-16	Generalized curve for a highly passivating alloy in an oxidizing environment with a high coolant flow velocity. Region (1) is marked by fast formation of passive layers, whose growth slows down as their thicknesses increase in region (2). In region (3), the outer layers of weaker iron oxides spall off due to shear forces from the flowing coolant, while the layers of chromia and silica densify underneath. Region (4) is marked by stable but extremely slow growth of the highly protective layers of chromia, silica and iron-chrome spinel oxides. . . . .	89
2-17	Weldability map for Fe-Cr-Al alloys, showing which alloys crack during gas tungsten arc welding (GTAW) due to hydrogen-induced cracking. TiC is added as a hydrogen sink to mitigate this problem [13]. . . .	93
2-18	Examples of low-chromium iron alloys upon exposure to LBE at 600°C. Note the thick oxide layers, as well as the LBE penetration beneath into the base metal, where rapid dissolution is taking place [7]. . . .	100

2-19 SEM image of Fe-1.25Si after exposure to 600°C reducing LBE for 300 hours. Note the thick layer of SiO <sub>2</sub> and FeSi <sub>2</sub> O <sub>4</sub> precipitates that have formed [7]. . . . .	101
2-20 EDX maps of oxidation of Fe-12Cr-1.25Si after exposure to 600°C LBE for 250 hours showing an outer layer of Cr and Si oxides plus an innermost layer of Cr and Si oxide precipitates, which act as barriers to further oxygen diffusion or element dissolution [7] . . . . .	102
2-21 SEM images and EDX linescans of martensitic alloys Optifer IV, F91 and EP-823 after exposure to flowing, oxidizing LBE at 470°C for 3,116 hours [14]. All three steels exhibit a surface oxide rich in iron between ten and twenty microns thick. . . . .	104
2-22 Growth rates of alloys Optifer IV, F91 and EP-823 after exposure to flowing, oxidizing LBE at 470°C. [14]. All three alloys' oxide layers exhibit square root growth rates, indicative of continued diffusional growth through the existing oxide layer. . . . .	105
2-23 Change in yield stress and ultimate tensile strength of F91 at ~12 dpa fast flux [15]. Note how mechanical properties are not noticeably affected above 450°C. This is due to the higher ability of defect pairs created by radiation to anneal out, or to diffuse to sinks. . . . .	106
2-24 Shift in properties related to ductility for irradiated HT-9, F91 and ORNL 9Cr-2WVTa . . . . .	107
2-25 Creep-rupture curve comparison of F91 and HT-9 [16] . . . . .	107
2-26 Fe-Cr binary phase diagram, showing the solubility limit of chromium in $\alpha$ -Fe in the lower-left [3] . . . . .	108
2-27 Modified Fe-Cr phase diagram in the low-Cr region based on work by Bonny et al. [17] . . . . .	109
2-28 Simulated diagrams of how microstructures would look with different amount of $\sigma$ -Cr phase precipitation. $\sigma$ -Cr is shaded purple in these diagrams. . . . .	111
2-29 Micrographs of $\sigma$ -Cr precipitation and its effects in Fe-Cr-Ni alloys [18]	111

2-30	Fe-Si binary phase diagram showing the solubility limit of Si in $\gamma$ -Fe [3]	113
2-31	Diagram showing zones expected to develop during operation of the composite. The scale has been exaggerated for demonstration purposes. . . . .	117
2-32	Selection of dimensions for the proposed FGC . . . . .	118
2-33	Diagram showing how weld overlaying works. To weld overlay the ID of a billet, a TIG torch is rotated inside the bore, or the billet turns around the torch. It deposits a spiral layer of material, with adjacent weld beads overlapping each other. The billet is turned as the torch is slowly retracted. Multiple layers can be deposited on top of each other to increase the thickness of the coating. . . . .	119
2-34	Diagram showing how extrusion works. A piston pushes the billet through a mandrel and die using a dummy block and hundreds of tons of force. This reduces the dimensions of the billet drastically. The ratio of diameter reduction to cross sectional area reduction is referred to as the extrusion ratio. . . . .	119
3-1	Gas mixing, delivery and analysis system used in the static corrosion experiments . . . . .	124
3-2	Schematic of LBE static corrosion test setup [7] . . . . .	125
3-3	Picture and cut-away drawing of LBE furnaces used in this study . . . . .	126
3-4	Polished and cleaned samples ready for exposure to LBE . . . . .	127
3-5	Test pieces of pure Fe and Cr used to indicate whether the cover gas was oxidizing or reducing with respect to $Fe_3O_4$ . . . . .	128
3-6	Test pieces of pure Fe and Cr after exposure to the cover gas in each environment, indicating the rough oxygen potential present during each experiment . . . . .	128
3-7	Example of the temperatures, moisture and oxygen levels recorded for the 600°C 124 hour experiment . . . . .	130
3-8	Photograph showing how samples were sectioned for analysis . . . . .	132

3-9	Processing schedule for the FGC developed in this study . . . . .	140
3-10	Billets of F91 as machined, ready for weld overlaying. The long billet on the right (#1) has been drilled to a 12.7 cm (5") ID to become coolant piping. The billet at the back right (#2) has been lathe-turned down to a 22.9 cm (9") OD to become fuel cladding. The third billet (#3) is to become bare F91 fuel cladding for another project. . . . .	141
3-11	Photographs of weld wire in various stages of production. First a forging billet was made, a slice of which is visible at the front of the figure. It was then drawn in a bar-and-wire mill to 12.7 cm (1/2") OD rod (on the right), and then to 6.35 mm (1/4") OD wire rod (at the back). Finally, it was wire drawn to 0.89 mm (0.035") solid core MIG weld wire (at the front-left). . . . .	143
3-12	Weld overlay procedure of the ID-clad billet in process. The first pass of deposited material is visible at the back of the billet, while bare metal waiting to be weld-overlaid is visible at the front. . . . .	144
3-13	Finished ID-clad weld overlaid billet . . . . .	145
3-14	Billets with fillets, ready for extrusion. The 1" radius fillets allow for easier insertion of the billets into the die, reducing the force necessary to begin extrusion. . . . .	146
3-15	Welding procedure for samples in the ASME-certified welding study	150
3-16	TTT Diagram for F91, showing that even slow cooling in air to $T_M$ for 12 minutes still forms 100% martensite [19] . . . . .	151
3-17	Diagram showing how EDX works in an SEM. X-rays generated by electron transitions in the sample enter the detector and are counted by energy. . . . .	157
3-18	Diagram of the Vickers indenter and example indents [20] . . . . .	158
4-1	Photographs of F91 and Fe-12Cr-2Si as received from the manufacturer. Samples were mounted in Bakelite, polished to 50 nm and swabbed with waterless Kalling's reagent for three seconds. . . . .	162

4-2	Fe-C binary phase diagram, showing two-phase regions ( $\alpha$ -Fe & Fe <sub>3</sub> C) for this alloy (shaded) [5]	163
4-3	Optical micrographs of F91 samples exposed to 600°C LBE at 200×. Samples exposed to reducing LBE show evidence of liquid metal attack channels, while those exposed to oxidizing LBE exhibit more uniform oxidation characteristics.	165
4-4	Optical micrographs of F91 samples exposed to 700°C LBE at 200×. Samples exposed to reducing LBE show evidence of liquid metal attack channels, while those exposed to oxidizing LBE exhibit more uniform oxidation characteristics. Large internal oxidation zones are visible on the oxidized samples.	166
4-5	SEM images of F91 exposed to 700°C reducing LBE for 506 hours. The lighter layer and channels beneath are LBE. A layer of LBE can be seen adhering to the surface of the metal, while channels of LBE penetration are seen progressing via liquid metal attack.	169
4-6	EDX elemental maps of F91 exposed to 700°C reducing LBE for 506 hours, 1,000×. The channels penetrating into the surface of F91 are confirmed to be LBE. A chromium depletion region was present throughout the region of LBE attack, suggesting that selective dissolution of chromium was the dominant attack mechanism. Silicon is present on the surface from the mounting medium, not from the sample. No oxide layers were observed.	170
4-7	SEM image of F91 exposed to 700°C oxidizing LBE for 506 hours, 1,000×. The lighter channels beneath the surface of the sample are LBE. No layer of LBE can be seen adhering to the surface of the metal. The surface of this sample is significantly rougher than those exposed to reducing LBE, suggesting that selective dissolution or removal of oxides, such as wüstite, was the dominant mode of attack.	171

4-8	EDX elemental maps of F91 exposed to 700°C oxidizing LBE for 506 hours, 750×. The channels penetrating into the surface of F91 are confirmed to be LBE. A chromium depletion region was present throughout the region of LBE attack, suggesting that selective dissolution of chromium was one attack mechanism. Silicon is present on the surface from the mounting medium, not from the sample. Light oxidation can be seen between channels of LBE attack. The lack of LBE adhered to the surface also suggests the surface is an oxide, as LBE cannot adhere as well to oxides as to clean metals. . . . .	172
4-9	Optical micrographs of Fe-12Cr-2Si samples exposed to 600°C LBE at 200×, showing no appreciable attack from either reducing or oxidizing LBE . . . . .	174
4-10	Optical micrographs of Fe-12Cr-2Si samples exposed to 700°C LBE at 200×, showing no appreciable changes after exposure to either reducing or oxidizing LBE . . . . .	175
4-11	Anomalous feature observed on the surface of Fe-12Cr-2Si after exposure to reducing LBE at 700°C for 247 hrs, 200× . . . . .	176
4-12	Fe-12Cr-2Si after exposure to 700°C reducing LBE for 506 hours, 250×. Note the absence of any visible oxide layers, due to the fact that those present are too thin to be seen at this magnification. . . . .	177
4-13	EDX elemental maps of Fe-12Cr-2Si exposed to 700°C oxidizing LBE for 506 hours, 25,000×. A very thin, 400 nm oxide layer can be seen, clearly distinct from the bare metal below. No LBE was detected adhering to this sample. The contrast on the EDX maps has been enhanced to make distinguishing features visible. The oxide layer in the middle of the SEI is enriched in silicon and depleted in iron. . .	178
4-14	Fe-12Cr-2Si after exposure to 700°C oxidizing LBE for 506 hours, 1,000×. Note the absence of any visible oxide layers, due to the fact that those present are too thin to be seen at this magnification. . . .	179



4-15	EDX elemental maps of Fe-12Cr-2Si exposed to 700°C oxidizing LBE for 506 hours, 50,000×. No LBE was detected adhering to this sample. A very thin, 400 nm darker region can be seen on some of the surface, clearly distinct from the bare metal below. The contrast on the EDX maps has been enhanced to make distinguishing features visible. The elemental maps show that the dark layer in the middle of the SEI is an oxide layer, enriched in silicon and chromium, and depleted in iron.	180
4-16	XPS survey spectra of Fe-12Cr-2Si samples exposed to LBE at 700°C for 70 hrs. Note how the iron, chromium and silicon peaks are much stronger on the sample exposed to oxidizing LBE.	181
4-17	Detailed XPS spectra around the 2p and 2p <sup>-</sup> lines for C, Fe, Cr and Si on the Fe-12Cr-2Si sample exposed to 700°C oxidizing LBE for 70 hours	182
4-18	Comparison of XPS spectra of Fe-12Cr-2Si exposed to reducing LBE for 506 hours before and after sputtering. Sputtering to a depth of 10 - 20 Å almost completely removed hydrocarbon surface contamination, uncovering the actual surface of the sample.	186
4-19	Detailed XPS spectra around the 2p and 2p <sup>-</sup> lines for C, Cr, Fe and Si on the Fe-12Cr-2Si sample exposed to 700°C reducing LBE for 506 hrs. The Kratos XPS software package was used to subtract background signal and fit Gaussian curves to the envelope created by the data. This envelope is always shown in pink.	187
4-20	XPS survey spectrum for Fe-12Cr-2Si after exposure to 700°C oxidizing LBE for 506 hours. Note that the iron peak is not present on this sample.	190
4-21	Detailed XPS spectra around the 2p and 2p <sup>-</sup> lines for C, Cr, Fe and Si on the Fe-12Cr-2Si sample exposed to 700°C oxidizing LBE for 506 hrs. The Kratos XPS software package was used to subtract background signal and fit Gaussian curves to the envelope created by the data. This envelope is always shown in pink.	191

4-22 SIMS concentration profiles for samples exposed to the cover gas conditions at 700°C . . . . .	194
4-23 SIMS concentration profiles for samples exposed to 700°C LBE for 70 hours . . . . .	195
4-24 SIMS concentration profiles for samples exposed to 700°C LBE for 245 hours . . . . .	197
4-25 SIMS concentration profiles for samples exposed to 700°C LBE for 506 hours . . . . .	198
4-26 SIMS concentration profiles for samples exposed to 600°C LBE for 504 hours . . . . .	200
4-27 Optical macrograph of a diffusion couple as-received from Bodycote, Inc. The carbon steel jacket can be seen surrounding the two metal coupons that make up the diffusion couple. The jacket has rusted due to etching in nital. . . . .	202
4-28 Optical micrographs of diffusion couples aged at 700°C and 750°C, 200×. All of these samples experienced little microstructural change beyond growth of the single interaction layer, likely due to silicon and carbon diffusion through the system. . . . .	204
4-29 Optical micrographs of diffusion couples aged at 800°C, 200×. All of these samples experienced significant microstructural changes. The growth of the interaction layers can be attributed to diffusion, while the coarsening of the F91 suggests that the aging temperature for these samples was above the tempering temperature for F91. . . . .	206
4-30 Chromium EMPA concentration profiles for diffusion couples in this study. Obvious outliers that did not fit the overall curves have been removed to improve the clarity of the overall shape of the curves. . .	208
4-31 Silicon EMPA concentration profiles for diffusion couples in this study. Obvious outliers that did not fit the overall curves have been removed to improve the clarity of the overall shape of the curves. . . . .	210

4-32	Correlation between regions of slope discontinuity, certain Si concentrations and microstructure for aged diffusion couples. On all samples, ferrite became the dominant phase at a silicon concentration of 0.6 wt. %. This is likely due to silicon's role as a bainite destabilizer and a ferrite stabilizer [21]. . . . .	211
4-33	Diffusion coefficients of selected solutes in iron, showing a sudden drop in diffusion at the BCC-FCC phase transition temperature [22] . . .	213
4-34	Nanohardness profiles for 700°C and 800°C diffusion couples. The overall hardness values for the unaged samples are higher because a lower indent depth was used. Scaling down by a factor of two provides a sufficient comparison with the rest of the data. . . . .	215
4-35	Optical micrographs of representative nanohardness grids taken on diffusion couples . . . . .	216
4-36	Slices of weld-overlaid extrusion billets. In each billet, the Fe-12Cr-2Si layer is visible as a region of different reflectivity either on the ID or the OD, and is demarcated with dotted black lines. . . . .	219
4-37	Layer interface on the ID-clad weld overlaid billet, 100×. Some mixing is present, seen as fingers of martensite poking into a grain of ferrite at the center of the photograph. Overall the interface and mixing layer was very thin. . . . .	220
4-38	Layer interface on the OD-clad weld overlaid billet, 50×. Some mixing from the melt zone is present, but more striking is the presence of carbides along grain boundaries. Grains of Fe-12Cr-2Si grow in columns perpendicular to the interface. Spears of carbon diffusion can also be seen in close-packed directions inside these grains, visible as black lines at 90° angles to each other. . . . .	221
4-39	Back sections of the extrusion billets after extrusion, showing the post-extrusion reductions in diameter, area and the surface conditions. The black crusty material is burned glass used as a lubricant during the extrusion process. . . . .	223

4-40	Optical micrographs of as-extruded product forms immediately prior to welding, 100×. Note the sharp interface between the two metals present in the ID-clad sample. Also note the relatively small grain size in both materials, and the ferritic grain shape of Fe-12Cr-2Si. . . . .	224
4-41	Optical micrograph montages of initial TIG-welded specimens. Individual photographs were taken at 50×. No post-processing was performed on any images except for stitching them together. Note that only the first pass undergoes significant mixing in all three samples. Each sample has a HAZ that is 1.5 mm thick. This shows what an F91 weld would look like without applying the proper post weld heat treatment. . . . .	226
4-42	Photo montage of the ASME-certified ID-clad weld, made by grinding a double bevel, filling the weld to 2.5 mm (0.1”) with Fe-12Cr-2Si and finally backfilling the weld with F91 weld wire. The boundary between the two welds has been delineated with black dots. Note the lack of any appreciable HAZ, showing that the proper quench and tempering heat treatment for F91 was performed. Individual images were taken at 50×. . . . .	229
4-43	Photo montage of the ASME-certified OD-clad weld, made by grinding a double bevel, filling the weld to 7 mm (0.275”) with F91 weld wire and finally backfilling the weld with Fe-12Cr-2Si. Note the lack of any appreciable HAZ, showing that the proper quench and tempering heat treatment for F91 was performed. Individual images were taken at 50×. . . . .	230

- 4-44 Superposition of the ID-clad optical montage with a 2-D Vickers hardness map of its surface. Regions of differing microstructure correspond directly to changes in hardness. The hardest area is the F91 weld, which approaches 400 HV at some locations. The Fe-12Cr-2Si portion of the weld is softer than the surrounding microstructure, due to a lack of carbon in that weld wire. There is a mild HAZ extending 2.5 mm (0.1”) from the weld boundary. This will likely disappear after further tempering according to the proper PWHT for F91. . . . . 232
- 4-45 Optical micrographs of ID and OD-clad as-extruded composite forms after exposure to 700°C LBE for 98 hours, 200×. In all cases, no preferential LBE attack sites were noted at the interface between the two metals. This suggests that galvanic corrosion will not be an issue should the cladding be completely breached in an accident. . . . . 233
- 4-46 SEM images of the ID-clad as-extruded composite after exposure to 700°C LBE for 98 hours. In all cases, no preferential LBE attack sites were noted at the interface between the two metals. This suggests that galvanic corrosion will not be an issue should the cladding be completely breached in an accident. The corrosion thickness noted at the interface between alloy F91 and the Fe-12Cr-2Si alloy is very similar to that of alloy F91 far from the bimetal interface. . . . . 235
- 4-47 SEM images of the OD-clad as-extruded composite after exposure to 700°C LBE for 98 hours. In all cases, no preferential LBE attack sites were noted at the interface between the two metals. This suggests that galvanic corrosion will not be an issue should the cladding be completely breached in an accident. The corrosion thickness noted at the interface between alloy F91 and the Fe-12Cr-2Si alloy is very similar to that of alloy F91 far from the bimetal interface. . . . . 236

5-1	Corrosion distances for alloy F91 exposed to LBE at both temperatures and environments. The exponents show that corrosion of alloy F91 in LBE follows close to a standard $\sqrt{t}$ law in a range of environments and temperatures. This behavior is typical of diffusion-limited corrosion processes. . . . .	244
5-2	Flowchart explaining how the diffusion data fitting code works. First, the user supplies the input file along with a range of independent diffusion parameters ( $D_0$ , the diffusion constant, and $E_A$ , the activation energy). Next “equivalent aging times” for the HIPing process (the control sample) are calculated using each pair of diffusion parameters, $D_0$ and $E_A$ . Next, an error function is generated using each parameter trio of $D_0$ , $E_A$ and the equivalent aging time for that pair of $D_0$ & $E_A$ . These error functions are compared to the entire data set, and a total mean squared error (MSE) sum is acquired. Finally the pair of $D_0$ and $E_A$ that produced the minimum MSE sum is chosen as the best fit. . . . .	249
5-3	A log-linear curve fit to location of minimum silicon content during reactor operation at 700°C . . . . .	253
5-4	Hydrogen production process efficiencies, showing the increase in efficiency by using a higher outlet temperature [23] . . . . .	259
5-5	Power and P/D ratio performance gains by increasing the coolant flow velocity and outlet temperature, based on the design by Nikiforova et al. [24]. The baseline design point of 2,400 MWTh is shown as compared to power contours for the new design. A P/D ratio of over 1.30 was deemed too large due to core size constraints, as the baseline design already filled all available space in the core. . . . .	260
5-6	Operating regime restrictions based on reasonable design constraints for an LBE cooled reactor. Pumping work, vessel size, pressure drop, heat exchangers and coolant flow velocity were considered when restricting the recommended operation region. . . . .	262

# List of Tables

1.1	Estimated worldwide reserves and consumption rates of fuels for large-scale baseline power generation . . . . .	40
1.2	Proposed coolants for Gen. IV reactors . . . . .	45
1.3	Relevant physical properties of selected Gen. IV reactor coolants . .	45
1.4	Relevant neutronic properties of selected Gen. IV reactor coolants. Smaller values of $\xi$ and larger numbers of collisions needed to thermalize are more neutronically favorable in fast reactor systems. . . . .	46
2.1	Summary of relevant diffusion data for oxidation and dissolution processes in the FeCrSiAl-LBE system . . . . .	66
2.2	Physical parameters for oxides and metals considered for the proposed FGC [12] . . . . .	74
2.3	Standard free energies of formation for oxides in the Fe-Cr-(Si,Al) system, in kJ/mol. Lower free energies indicate which oxides are more likely to form, assuming the oxygen potential is high enough to form them all. . . . .	85
2.4	Summary of techniques that can prevent corrosion by liquid lead and LBE in steel . . . . .	95
2.5	Composition of the Russian Fe-Cr-Si alloy EP-823, in wt. % [14] . .	102
3.1	Compositions of F91, Fe-12Cr-2Si, lead and bismuth in weight percent used in this study as verified by ICP-MS. Oxygen concentrations were subtracted, as they were subject to change by the cover gases during the experiments. . . . .	122

3.2	Sample test matrix for static corrosion experiments showing actual aging times . . . . .	129
3.3	Test matrix for diffusion study samples . . . . .	135
3.4	Point spacings for diffusion couples analyzed by EMPA . . . . .	137
3.5	Relevant parameters and grid spacings for nanohardness tests on diffusion couples . . . . .	138
3.6	Specified chemistry in weight percent for Fe-12Cr-2Si weld wire . . .	139
4.1	Maximum corrosion distances for F91 samples exposed to static LBE	168
4.2	XPS binding energy peaks for C, Cr, Fe and Si on the sample of Fe-12Cr-2Si exposed to oxidizing LBE at 700°C for 70 hrs. All measured peak energies have been shifted down by 1.2 eV except for carbon, which was used as the reference. The most likely matches are in bold.	184
4.3	XPS binding energy peaks for C, Cr, Fe and Si on the sample of Fe-12Cr-2Si exposed to reducing LBE at 700°C for 506 hrs. All measured peak energies have been shifted down by 0.3 eV except for carbon, which was used as the reference. Most likely matches are in bold. . .	189
4.4	XPS binding energy peaks for C, Cr, Fe and Si on the sample of Fe-12Cr-2Si exposed to oxidizing LBE at 700°C for 506 hrs. All measured peak energies have been shifted down by 2.3 eV except for carbon, which was used as the reference. Most likely matches are in bold. . .	192
4.5	Summary of SIMS data, showing total interaction layer thickness, proposed interaction mechanisms, enrichment zone order and any depletion zones present. Peak locations are listed in order starting with the outer surface of the sample. Peaks found together are marked with ampersands. Stronger depletion zones are marked in bold. . . . .	199
4.6	Average thickness of the interaction zone for 700°C and 750°C aged diffusion couples. Many points were taken, and the uncertainty is twice the standard error of each sample's measurements. . . . .	205



4.7	Maximum interaction zone thicknesses for diffusion couples aged at 800°C. Samples that did not exhibit one or more zones are marked out with “—” . . . . .	206
4.8	Vickers hardness data for base materials in diffusion couples. Data were taken at least 2 mm from the interface on either side to track any tempering (in F91) or hardening (in Fe-12Cr-2Si) that took place. . . . .	214



# List of Abbreviations and Symbols

## Abbreviations

ABWR	Advanced Boiling Water Reactor	GFR	Gas Fast Reactor
ASME	Amer. Soc. of Mechanical Eng.	GTAW	Gas Tungsten Arc Welding
at. %	atomic percent	HAZ	Heat Affected Zone
BP	Boiling Point	HIP	Hot Isostatic Pressing
BTU	British Thermal Units	HV	Hardness Vickers
BWR	Boiling Water Reactor	ICP-MS	Inductively Coupled Plasma Mass Spectroscopy
CFC	Corrosion Fatigue Cracking	ID	Inner Diameter
CFM	Cubic Feet per Minute	LBE	Lead-Bismuth Eutectic
DBTT	Ductile to Brittle Transition Temp.	LBEFR	Lead-Bismuth Eutectic Fast Reactor
DNB	Departure from Nucleate Boiling	LFR	Lead Fast Reactor
DOE	(U.S.) Department of Energy	LME	Liquid Metal Embrittlement
dpa	displacements per atom	LOFA	Loss of Flow Accident
EBR	Experimental Breeder Reactor	LWR	Light Water Reactor
EDM	Electrical Discharge Machining	MIT	Massachusetts Institute of Tech.
EDX	Energy Dispersive X-ray analysis	MP	Melting Point
EMPA	Electron Microprobe Analysis	MSE	Mean Squared Error
EPR	European Pressurized Reactor	MSR	Molten Salt Reactor
EPRI	Electric Power Research Institute	MT	Metric Ton (1,000 kg)
FAC	Flow Assisted Corrosion	MWh	Megawatt-Hours
FGC	Functionally Graded Composite	MWTh	Megawatts Thermal
F/M	Ferritic/Martensitic (steel)	NEI	Nuclear Energy Institute
FWHM	Full Width at Half Maximum		
GESA	Gepulste Elektronen Strahl Anlage		

Abbreviations (continued)

NIST	National Institute of Standards and Technology	SCWR	Supercritical Water Reactor
OD	Outer Diameter	SEI	Secondary Electron Image
ODS	Oxide Dispersion Strengthened	SFR	Sodium Fast Reactor
ORNL	Oak Ridge National Laboratory	SEM	Scanning Electron Microscope
OX	Oxidizing Environment	SIMS	Secondary Ion Mass Spec.
PBMR	Pebble Bed Modular Reactor	SSTAR	Small Sealed Autonomous Transportable Reactor
ppb	parts per billion	TIG	Tungsten Inert Gas (welding)
ppm	parts per million	TTT	Time and Temperature Transformation (diagram)
PRA	Probabilistic Risk Assessment	TWh	Terawatt-Hours
PWHT	Post-Weld Heat Treatment	UT	Ultrasonic Testing
PWR	Pressurized Water Reactor	VAR	Vacuum Arc Remelting
PUREX	Pu/U Recovery by Extraction	VHTR	Very High Temperature Reactor
RED	Reducing Environment	WDS	Wavelength Dispersive Spec.
RPM	Revolutions Per Minute	wt. %	weight percent
SCC	Stress Corrosion Cracking	XPS	X-ray Photoelectron Spec.
SC-H <sub>2</sub> O	Supercritical Water	ZJ	Zettajoules ( $1 \times 10^{21}$ J)
SCK-CEN	Studiecentrum voor Kernenergie - Centre d'Etude de l'énergie Nucléaire		

Symbols

A	Area	p	Pitch
$A_c$	Cross Sectional Area	R	Ideal Gas Constant
$C_i$	Concentration of Species $i$	$S_i$	Solubility of Species $i$
D	Diffusion Constant	T	Temperature
$\tilde{D}$	Interdiffusivity Coefficient	$T_M$	Martensite Transformation Temperature
$D_0$	Infinite Diffusivity	t	Thickness
d	Diameter, Average Grain Size	u	Neutron Lethargy
E	Young's Modulus	z	Vertical Height
$E_A$	Activation Energy	$\alpha$	Thermal Expansion Coefficient
$E_0$	Initial Energy	$\lambda$	Wavelength, Half-Life
$E_f$	Final Energy	$\mu$	Viscosity
g	Acceleration Due to Gravity	$\xi$	Average Lethargy Gain
$K_{eq}$	Equilibrium Constant	$\rho$	Density
k	Thermal Conductivity	$\sigma$	Stress, Nuclear Cross Section
$k_y$	Hall-Petch Strength Constant	$\sigma_y$	Yield Stress
$\dot{m}$	Mass Flow Rate	$\tau_w$	Wall Shear Stress
$\ddot{m}$	Mass Flux	$\nu$	Poisson's Ratio
P	Pressure	$\Delta G$	Gibbs Free Energy
$P_{sat}$	Saturation Vapor Pressure	$\langle \# \rangle$	Collisions to Thermalize
$P_z$	Perimeter		



# Chapter 1

## Introduction

### 1.1 The Need for Gen. IV Reactors

The current fleet of nuclear reactors in the United States and around the world has served as a dependable workhorse for baseline power generation, supplying many developed countries with up to 75% of their electricity demand. While numerous methods exist for energy production, nuclear power is currently the only method that both produces no greenhouse gases during power production and can reliably supply baseline electricity.

Traditional fossil fuel-based sources of energy result in large amounts of pollutants and waste. Producing energy by combustion of anything, be it coal, natural gas, oil, wood or others, produces large amounts of carbon dioxide, sulfur oxides, and other greenhouse gases. Recent international agreements, such as the Kyoto Protocol, mandate that the world rapidly reduce its greenhouse gas emissions. In addition, the aforementioned combustion-based sources of energy (except for wood) are completely non-renewable, and theories abound as to when the world will run out of recoverable sources. While uranium is also a non-renewable resource, the world's uranium supply is expected to last much longer than any fossil fuel source at predicted rates of energy consumption, as shown in Table 1.1.

Renewable energy sources, which include solar, wind, geothermal, hydroelectric and biomass energy production, have not yet evolved to the point where they can

Fuel Source	Coal	Oil	Natural Gas	Uranium
Estimated Reserves <sup>1</sup> (ZJ) [25]	290.0	18.4	15.7	2,500 <sup>2</sup> [26]
World Consumption (ZJ/yr)	0.134 <sup>3</sup> [27]	0.18 <sup>4</sup> [28]	0.11 <sup>5</sup> [29]	0.0242 <sup>6</sup> [29]
Predicted Year of Depletion <sup>7</sup>	2148	2056	2063	2277

<sup>1</sup>Total reserves include economically recoverable sources, economically prohibitive resources and conservative estimates of speculated, undiscovered sources. Actual numbers may be much lower depending on demand and availability.

<sup>2</sup>This number includes the use of breeder reactors, which produce more fissile material from <sup>238</sup>U than they consume.

<sup>3</sup>Converted from 127.548 quadrillion BTU (2006).

<sup>4</sup>This number corresponds to 30.8 billion barrels per year (2008).

<sup>5</sup>Converted from 2,976,552 million m<sup>3</sup> per year at an average energy value of 37 MJ/m<sup>3</sup> (2006).

<sup>6</sup>Converted from 2,768 TWh produced worldwide per year (2005).

<sup>7</sup>Calculated by assuming a 3% increase in consumption per year. Code is attached in Appendix A.

Table 1.1: Estimated worldwide reserves and consumption rates of fuels for large-scale baseline power generation

reliably supply the baseline energy demand for the United States. This is due to their intermittent nature, as sources of energy such as wind, solar or tidal motion do not produce a constant supply of energy at times when they are most needed. Even hydroelectric energy production plants can be interrupted by periods of drought, or other depletions of the water reservoirs that power them [30]. Energy storage mechanisms have not yet evolved to the point where storing energy produced by wind and/or solar energy would prove economical.

These energy sources are intermittent in nature; solar power only works during daylight hours, and wind power only produces energy when the wind is blowing. Hydroelectric power plants, while emission-free, severely disrupt the ecosystems where they are located by restricting or rerouting the water supply. Geothermal power works well for saving energy in heating and cooling individual households, but it cannot yet produce enough energy to meet the baseline power needs of a large, industrialized country.

The fleet of nuclear reactors currently in service and being constructed – the Generation III and III+ reactors – have served us well during the past 40 years.



These reactors have experienced no accidents in the United States which resulted in premature loss of life to date, and publicly known incidents such as Three Mile Island are actually examples of the success of reactor safety systems, rather than failures, due to the ability of the safety systems to safely contain the material in the containment building during a meltdown.

New reactors have been licensed and construction has begun, but the designs are largely evolutionary and rely on currently used light water reactor (LWR) technology. The use of water as a coolant has been successful so far, but the physical and chemical nature of using water sets an upper bound on the amount of energy that can be extracted in a thermodynamic cycle. The water must be highly pressurized, and thus all the components in a reactor that face the coolant must be able to tolerate pressures up to 25 MPa at temperatures up to 350°C. In addition, water is a relatively poor conductor of heat, requiring a large flow rate in order to extract enough heat from the system. Water also boils at a relatively low temperature even when highly pressurized, making the design of an LWR difficult from both a neutronic and a thermodynamic standpoint. The fact that water must be treated as a two-phase coolant means the temperature, pressure and quality of the water must be carefully controlled in order to extract the most heat while ensuring the safety of fragile components.

A drastic deviation from the evolutionary path of LWR design will soon be required to meet the ever-rising energy demands of the world in order to more efficiently extract energy from the same fuel while simultaneously improving safety, reducing the possibility for proliferation and simplifying reactor design.

### **1.1.1 Summary of the Goals of the Gen. IV Reactor Program**

Commercial nuclear plants operating in the U.S. have been largely evolutionary in design. Many improvements have been made to the original pressurized water reactor (PWR) and boiling water reactor (BWR) designs to increase efficiency, improve safety and simplify plant design. However, they have all evolved from the original basic designs from reactors that began operation up to forty years ago. [31]. New designs, such as the European pressurized reactor (EPR) and the AP-1000, are still subject to

many of the same physical limitations as the old designs because of the choice of light water as the coolant. In order to make large improvements in the efficiency, safety and reliability of commercial nuclear reactor systems, a revolutionary, rather than an evolutionary, approach must be implemented.

These revolutionary approaches will be necessary to achieve the goals of the Gen. IV nuclear program, paraphrased below [32]:

- Sustainability 1 – Provide sustainable energy production with high fuel utilization and minimal environmental effects.
- Sustainability 2 – Minimize and manage nuclear waste and reduce the burden of maintaining long-lived waste.
- Economics 1 – Clear life-cycle cost advantage over other methods of electricity production.
- Economics 2 – Level of financial risk will be comparable to other methods of energy production.
- Safety and Reliability 1 – Excel in safety and reliability.
- Safety and Reliability 2 – Very low likelihood and degree of damage to the reactor.
- Safety and Reliability 3 – Eliminate or reduce the need for off-site response.
- Proliferation Resistance – Provide increased physical protection against terrorism, and assure by design that Gen. IV reactors are the least attractive route for diversion or theft of fissile material.

Current commercial power plants employ a “once-through” fuel cycle, where the fuel is removed from the reactor and treated as waste once it reaches a predetermined burn-up level. This results in only a few percent of the fissile material in the core being used to create heat, and a large amount of waste and inefficiency considering the amount of fuel in the core. Generation IV technologies must either use a closed fuel

cycle, where the fuel is continuously used and reprocessed throughout the lifetime of the reactor, or a multiple-pass fuel cycle where the fuel is separated into fissile material and waste, and the fissile material is refabricated into fresh fuel a fixed number of times.

Generation III reactor designs must employ active systems to maintain coolant flow, monitor reactor safety and prevent damage in the case of a thermal transient or an accident. Each of these systems has a reliability of less than 100%, because no system is perfect. The more active systems that exist in a plant's design, the more complex and expensive it becomes, even if it improves safety. For example, the Advanced Boiling Water Reactor (ABWR) employs more coolant loops, pumps, heat exchangers, relief valves, high pressure core spray systems, control rods and vessel penetrations than conventional BWRs of the same power rating [33]. This both compromises the economic viability of the plant and creates increased maintenance work to ensure proper operation.

Generation IV reactors must improve the safety, the operating cost, and the reliability of nuclear reactors through design simplification and the implementation of passive systems. The constraints imposed by using light water as a coolant require the maintenance of high pressure levels in the cooling systems of the reactor [33]. Doing so puts high stress on mechanical components. In addition, the loss of this pressure can cause coolant voiding and thermal transients, which in turn can lead to core damage.

Many Generation IV designs use coolants that remain in a single phase throughout operation, resulting in more predictable reactor operation. This allows the design to be simplified. Some single phase coolants do not need conventional LWR components such as steam dryers, pressurizers or coolant pumps; nor do they need as many active safety systems. One example of this is the small sealed autonomous transportable reactor (SSTAR), which uses only passive cooling and safety systems [34]. This simplified design reduces the anticipated need for off-site response.

Closing the fuel cycle and simplifying the design of a reactor also presents great advantages against proliferation and terrorism. A reactor whose safety systems are

more passive, compact and easily controlled is inherently less vulnerable to attack. Closing the fuel cycle directly results in less waste, less fissile material moving around and outside the plant, and less of a chance for these materials to be stolen or otherwise compromised. This will be due to the use of reprocessing schemes other than the Plutonium Uranium Recovery by Extraction (PUREX) process, which was originally designed to separate fissile uranium and plutonium for weapons [35]. More advanced reprocessing schemes will not include a step where separated uranium or plutonium are present, making them safer to operate from a proliferation point of view.

These factors paint a more favorable economic picture for Generation IV technologies. The increased efficiency and the capability to provide process heat for hydrogen production both increase the amount of energy available per unit of fuel. Simpler designs, passive safety systems and a reduced plant footprint all reduce the materials cost of the reactor, especially during the initial construction phase when the financial risk is greatest. Lowering the construction costs decreases both the principal amount and the payback period of the loan, resulting in lower interest rates due to lower financial risk. The increased reliability as well as the resistance to proliferation, external attack and accidents all decrease the risk of building and operating a Generation IV reactor, and they all have positive, direct impacts on its financing.

### **1.1.2 Comparison of the Proposed Coolants for the Gen. IV Program**

Six coolants have been selected by the Department of Energy (DOE) as viable options for Gen. IV reactor coolants [32]. These coolants are summarized in Table 1.2, along with the reactor systems in which they will be used. These coolants have been identified as possessing superior properties to others considered, and they allow for reactor designs that meet the goals of the Gen. IV program. Each coolant has specific advantages and disadvantages, all relating to their physical properties, which are summarized in Table 1.3.

The liquid metals and molten salt have superior heat conductivities and heat

Coolant	Reactor(s)	Acronym(s)
Helium	GFR, VHTR, PBMR	<b>Gas Fast Reactor, Very High Temp. Reactor Pebble Bed Modular Reactor</b>
Liquid lead or LBE	LFR, LBE-FR	<b>Lead Fast Reactor, LBE Fast Reactor</b>
Liquid sodium	SFR	<b>Sodium Fast Reactor</b>
Molten salt	MSR	<b>Molten Salt Reactor</b>
Supercritical water	SCWR	<b>Supercritical Water Reactor</b>

Table 1.2: Proposed coolants for Gen. IV reactors

Coolant	M.P. (°C)	T <sub>out</sub> (°C)	B.P. (°C)	$\rho c_p$ $(\frac{J}{cm^3 \cdot K})^1$	$k$ $(\frac{W}{m \cdot K})^1$	P <sub>reactor</sub> (MPa)	$\mu$ (Pa · s) <sup>1</sup>
Helium [36]	-272	950	-269	0.0143 [37]	0.0357	7.0	$4.111 \cdot 10^{-5}$
LBE [38]	123.3	700	1,670	1.37	17.5	0.1	$1.0 \cdot 10^{-3}$
Lead [38]	327.4	700	1,737	1.51	19.9	0.1	$1.3 \cdot 10^{-3}$
Sodium [39]	97.8	550	892	1.03 [40]	64.9 [41]	0.1	$2.2 \cdot 10^{-4}$ [41]
Molten Salt <sup>2</sup> [39]	396	700	2,500	1.72	0.39	0.1	$1.18 \cdot 10^{-3}$
SC-H <sub>2</sub> O [42, 43]	0	500	100	0.225	0.09	22.1	$3 \cdot 10^{-5}$

<sup>1</sup>Selected property is at the given outlet temperature and pressure.

<sup>2</sup>The salt chosen for this comparison is (3Na – 2K – 5Mg)Cl<sub>x</sub>.

Table 1.3: Relevant physical properties of selected Gen. IV reactor coolants

capacities relative to the other coolants. The high boiling points of the liquid metals ensure that the system will not need to be pressurized to remain in the liquid phase. Instead, an inert cover gas, such as argon, is all that is necessary to exclude air from the system. This means that structural materials in the reactor do not have to be able to tolerate a higher operating pressure; they only need to withstand their own weight and that of the coolant. The liquid metals and molten salt also have higher atomic masses than the other three proposed coolants, which make them particularly suitable for fast reactors. This is because they moderate neutrons in the reactor far less than the other coolants, keeping the spectrum faster. This moderation is most easily described using the average lethargy gain, which is the average logarithmic amount of energy loss during an elastic collision. Lethargy ( $u$ ) is defined as the logarithmic loss of energy during an elastic collision, given by the following:

$$u = \ln \left( \frac{E_0}{E_f} \right) \quad (1.1)$$

Coolant	Atomic Mass	$\xi$	Number of collisions needed to thermalize
Helium	4	0.425	34
Sodium	22.99	0.0845	172
Lead	207.2	0.0096	1507

Table 1.4: Relevant neutronic properties of selected Gen. IV reactor coolants. Smaller values of  $\xi$  and larger numbers of collisions needed to thermalize are more neutronically favorable in fast reactor systems.

where  $E_0$  is the initial energy and  $E_f$  is the final energy after one collision. The average lethargy gain ( $\xi$ ) of a nucleus with atomic mass  $A$  is given by the following [44]:

$$\xi = \langle \Delta u \rangle = 1 - \frac{(A-1)^2}{2A} \ln \left( \frac{A+1}{A-1} \right) \quad (1.2)$$

This can be used to obtain the average number of collisions needed by a neutron to “thermalize,” or to decrease in energy from its initial energy, around 2 MeV, to the thermal range, below 1 eV. This is easily computed from the average lethargy gain:

$$\langle \# \rangle = \frac{\ln \left( \frac{E_0}{E_f} \right)}{\ln \left( \frac{E_i}{E_{i-1}} \right)} = \frac{\ln \left( \frac{2 \text{ MeV}}{1 \text{ eV}} \right)}{\xi} = \frac{14.5}{\xi} \quad (1.3)$$

These three values for three example coolants considered for Gen. IV reactors are summarized in Table 1.4.

The liquid metals do have some disadvantages. Both oxygenated sodium and LBE are reactive with the structural materials in a reactor, thus limiting their potential use as coolants and their maximum temperatures inside the reactor. LBE is corrosive to many materials through the processes of liquid metal attack and transportation of dissolved oxygen to the metal surface [45]. Sodium is a powerful reducing agent that can reduce oxides found on stainless steels. This effect can remove the hardness and lubrication that passivating oxides normally provide, placing a wastage and erosion limit on sodium reactor operation [46, 47]. This stands in contrast to helium, which forms no compounds with any components in the reactor, allowing the outlet temperature of helium cooled/moderated reactors such as the VHTR and the PBMR to

vastly exceed that of the SFR or the LFR.

The higher densities of lead and LBE also require structural components that can support the weight of the large volume of coolant that is needed to fill the reactor pool. Finally, there is the fact that the molten coolants' freezing temperatures are above room temperature, so there is a possibility that the coolant may freeze if all sources of heat are lost. However, industry experience with liquid metal cooled reactors such as EBR-II and Russia's experience with lead-cooled submarine reactors has shown that this is not a significant issue given adequate thermal insulation.

Numerous differences arise between the liquid metals that help make a case for or against either one. From a standpoint of economics, a smaller reactor requires fewer materials and is therefore less expensive. The lower moderation provided by lead or LBE (as compared to sodium) results in a smaller reactor, because more neutrons stay in the fast spectrum. This in turn leads to a higher fast flux (see Table 1.4). LBE's higher number density and neutron reflectivity also result in less neutron leakage in an LBE reactor, leading directly to a higher fast flux and further decreasing the size of the reactor. Heavy coolants such as lead and LBE are also self-shielding to gamma radiation, reducing the dose to workers [48, 49]. However, the price of sodium is lower per pound than for lead, and due to sodium's far lower density much less sodium is needed to fill a reactor. In July 2010, the prices for one kilogram of 99.9% pure sodium was \$3.30, one kilogram of lead was \$1.74 and one kilogram of bismuth was \$13.40. This leads to a price of \$8.15 per kilogram of LBE [50]. The coolant inventory for an LBE-cooled reactor has been calculated at an average of 8,682 MT per GWe [51], while that for sodium is 3,407 MT per GWe (SuperPhenix I) [52]. This translates into a factor of 6.3 lower cost for the coolant in the SFR compared to an equivalent LFR. It should be noted that the density of LBE is over ten times that of sodium, so the entire reactor structure would be much smaller while accommodating the same coolant inventory.

From a safety standpoint, each liquid metal has its own advantages and disadvantages. Sodium does not become activated by neutrons, while the bismuth in LBE will activate and decay into polonium, which makes the primary coolant highly radioac-

tive. LBE is safer from the standpoint of chemical reactivity, as it does not react violently with any material that could be present in or around the reactor. Sodium reacts explosively with water and oxygen to release hydrogen gas, which leads to higher safety risks. Liquid metal coolants are not transparent, and therefore direct observation of materials in the core is not possible without first draining coolant inventory. There exists a long history of sodium-cooled reactors, such as EBR-II, that have well-developed fuel handling procedures and an excellent record of keeping track of materials in the core. Material tracking is therefore not expected to present a significant challenge to operation and fuel management in a liquid metal-cooled reactor.

In summary, each coolant has properties that make it preferable for specific applications. The reasons for a high amount of interest in the development of lead and lead-bismuth cooled reactors will now be discussed.

### **1.1.3 The Case for Liquid Lead and LBE as a Reactor Coolant**

All six of the coolants mentioned in Table 1.3 have been selected by the DOE as the most scientifically and commercially viable coolants for reactor designs. This suggests that the nuclear scientific community as a whole believes that each of the six technologies can be developed on a commercial scale in a reasonable amount of time. It is therefore the opinion of the author that the biggest determining factor as to which coolant is most viable will be the economics of each individual type of reactor. LBE's physical and chemical properties lead directly to a more economical reactor design with equivalent or better safety characteristics.

The high average atomic mass of LBE makes it very good at reflecting neutrons back into the core without moderating them out of the fast flux region. This results in a smaller reactor design able to support a given fast flux level, which means that a lower coolant inventory and fewer structural materials will be required. This feature of LBE-cooled reactors has allowed designs such as the SSTAR reactor to be developed, which has a small, long-lived 'battery' core at its center [53]. Its high density, thermal conductivity and high specific heat capacity allow the coolant inventory to be further



reduced from that in other designs. This leads to a smaller pitch to diameter ratio, thereby increasing the fissile material density in the core and increasing the power density.

LBE's thermodynamic properties also lead to a very useful feature: they can be cooled via natural convection. LBE's superior heat removing abilities (surpassed only by sodium among the candidates in Table 1.3) lower the value of the required flow rate through the fuel assemblies, allowing the necessary coolant speeds for heat removal during shutdown to be achieved by natural convection alone. No external pressure head is needed, and many designs, such as some LFRs and the SSTAR reactor, do not require electromagnetic pumps to move coolant through the core [53].

Various physical properties of LBE also contribute to its candidacy as a preferred coolant. Its low melting point of 123.5°C makes reactor startup easy compared to startup in a reactor cooled by pure lead or certain molten salts. The low melting point coupled with LBE's high heat capacity helps to ensure that the coolant will be less likely to freeze in temporarily cold sections of the reactor, decreasing the risk of a loss of flow accident (LOFA) due to temperature fluctuations. This has been identified as a cause for concern for coolants whose melting points exceed room temperature, including LBE [54]. LBE's high boiling point of 1,670°C also ensures that there cannot be a drop in heat flux due to coolant boiling, as might occur in a situation such as departure from nucleate boiling (DNB) in light water reactors. Accident scenarios for the LFR show that the peak temperature reached in the core, even during an accident, is lower than the boiling temperature of LBE by a factor of 1.85 [24].

These properties of LBE coolant make possible a number of reactor concepts and designs that could not be achieved with other coolants. While all six coolants are capable of producing power in large, stationary commercial power plants, LBE-cooled reactors offer a wider range of compact and transportable designs due to its favorable physical, chemical and neutronic properties. Reactor concepts such as the SSTAR reactor or other 'battery' reactors consist of a fully enclosed, long-lived core that can be 'plugged in' to surrounding power conversion and heat removal equipment. Once

the fuel in the battery reactor is extinguished, the core can be disconnected, shipped back to the vendor or country of origin, and replaced with a fresh one. This allows countries that do not have the capability to produce nuclear fuel (or those for whom proliferation is a significant concern) to still have a source of safe and proliferation-resistant nuclear power.

The high fast flux levels attainable using an LBE-cooled core also lead to systems better suited to applications where high fluxes and higher power densities are desired. A reactor with a high fast flux is more suited to burning spent fuel, since a higher flux directly corresponds to less time needed to achieve the same burn-up. In a fast reactor, high flux levels also lead to a higher power density, which can be beneficial when designing reactors where space is at a minimum, such as on a submarine.

#### **1.1.4 Material Compatibility Issues with Lead and LBE**

The one major drawback to using lead and/or bismuth as a high temperature coolant is corrosion. Like many working fluids, oxygen is soluble to some degree in both lead and LBE. The transport of dissolved oxygen in the working fluid requires materials either to be protectively coated or to form their own coating via passivation. Many materials possess the ability to do this, and many working fluids can carry sufficient oxygen to induce passivation in materials such as stainless steels. The main difference that makes lead and LBE so incompatible with most materials is its behavior in environments that are below the potential (a combination of oxygen concentration and temperature) for forming protective iron oxides.

The behavior of stainless steels in gases such as air or steam is mainly dependent on the oxygen concentration in the working fluid. These steels have the ability of self passivation at moderate oxygen potentials, and they are not significantly attacked in reducing (oxygen poor) environments. The use of a gas such as helium removes this problem altogether, as it is inert. Liquid sodium is also fairly inert with respect to the austenitic stainless steels used in reactors, so it does not create a significant corrosion problem. Its corrosion is also highly predictable at certain temperatures and oxygen potentials. Lead and LBE present a special case, as corrosion mechanisms change

completely in the absence of sufficient oxygen to self-passivate.

Many metals have high solubilities in lead and LBE. Without an oxide layer protecting the surface of the metal, materials are free to dissolve into the working fluid. Nickel has a particularly high solubility of 4.8 wt. % in LBE at 700°C [55]. Alloys with even a few percent nickel are subject to severe liquid metal attack and dissolution in lead and LBE systems. This problem is further aggravated by the fact that the coolant is flowing in a thermal loop. In this situation, materials in the hot leg dissolve faster and precipitate out of solution in the cold leg, reintroducing the capability for dissolution as the working fluid returns to the hot leg. This creates a transport cycle, where formerly structural material in the hot leg is removed and deposited in the cold leg, simultaneously weakening the hot leg structural materials and clogging the pipes in the cold leg.

Pure iron oxide is a poor barrier to corrosion over the potential temperature range of operation (600 - 700°C), due to a phase transformation from magnetite to wüstite at 570°C [3]. Wüstite is a porous, brittle oxide phase that does not protect the underlying metal. Typical nickel-containing austenitic stainless steels therefore cannot be used in lead or LBE systems above this temperature, as without a protective iron oxide layer, the working fluid can leach nickel from both the base metal and any nickel bearing oxides, leading to porosity and further attack.

Both of the situations described above would lead to accelerated corrosion in regions where oxygen has been depleted, such as in pits or crevices, which function as powerful corrosion accelerators for materials in lead or LBE. As oxygen inside a pit, crack or crevice is consumed, it is not replenished by oxygen-bearing fluid from outside the crevice, as there is no way for fresh fluid to flow into the crevice. As a result, the oxygen potential can drop dramatically inside the crevice, thinning or even eliminating the protective passive oxide layer (if one exists) and leaving bare metal exposed to a very reducing environment. This causes crevices or pits to grow, resulting in stress concentrators and localized wall thinning.

Any material expected to perform well in LBE must be able to remain protected in such a severe case of crevice corrosion, as many crevices will exist in any reactor

by design. These crevices will exist at any location where two materials are touching or nearly touching. This can be accomplished by means of either an external coating, which would be applied to the part before service, or an intrinsic coating grown by the material itself. There exist a number of coatings that have performed very well at protecting the base metal, such as the Gepultse Elektronen Strahl Anlage (GESA) process developed by Müller et al. [56]. This coating will be discussed in the next chapter.

It is much more desirable from standpoints of economics, maintenance and reactor longevity to have a material that can create and regenerate its own coating in even the most reducing environments. Such a material must be able to form a fully dense oxide layer at extremely low potentials, and that layer must remain stable should the potential temporarily drop below the level required to reform it.

### **1.1.5 One Solution - A Functionally Graded Composite (FGC)**

A review of work on materials for lead and LBE to date reveals no single material that can both resist corrosion and withstand operating stresses at temperatures up to 700°C and compete economically. Rather than develop one single alloy with a complex composition or microstructure, a composite material whose layers satisfy requirements individually can function effectively as a system in the harsh environment of lead or LBE at 700°C.

This composite would require a corrosion-resistant layer to prevent liquid metal attack or oxidation in all environments and a structural layer to provide strength. The corrosion-resistant layer will rely on chromium and silicon to form a highly protective scale. It must be able to protect the composite from liquid metal attack or oxidation in a large range of oxygen potentials. These oxygen concentrations could be high enough to form lead or bismuth oxides, and low enough so that chromium oxide cannot form. However, the corrosion-resistant layer will not be capable of being structural, as it will be susceptible to radiation embrittlement. Therefore a structural layer must act as the backbone of the composite, providing the tensile strength, creep resistance and radiation resistance to keep its shape over the lifetime of the reactor. Finally,

these two layers must be microstructurally similar enough to form a tightly-bound interface, keeping the corrosion-resistant layer attached to the structural layer.

This approach has been widely used in the nuclear industry. Light water reactors typically use this composite approach in two places: the pressure vessel and the fuel cladding. Pressure vessels are made of thick carbon steel, which acts as the structural layer that hold the pressure. This is clad with a liner of stainless steel, applied by weld overlaying, which serves as the corrosion-resistant layer of the pressure vessel [57]. In fuel cladding tubes, which hold the fissile fuel in a reactor, tubes made of a zirconium alloy, such as Zircaloy-4 (Zr-1.5Sn-0.2Fe [58]), are clad on the inside with pure zirconium [59]. The pure zirconium acts as the corrosion-resistant layer, while the zircaloy acts as the structural layer. The zirconium liner on the inside of this type of fuel cladding, known as barrier fuel, helps prevent fuel-clad interaction [60]. These two groups of materials are not suitable for high-temperature fast reactor applications, so while the concepts may be similar, the choices for materials and dimensions must change.

### 1.1.6 General System Description

The proposed FGC relies on a thin corrosion-resistant layer based on the Fe-Cr-Si system. The presence of enough chromium and silicon creates a synergistic effect that forms an extremely thin, dense and corrosion-resistant scale on the surface of the metal. This oxide layer will be able to resist corrosion from both liquid metal attack (dissolution) and internal oxidation at any oxygen potential that could be encountered in an LBE-cooled reactor. The scale will do so by acting as a diffusion barrier to both oxygen ingress and metal dissolution, eliminating the problem of corrosion in these systems.

This corrosion-resistant layer will be supported by a structural layer made of a ferritic/martensitic material with a similar composition. A ferritic/martensitic microstructure was chosen for its superior resistance to radiation and its lack of change in physical properties at high dose rates [16]. This structural layer will possess superior resistance to creep resistance and radiation resistance, as backed up by extensive

industry experience and data. The corrosion-resistant layer will be weld-overlaid onto the structural layer to provide excellent interface characteristics, and ensure a smooth microstructural transition between the layers. The structural layer will also excel in corrosion resistance when compared to austenitic stainless steels, which have been shown to undergo severe attack above the wüstite formation temperature [61]. In the event of total cladding breach, the structural layer will corrode at a manageable, well-understood rate, as compared to the rapid, unpredictable nature of corrosion of austenitic stainless steels in LBE above 600°C.

## 1.2 Research Objectives and Thesis Goals

The main goal of this thesis is to design, produce and evaluate the effectiveness of an FGC material that will be successful at eliminating the problem of accelerated corrosion in lead- and LBE-cooled reactors and other systems, such as spallation sources. A graded material allows for the use of materials with specific advantages (corrosion resistance, strength, etc.) in a systems approach to achieve the maximum performance. However, a composite material presents a number of additional challenges when compared to a single alloy, as the interface between two different materials is often the weakest point in the FGC from a number of standpoints.

### 1.2.1 Performance Requirements of the FGC

The FGC proposed in this thesis must show highly favorable behavior as a complete system in the following areas:

- Corrosion Resistance - The layer of the FGC that faces the liquid metal coolant must be able to resist corrosion over its entire lifetime. This layer must be able to form its own passive coating upon exposure to LBE, even at very low oxygen potentials. This will ensure that should the protective film be breached for any reason, it can be reformed by the material even in the low oxygen environment of a crevice.

- Diffusional Stability - Joining the layers of the composite will result in diffusional mixing, due to differences in chemical potentials across the interface. The concentrations of corrosion resistant elements will be higher in the layer facing the liquid metal than in the underlying structural layer. This will result in a dilution layer at the interface, where the concentrations of one or more corrosion resistant elements could drop below the level necessary to reform the protective passivating layer. The thickness of this dilution layer will increase with time and higher temperatures. The evolution of the diffusional dilution layer must therefore be well understood, and its thickness must be measured as functions of time and temperature. This will allow for selection of a cladding layer thickness that does not compromise the corrosion resistance of the surface in contact with the lead or LBE.
- Microstructural Mixing - The two layers of the FGC must be in excellent mechanical contact, with little stress resulting from a microstructural mismatch. This requires that the two layers of the FGC have the same base microstructure; a ferritic layer joined to an austenitic layer would present mismatch problems. A sudden change in microstructure could result in accelerated corrosion should the cladding be completely breached. A mechanically and microstructurally sound interface will be the key to success during the various processing steps, where the two layers will be subject to immense forces. This will ensure that the layers stay bound during processing.
- Radiation Resistance - The composite as a whole, as well as the two individual layers, must be resistant to radiation swelling and embrittlement. Crystal structures and elemental concentrations must be designed with this in mind. The radiation embrittlement resistance of the cladding layer will not be quite as important, as an extremely thin, well-bonded layer will not be structural in any way. The interface will be of particular importance, as it has been shown that irradiation of composite materials accelerates diffusion (known as irradiation induced mixing) [62]. This property is most important for in-core

applications, such as fuel cladding. Radiation resistance is not a significant concern for ex-core applications, such as coolant piping.

- Mechanical Properties - The composite must be able to perform its necessary structural function as both coolant piping and fuel cladding for the lifetime of the reactor. Long, thin tubes of fuel cladding must be resistant to thermal creep and radiation induced creep. This places limits on the structural base layer of the FGC, as it must bear all the forces placed on the composite.

While it is notable just to create a new material that provides exceptional resistance to lead and LBE corrosion, in the end it doesn't mean much for future reactor designs if it cannot be fabricated on a commercial scale. A number of studies have been performed that evaluate the excellent corrosion resistances of many new, exotic alloys such as HCM12A [63], Kanthal-22 [64] and others [65, 66, 67], as well as the resistances of coatings designed to resist lead and LBE corrosion [68]. However, the majority of the alloys that show the most favorable results are not currently made in significant quantities (more than a few kg) by any commercial entity in the world today. This leaves much work to be done in order to rationalize using lead or LBE as a Gen. IV reactor coolant with these new materials, especially as the U.S. DOE has broadened its main focus away from gas-cooled reactors. It is currently reconsidering all the originally proposed Gen. IV coolants equally for reasons of re-evaluating the effectiveness of each one based on new research [32].

### **1.2.2 Impact of Success of the FGC**

The immediate implications for the success of the proposed composite material are:

- An increased thermodynamic efficiency due to a higher outlet temperature
- A higher hydrogen production efficiency due to more heat at higher temperatures
- An increased power density due to a higher permissible coolant speed



- A decreased core size, vessel size and plant footprint due to increased power density
  
- A safer design due to a drastic decrease in corrosion during an accident scenario

These advantages illustrate the need for such as composite. They also indicate just how much more viable lead and LBE become as potential reactor coolants should the corrosion problem be solved.

The successful development of this FGC represents an enabling technology for lead and LBE-cooled reactors, as well as other systems, such as neutron spallation sources. The success of this FGC means that oxygen control need not be as stringent, as the FGC will resist corrosion equally well at a wide range of oxygen concentrations. This completely removes the concern for catastrophic fuel cladding failure due to liquid metal attack, increasing the possible outlet temperature of these reactors from 550°C (the current limit) to 700°C. The new limit on outlet temperature will therefore be a function of the structural integrity of other reactor materials, *not* corrosion. This vastly increased outlet temperature represents huge gains in efficiency, both for thermal to electrical energy conversion as well as thermal energy to hydrogen production. This new system causes lead- and LBE-cooled reactors to become the most viable Gen. IV technology from standpoints of engineering feasibility and economics.

This sentiment has been echoed in very recent reports about the viability of comparable Gen. IV fast reactor technologies. The most recent MIT/EPRI/NEI advanced fuel cycle report states the following:

“... structural material corrosion has limited the actual peak coolant temperatures of LFRs to levels lower than SFRs resulting in lower thermal-to-electricity efficiency. Corrosion problems also limit the velocity of lead coolant through the reactor core, resulting in larger, more costly, reactor cores. New high-temperature metal alloys that are corrosion resistant in lead have been developed in the laboratory but have not been tested under the full set of credible reactor conditions. If the corrosion resistant characteristics of these alloys are confirmed for realistic reactor conditions and assuming that there are no other unexpected challenges, LFRs could become an attractive alternative to SFRs.” [69]

### 1.3 Outline

Chapter 2 presents the background information necessary to understand various aspects of this thesis insofar as the design of a corrosion-resistant composite for use in lead and LBE reactors is concerned. The characteristics of corrosion due to liquid lead and LBE will be discussed. Both the mechanisms by which corrosion occurs, as well as the effects of this corrosion on the underlying structural material, will be considered. Methods of corrosion control will be discussed, including control of molten metal chemistry (including oxygen), control over other aspects of the corrosive environment, and finally, the engineering of a corrosion resistant material. With these in mind, the selection of the alloy compositions, thicknesses, microstructures and layers comprising the composite will be derived using relevant data from the literature as well as thermodynamic calculations, known properties and phase diagrams. The specific dimensions of the composite will be chosen based on the intended uses, thermal-hydraulic constraints in the reactor, strength requirements, radiation embrittlement limits, corrosion limits, and finally the diffusional stability of the composite.

Chapter 3 summarizes the experimental methods used to fabricate the composite, test its properties and evaluate its effectiveness at meeting the required criteria. First, a description of the static corrosion setup will illustrate how the resistance of each alloy to liquid LBE at various times, temperatures and in different environments was

determined. Next, methods of testing the diffusional stability of the composite, as well as extrapolation to longer times, will be discussed. Fabrication of the samples as well as the effects of fabrication on the test results will be considered. A description of steps undertaken at commercial facilities to produce meaningful amounts of the FGC will be detailed. Relevant parameters from each step will be explained with the aim of illustrating how these parameters affect the integrity and performance of the FGC, both during subsequent processing steps as well as during operation. Following this will be descriptions of auxiliary tests performed on the FGC to evaluate the viability of further commercial steps, such as welding pipes made from the composite. Finally, a brief description of each analysis method will be given along with the relevant information that each method yields for evaluating the effectiveness of the FGC.

Chapter 4 summarizes the results from each group of experiments. Data and micrographs from the corrosion studies will be presented to demonstrate the corrosion resistance of the cladding layer, as well as what could be expected to happen should that outer corrosion resistant cladding be breached. This will yield to an expected corrosion zone thickness that must be accounted for when choosing the final dimensions of the composite. Electron microprobe analysis (EMPA) results from the diffusion studies will detail the degree of diffusion of Cr and Si from the cladding to the base material, as well as carbon from the base material into the cladding. Chromium and silicon must remain at high enough levels to continue to protect the FGC. Carbon diffusion will increase the hardness of the corrosion-resistant layer, both during processing and during operation. Microstructures and hardness data will shed light on microstructural changes in the composite, both in the bulk as well as at the interface between the two layers. Detailed microstructures and hardness profiles will show how the composite properties changed during each processing step. A preliminary tungsten inert gas (TIG) welding study demonstrates what happens to the first three weld overlay layers, while an ASME certified FGC welding study shows how welding the FGC in the field would take place, as well as the microstructural changes that arise from the welding process. Finally, a composite breach study shows what would happen should the cladding be completely breached from a standpoint of accelerated

galvanic corrosion and anodic dissolution into oxygen-deprived LBE.

Chapter 5 presents a discussion evaluating the overall effectiveness of this composite at raising the temperature limit on lead and LBE reactors. The corrosion resistance of each layer will be discussed based on the results, and extrapolations for corrosion resistance at the end of life of each product form will be made based on the data in this thesis. Diffusional characteristics will then be explained, and a model for extrapolating critical diffusion distances over the lifetime of the composite will be presented. The successes and shortcomings of each processing step will be detailed, and suggestions to improve each process will be given based on measured data and the literature. Special attention will be given to tailoring each processing step to ensure success with the next, as the FGC must exit each processing step at optimal conditions for the next one to begin. Following this will be a discussion on the quality of the ASME certified weld, along with implications on how to perform these welds in the field. Finally, the implications of this composite from standpoints of both reactor design and economics will be discussed, as this composite represents an enabling technology for lead- and LBE-cooled reactors.

Chapter 6 will summarize the results of this thesis, mainly with respect to the performance and processing of the FGC. Future work necessary for further evaluating the success and ultimate performance abilities of the composite will be discussed. This will include additional testing, radiation damage testing and recommendations for the next iteration of the composite.

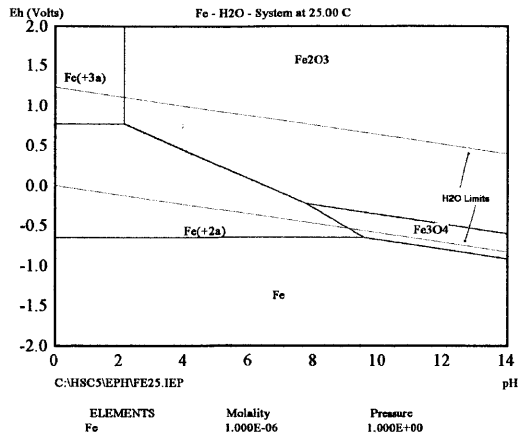
# Chapter 2

## Background

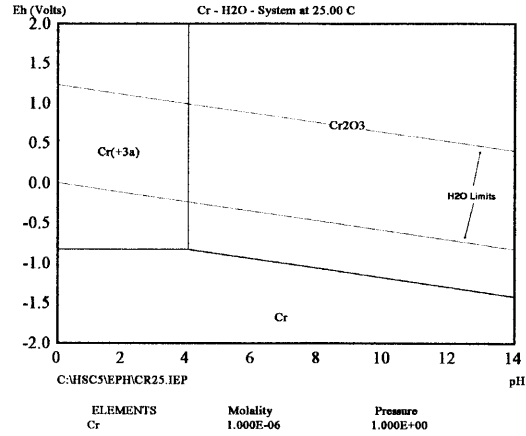
### 2.1 Characteristics of Liquid Metal Corrosion

Liquid metals exhibit key differences in corrosion characteristics when compared with familiar coolants such as water and inert gases. Without accounting for dissolved species (such as chlorides in seawater), the corrosion rates of many working fluids on most steels are mainly functions of oxygen concentration. High oxygen concentrations will rapidly corrode materials, such as wrought iron, by general corrosion, in which oxygen combines with iron to produce iron oxides, the familiar “rust” that one observes. This rust is not structural and flakes away easily, exposing fresh metal and beginning the corrosion process again. Stainless steels resist this corrosion by forming a passive oxide layer, whereby chromium oxide or mixed iron-chromium spinel oxides form rapidly in the presence of oxygen, creating a physical barrier that prevents further attack [11]. Decreasing the oxygen potential reduces the corrosion rate of non-passivating materials, while doing so for passivating materials can prevent the formation of the passive layer, as can be seen in the Pourbaix diagrams for passivating elements such as iron and chromium (see Figure 2-1). If this happens, the bare metal becomes subject to dissolution by the liquid metal, thus accelerating corrosion if the passive layer becomes unstable.

Liquid metals have the added disadvantage that the working fluid itself is highly corrosive, in addition to effects of the dissolved oxygen and other species the fluid



(a) Pourbaix diagram for pure Fe



(b) Pourbaix diagram for pure Cr

Figure 2-1: Pourbaix diagrams for pure Fe and pure Cr showing oxide stability zones in water as functions of pH and potential. Diagrams were generated using the HSC chemistry software package, version 5.1, by Outokumpu, Inc. Analogous regions exist for these metals in LBE. Zones where the pure metal is stable in LBE are subject to corrosion via dissolution.

may contain. Liquid metals such as lead, bismuth and LBE, can dissolve significant amounts of other metallic elements and have the ability to form alloys with the underlying steels. This adds rapid dissolution to the list of methods of corrosion. Any oxides present in the liquid metal, including PbO and Bi<sub>2</sub>O<sub>3</sub> from high oxygen concentrations, can circulate in the system and severely erode structural components, resulting in erosion-corrosion.

### 2.1.1 Thermodynamic Basis for Liquid Metal Attack by Lead and LBE

The thermodynamic basis for liquid metal attack of a self-passivating material mainly follows two methods, which are functions of the amount of dissolved oxygen in the liquid metal, the temperature, the stress levels in the material (both static and cyclic), the actual liquid metal and the composition of the material being corroded. The main difference between these processes is whether or not a passivating oxide layer is able to form. This potential for passive layer formation delineates whether or not the environment is considered oxidizing or reducing with respect to the passivating

layer. Oxidizing environments will encourage the formation of the passive layer, while reducing environments inhibit it. The presence of the passive layer introduces additional complications, while its absence opens the door for other accelerated forms of corrosion.

For most steels, this delineation can be determined from the Ellingham diagram, which identifies regions of metal/metal oxide stability as functions of temperature and Gibbs free energy. The relevant Ellingham diagram for the steels considered in this thesis is shown in Figure 2-2 [1]. In this diagram, the metal oxide is more stable above the solid line for a particular oxide, while the reduced metal is more stable below the solid line. The specific line to use when determining whether or not an environment is oxidizing or reducing for the material depends on which oxide(s) form thin, fully dense, passivating films.

#### **2.1.1.1 Oxidizing Environments**

In oxidizing environments, dissolved oxygen present in the liquid metal rapidly forms oxides. For purposes of maximum protection, the most protective oxides are those that are stable at lower oxygen potentials, in particular those containing chromium and silicon. This causes passive layers containing  $\text{Cr}_2\text{O}_3$ ,  $\text{SiO}_2$ ,  $\text{Fe}(\text{Fe}_x\text{Cr}_{2-x})\text{O}_4$  and  $\text{Fe}(\text{Fe}_x\text{Si}_{2-x})\text{O}_4$  to form first, as opposed to iron oxides, resulting in an iron oxide layer outside the iron-chromium-silicon mixed oxide layer [45]. This passivating layer resists further corrosion by two methods. First, it physically prevents any liquid metal from coming into contact with the underlying base metal, where the liquid metal could attack the base metal by dissolution. Second, it acts as an effective barrier against oxygen diffusion into the metal, cutting the corrosion current down by several orders of magnitude as compared to exposed metal. Comparison of diffusion coefficients by Bowen et al. and Hagel et al. for chromium in iron vs. chromium in  $\text{Cr}_2\text{O}_3$  illustrates this effect very well [70, 71]. The presence of a passivating oxide layer inhibits liquid metal dissolution by the same mechanism, as diffusion coefficients of metals in metal oxides are many orders of magnitude lower than those in metals. A compilation of relevant diffusion data from the literature show a number of experimental correla-

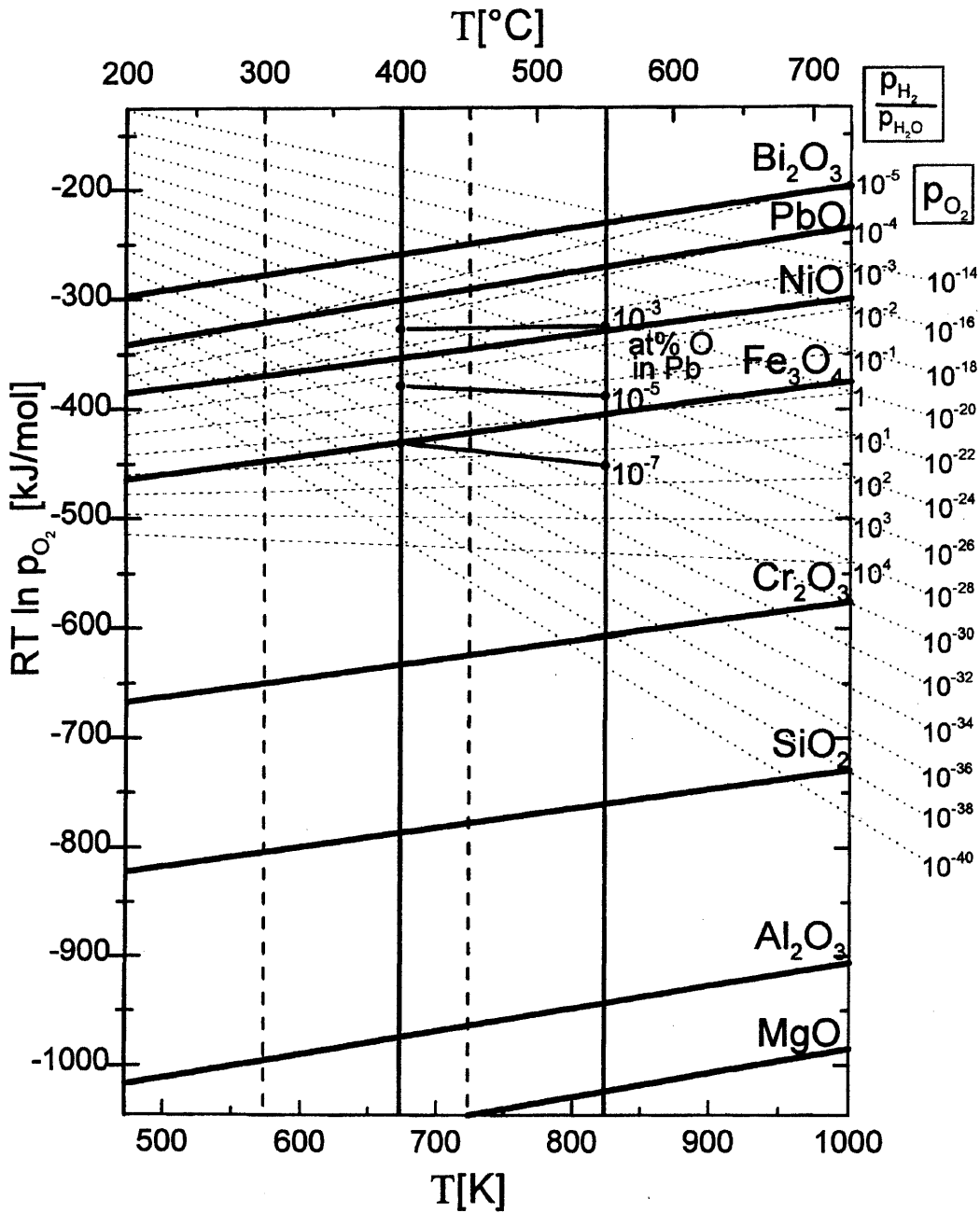


Figure 2-2: Ellingham diagram for metal/metal oxide systems found in this study [1]. Oxides are stable above each solid line, and metals are stable below each solid line. Oxygen concentrations and corresponding hydrogen to water vapor ratios are shown with dotted lines.



tions for the diffusion of oxygen and various metals in the FeCrSiAl-LBE system. These values, the temperature ranges for which they are valid and the references are summarized in Table 2.1. Figure 2-3 portrays this information in graphical form for easier comparison. This figure shows how passive layers prevent both oxidation and dissolution by acting as a diffusion barrier. The passive layer does grow over time, as the corrosion current and oxygen diffusion coefficients are not zero. However, because the interdiffusivities are so low in oxides, layer growth is extremely slow compared to growth in the absence of oxides. Dissolution is also extremely slow, as once the first few atomic layers of a metal oxide are exposed to the liquid metal, others cannot easily diffuse to the surface to take their place. The corrosion current for passive films can be approximated as zero as compared to the corrosion current on exposed metal.

A determination as to whether or not a passivating layer of a certain composition will be stable in liquid lead or LBE can be made by considering the Gibbs free energies of the metal alloying elements in the oxides as opposed to those of those metals in liquid lead or LBE as a function of temperature. The stability of oxygen in these oxides is always higher than in the liquid metal, as has already been shown in the Ellingham diagram in Figure 2-2.

### **2.1.1.2 Reducing Environments**

In reducing environments with respect to the protective oxide, there is no passivating film present to protect the underlying base metal. The metal is therefore subject to extremely fast liquid metal attack, the degree of which is determined by the solubility of a particular element, plus kinetics if the material is part of a thermal loop. Liquid metals attack many materials by dissolution. In this process, the liquid metals form liquid solutions with different elements present in the base metal, leaching them out and weakening the underlying structural material. The speed at which a large volume of liquid metal will dissolve a material is dependent on the solubility of that element in the liquid metal, which is in turn determined by the binary phase diagram between the liquid metal and that element. Relevant phase diagrams for elements in typical stainless steels in LBE are shown in Figure 2-4 [2, 3, 4, 5]. The most important

Solute	Solvent	Diffusion Correlation ( $\tilde{D}$ ) <sup>1</sup>	Cited Temp. (°C)	Ref.
Fe	$\alpha$ -Fe	$3.09 \times 10^{-4} e^{\left(\frac{-244800}{RT}\right)}$	790 - 920	[72]
Fe	Fe-9Cr	$9.3 \times 10^{-4} e^{\left(\frac{-115800}{RT}\right)}$	496 - 1,198	[73]
Fe	Fe-11.83Cr	$2.9 \times 10^{-3} e^{\left(\frac{-244764}{RT}\right)}$	660 - 890	[74]
Fe	FeSi	$3 \times 10^{-4} (20N_{Si}) e^{\left(\frac{-240800}{RT}\right)}$	740 - 1,100	[75]
Fe	Fe <sub>0.94</sub> O	$8.6 \times 10^{-7} e^{\left(\frac{-122800}{RT}\right)}$	700 - 1,340	[76]
Fe	Fe <sub>3</sub> O <sub>4</sub>	$5.2 \times 10^{-4} e^{\left(\frac{-230000}{RT}\right)}$	699 - 983	[77]
Fe	Cr <sub>2</sub> O <sub>3</sub>	$7 \times 10^{-8} e^{\left(\frac{-245000}{RT}\right)}$	700 - 1,100	[78]
Fe <sup>+3</sup>	SiO <sub>2</sub>	$6 \times 10^{-7} e^{\left(\frac{-288960}{RT}\right)}$	500 - 1,000	[79]
Fe	LBE	$4.9 \times 10^{-7} e^{\left(\frac{-44100}{RT}\right)}$	Not Cited	[80]
Cr	$\alpha$ -Fe	$8.52 \times 10^{-3} e^{\left(\frac{-250622}{RT}\right)}$	797 - 877	[70]
Cr	Fe-12Cr	$1.29 \times 10^{-3} e^{\left(\frac{-230538}{RT}\right)}$	797 - 1,402	[81]
Cr	Cr <sub>2</sub> O <sub>3</sub> <sup>2</sup>	$1.37 \times 10^{-5} e^{\left(\frac{-255642}{RT}\right)}$	1,045 - 1,550	[71]
Cr	Pb-17Li	$8 \times 10^{-11}$	500	[82]
Si	$\alpha$ -Fe	$1.7 \times 10^{-4} e^{\left(\frac{-228670}{RT}\right)}$	496 - 1,198	[73]
Si	Fe <sub>x</sub> Si <sub>1-x</sub>	$7.35 \times 10^{-5} (1 + 12.4N_{Si}) e^{\left(\frac{-219610}{RT}\right)}$	900 - 1,450	[83]
Si	SiO <sub>2</sub>	$8 \times 10^{-5} e^{\left(\frac{-501722}{RT}\right)}$	1,250	[84]
Al	$\alpha$ -Fe	$1.8 \times 10^{-4} e^{\left(\frac{-219990}{RT}\right)}$	496 - 1,198	[73]
Al	Al <sub>2</sub> O <sub>3</sub> <sup>3</sup>	$1.52 \times 10^{-22} e^{\left(\frac{-88869}{RT}\right)}$	1,333 - 1,818	[85]
O	BCC Fe	$3.7 \times 10^{-6} e^{\left(\frac{-97283}{RT}\right)}$	Not Cited	[86]
O	Fe <sub>3</sub> O <sub>4</sub>	$4.3 \times 10^{-11} e^{\left(\frac{-211000}{RT}\right)}$	505 - 650	[87]
O	Cr <sub>2</sub> O <sub>3</sub>	$6.9 \times 10^{-15} e^{\left(\frac{-111204}{RT}\right)}$	800 - 900	[88]
O	SiO <sub>2</sub> <sup>4</sup>	$2.1 \times 10^{-14} e^{\left(\frac{-111000}{RT}\right)}$	706 - 1,018	[89]
O	Al <sub>2</sub> O <sub>3</sub>	$1.12 \times 10^{-7} e^{\left(\frac{-155000}{RT}\right)}$	1,500 - 1,770	[90]
O	Pb	$1.48 \times 10^{-7} e^{\left(\frac{-25940}{RT}\right)}$	880 - 1,135	[91]
O	Pb	$6.62 \times 10^{-9} e^{\left(\frac{-16150}{RT}\right)}$	800 - 1,100	[92]
O	LBE	$2.39 \times 10^{-6} e^{\left(\frac{-43073}{RT}\right)}$	200 - 1,000	[93]

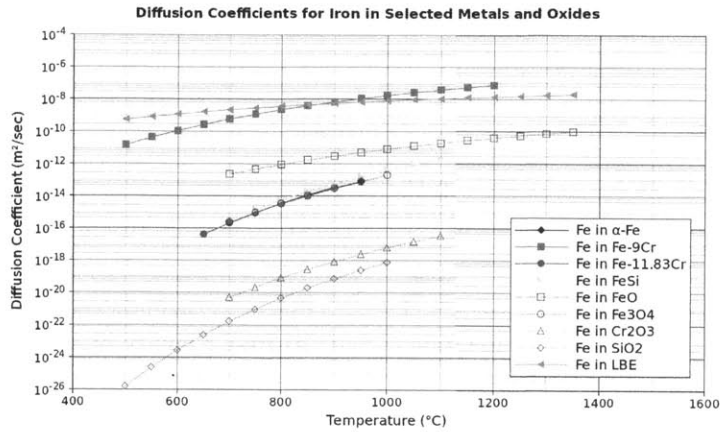
<sup>1</sup> $D_0$  is in units of m<sup>2</sup>/sec,  $E_A$  is in units of  $\frac{J}{mol}$ , T is the absolute temperature.

<sup>2</sup> $D_{eff}$  for Cr<sub>2</sub>O<sub>3</sub> film averaging both bulk and grain boundary diffusion

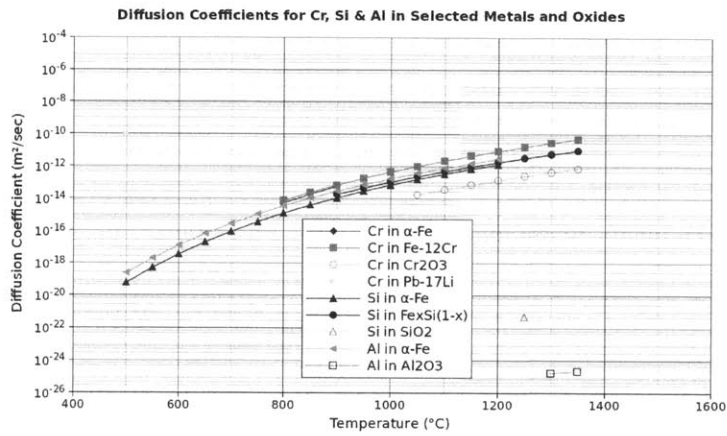
<sup>3</sup>Data for Al diffusion in Al<sub>2</sub>O<sub>3</sub> were obtained by simulation rather than by experiment.

<sup>4</sup>This value is for crystalline  $\beta$ -SiO<sub>2</sub>. Data are one order of magnitude lower for network glasses [89].

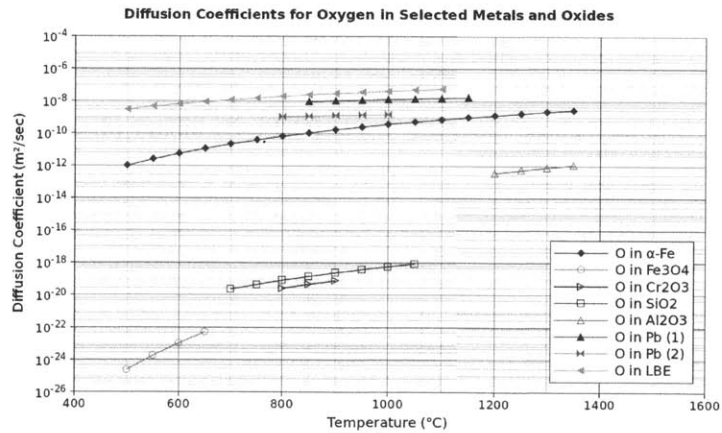
Table 2.1: Summary of relevant diffusion data for oxidation and dissolution processes in the FeCrSiAl-LBE system



(a) Diffusion coefficients for iron

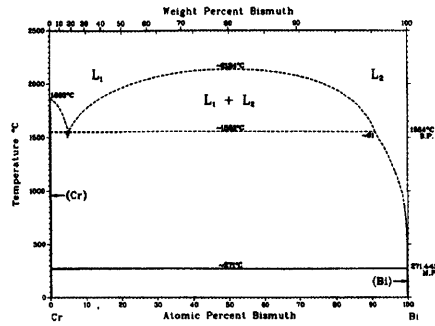


(b) Diffusion coefficients for chromium, silicon and aluminum

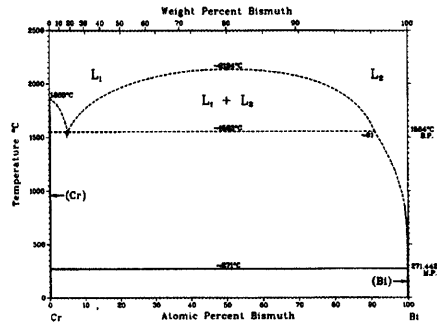


(c) Diffusion coefficients for oxygen

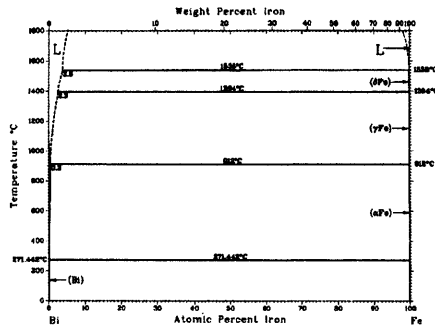
Figure 2-3: Examples of diffusion coefficients for metals and oxygen in relevant metals and oxides. Data are plotted over cited temperature ranges given in Table 2.1. Markers for metals are solid, while those for oxides are hollow. Note how much lower diffusion coefficients are for chromium and silicon oxides.



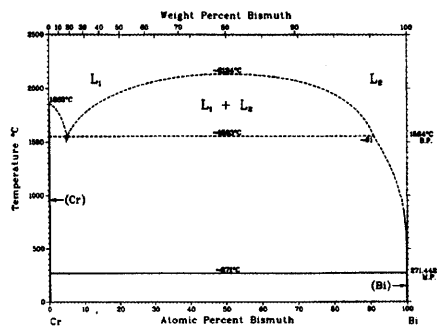
(a) Bi-Cr binary phase diagram



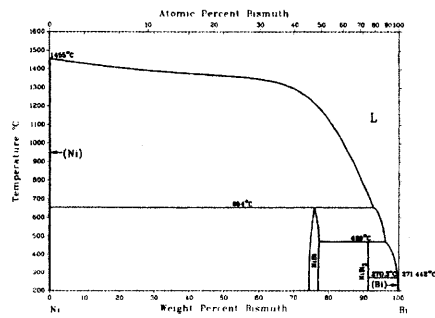
(b) Pb-Cr binary phase diagram



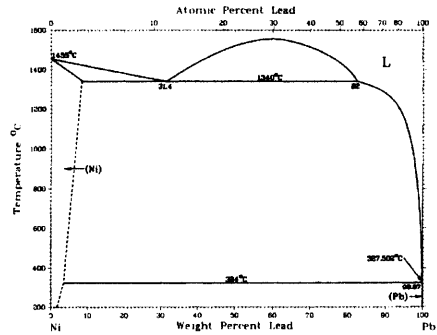
(c) Bi-Fe binary phase diagram



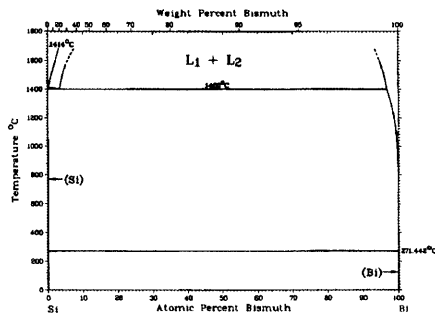
(d) Pb-Fe binary phase diagram



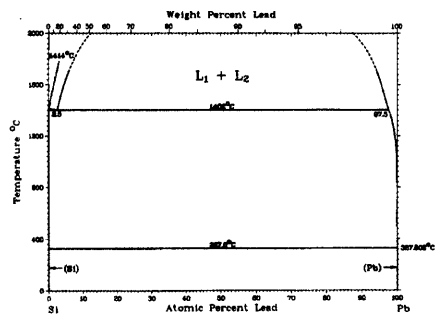
(e) Bi-Ni binary phase diagram



(f) Pb-Ni binary phase diagram



(g) Bi-Si binary phase diagram



(h) Pb-Si binary phase diagram

Figure 2-4: Relevant phase diagrams for stainless steels in liquid LBE [2, 3, 4, 5]. The most important features to note on these phase diagrams are the stability lines between the liquid phase and the two phase region on the high-Pb or the high-Bi side of each binary phase diagram.

features to note on these phase diagrams are the stability lines between the liquid phase and the two phase region on the high-Pb or the high-Bi side of each binary phase diagram. Iron and silicon exhibit very low solubilities in both lead and bismuth, as can be seen in Figures 2-4c, 2-4g, 2-4d & 2-4h. In these phase diagrams, the solubility line is so close to pure liquid lead or bismuth at relevant temperatures ( $\leq 700^\circ\text{C}$ ) that it is not discernible from the phase diagram.

This stands in stark contrast to binary phase diagrams for chromium and nickel (see Figures 2-4a, 2-4e, 2-4b & 2-4f), where the single phase region clearly exists far away from the pure liquid metal. The solubility of chromium in LBE (43 ppm wt. [94]) is much lower than that of Ni (46,132 ppm wt. [94]), but still noticeably higher than the solubilities of iron (32 ppm wt. [94]) or silicon (7 ppm wt. [95]). This is not expected to affect the material, because chromium bound in a passivating layer will not be as susceptible to liquid metal attack. This layer will partially form in air before ever being exposed to liquid lead or LBE. It is unlikely that the oxygen potential will ever fall below the potential necessary for  $\text{Cr}_2\text{O}_3$  formation, except in a crevice, where the oxygen concentration will quickly become depleted.

### 2.1.2 Mechanisms of Corrosion in Liquid Lead and LBE

A number of corrosion mechanisms are likely to occur in a composite used in a reactor that uses liquid lead or LBE as a coolant. Each one will be described here, even though the successful development of the proposed FGC will prevent many of these corrosion mechanisms from occurring.

**General Corrosion / Wastage** - A material that does not form a passivating layer in an oxidizing environment is subject to the rapid formation of oxides, followed by subsequent oxide separation from the metal surface. A good example of this is pure iron, which does not form a passivating layer at temperatures above  $570^\circ\text{C}$ . An examination of the iron-oxygen phase diagram shown in Figure 2-5 shows that at  $570^\circ\text{C}$ , the stable oxide phase changes from magnetite ( $\text{Fe}_3\text{O}_4$ ) to wüstite ( $\text{Fe}_x\text{O}$ ,  $x = 0.85 - 0.95$ ) [96]. Studies have observed that magnetite forms a relatively dense oxide layer [67], which forms an effective barrier to further corrosion by preventing

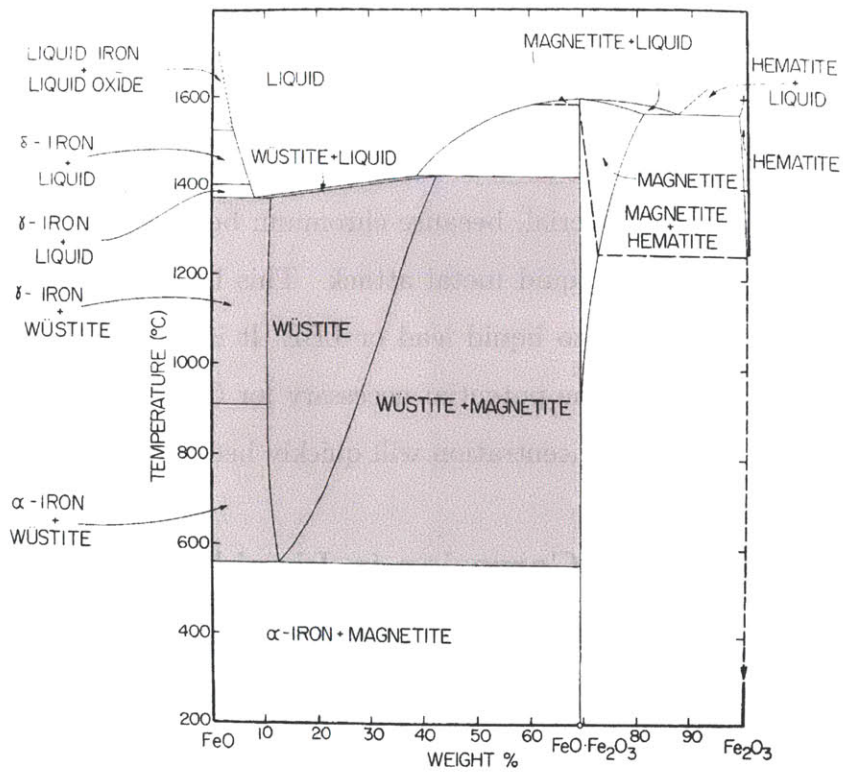


Figure 2-5: Iron-oxygen binary phase diagram, showing magnetite to wüstite phase change at 570°C [6]. Areas of wüstite stability are shaded.

oxygen diffusion into the metal from the coolant and by physically preventing contact between the base metal and the liquid metal. Wüstite, however, has been shown to form thick, porous layers of oxide that easily spall off in the presence of compressive stresses that form during oxidation [97]. These stresses could be caused by external forces, lattice mismatch stress due to thermal expansion between the metal and the oxide [98], and shear stress due to coolant flow, all of which will be present in a liquid metal cooled reactor. In addition, wüstite forms with a high degree of porosity above 570°C. This is due to a widely variable stoichiometry as can be seen in the Fe-O phase diagram in Figure 2-5, where different chemistries have different thermal expansions as temperature increases. This would allow liquid mixing and capillary action to draw LBE into the oxide layer, making contact with the underlying metal. The result would be the formation of a myriad of mini-crevices inside these capillary channels, where oxygen would be quickly consumed and the reducing liquid metal would rapidly attack the bare metal. Previous studies of non-passivating iron alloys have shown extremely rapid corrosion due to LBE penetration beneath the oxide layer and subsequent attack of the base metal [7]. Finally, it has already been shown in Figure 2-3 that the diffusion coefficient of iron is orders of magnitude higher in FeO than in Fe<sub>3</sub>O<sub>4</sub>, indicating that should solid wüstite form, it will prove ineffective at slowing down diffusion.

**Anodic Dissolution / Galvanic Corrosion** - For a passivating material in an oxidizing environment, fracture of the passivating film can lead to disastrous consequences if the film cannot quickly reform. This inability to repassivate could be caused by two different factors, both of which lead to the same end result. First, if the initial formation of the passive film caused the underlying material to become depleted in protective elements such as chromium and silicon, then exposure of the underlying base metal would not result in repassivation due to a lack of beneficial elements directly underneath the passive layer. This effect has been shown to occur in a number of different environments, both oxidizing and reducing with respect to iron oxides [99]. Second, if the composite is diffusionaly unstable (diffusional dilution occurs very quickly), the underlying base metal can become depleted in passivating

alloying elements via migration away from the surface down a chemical potential gradient. This could occur if the diffusion coefficient for that alloying element in the composite was too large, or if the cladding layer of the composite were too thin. Either way, both of these scenarios result in the inability of the composite to reform its protective oxide layer.

The effects of this inability to repassivate would be disastrous. The corrosion potential for a bare metal is far lower than that of its passivating oxide, as evidenced by the high reduction potentials of passivating metals (such as Cr or Al) as compared to those for Pb or Fe [11]. This in effect sets up a localized electrochemical cell, in which a voltage difference provides the driving force for both the dissolution of the anode (exposed base metal) and oxygen gas formation on the cathode (passivated region). Furthermore, conservation of charge requires that the current that leaves the anode must be equal to that which enters the cathode. The surface area of the exposed anode is far smaller than that of the cathode, so the amount of dissolution per unit of surface area required to sustain conservation of charge is proportional to the factor of surface area difference between the cathode and the anode. The “electrolyte” in this electrochemical cell is extremely conductive, being a liquid metal. This situation would lead to drastically accelerated corrosion at any location where the passive film would be breached. A diagram that illustrates this process is shown in Figure 2-6.

**Stress Corrosion Cracking (SCC)** - In the case that the metal can repassivate itself, the composite will still be subject to SCC in the presence of a sufficient static stress. During SCC, a stress high enough to fracture the oxide layer results in rapid repassivation of the exposed material. The formerly cracked region has healed itself; however, the discontinuity in the oxide layer morphology as a result of this healing process forms a region of stress concentration in that layer. Continued stress application can cause more fracture/repassivation cycles at that initial point. This can lead to accelerated crack propagation through what superficially appears to be corrosion-free material, as the site of SCC initiation will continue to fracture deeper and deeper while the rest of the oxide layer remains untouched.

The initiation and propagation of stress corrosion cracking requires the combina-



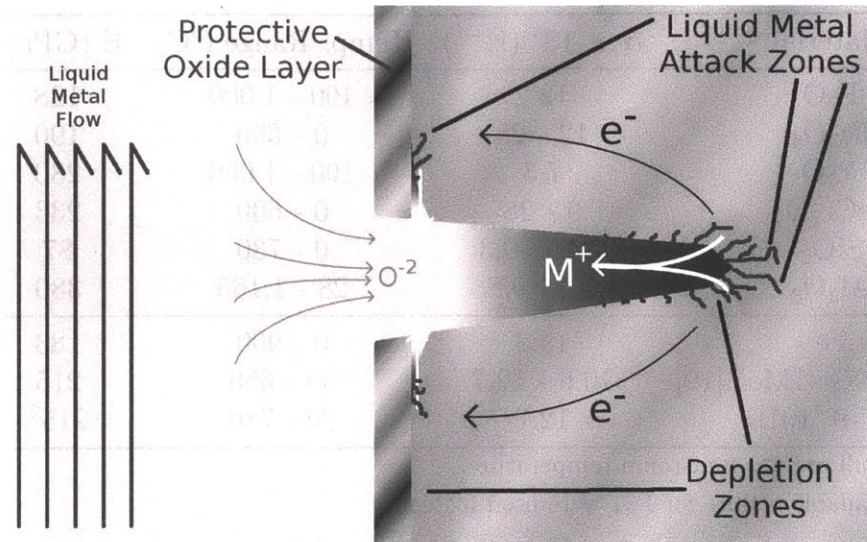


Figure 2-6: Diagram showing how passive layer breaching would lead to accelerated anodic dissolution. The zones beneath the oxide have been depleted in passivating metals, leading to accelerated dissolution and liquid metal attack. The deepest part of the crevice lacks sufficient oxygen to passivate, and is attacked by liquid metal dissolution.

tion of a sufficient stress, a corrosive environment and a material susceptible to this mode of cracking. In the case of the stainless steels used in lead and LBE reactors, this corrosive environment is always present. Corrosion is possible as long as sufficient oxygen exists, and the material will always be susceptible to corrosion unless it becomes depleted in passivating alloying elements, at which point it would become more susceptible to anodic dissolution or general corrosion. The main factor that can initiate SCC given the materials in the proposed FGC is therefore the presence of a tensile stress. The main causes of these stresses in the oxide layer are differences in thermal expansion and deformation of the underlying base metal, assuming a properly adherent oxide layer. Large stresses with differences in thermal expansion or density can cause the oxide layer to separate from the metal surface, more greatly affecting the general corrosion resistance of the FGC.

The difference in thermal expansion between the oxide and the base metal results in a stress that is dependent on a number of factors, as derived by Tien and Davidson

Material	$\alpha \times 10^6$ (K <sup>-1</sup> )	Temp. Range (°C)	E (GPa) <sup>1</sup>	$\nu$
FeO	12.2	100 - 1,000	128	0.36
Fe <sub>3</sub> O <sub>4</sub>	12 - 25	0 - 600	190	0.29
Cr <sub>2</sub> O <sub>3</sub>	7.3	100 - 1,000	280	0.29
FeCr <sub>2</sub> O <sub>4</sub>	9 - 28	0 - 600	233	0.31
SiO <sub>2</sub>	7.4 - 30.3	0 - 730	87	0.07
Al <sub>2</sub> O <sub>3</sub>	5.1 - 9.8	28 - 1,165	380	0.24
Fe	15.3	0 - 900	183	0.29
F91 (Fe-9Cr-1Mo) [19]	10.6 - 12.7	50 - 650	215	0.33
HT-9 [101]	12.7	20 - 780	215 <sup>2</sup>	0.33 <sup>2</sup>

<sup>1</sup>Elastic moduli are given at room temperature.

<sup>2</sup>Data not available, values for F91 were used instead.

Table 2.2: Physical parameters for oxides and metals considered for the proposed FGC [12]

[100]:

$$\sigma_{oxide} = \frac{-E_{oxide}\Delta T(\alpha_{metal} - \alpha_{oxide})}{\frac{E_{oxide} t_{oxide}}{E_{metal} t_{metal}}(1 - \nu_{metal}) + (1 + \nu_{oxide})} \quad (2.1)$$

where  $E$  is the Young's modulus,  $\Delta T$  is the change in temperature from the temperature at which the oxide formed,  $\alpha$  is the coefficient of thermal expansion,  $t$  is the thickness and  $\nu$  is Poisson's ratio. In this particular FGC, the thickness of the oxide layer must be very small to avoid significant corrosion or underlying element depletion, so the ratio  $\frac{t_{oxide}}{t_{metal}}$  is approximately zero, and Equation 2.1 simplifies to:

$$\sigma_{oxide} = \frac{-E_{oxide}\Delta T(\alpha_{metal} - \alpha_{oxide})}{1 + \nu_{oxide}} \quad (2.2)$$

The values of the properties used in Equation 2.2 for the relevant oxides that are considered for the proposed FGC are summarized in Table 2.2. In order to account for the total stress that can propagate SCC through the material, the stress on the interface caused by thermal expansion must be added to the static stress placed on the part as a result of design. The most extreme stress experienced by this material during normal operation will be during plant shutdown, when the part is at its coldest, because oxides will grow the most during the highest temperature operation of the reactor. Temperature differences could be as high as 700°C in this case. Sound design

will result in the total stress being smaller than that the amount that is necessary for SCC propagation by a wide margin. This is because liquid metal reactors do not require high pressures to operate.

**Liquid Metal Embrittlement (LME)** - LME is more of a concern than SCC, given the combination of high stress and hot liquid metal that parts in an LBE-cooled reactor will be subject to. LME occurs when a metal is in contact with a liquid metal while simultaneously undergoing a tensile stress [11]. This would be a constant concern for fuel cladding, as pressure from fission gases could build up inside the cladding at tens to hundreds of MPa. Plenum pressures in fuel pins in EBR-II were measured at up to 15 MPa, and a commercial-size reactor would experience an even higher burnup [102]. Liquid metals, such as LBE, can diffuse quickly along grain boundaries or preferentially dissolve them, causing rapid and severe embrittlement of the material. This has been shown to occur in alloy F91 by Long and Dai [103]. Again, LME requires the maintenance of a tensile stress to propagate, like SCC. A material that cannot support enough tensile stress to propagate LME would be more resistant to this failure mechanism.

**Corrosion Fatigue Cracking (CFC)** - This mechanism is similar to that of SCC, but it involves a cyclic stress instead of a static one. CFC can cause very rapid part failure in the event of a high cyclic stress frequency as a stress that cannot initiate SCC superimposed with a cyclic stress can propagate a crack. This can occur as a result of vibrations or resonances in the reactor design. If this superposition of stresses occurs, it can exceed the propagation stress for CFC, especially with a pre-existing flaw acting as a stress concentrator. These flaws could exist due to defects from processing, scratches or abrasions incurred during plant operation, or, in the case of the fuel cladding, from void creation and radiation swelling.

The main difference between CFC and SCC is the presence of corrosion products in the crack. CFC is more likely to occur in systems such as liquid LBE, as LBE ingress into the crack can cause dissolution, with the fastest mass flux at the crack tip. This is because the tip of the crack would be the most depleted in oxygen, resulting in the lowest stability (or lack of stability) of a passive oxide layer. As a

result, the fractures tend to be transgranular, while those of SCC are intergranular [11]. Cyclic stresses could be present in LBE-cooled reactors due to pumping of the coolant, where pressure variations can cause crack propagation. In addition, thermal expansion stresses from startup and shutdown can contribute to low-frequency CFC.

**Dissolution / Flow Assisted Corrosion (FAC) / Mass Transport** - For materials that do not form a passive film, due to a lack of beneficial alloying elements or absence of a reducing environment, the liquid metal is free to alloy with the material and dissolve it. The thermodynamic basis for this was shown in the binary phase diagrams in Figure 2-4. In static environments, liquid lead and bismuth can quickly saturate with soluble alloying elements, especially if those elements have particularly low solubilities, such as iron and silicon. However, a reactor that uses lead or LBE as a coolant would have large mass flows and temperature gradients, paving the way for accelerated dissolution and mass transport.

Materials that form an unstable film that can be easily dissolved in flowing coolant, such as wüstite in LBE, are subject to accelerated corrosion rates by FAC. In this scenario, the unstable film is simultaneously formed and dissolved into the flowing coolant, exposing fresh metal for more film formation. This process can lead to higher corrosion rates than those from dissolution alone.

As can be seen on the binary phase diagrams and the solubility curves in Figure 2-7, the solubilities of alloying elements in liquid lead, bismuth and LBE are strongly dependent on temperature. The difference in temperature between the hot leg and the cold leg of a reactor becomes the driving force in a mass transport loop, as the material dissolves more easily in the hot leg. Upon entering the cold leg, the liquid metal becomes supersaturated in that alloying element, and some of it drops out of solution. This coolant then re-enters the hot leg, dissolves more material up to its saturation point, and the cycle continues. A diagram of this process is shown in Figure 2-8.

In addition to generalized liquid metal attack by dissolution, the grain boundaries of some metals are particularly susceptible to dissolution and liquid metal attack. These are typically metals that have high grain boundary free surface energies. Ma-

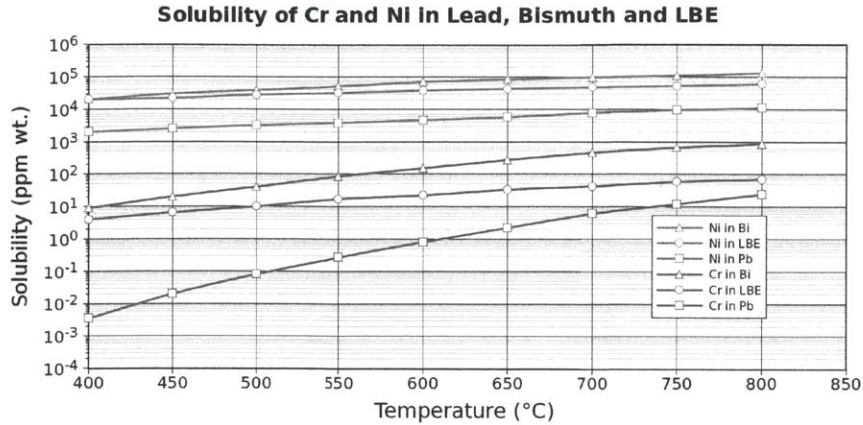


Figure 2-7: Solubilities of Cr and Ni in liquid lead, LBE and bismuth as functions of temperature [7]. These were derived from the binary phase diagrams for each combination of metals.

materials with a high degree of internal stress, such as fully hardened martensite, are particularly susceptible to this phenomenon. Müller et al. have observed LBE preferentially attacking grain boundaries, subsequently causing rapid dissolution nearby as the hollowed-out grain boundary quickly becomes depleted in oxygen [104].

### 2.1.3 Kinetics of Corrosion in Lead and LBE

While an actual reactor is a non-isothermal flowing system that functions as a mass transport loop, budget and time constraints forced the experiments in this thesis to be conducted in an isothermal, static system. A description of corrosion kinetics in static environments will be given first, followed by how the kinetics would change in the dynamic environment of a reactor coolant loop.

#### 2.1.3.1 Static Corrosion

In the absence of any active system for mass transport, the only motion possible in the corrosive environment is due to convection currents and diffusion in the liquid metal. These processes produce a very slow flow that can be neglected when considering corrosive processes, unless the system is a natural circulation loop where higher flow rates naturally occur. In addition, an isothermal experiment results in a fixed value for the solubilities of the different elements in the liquid metal. The two competing

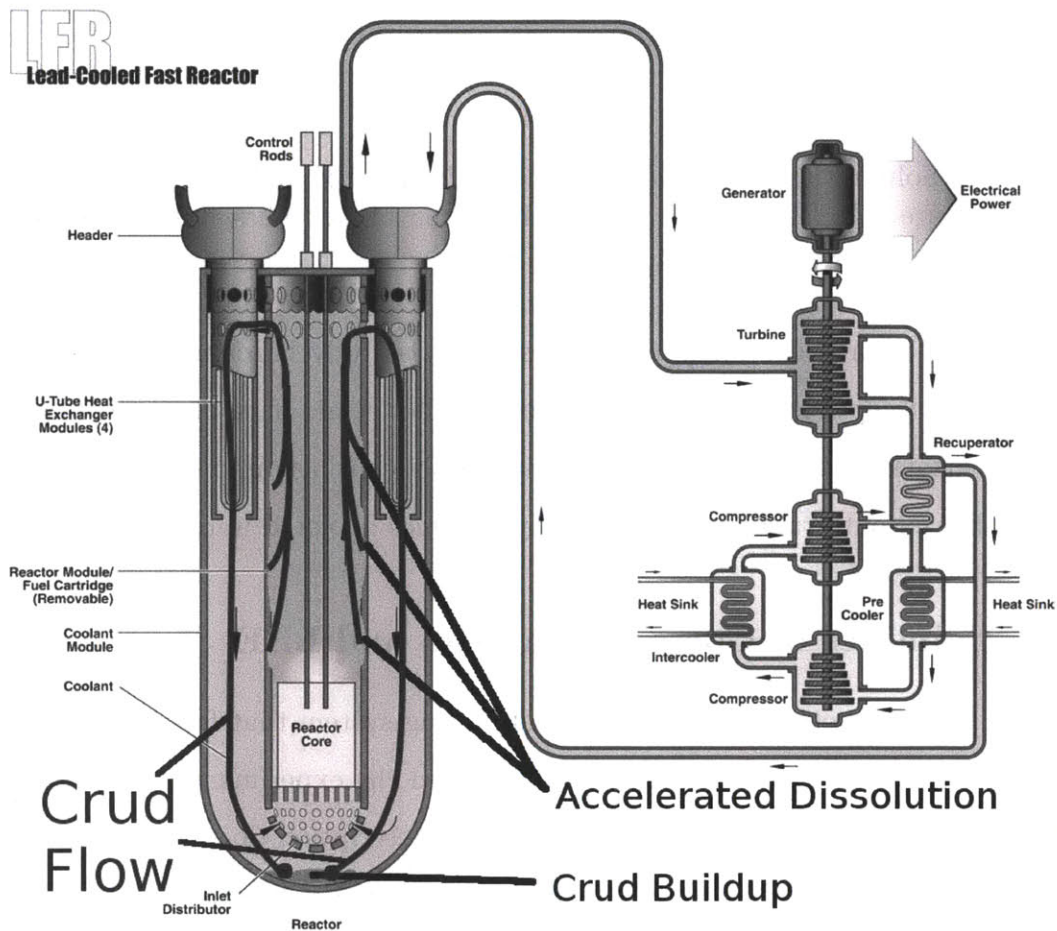


Figure 2-8: Diagram of how mass transport works in a flowing liquid metal loop, such as in the LFR. Solubilities increase as a function of temperature, so materials dissolve more in the hot leg. When the solubility drops in the cold leg, these materials drop out of solution. This cycle causes faster dissolution in the hot leg and crud buildup in the cold leg. (Photo courtesy of INL [8])

processes for corrosion in static, isothermal environments are therefore dissolution (liquid metal attack) and oxidation. The driving force for dissolution is simply the difference in concentration of a particular alloying element between the compositions of the base metal and the liquid metal. The mass flux due to dissolution is therefore proportional to this concentration difference, and is given by the following equation:

$$\dot{m} = K (C_{i,sat}(T) - C_i(T)) \quad (2.3)$$

where  $\dot{m}$  is the mass flux (change in mass per unit area),  $C_{i,sat}$  is the maximum solubility of element  $i$  at absolute temperature  $T$ , and  $C_i(T)$  is the actual concentration of element  $i$  at temperature  $T$  in the liquid metal. In a static system, the speed of dissolution will mainly be governed by diffusional mixing of the solute in the liquid metal, which is a function of the diffusion coefficients of that solute, both in the liquid metal and in the base metal. On the whole, diffusion occurs more quickly in the liquid metal than in the base metal. During steady state, the diffusion coefficient of the solute in the outermost layer of the base metal, be it bare metal or oxide, is the dominating factor in the dissolution process. This will be preceded by faster dissolution at the surface of the bare metal, as an initially larger difference in concentration will lead to a faster mass flux.

Models were developed to illustrate this effect using MatCalc, a comprehensive materials science software package built around the ThermoCalc thermodynamic database, written by Ernst Kozeschnik et al. [105]. The multicomponent diffusion package was used to simulate the boundary between the liquid metal and the base metal when a passive layer of varying thickness was present or absent altogether. Values for interdiffusivities were calculated from Table 2.1. Because the base metal and liquid metal thicknesses were so much thicker than any typical oxide coating, they were modelled as semi-infinite slabs, while the oxide coating was assumed to be a  $2\ \mu\text{m}$  thick layer of pure  $\text{Cr}_2\text{O}_3$ . Figure 2-9 shows two such models for comparison. The first model shows the oxygen concentration in a bare metal, assuming that an oxide does not form. The second model shows the oxide concentration as a

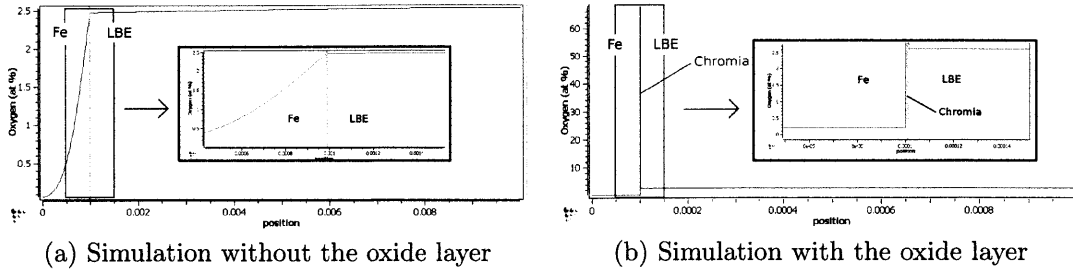


Figure 2-9: MatCalc simulations of oxygen diffusion in  $\alpha$ -Fe immersed in 700°C oxygen-rich LBE for one hour, with and without a 2  $\mu\text{m}$  thick layer of chromium oxide. The thin chromium oxide layer acts as a very effective barrier to oxygen diffusion due to the low diffusivity of oxygen through chromia. The initial oxygen concentration of the  $\alpha$ -Fe was assumed to be zero, and diffusion coefficients were assumed to be independent of concentration. The formation of oxide phases was also not considered in this simulation.

function of depth with a 2  $\mu\text{m}$  thick layer of pure  $\text{Cr}_2\text{O}_3$  on top of the metal surface. A model was not developed for wüstite, as it is nonpassivating above 570°C [96]. Diffusion coefficients were taken from Table 2.1 at 700°C in meters per second as follows:  $\tilde{D}_{O \text{ in } Fe} = 2.2 \times 10^{-11}$ ,  $\tilde{D}_{O \text{ in } LBE} = 1.16 \times 10^{-8}$ ,  $\tilde{D}_{O \text{ in } Cr_2O_3} = 8 \times 10^{-21}$  (extrapolated) [86, 93, 88]. The two models show how much a 2  $\mu\text{m}$  layer of fully dense  $\text{Cr}_2\text{O}_3$  restricts the diffusion of oxygen into the metal, preventing internal oxidation. The oxygen concentrations present below the  $\text{Cr}_2\text{O}_3$  scale are only sufficient to grow  $\text{Cr}_2\text{O}_3$  or  $\text{SiO}_2$ , which would continue to enhance this protective effect.

### 2.1.3.2 Flow Assisted Corrosion

In the presence of sufficient mass flow, solute atoms that diffuse out of the metal into the coolant are carried away by mass transfer processes. A non-isothermal system ensures a continuous flow of coolant (unsaturated in the solute) to the hot leg of the loop. The ability of a flowing loop to dissolve material from the hot leg depends on the difference in inlet and outlet temperature, the solubility of that species in the coolant, and the mass flow rate of the coolant. Balbaud-Célérier and Barbier have represented the four main regimes of flow assisted corrosion schematically, as shown in Figure 2-10 [9].

For coolant velocities that are negligibly small (see region A in Figure 2-10),



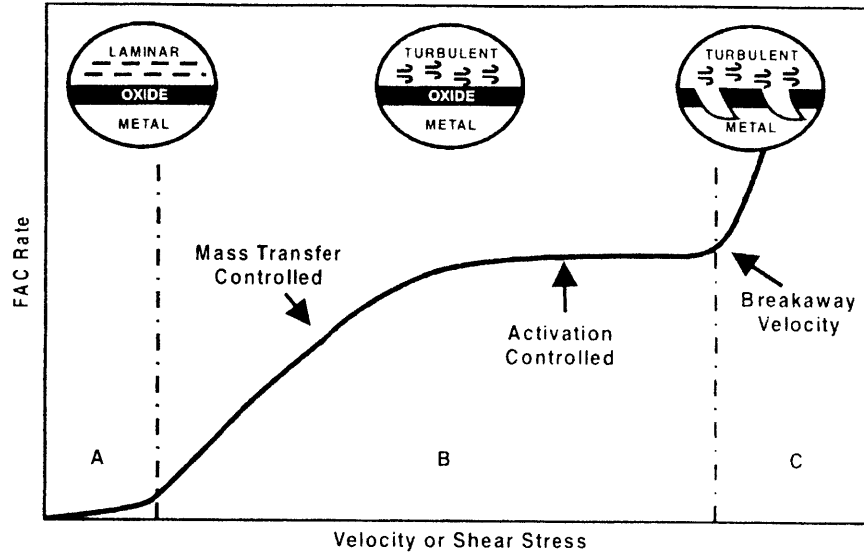


Figure 2-10: Regimes of flow assisted corrosion, showing mass loss rate vs. coolant velocity [9]

the corrosion rate is determined by the diffusion rate of the solute in the metal, as explained in Section 2.1.3.1. For sufficiently low, yet non-negligible, coolant velocities (see the left half of region B in Figure 2-10), diffusion of the solute into the bulk of the coolant from the base metal is still the limiting step in the process. Consequently the dissolution rate will grow proportionally to the mass flow rate in the loop, because the limiting step in removing material from the hot leg is not dissolution, but rather transport away from the hot leg.

As the coolant flow velocity increases (see the right half of region B in Figure 2-10), the assumption of a static boundary layer at the coolant-metal interface begins to break down as laminar flow gives way to turbulent flow. The concentration of the solute at the coolant-metal interface can then be assumed to be a function only of distance through the hot leg, leading to a model based on simple pipe geometry. In this case, the force that drives dissolution is the difference in solute concentration. We assume that the loop has sections with sufficient length and surface area for the concentrations of the dissolved species in the liquid metal to reach equilibrium in each section. For a single such species, the mass transport rate can now be found via the

following equation:

$$\frac{d\dot{m}_{species}(x)}{dt} = \dot{m}_{coolant}(S(T_H(x)) - S(T_C(x)))dA \quad (2.4)$$

where  $\dot{m}_{species}$  is the mass change in the base metal per unit area,  $\dot{m}_{coolant}$  is the mass flow rate of coolant,  $S(T)$  is the solubility of that species as a function of temperature,  $T_H$  is the absolute temperature in the hot leg and  $T_C$  is the absolute temperature in the cold leg. In reality, the concentration of each alloying element in the liquid metal changes the solubilities of the others, which are all functions of temperature. Therefore the equation that relates the total mass transport of the loop to the solubilities and temperatures is:

$$d\dot{m}_{total} = \dot{m}_{coolant}dA \sum_i^n [S_i(T_H(x), c_{j \neq i}(T_H(x))) - S_i(T_C(x), c_{j \neq i}(T_C(x)))] \quad (2.5)$$

where  $c_j(T)$  is the concentration of species  $j$  at absolute temperature  $T$ . While the presence of other species tends to deter the dissolution of others due to a shift in the chemical potential of each species [106], the overall effect of large amounts of dissolution outweighs this competition. This is because mass transport in a thermal loop removes material from the hot leg by dissolution, which then precipitates out of solution in the cold leg of the loop. This results in a large amount of mass transport of dissolved species due to flow assisted corrosion.

If the coolant has a sufficiently high velocity, so that shear forces can spall off the oxide layer, or if the coolant contains solid phases that impinge upon the oxide layer with sufficient force, erosion-corrosion will take place. In this scenario, sizable pieces of oxide (and perhaps base metal) are broken off, quickly eclipsing the effects of any dissolution that takes place (see region C in Figure 2-10). Due to the relatively low flow speeds (1 - 4 m/s) of liquid lead and LBE [24], this scenario is most likely to happen if there are solid phases present in the liquid metal coolant. This is most likely to occur if the oxygen potential rises above that for PbO or Bi<sub>2</sub>O<sub>3</sub> formation.

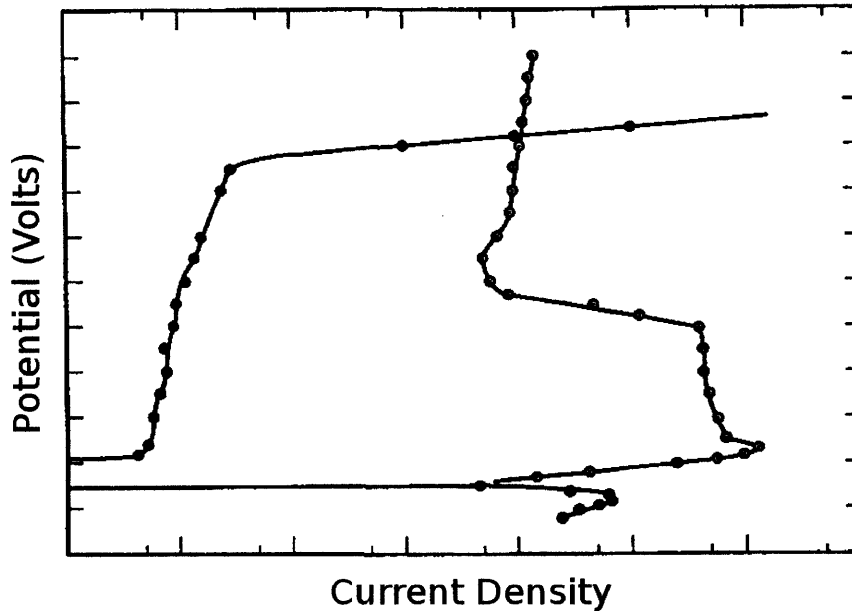


**Fig. 7. Anodic polarization of iron and chromium in normal sulfuric acid:  $\circ$ , Fe;  $\bullet$ , Cr.**

Figure 2-11: Example potential-current curves for Fe and Cr in sulfuric acid, demonstrating how and at what potentials passivation drastically lowers the corrosion rate [10]. Data to the left of the graph represent lower corrosion currents. The regions of each curve where the corrosion current suddenly drops between voltages of -0.4 V and 1.2 V represent regions of passivation.

## 2.2 Prevention of Liquid Metal Corrosion

### 2.2.1 Passivation of Alloys in Lead and LBE by Oxide Formation

As has been shown in Section 2.1.3, the most effective way to prevent liquid metal corrosion is to have a physical barrier present on the base metal whose diffusion characteristics are orders of magnitude slower than those of the base metal. This can be accomplished in a number of ways, as long as the passive layer remains stable. Alloys that undergo passivation are marked by a region of very low corrosion current on a potential-current diagram. An example of these diagrams that contrasts a non-passivating material (pure iron) with passivating ones (pure chromium and Fe-10.5Cr) in an oxidizing environment (sulfuric acid) is shown in Figure 2-11. Looking at the

curve for iron, one can see that starting at about 0.25 V there is a moderate drop in corrosion current for iron as it forms an oxide. However, looking at the curve for chromium, one can see that there is a severe (4 - 6 orders of magnitude) drop in corrosion current around -0.7 V (very close to the formation potential for  $\text{Cr}_2\text{O}_3$  [11]) that continues until 1.2 V. The Pourbaix diagrams for iron and chromium are shown for reference in Figure 2-1, to show how features on the potential-current diagrams match up with those on the Pourbaix diagrams. Alloys that are said to passivate all possess a similarly drastic change in corrosion current at and above the formation potential of their passivating oxides. Below this level the electrochemical potential favors the reduced metal instead of the oxide.

Passivation in liquid metals (as well as in many oxygenated environments) is normally characterized by an initially fast formation of a dense oxide layer. The growth of this layer is inversely proportional to its thickness. The thicker it gets, the more difficult it is both for solutes to diffuse to the surface to form oxides and for oxygen to diffuse through the passive layer to form a region of internal oxidation. Figure 2-12 shows an example curve of passive corrosion rate versus time, illustrating that the rate of corrosion decays exponentially with time as the layer grows in thickness at a decreasing rate. Passivation can also be composed solely of a layer of adsorbed oxygen on the surface. The presence of oxygen on the metal surface physically prevents the liquid metal from coming into contact with the structural material, protecting it just as a passivating oxide layer would.

While the formation of passive layers in Fe-Cr-x alloys starts almost instantaneously, it does not form fast enough to completely preclude diffusion from taking place. Oxides that form at high oxygen potentials form first, and then their presence lowers the oxygen potential such that only more stable oxides can form at the metal/film interface. For that reason, a multilayered (rather than a single layered) oxide film often forms on the surface of Fe-Cr-x alloys. Numerous studies of various Fe-Cr alloys, such as F91 [107], HT-9 [108] and HCM12A [109] show that up to five oxide layers tend to form on these steels in oxidizing environments such as in LBE or supercritical water. A schematic of which oxide layers tend to form, and in which

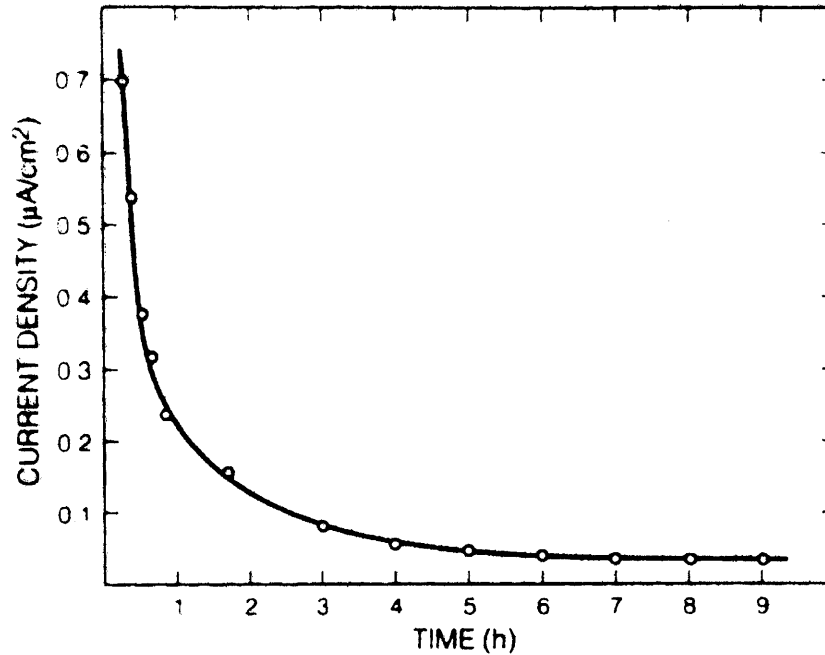


Figure 2-12: Example curve of passive corrosion rate versus time [11]. Formation of the passive layer is marked by fast formation, immediately followed by a sharp decrease in corrosion current density due to protection of the underlying metal by the passivating oxide.

Temperature/Oxide	FeO	Fe <sub>3</sub> O <sub>4</sub>	Cr <sub>2</sub> O <sub>3</sub>	SiO <sub>2</sub>	Al <sub>2</sub> O <sub>3</sub>
0°C (273 K)	-245.6	-1,018.0	-1,060.0	-824.4	-1,583.0
717°C (1,000 K)	-198.2	-795.1	-877.0	-698.0	-1,362.0

Table 2.3: Standard free energies of formation for oxides in the Fe-Cr-(Si,Al) system, in kJ/mol. Lower free energies indicate which oxides are more likely to form, assuming the oxygen potential is high enough to form them all.

order, is shown in Figure 2-13. As for the time dependence of these oxide's formation, studies have shown that a layer of is typically the first to form [7], as the Ellingham diagram (see Figure 2-2) shows that its potential is the lowest. This oxide layer is extremely thin - on the order of tens to hundreds of nanometers. Iron oxides then grow via diffusion of iron ions through this layer. The diffusion through this layer of Cr<sub>2</sub>O<sub>3</sub> is dependent on the layer thickness, the corrosion potential and the film composition [110]. This is supported by looking at the standard free energies of formation of the oxides in question, shown in Table 2.3 [111]. In the Fe-Cr-Si system, the free energy of Cr<sub>2</sub>O<sub>3</sub> is the lowest, suggesting that it would form first. Magnetite is slightly

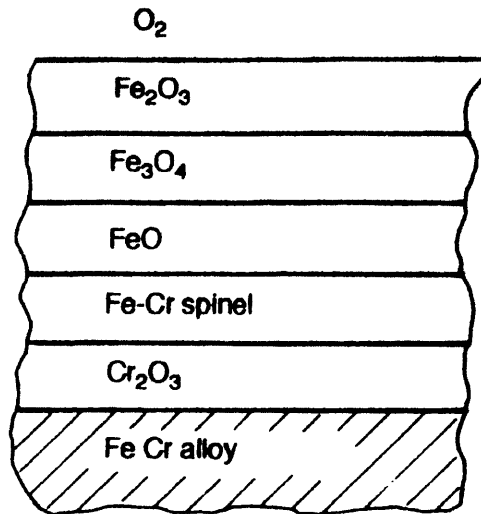


Figure 2-13: Schematic of all possible oxide layers formed upon exposure of an Fe-Cr alloy to an oxygenated environment [12]. Not all of these oxides will form on every Fe-Cr alloy. The lower the oxygen concentration, the less likely it is that  $Fe_2O_3$  and  $FeO$  will form.

higher, while that of silica is much higher. This suggests that silica would only form preferentially if the oxide potential were too low to support the rapid growth of either magnetite or chromia. In the Fe-Cr-Al system, alumina is clearly preferred, and is expected to form an excellent scale based on the free energy information.

A layer this thin allows for diffusion of some iron through it, which is immediately oxidized by dissolved oxygen in the liquid metal. Note that the oxide layers shown in Figure 2-13 are stacked in order of oxygen content, as well as in order of increasing oxygen potential. This is likely due to the fact that all these oxide layers act as diffusion barriers to further oxidation, as the diffusion coefficients for oxygen are far lower in the oxide layers than in the base metal or the liquid metal. Therefore, the oxygen content in an oxide layer will be higher the further away it is from the base metal, and the oxidation state of the iron atoms in successive layers will increase. The formation of an iron-chromium spinel oxide is likely due to both a deficiency of chromium for forming stoichiometric oxide and to a slow, but measurable, diffusion of chromium into the iron oxide layers over time.

As discussed before, above  $570^\circ C$  the only highly stable form of pure iron oxide

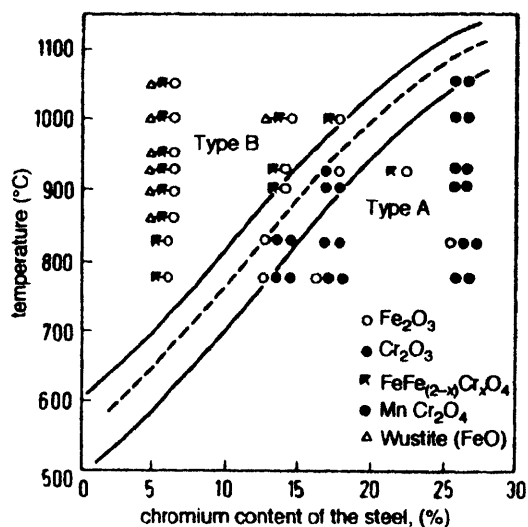
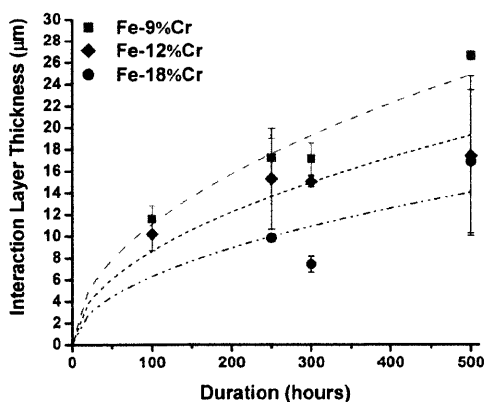
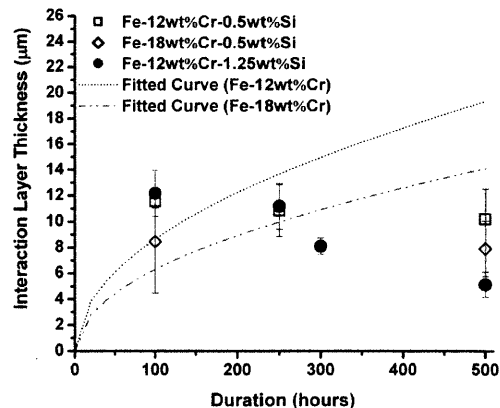


Figure 2-14: Diagram showing the stability of wüstite as functions of temperature and chromium content [12]. Note that the lowest wüstite stability temperature increases with added chromium.

is wüstite, which is non-structural. The addition of chromium has been shown to increase the temperature of this change in stability, as shown in Figure 2-14. Therefore alloys that can still successfully repassivate above 570°C in liquid lead will likely possess different corrosion kinetics/behavior than would be expected in less extreme environments. In the beginning, oxide layers would form as in Figure 2-13. After this initial formation, the layers of wüstite would likely abrade or dissolve away even in slow flowing liquid metal, resulting in a decreasing oxide layer thickness. This would eventually reach an asymptotic value of the thickness of the stable Cr and Fe-Cr spinel oxides. Previous studies in the Fe-Cr-Si system by J. Y. Lim have shown that this phenomenon indeed takes place for sufficiently passivated alloys, as shown in Figure 2-15. Note how the oxide layers in the Fe-Cr alloys in Figure 2-15a continue to grow over time, while those of the Fe-Cr-Si alloys in Figure 2-15b shrink to an asymptotic level after initial growth. This is due to the order and rate of formation for different oxide layers in this system. Iron oxides are typically fast growing, so a layer of iron oxides will form on all Fe-Cr and Fe-Cr-Si layers. However, the presence of enough Cr and Si together causes chromium and silicon oxides to form underneath, where the oxygen concentration is not sufficient to form iron oxides. In both alloys



(a) Oxide growth rates for Fe-Cr alloys



(b) Oxide growth rates for Fe-Cr-Si alloys

Figure 2-15: Example oxide layer thicknesses versus time for Fe-Cr and Fe-Cr-Si alloys. Note that the Fe-Cr alloys continue to grow oxide layers, while the Fe-Cr-Si alloys' oxide thicknesses decrease over time after initial growth. [7]

the iron oxides eventually slough off, but they continue to grow in the Fe-Cr system due to an inability to prevent further oxygen diffusion to the metal surface. Fe-Cr-Si alloys do not continue to grow iron-only oxides, so these iron-based oxides disappear with time. This is the process that is responsible for the shape of the corrosion curve for Fe-Cr-Si alloys in Figure 2-15b. Note that this effect becomes more exaggerated with increasing silicon content. A diagram of the phases of oxide growth for highly passivating alloys such as Fe-Cr steels with accompanying explanations of growth regimes is shown in Figure 2-16.

## 2.2.2 Methods for Prevention of Lead and LBE Corrosion

A number of methods can be employed to control corrosion by liquid lead and LBE. All have their strengths and weaknesses, including each one's effectiveness and cost. Before a discussion of which method is the most feasible for this study, they will all be presented for comparison.

### 2.2.2.1 Oxygen Control

The simplest method for prevention of corrosion from a theoretical standpoint is to control the oxygen potential. This could involve bubbling oxygen and/or hydrogen



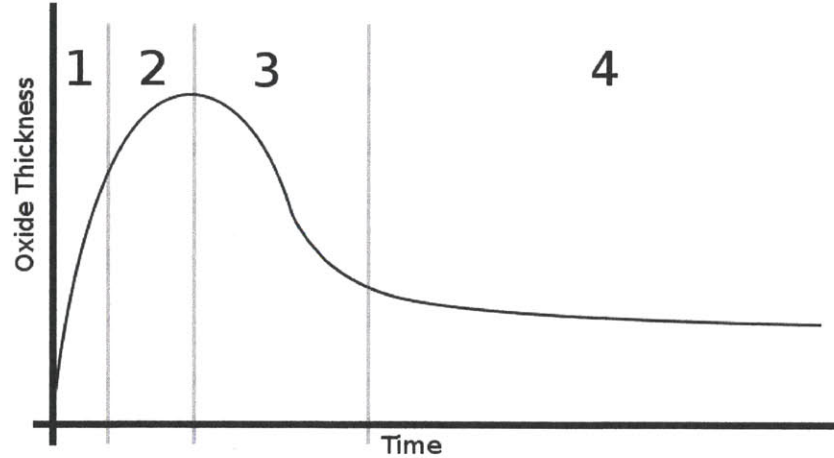
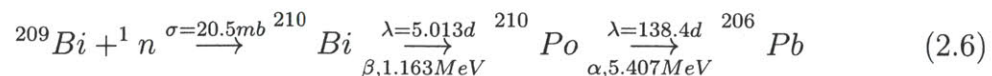


Figure 2-16: Generalized curve for a highly passivating alloy in an oxidizing environment with a high coolant flow velocity. Region (1) is marked by fast formation of passive layers, whose growth slows down as their thicknesses increase in region (2). In region (3), the outer layers of weaker iron oxides spall off due to shear forces from the flowing coolant, while the layers of chromia and silica densify underneath. Region (4) is marked by stable but extremely slow growth of the highly protective layers of chromia, silica and iron-chrome spinel oxides.

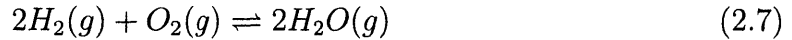
through to bring the oxygen potential up or down [112], or by adding amounts of lead or bismuth oxide that would increase the amount of dissolved oxygen in the coolant [112]. Oxygen control will be necessary in an actual lead or LBE cooled reactor, as oxygen ingress due to leaks, as well as hydrogen production from neutron irradiation, could change the oxygen potential in the coolant over the lifetime of the reactor.

There exist a number of methods for controlling and measuring the oxygen concentration of liquid lead or LBE. Direct measurement is possible by electrochemical methods as performed by Honma et al. [92]. However, doing so in a reactor would require periodic sampling of the coolant into a very controlled environment, which would be further complicated by neutron activation in the coolant. This increases the dose to plant workers, as bismuth has a high cross section for neutron capture and for transmutation to polonium (a relatively long-lived isotope) via the following reaction [113]:



Advantages of this method (oxygen control) include a wider selection of possible materials, as a cheaper material could be chosen if its passivating potential could be maximized by tightly controlling the oxygen concentration throughout the reactor. Drawbacks of this method include the need for constant monitoring of oxygen levels, as the oxygen potential must be maintained at an optimal level. The largest drawback of relying on direct oxygen measurement and control is the inability to measure or control it in the most critical regions, which are crevices or occluded regions. Therefore relying on a measurement gives a false sense of security about what is actually happening in the most corrosion-prone regions of the reactor.

Indirect measurement is a much safer, less costly and less difficult way of measuring the oxygen content of liquid lead or LBE. Without directly measuring the concentration of oxygen, one can use the equilibrium equation (Equation 2.7) for water vapor to change the amount of oxygen present in the coolant by controlling the amount of hydrogen and moisture that bubbles through the coolant:



The diffusion coefficients of oxygen and hydrogen are very, very fast (see Section 2.1.3.1) at the proposed operating temperatures for a liquid metal cooled reactor (550 - 700°C). Equilibrium between the vapor phases above the coolant will be achieved very quickly with respect to oxygen concentration fluctuations in the reactor, which could occur over days or even weeks. One can therefore write Equation 2.7 in terms of a rate constant equation by using the partial pressures of the gases as concentrations, as shown below:

$$K_{eq} = \frac{[P_{H_2O}^2]}{[P_{H_2}^2][P_{O_2}]} \quad (2.8)$$

and  $K_{eq}$  is the rate constant for the equilibrium reaction. This rate constant follows an Arrhenius relationship related to the difference in Gibbs free energy and the temperature:

$$K_{eq} = e^{\left(\frac{(2\Delta G_{H_2O}^0(g) - 2\Delta G_{H_2}^0(g) - \Delta G_{O_2}^0(g))}{RT}\right)} \quad (2.9)$$

The Gibbs free energies of pure elements are defined as zero, so combining Equations 2.8 & 2.9 and simplifying yields:

$$P_{O_2} = \left( \frac{P_{H_2}}{P_{H_2O}} \right)^2 e^{\left( \frac{2\Delta G_{H_2O(g)}^0}{RT} \right)} \quad (2.10)$$

where  $\Delta G_{H_2O(g)}^0 = -247,500 + 55.85T \left[ \frac{kJ}{mol} \right]$  [7]. By bubbling a gas with a known hydrogen concentration and moisture level through the coolant, one can theoretically know the oxygen content in the coolant. Lines of constant  $H_2/H_2O$  ratios were plotted on the Ellingham diagram in Figure 2-2 for convenient determination of the parameters for this method at different temperatures [1]. This measurement can be used to control the oxygen concentration, albeit at a lesser degree than direct measurement and metal oxide addition. As can be seen on the Ellingham diagram, large regions exist between the oxygen stability lines, so fine control of the oxygen concentration may not be necessary.

The drawbacks of the indirect oxygen measurement method are the same as those for direct oxygen measurement, as well as the hindrance of reduced measuring precision. No method of oxygen measurement or control can actually measure or control the oxygen potential inside a tight crevice. The lack of flow in a crevice produced by an occluded region or a very thin gap can cause all the oxygen to be consumed in that area, no matter what the oxygen potential is outside the crevice or occluded area. Therefore, any measurement technique provides a false sense of security when dealing with a complex system like an LBE-cooled reactor.

### 2.2.2.2 Oxide Layer Engineering

An alternative method for controlling liquid metal corrosion is to design a material that forms its own protective layer over a wide range of oxygen concentrations. This immediately removes the need for tight oxygen control; however, it severely restricts the choice of materials that can be considered. Only materials that form a thin, protective, adherent and stable scale at all possible oxygen potentials can be considered.

Chromium is the canonical choice for making a steel that is resistant to corrosion

due to the formation of a passive scale. However, previous studies by J. Lim [7] and Weisenburger et al. [104] have shown that Fe-Cr alloys are not sufficient to protect against LBE dissolution. This is because liquid metal penetrates the oxide layer, allowing oxygen to diffuse through channels of liquid metal into the base metal to grow an internal oxidation layer. Therefore, the addition of one or more additional strong scale formers is required. Looking at Ellingham diagrams leads to silicon and aluminum as logical choices. Both silicon and aluminum are used to ‘kill’ steel, or deoxidize it, during casting [114]. In addition, aluminum is used in small amounts to control the grain size of metals. It does so by forming aluminum nitrides which inhibit grain growth, by precipitating on primary grain boundaries and pinning them, allowing other grains to nucleate and grow [115, 116]. They therefore impart extra strength to the steel via the Hall-Petch relation:

$$\sigma_y(d) = \sigma_{y_0} + \frac{k_y}{\sqrt{d}} \quad (2.11)$$

where  $\sigma_{y_0}$  is the yield stress of the material as a single crystal,  $\sigma_y$  is the yield stress as a function of the average grain size ( $d$ ), and  $k_y$  is a strengthening constant unique to each material [117]. Studies by J. Y. Lim have shown that the addition of silicon to an Fe-Cr alloy drastically changes the oxide formation characteristics, causing a thin layer of  $\text{SiO}_2$  to grow beneath the  $\text{Cr}_2\text{O}_3$  layer. This layer acts as an excellent diffusion barrier, preventing further corrosion [7]. Studies by J. Lim et al. have shown that while FeAl alloys require an inordinate amount of Al (4 - 15 wt. %) to be protective in LBE from a structural standpoint, alloying less Al with some Cr and a small amount of yttrium (Kanthal-22, FeCrAlY) produces extremely favorable results in terms of corrosion resistance [118, 68]. These alloys resist corrosion by rapidly forming a layer of  $\text{Al}_2\text{O}_3$ . The protective ability of this layer is further enhanced by the presence of Cr. This is thought to be due to a synergistic effect between the two oxide scales, analogous to the one that exists between  $\text{Cr}_2\text{O}_3$  and  $\text{SiO}_2$ . Looking at the Ellingham diagram shows that the oxidation potential for alumina is orders of magnitude lower than that of silica, suggesting that these alloys would perform better in extremely

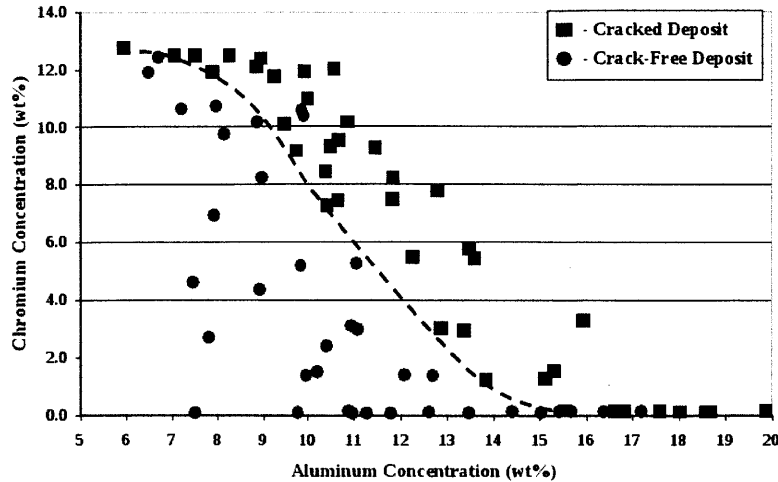


Figure 2-17: Weldability map for Fe-Cr-Al alloys, showing which alloys crack during gas tungsten arc welding (GTAW) due to hydrogen-induced cracking. TiC is added as a hydrogen sink to mitigate this problem [13].

low oxygen environments such as crevices.

The addition of aluminum presents a major problem for commercial fabrication. Studies have shown that aluminum-bearing alloys experience problems during welding due to hydrogen cracking. FeCrAl alloys can become severely compromised by hydrogen embrittlement and subsequent cracking after welding, even after a proper post-weld heat treatment [119]. TiC must be added in order to trap any remaining hydrogen, but the presence of this second phase complicates the situation regarding the microstructure of the metal and the neutronics in a reactor. Studies by DuPont et al. have shown that adding aluminum to iron in a weld limits the amount of chromium that can be added without susceptibility to severe cracking [13]. Figure 2-17 presents a weldability map for Fe-Cr-Al alloys that shows where hydrogen-induced cracking occurred during welding of these alloys [13]. In addition, adding TiC to prevent cracking ends up with the precipitation of TiC on phase boundaries, leading to microstructural inhomogeneity in the weld.

### 2.2.2.3 Other Methods

A number of other methods have been developed to protect against lead and LBE corrosion by applying a coating to the metal surface. Many of these coatings suffer

from problems of adhesion and cracking, including precipitated coatings developed by Weisenburger et al. [68]. The Gepulste Elektronen Strahl Anlage (GESA) process developed by Engelko et al., however, has produced thin surface coatings of 10 - 100  $\mu\text{m}$  that have been immensely successful at resisting LBE corrosion, even above the magnetite-wüstite phase transformation [56]. The GESA process works by coating a more ordinary steel, such as F91, with a precipitated coating as described by Weisenburger et al. [68]. The surface of the steel is then exposed to a pulsed electron beam with a power density of up to 6 MW/cm<sup>2</sup> and pulse durations of 5 - 250  $\mu\text{s}$  in order to locally melt the steel, in effect producing a composite of FeCrAlY cladding GESA-melted onto a base layer of F91. These coatings have shown excellent resistance to LBE corrosion in both oxidizing and reducing environments [68].

The two major drawbacks to this method are its cost and its limited applicability. Applying a coating via electron beam pulses is extremely slow compared to many other commercial cladding processes, such as weld-overlaying or sleeve co-extrusion. In addition, the electron beam must be able to physically reach the surface, restricting the types of parts that can be coated to those with an exposed surface. The inner diameters of narrow pipes cannot be processed using the GESA process, ruling out the use of this method on LBE coolant piping. Finally, any further welding would dilute the GESA-applied coating by localized melting, so the GESA coating would have to be reapplied after welding. A second post-GESA heat treatment would then be needed to remove any heat affected zones present as a result of the welding and/or the GESA process.

A summary of modern methods for preventing lead and LBE corrosion is shown in Table 2.4. The available methods are compared in terms of the required amount of oxygen control, the effectiveness at preventing corrosion, commercial applicability and relative cost.

Process	O <sub>2</sub> control required	Corrosion prevention	Commercial applicability	Relative cost
Metal/Metal Oxide	Precise	Fair to good	Good, in practice today	Medium
H <sub>2</sub> O Equilibrium	Some	Fair to good	Excellent, in practice today	Inexpensive
Oxide Engineering	Little	Fair to excellent	Excellent, in practice today	Inexpensive
FeCrAlY Precip.	Little	Excellent	Very poor, due to cracking	Expensive
FeCrAlY GESA	Little	Outstanding	Poor, needs exposed surface	Expensive

Table 2.4: Summary of techniques that can prevent corrosion by liquid lead and LBE in steel

## 2.3 Selection of FGC Layer Alloys

When designing the composition of the proposed FGC, there was an extremely wide range of materials from which to choose. In addition to their performance in laboratory experiments, much emphasis was placed on current commercial viability, cost and neutronics when determining the composition of each layer. Commercial availability also played a defining role in choosing the layers.

First, a summary of previous work on the alloy system of choice will be given, followed by the selection processes for the layers, and finally, the properties that will define successful selection of the materials for the proposed FGC.

### 2.3.1 Requirements for Materials in a Lead- or LBE-Cooled Gen. IV Reactor

Any material to be used in a high flux fast reactor must be able to withstand the harsh corrosion, thermal, mechanical and radiation environment. It must be stable in many respects over the lifetime of the plant. The choice to use a composite instead of a single alloy introduces new complications, since the presence of an interface results in added constraints on the material's stability.

First, the structural layer of the composite must provide the backbone for the entire FGC. This means that when choosing the thickness of the composite, the structural layer must meet all the strength requirements alone, which may result in a slightly thicker pipe wall when an FGC is used in place of a conventional metal.

The composite must also meet strength requirements in terms of tensile strength and creep resistance. While liquid metal reactors do not require any pressurized gas to operate, they must be able to withstand the immense weight of the pool of coolant above them. In addition, fuel swelling and fission gases will both contribute to radial stresses in the fuel cladding, which will have undergone much radiation damage during reactor operation.

The structural layer must be stable with respect to radiation, meaning that it does not appreciably suffer from void swelling, neutron activation, radiation embrittlement (including a change in the ductile-to-brittle transition temperature) and radiation-induced creep. This composite, especially in the form of fuel cladding, will be exposed to several hundred displacements per atom (dpa) during the lifetime of the plant or during fuel exposure. Many materials, especially austenitic steels, suffer significant swelling due to the formation of voids due to the accumulation of vacancies [16]. In addition, materials that activate and decay via alpha emission generate helium, which can incorporate into the microstructure along grain boundaries and in voids, stabilizing them, severely embrittling the material [120]. Because the reactor will eventually be decommissioned, there should not be an appreciable amount of materials that produce long-lived isotopes when neutronically activated. This helps ensure continued safety to plant workers even at the end of the reactor's life. Finally, materials that are resistant to thermal creep can be subject to irradiation-induced creep. Fortunately, temperatures of 650 - 700°C are high enough that most radiation damage is annealed out. At these temperatures, vacancy-interstitial pairs recombine before they can migrate apart and cause significant damage. This is reflected in a smaller change in the mechanical properties of steels at high temperatures (500 - 700°C) than at lower temperatures (300 - 450°C) [16].

The cladding layer must excel at resisting corrosion by lead or LBE. The passive film formed by the material must be thin enough to prevent depletion of the underlying material of beneficial alloying elements. This will ensure that should the passive layer become compromised, the composite will not be subject to accelerated dissolution. The scale must also be highly adherent to the base metal and able to resist



stresses from thermal expansion and radial swelling in the fuel cladding. A low lattice mismatch stress between the cladding material and its oxide is therefore desired. This scale must remain stable even at oxygen potentials below that of chromium oxide formation, as the literature has shown that should a crack develop, chromia alone has been shown to be insufficient to protect against rapid dissolution at sufficiently low concentrations [7]. This necessitates the choice of an alloying element in addition to chromium. Based on the literature above, silicon and aluminum are the only two choices that don't present any neutron activation issues and that form a sufficiently strong, dense scale. The cladding must also be as ductile as possible, as tubes of fuel cladding can undergo significant bowing during operation, and the protective layer must be able to deform without breaking. This last point also requires resistance to SCC/LME. These considerations along with economics and immediate commercial feasibility rule out any external surface modification, such as GESA treatment of Fe-CrAlY coatings. Oxide layer engineering therefore stands out as the logical choice to ensure corrosion resistance over the widest range of oxygen potentials.

It is necessary to engineer the composite so that the interface is not a structurally weak point, as is often the case in such systems. For this reason the two layers must be microstructurally similar, preferably with similar crystal structures and thermal expansion coefficients. This is especially important during composite processing, when the material will be subject to the highest amount of stress. There are a number of possible methods for joining the two layers, including diffusion bonding, sleeve co-extrusion, weld overlaying and surface treatment. Of these, weld overlaying includes the highest amount of microstructural mixing. Furthermore, it is already carried out on a commercial, industrial scale: fossil-fuel plants make wide use of high-chromium weld overlaying to protect the hottest waterwall tubes in the plant [121]. This will be critical to the success of the composite, as the presence of too sharp of an interface (a sudden change in microstructure) during processing steps such as extrusion could lead to layer delamination. In addition, diffusion can be accelerated by radiation, so the diffusion coefficients for the passivating alloying elements (chromium, silicon and/or aluminum) should be relatively small. A good match in chemical composition

should also exist, so that the differences in elemental concentrations are not so high that a fast diffusion flux would be present across the interface.

Finally, one must be able to manufacture the materials needed for making the composite in commercial quantities using current commercial processes, if the composite is to be considered for use in a full-scale reactor in the near future. The processing steps must be chosen so that scalability is a non-issue, because once lead or LBE reactors are being built, the demand for fuel cladding will be measured in kilometers, not meters. The materials must therefore be able to be processed to achieve a range of strengths, as working with fully annealed material will make processing easier, while some degree of hardening before deployment will impart the strength the composite needs to retain its structural integrity throughout the lifetime of the reactor. This last point is mainly a constraint on the structural material, as the cladding layer will be too thin and soft to serve any structural purpose, and would actually benefit from being the softer of the two. This is because it is the layer that will grow oxides that could be susceptible to SCC. If the material is too soft to resist deformation, then a sufficient stress to propagate SCC cracks will not exist.

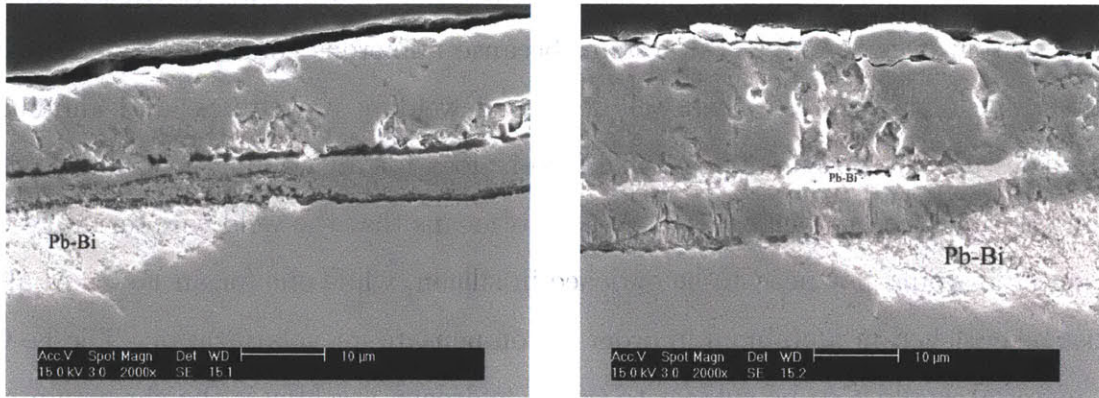
Weldability of the composite is absolutely critical. Components such as coolant piping will have to be assembled at the plant, and certified welding procedures must be used. The condition of weldability further precludes the use of any coating process, such as precipitation coating or GESA, as parts with complex shapes must be able to be manufactured and welded on-site without any significant dilution. The materials must also not suffer any sort of phase separation, even during melting. There is an expectation that rewelding without the proper quench-and-temper heat treatment for quenched and tempered materials, such as F91, may take place in the field. The use of FeCrAl alloys may not be possible, as the only way to employ sufficient amounts of chromium (>10 wt. %) and aluminum (>5 wt. %) without susceptibility to cracking is to add a hydrogen sink such as TiC [13]. Doing so could cause a phase separation in the weld material [119] that would become the weak point in such an alloy. From a standpoint of weld certification, it takes seven years on average to qualify new materials and procedures for the ASME code. This process can only occur once the

problems with welding have been solved. It therefore makes sense to choose the Fe-Cr-Si system over the Fe-Cr-Al system, because numerous common Fe-Cr-Si alloys (405 stainless steel, etc.) have well-developed welding procedures, and aluminum volatilizes easily during welding while silicon does not in welding procedures other than gas tungsten arc welding (GTAW). This means that the weld wire for an Fe-Cr-Si material would not need to be enriched in silicon, while one for an Fe-Cr-Al alloy must be enriched in aluminum in order to compensate for volatilization. The Fe-Cr-Al material would also be subject to severe hydrogen cracking if the chromium and aluminum concentrations cross the weldability boundaries, as found by DuPont et al. [13]. This would result in localized areas of susceptibility to corrosion surrounded by microcracked regions.

### **2.3.2 Previous Work in the Fe-Cr-Si System**

It has been noted in the literature that the materials in the Fe-Cr-Si system show high resistance to lead and LBE corrosion. Work on alloys such as HCM12A and SAVE-12, as well as extensive studies by J. Y. Lim in the Fe-Cr-Si system, have shown that at least 10 wt. % Cr is necessary to impart good corrosion resistance, and that the addition of small amounts of Si has been shown to significantly improve corrosion resistance [7]. Fe-Cr alloys with over 10 wt. % chromium have been shown to form a trilayer oxide structure, with a thin layer of  $\text{Cr}_2\text{O}_3$  next to the base metal, followed by a layer of  $\text{FeCr}_2\text{O}_4$  spinel oxide, and finally a layer of either magnetite or wüstite depending on the temperature. J. Y. Lim has shown that adding silicon, even in amounts as small as 1.25 wt. %, results in the formation of small  $\text{SiO}_2$  precipitates beneath the  $\text{Cr}_2\text{O}_3$  oxide layer, and the morphology of these suggests that they form after the  $\text{Cr}_2\text{O}_3$  layer formation. It has also been noticed that the presence of these  $\text{SiO}_2$  precipitates is accompanied by a reduced oxide layer thickness, mainly due to the shrinking or even the absence of an iron oxide layer.

A summary of studies conducted by J. Y. Lim et al. is now presented. These studies illustrate how the Fe-Cr-Si system behaves in LBE, and they provide an interesting point of comparison with the findings of this project. The author exposed



(a) Fe-1Cr after exposure to 600°C LBE for 500 hours (b) Fe-2.25Cr after exposure to 600°C LBE for 500 hours

Figure 2-18: Examples of low-chromium iron alloys upon exposure to LBE at 600°C. Note the thick oxide layers, as well as the LBE penetration beneath into the base metal, where rapid dissolution is taking place [7].

Fe-Cr, Fe-Si and Fe-Cr-Si alloys of varying compositions to liquid lead bismuth at 600°C for durations of 100 - 500 hours in a reducing environment, using the water vapor equilibrium method of oxygen control. The pressure ratio of  $H_2/H_2O$  was maintained at or near 1,000. Samples were exposed to the liquid LBE and analyzed by a variety of methods.

Low-Cr alloys generally exhibited heavy oxidation and dissolution attack. Examples of low-Cr alloy corrosion in LBE are shown in Figure 2-18. These alloys were marked by the presence of a thick iron oxide layer outside a thinner, but still significant, layer of Fe-Cr mixed oxide. These layers were clearly insufficient to protect against LBE attack, as it penetrated through oxide layers in both alloys and caused rapid dissolution to take place.

Fe-Si alloys also exhibited large internal oxidation zones, as can be seen in Figure 2-19. This is likely due to both the 1:2 ratio of Si:O, which would form a more discontinuous scale, as well as to the fact that  $SiO_2$  formation is reported to be very slow as compared to the formation rates of iron and chromium oxides [122]. It can be seen from the figure that silicon oxidizes as precipitates rather than as a continuous scale; consequently, the internal oxidation layer in the Fe-Si alloy was much thicker since oxygen had many fast diffusion paths on grain boundaries between  $SiO_2$  and

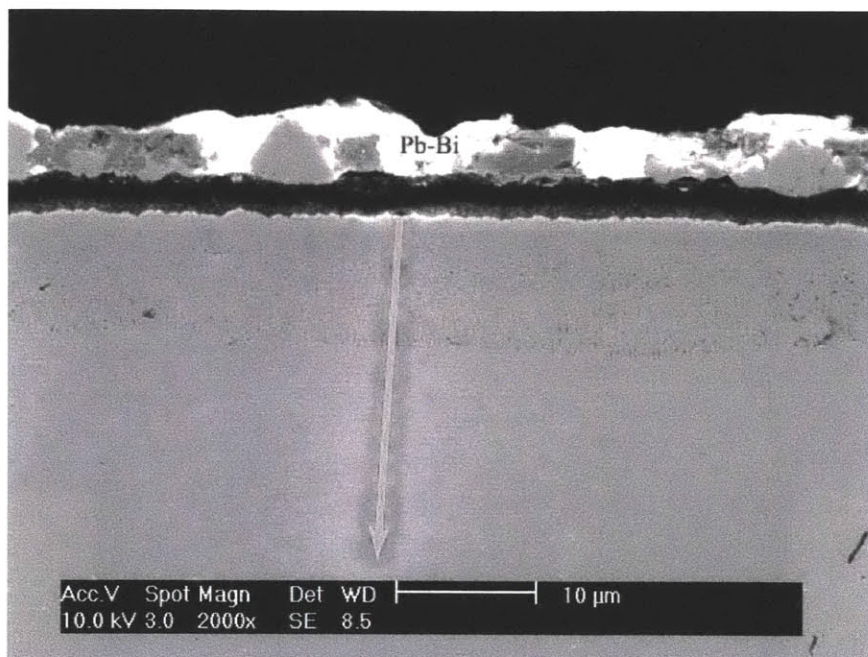


Figure 2-19: SEM image of Fe-1.25Si after exposure to 600°C reducing LBE for 300 hours. Note the thick layer of  $\text{SiO}_2$  and  $\text{FeSi}_2\text{O}_4$  precipitates that have formed [7].

$\text{FeSi}_2\text{O}_4$  precipitates. Therefore, it would be beneficial for a stable oxide such as  $\text{Cr}_2\text{O}_3$  to form before  $\text{SiO}_2$  does. This gives it time to form a thin, dense  $\text{SiO}_2$  layer adjacent to the base metal, forming the best possible barrier to oxygen diffusion or LBE penetration into the metal.

Fe-Cr-Si alloys showed much more promising results. The combination of chromium and silicon appears to have formed a fully dense, non-porous layer of  $\text{Cr}_2\text{O}_3$ , with precipitates of  $\text{SiO}_2$  and  $\text{Fe}(\text{Cr}, \text{Si})_2\text{O}_4$  forming beneath, as shown in Figure 2-20. It still appears that the Cr-Si oxide network that forms below the  $\text{Cr}_2\text{O}_3$  layer is not sufficiently dense, suggesting that the concentration of one or more alloying elements is still too low in this alloy. The cladding layer of the FGC must have enough Cr and Si to form a dense scale layer: if chromium and silicon levels are too low, they will merely form a network of interspersed precipitates as shown in Figure 2-20.

Not all Fe-Cr-Si alloys have shown promising results. Studies on Russian Fe-Cr-Si alloys have exhibited unfavorable corrosion rates while still possessing what would be thought as sufficient chromium and silicon to self-passivate. The closest example to this work is alloy EP-823, whose composition is shown in Table 2.5. EP-823 showed

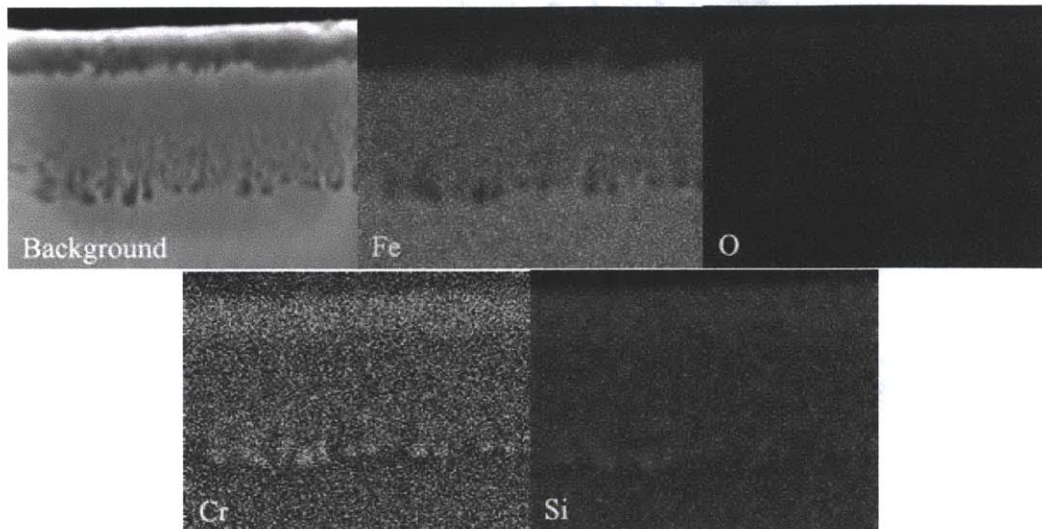


Figure 2-20: EDX maps of oxidation of Fe-12Cr-1.25Si after exposure to 600°C LBE for 250 hours showing an outer layer of Cr and Si oxides plus an innermost layer of Cr and Si oxide precipitates, which act as barriers to further oxygen diffusion or element dissolution [7]

Element	Fe	Cr	Si	Ni	Mo	Mn	V	Nb	W	Ti	C
Composition (wt. %)	Bal	12	1.8	0.89	0.7	0.67	0.43	0.4	1.2	—	0.14

Table 2.5: Composition of the Russian Fe-Cr-Si alloy EP-823, in wt. % [14]

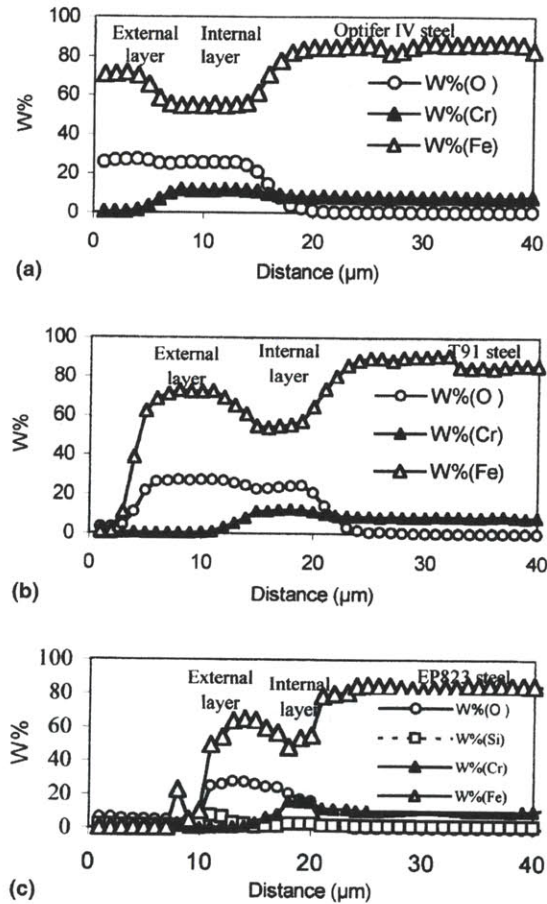
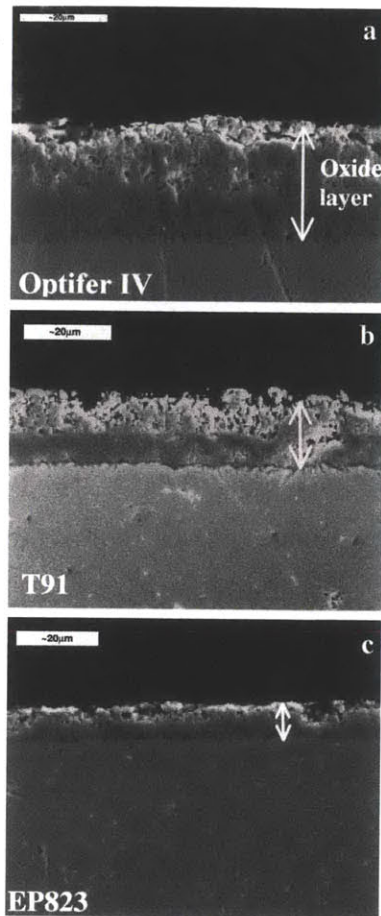
more favorable results as compared to similar Fe-Cr martensitic steels without silicon, such as F91. SEM images (shown in Figure 2-21a) and accompanying elemental linescans (shown in Figure 2-21b) demonstrate that alloy EP-823 produces a thinner, more Cr-rich scale than Optifer IV or F91 [14]. However, the scale is still on the order of tens of microns in thickness, and it contains a significant amount of iron. The fact that the oxide thickness grows with a square root law (see Figure 2-22) indicates that the oxide layer continues to grow by diffusion, most likely of iron, through the oxide layer. This is not the behavior that would be desired from a protective alloy.

### **2.3.3 Selection of FGC Layers**

The two different layers must meet different requirements, but the choice of the first will still influence the choice of the second. Here, the rationalization for which choices were made in this study will be given, with special emphasis on the requirements put forth in Section 2.3.1.

#### **2.3.3.1 Structural Layer**

Because the Fe-Cr-Si system was chosen for corrosion resistance, the structural layer must have as similar a chemistry as possible to the cladding layer. Austenitic steels were excluded from this study due to the radiation swelling reasons cited by Klueh [16], as well as for the fact that many of them contain nickel, which is far too soluble in lead and LBE. Nickel is often present in steels as an austenite stabilizer [21]. With these facts in mind, ferritic/martensitic Fe-Cr based steels such as F91, HT-9, NF616, EUROFER, F82H, HCM12A, Oak Ridge National Laboratory (ORNL) 9Cr-2WVTa, MA957 oxide dispersion strengthened (ODS) steel, and PM2000 ODS were considered on the basis of strength, chemistry, creep resistance, radiation resistance and fabricability. The easiest way to pare down the choices was to see which ones could actually be procured. A wide variety of alloys in this system have been considered for the purposes of structural properties and corrosion resistance as summarized by Klueh [16]; however, few of these are commercially available in large amounts, if at all. It



(a) SEM images of cross sections of (a) Optifer IV, (b) F91 and (c) EP-823 after exposure to LBE. Note the thick, porous oxide layer present on all three steels.

(b) EDX linescans of oxide layers on (a) Optifer IV, (b) F91 and (c) EP-823. The internal oxide layer is enriched in Cr in all three alloys, while that of EP-823 is also enriched in silicon. All three oxide layers are rich in iron, which indicates continued oxide growth over time by diffusion through the existing oxide layer.

Figure 2-21: SEM images and EDX linescans of martensitic alloys Optifer IV, F91 and EP-823 after exposure to flowing, oxidizing LBE at 470°C for 3,116 hours [14]. All three steels exhibit a surface oxide rich in iron between ten and twenty microns thick.



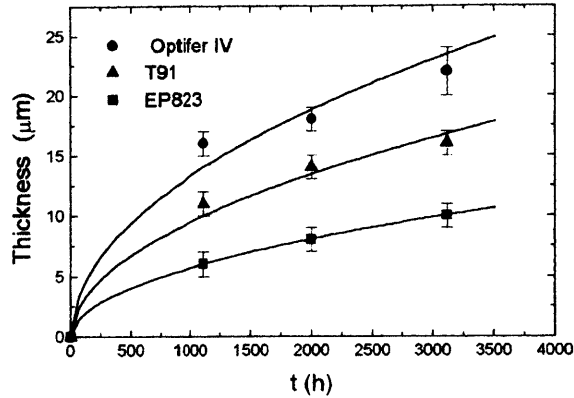


Figure 2-22: Growth rates of alloys Optifer IV, F91 and EP-823 after exposure to flowing, oxidizing LBE at 470°C. [14]. All three alloys' oxide layers exhibit square root growth rates, indicative of continued diffusional growth through the existing oxide layer.

was not desirable to perform tests on small laboratory coupons without the knowledge that the work could be easily scaled up to the level of hundreds of tons. That left HT-9 (Fe-12Cr-1MoVW), manufactured by Sandvik, and F91 (Fe-9Cr-1MoNbVW), manufactured by Vallourec & Mannesmann.

There is an extremely large database on the radiation response of HT-9, due to its selection as the structural material in the Clinch River Breeder Reactor and the EBR-II liquid sodium cooled reactor. This is not the case for F91. This is because F91 was only selected as a material for the steam generator in EBR-II, while HT-9 was chosen for in-core structural components [16]. Nevertheless, enough data have been accumulated since then to make an educated decision between the two based on how their mechanical properties change with irradiation. The most easily measurable properties affected by radiation are yield stress and ultimate yield strength. Figure 2-23 shows the change in these two parameters for F91 as performed in EBR-II at ~12 dpa. It is clear that beyond 450°C, there is no notable difference in yield stress or ultimate tensile strength. This is likely due to the fact that at higher temperatures, the defects produced by radiation are freer to move throughout the crystal structure of the steel, and many more of them end up recombining and healing some of the radiation damage.

Properties related to ductility that change with exposure to radiation can be

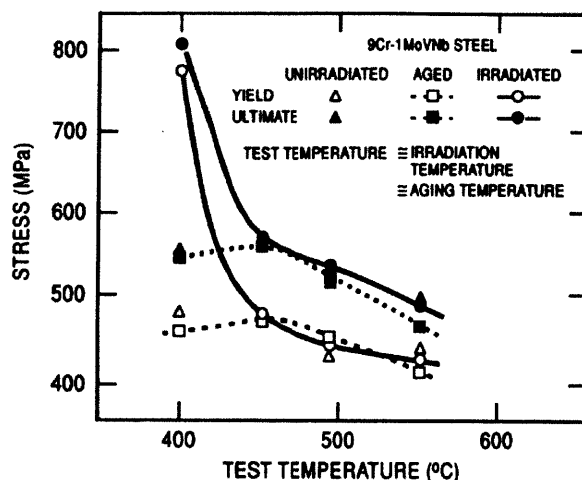
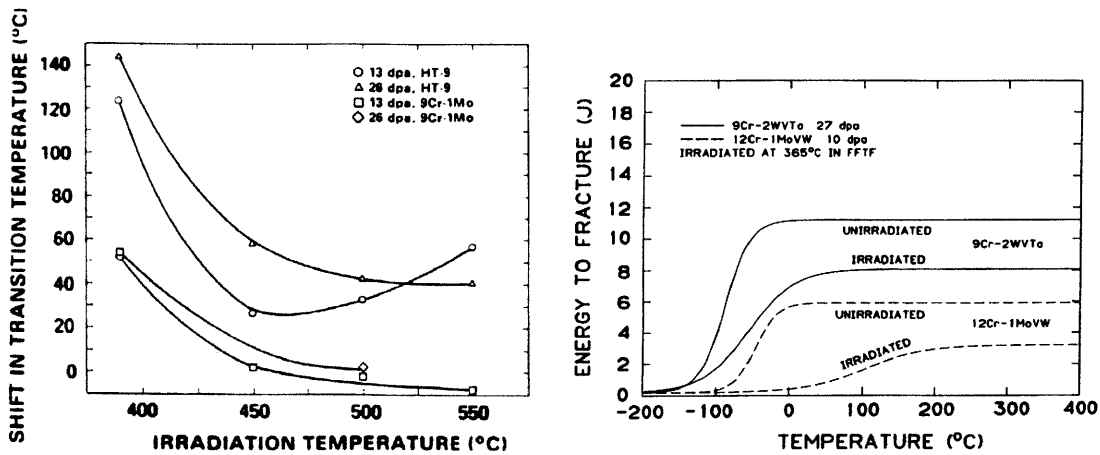


Figure 2-23: Change in yield stress and ultimate tensile strength of F91 at  $\sim 12$  dpa fast flux [15]. Note how mechanical properties are not noticeably affected above  $450^{\circ}\text{C}$ . This is due to the higher ability of defect pairs created by radiation to anneal out, or to diffuse to sinks.

also compared for the two alloys, such as the shift in the ductile-to-brittle transition temperature and the Charpy impact energy. Figure 2-24 shows two such curves comparing irradiated HT-9 with F91 and ORNL 9Cr-2WVTa, a reduced activation steel developed by Oak Ridge National Lab as a next generation iteration on F91. In both cases, alloys based on F91 show markedly better ductile properties than HT-9. The creep-rupture strength of F91 is also higher than that of HT-9, as Klueh showed in a recent review of the literature [16]. These curves are reproduced in Figure 2-25 to illustrate this point. Note that F91 excels compared to HT-9 at higher temperatures. This is likely due to the niobium and vanadium additions present in F91, which form fine carbides and carbonitrides that impede dislocations from moving, helping to slow typical creep mechanisms [125].

A recent study has suggested that ferritic/martensitic (F/M) steels may just have longer incubation periods, and eventually exhibit similar swelling tendencies as those for austenitic steels [126]. However, this is likely due to the fact that the alloys tested and reviewed in this study were of uniform microstructure, such as simple tertiary Fe-Cr-Ni alloys and 316 stainless steel. By contrast, the fine grained nature of F/M steels provides numerous sinks where defects can annihilate, including a high density of grain boundaries, dislocations and MX precipitates, where M is primarily niobium



(a) Shift in ductile to brittle transition temperature for HT-9 and F91 after 26 dpa fast flux irradiation [123] (b) Shift in Charpy impact energy for HT-9 (12Cr-1MoVW) and ORNL 9Cr-2WVTa. Note that in both cases, the impact energy of HT-9 is about half that of the ORNL steel [124].

Figure 2-24: Shift in properties related to ductility for irradiated HT-9, F91 and ORNL 9Cr-2WVTa

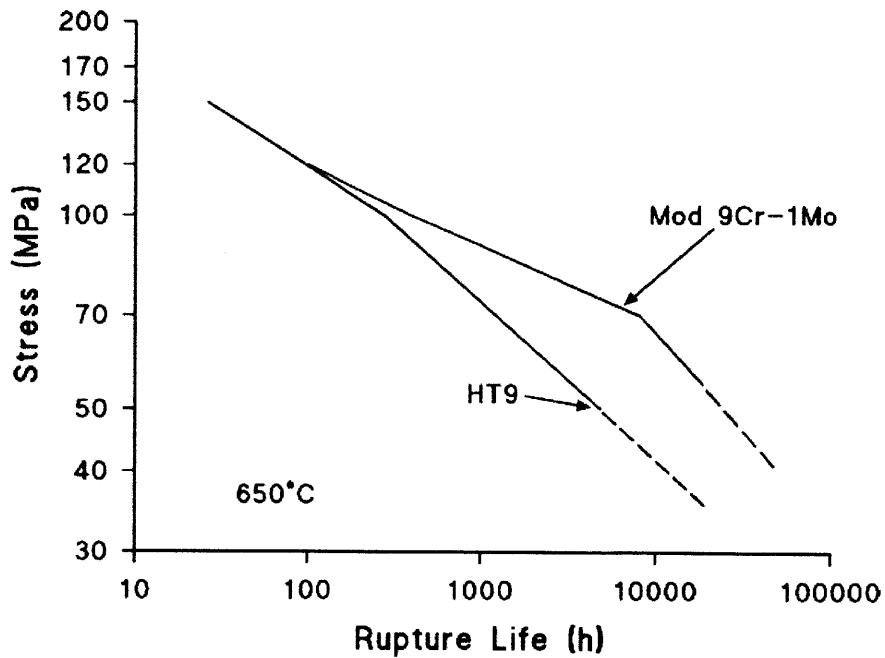


Figure 2-25: Creep-rupture curve comparison of F91 and HT-9 [16]

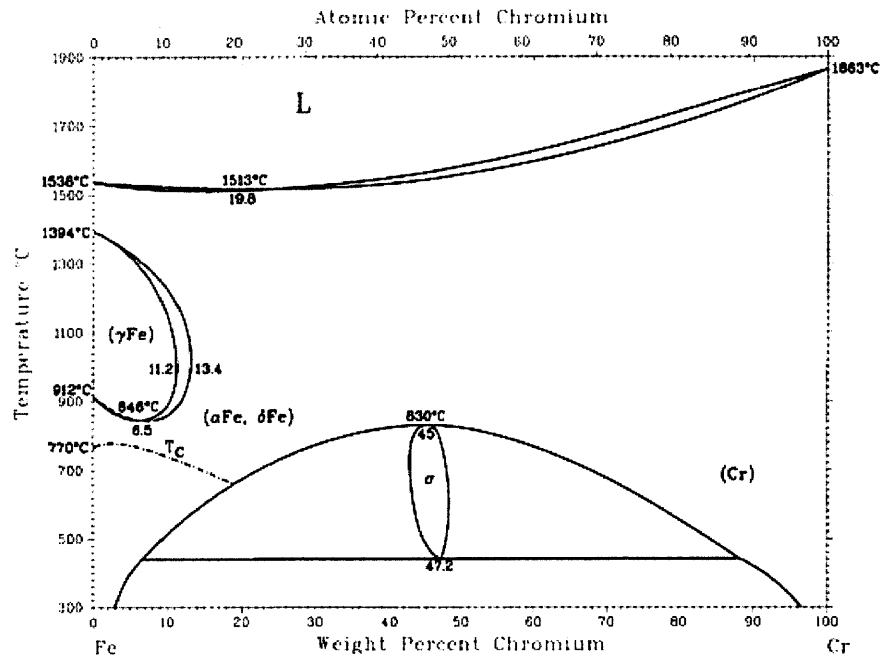


Figure 2-26: Fe-Cr binary phase diagram, showing the solubility limit of chromium in  $\alpha$ -Fe in the lower-left [3]

or vanadium and X is carbon or nitrogen [16] in F91. These MX precipitates exist both on grain boundaries and inside the grains themselves, preventing the movement of dislocations through the material and imparting superior creep resistance.

From a microstructural point of view, while chromium does add corrosion resistance, it also leads to deleterious effects. The phase diagram for iron-chromium is shown in Figure 2-26. The important feature here is the solubility line for chromium in  $\alpha$ -Fe. At concentrations higher than this line, a phase separation can take place into  $\alpha$ -Fe and  $\sigma$ -Cr.  $\sigma$ -Cr has plate-like grains, is more brittle, and its phase boundaries are subject to intergranular fracture [18]. Therefore, the structural material of choice should not be subject to any phase separations. It may be worrisome that even at 500°C, the solubility limit of chromium drops to 9 wt. %. However, this should not be of concern for two reasons. First, phase separations would take too long to manifest at such low temperatures. Second, recent computational investigations and experimental literature reviews by Bonny et al. have suggested a change is needed in the currently accepted Fe-Cr phase diagram [17]. The conclusive figure from this search is shown in Figure 2-27. The experimental data suggest that Cr is actually

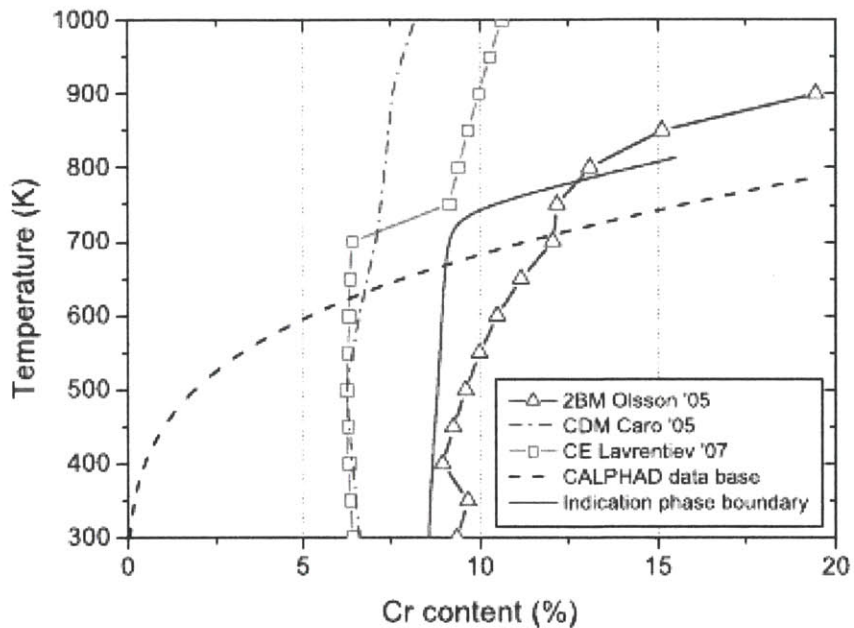


Figure 2-27: Modified Fe-Cr phase diagram in the low-Cr region based on work by Bonny et al. [17]

much more soluble in  $\alpha$ -Fe at temperatures below 650°C than previously thought. This should alleviate any concerns that  $\leq 10$  wt. % chromium steels may form  $\sigma$ -Cr. In addition, the presence of manganese and nitrogen preclude the formation of  $\sigma$ -Cr. They do so by suppressing the sigma solvus temperature to levels below annealing temperatures, such that  $\sigma$ -Cr will not be formed during processing [127]. However, 12Cr steels still present a problem, as experimenters have had difficulty preventing  $\sigma$ -Cr and  $\delta$ -Fe formation in 12 wt. % Cr steels [16]. Manganese can be added as an austenite stabilizer to remove these phases, as well as scavenge any free sulfur present in the metal during casting. In conclusion, a 9 - 10 wt. % Cr steel is the most logical choice to ensure microstructural stability.

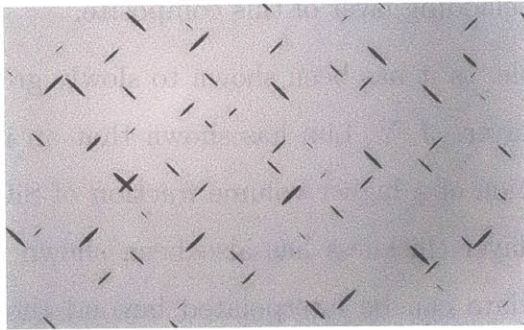
Based on a review of the recent literature, F91 was chosen as the structural layer in the composite. Compared to HT-9, F91 has superior microstructural stability, higher creep resistance, a lower shift in ductile-to-brittle transition temperature, a higher Charpy impact energy, a higher creep-rupture life and an absence of change in yield stress under irradiation. HT-9 has been around longer, and it is less expensive

to produce since F91 requires a more careful heat treatment. However, since F91 can handle greater stresses, parts made out of F91 can be thinner than their HT-9 counterparts. This directly reduces the material cost of making parts out of F91.

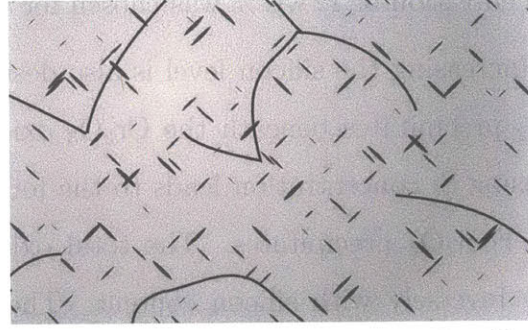
### 2.3.3.2 Cladding Layer

The cladding layer selected is an Fe-Cr-Si alloy. In choosing the composition of this alloy, the benefits of added corrosion resistance will be considered along with microstructural, macrostructural and radiation considerations to find the best balance of properties. The ultimate goal of this process is to ensure that the cladding remains intact over decades of fast reactor operation. As mentioned before, more chromium and silicon increase the corrosion resistance of ferritic/martensitic steels. Therefore, it is desired to maximize the concentrations of chromium and silicon without entering a regime of deleterious effects. The effects of increasing the concentration of each element will be considered individually.

As mentioned in Section 2.3.3.1, the addition of too much chromium can lead to  $\sigma$ -Cr precipitation. This is clear from the phase diagram (see Figure 2-26) and from experiments by Ravindranath et al. [128, 129]. However, just the existence of  $\sigma$ -Cr will not necessarily weaken the structure of the cladding layer. When an alloy undergoes a phase separation, the amount of the alloy that undergoes the transition (and the links between differently phased sections of the alloy) are dependent on the concentrations of each alloying element as well as the number of nucleation sites that can induce phase separation. The presence of enough  $\sigma$ -Cr would clearly be devastating to a material from a microstructural point of view, as the elongated phases of  $\sigma$ -Cr will form networks in which cracks can propagate along phase boundaries [128]. This could cause transgranular, brittle fracture in preferential directions of  $\sigma$ -Cr growth. However, moving slightly over the solubility limit would result in a very low volume fraction of  $\sigma$ -Cr. Furthermore, Fe-12Cr alloys have been shown to possess a relatively large number of fine precipitates and dislocations [16], all of which would act as nucleation sites to precipitate a phase from a supersaturated solution of Cr in  $\alpha$ -Fe. A diagram of how the microstructure might look with different amounts

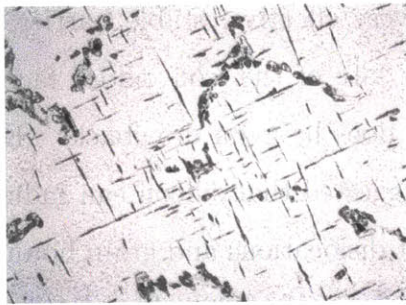


(a) Diagram of a system with too little  $\sigma$ -Cr to cause embrittlement

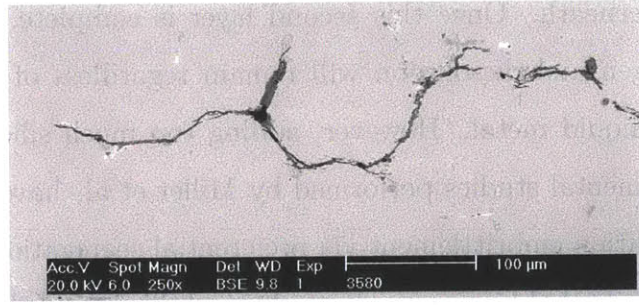


(b) Diagram of a system with enough  $\sigma$ -Cr to cause embrittlement.  $\sigma$ -Cr tends to form highly oriented platelets, forming weak directions in the material.

Figure 2-28: Simulated diagrams of how microstructures would look with different amount of  $\sigma$ -Cr phase precipitation.  $\sigma$ -Cr is shaded purple in these diagrams.



(a) Optical micrograph of  $\sigma$ -Cr forming on prior austenitic grain boundaries and as highly oriented platelets



(b) SEM image of a crack proceeding directly along  $\sigma$ -Cr phase boundaries, showing severe weakening of the material at the phase boundary

Figure 2-29: Micrographs of  $\sigma$ -Cr precipitation and its effects in Fe-Cr-Ni alloys [18]

of  $\sigma$ -Cr is shown in Figure 2-28, while actual micrographs of  $\sigma$ -Cr precipitation and associated cracking as measured by Babakr et al. are shown in Figure 2-29. Note how the platelets of  $\sigma$ -Cr are highly aligned, which provides fast fracture directions along which a crack can propagate. Clearly such a situation should be avoided; however, a chromium concentration of 1 - 2 wt. % over the solubility limit is not expected to produce severe enough  $\sigma$ -Cr precipitation to adversely affect a thin layer of cladding material.

Therefore, based on work in the Fe-Cr-Si system by J. Y. Lim, and on reasonable assumptions about the prevention of secondary phase precipitation, a chromium

concentration of 12 wt. % was chosen for the cladding layer of this composite.

Increasing the silicon level is also desirable, as it has been shown to slowly grow  $\text{SiO}_2$  precipitates beneath the  $\text{Cr}_2\text{O}_3$  oxide layer. J. Y. Lim has shown that an increasing Si concentration leads to the formation of a higher volume fraction of  $\text{SiO}_2$  and  $\text{FeSi}_2\text{O}_4$  precipitates. The total oxide layer thickness has also been shown to vary inversely with silicon content. These data can be interpolated beyond those collected by J. Y. Lim to say that further increasing the silicon concentration should theoretically produce a fully dense, thin layer of  $\text{SiO}_2$ . The speed of formation of this layer is also expected to be proportional to the silicon content as well as the chromium content, as a higher chromium content would lead to faster formation of a thinner oxide layer, allowing enough oxygen to enter to form a layer of  $\text{SiO}_2$  directly underneath. Once this second layer is complete, a very effective, stable barrier to oxygen and dissolution will remain regardless of the fate of the iron oxides facing the liquid metal. However, adding too much silicon does have its drawbacks. Experimental studies performed by Miller et al. have suggested that silicon can induce radiation embrittlement via preferential segregation at dislocations and grain boundaries, probably as a result of physical displacement by radiation [130]. As mentioned before, Fe-12Cr alloys tend to have a high density of dislocations, so this segregation could be severe given too much silicon. Examining the Fe-Si phase diagram (shown in Figure 2-30) shows a solubility limit of 1.9 wt. % Si in  $\gamma$ -Fe. The composite will exist as  $\gamma$ -Fe during processing. In order to preclude any phase transformations in the cladding layer, it is not advisable to deviate too much from this limit. Silicon could also contribute to radiation embrittlement by lowering the activation energy for diffusion of certain defects, especially vacancies generated by radiation. Silicon is a substitutional impurity in  $\alpha$ -Fe that would allow for easier diffusion as compared to the rest of the crystal [131]. Finally, the presence of too much silicon can lead to the precipitation of Si-rich precipitates, mainly Fe-Si intermetallic compounds, that would lead to localized depletion of silicon in the matrix [132].

Therefore, based on concerns relating to radiation embrittlement due to silicon segregation, the desire to avoid Si-rich phase precipitation, and a need to go beyond



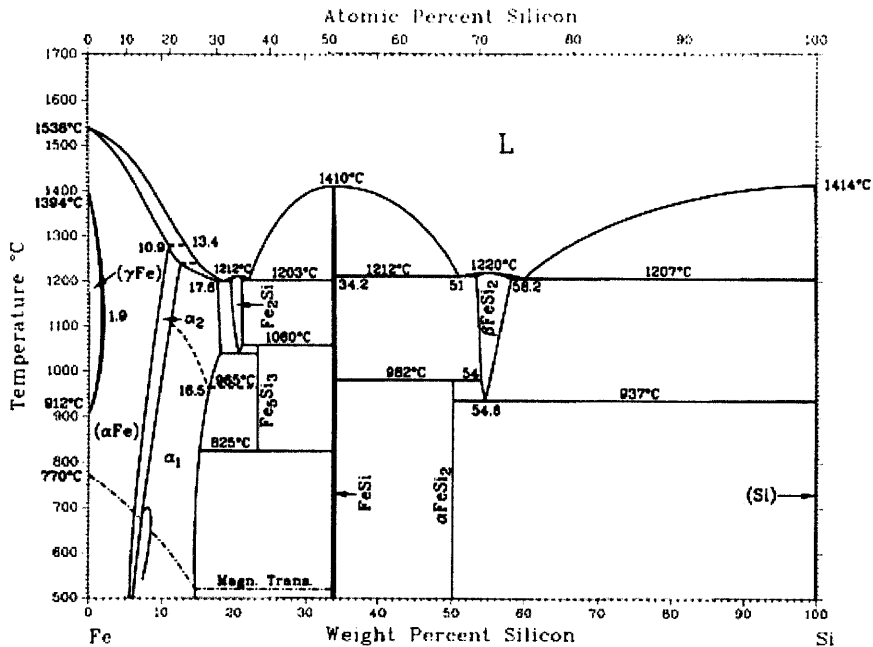


Figure 2-30: Fe-Si binary phase diagram showing the solubility limit of Si in  $\gamma$ -Fe [3]

1.25 wt. % Si as noted in J. Y. Lim's work, a silicon concentration of 2.0 wt. % was chosen for the cladding layer of this composite.

Other alloying elements were considered, but it was desired to test just the basic three elements in this first iteration. Adding more alloying elements complicates things exponentially. The final composition of this composite's cladding layer was chosen to be Fe-12Cr-2Si.

### 2.3.4 FGC Success Criteria

To summarize, the FGC must satisfy the following requirements in order to be considered successful:

- It is corrosion resistant in LBE, in both oxidizing and reducing environments.
- It retains required tensile strength at high temperatures without embrittlement.
- It resists radiation swelling, radiation-induced creep and loss of ductility.
- It can be produced at low cost.

- It can be produced commercially using current technology.
- It is available in large enough quantities to be commercially applicable.
- It is weldable and heat treatable in the field.
- It possesses good interface characteristics, with little diffusional dilution of the cladding layer, and no degradation in mechanical properties.

## 2.4 Selection of Composite Dimensions and Processing Steps

With the materials for the composite selected, attention must now be given to the dimensions of the composite. While the exact form or dimensions developed in this work may not be used in a reactor, it should be as close as possible so that results from this study can be easily extended to use in actual reactors.

### 2.4.1 Thermal-Hydraulic Constraints

The fact that the structural layer must provide all of the strength for the FGC means that the composite must be slightly thicker than the same part made out of bare F91. The most critical location for examining the effects of this change is in the fuel cladding, where using the composite has the immediate effect of increasing the diameter of the fuel cladding. The following analysis is adapted from that given in Todreas & Kazimi's book [133]. Suppose a reactor was designed whose fuel cladding rods have diameter of  $D$  and whose core is designed with a pitch to diameter ratio of  $\frac{P}{D}$ . The surface area  $A_c$  and perimeter  $P_z$  through which coolant flows around each fuel pin is then:

$$A_c = P^2 - \frac{\pi D^2}{4}; P_z = 2\pi D \quad (2.12)$$

The pressure drop in a vertical channel is given by the following equation:

$$-\frac{dp}{dz} = \left(\frac{dp}{dz}\right)_{accel.} + \left(\frac{dp}{dz}\right)_{fric.} + \left(\frac{dp}{dz}\right)_{grav.} = \frac{d}{dz} \left(\frac{G_m^2}{p_m^+}\right) + \frac{1}{A_c} \int_{P_c} \tau_w dP_z + \rho_m g \cos \theta \quad (2.13)$$

Averaging the shear stress across the perimeter of the cross section removes the need for the contour integral giving the shear stress of each infinitesimal component, which reduces the frictional term to:

$$\left(\frac{dp}{dz}\right)_{friction} = \frac{\tilde{\tau}_w P_z}{A_c} \propto \frac{P_z}{A_c} \propto \frac{2\pi D}{P^2 - \frac{\pi D^2}{4}} \quad (2.14)$$

Now, if the cladding layer were to be applied to the tubing with thickness  $t$ , then the diameter of the fuel cladding would increase by  $2t$ , its pitch  $P$  would remain the same, and the cross sectional area  $A_c$  would be reduced by  $(\pi t(2D + t))$ . Taking example dimensions from the SCK-CEN research center's MYRRHA lead-bismuth subcritical reactor and the lead fast design from Nikiforova et al. [24], we shall assume an original fuel cladding diameter of 6.35 mm with an extra cladding layer of 100  $\mu\text{m}$  and a pitch to diameter ratio of 1.3. Taking the ratio of the proportionality constants for the frictional term of the pressure drop in Equation 2.14 leads to a 9.2% increase in frictional pressure drop, which results in a proportional increase in the pumping work required. Therefore, it is not desired to constrict the reactor geometry too much, as that will put a strain on the pump.

## 2.4.2 Reactor Physics Considerations

None of the alloying elements in question suffer from excessive neutron activation or act as neutron poisons in the core, so from a neutronics standpoint the proposed composite is satisfactory. In addition, the fact that the proposed increase in operating temperature would allow the same power level to be achieved using a smaller core by shrinking the pitch to diameter ratio (at the cost of more pump work). This decreases the volume of coolant in the core, and therefore the amount of moderation that takes place. This serves to ensure a faster neutron spectrum in the reactor.

### 2.4.3 Strength Constraints

The superior tensile and creep strengths of F91 allow parts in the reactor to be made from thinner tubing than their HT-9 counterparts. However, F91 does encounter a drop in tensile strength and creep resistance above 600°C, restricting its recommended operating temperature [19]. An alternative solution is to use thicker walled components, putting constraints on the design of the reactor core. This is only expected to create difficulty when choosing the fuel cladding dimensions, as coolant piping is generally outside the core and can be made thicker without having to worry about the issues of neutronics and heat transfer. Figure 2-25 shows that the creep rupture strength of alloy F91 after three years (26,280 hours, or one fast reactor fuel cycle) at 650°C is 40 - 50 MPa. This is a good estimation of the pressure that the cladding will experience as a result of fission gas buildup.

### 2.4.4 Corrosion & Diffusion Constraints

When choosing the final dimensions of the composite, regions of corrosion susceptibility must be considered both at the outer edge of the cladding and at the clad-base metal interface. The outer corrosion layer must account for both a zone of oxidation and a zone of underlying elemental depletion, as chromium and silicon will migrate towards the outer surface of the cladding. The interface must allow for a layer of diffusional dilution, as well as a mixing layer from any processing steps that involve melting. Figure 2-31 shows a schematic of how various zones in the composite are expected to develop. The thickness of the cladding must be able to contain all these zones, allowing for a region of unchanged cladding in between should the corrosion zone and the elemental dilution zone be breached. The thickness of the diffusion layer is defined as where the concentration of silicon would be expected to fall below a lower threshold level. Chromium would not be the limiting factor here, because a minimum level of 10 wt. % (to be considered stainless) will exist slightly inside the F91 layer, while a minimum concentration of 1.25 wt. % Si (based on J. Y. Lim's work) will exist somewhere in the cladding layer.

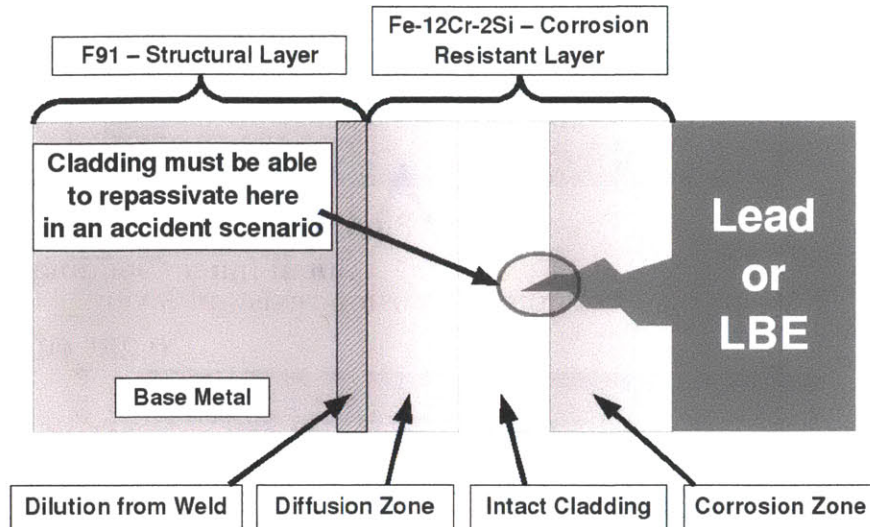


Figure 2-31: Diagram showing zones expected to develop during operation of the composite. The scale has been exaggerated for demonstration purposes.

## 2.4.5 Selection of Dimensions

Taking the above information into consideration, fuel cladding and coolant piping dimensions were chosen as detailed in Figure 2-32. The coolant piping dimensions were chosen to approximate  $1\frac{1}{2}$  inch schedule 80 piping, which calls for a 3.81 cm (1.50 inch) inner diameter (ID) and a 4.83 cm (1.90 inch) outer diameter (OD), giving a wall thickness of 0.51 cm (0.20 inches). In order to keep the 3.81 cm ID, the OD was made thicker to accommodate a cladding layer on the inside that is 0.75 mm (30 mil) in thickness.

This large thickness was used because coolant piping is expected to last the lifetime of the reactor, which could be as long as 60 years. The fuel cladding dimensions were taken from existing lead and LBE cooled reactor designs, such as those in Nikiforova et al. [24] and SCK-CEN's MYRRHA reactor. Because the estimated fuel cycle will be only three years, a thinner cladding layer is required. The cladding layer on the fuel cladding should be kept as thin as possible. This will provide as much space as possible for the structural layer, as necessitated by the reasons mentioned in Section 2.4.1, and it will avoid excessive radiation embrittlement due to silicon phase precipitation as described in Section 2.3.3.2.

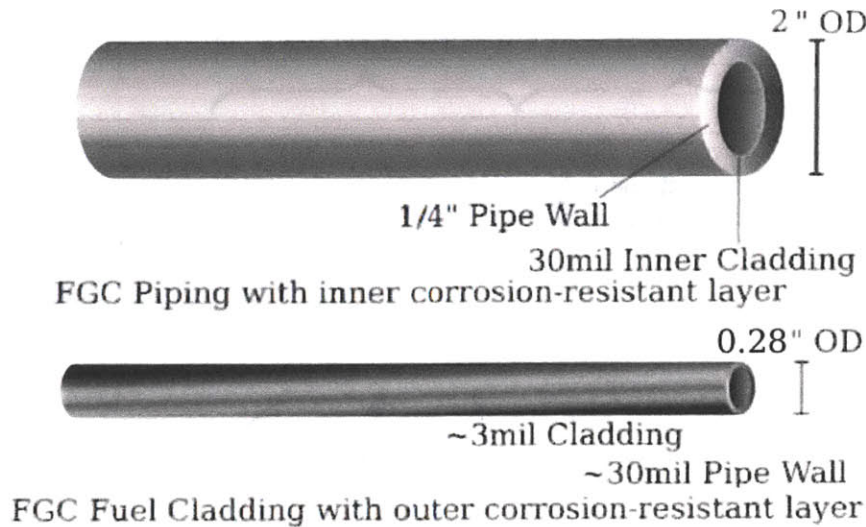


Figure 2-32: Selection of dimensions for the proposed FGC

## 2.4.6 Selection of Processing Steps

Processing steps were selected that preserve both the soundness of the interface between FGC layers and the toughness of the F91 structural layer. The integrity of the interface was tested at every processing step after the cladding is applied, so a method that provides good adhesion and microstructural mixing was required to deposit the Fe-12Cr-2Si onto the F91 layer. The best method is weld overlaying, in which successive deposits of Fe-12Cr-2Si weld wire are applied, first onto a billet of F91, then on top of the previous layers. A diagram showing how weld overlaying works is shown in Figure 2-33. This method required the fabrication of solid core weld wire, as opposed to the manufacture of a second hollow billet of Fe-12Cr-2Si to use as a 'sleeve' during co-extrusion. The welding process selected for the overlay was gas tungsten arc welding (GTAW), because there is an extensive database of welding parameters for this process on similar metals, and it produces a very high yield with few defects. Any defects caused by weld overlaying could compromise the outcome of subsequent processing steps.

Following weld overlay and billet cleanup, hot extrusion was chosen to reduce the size of the billet as much as possible. Extrusion involves heating the billet to nearly the melting point, applying a lubricant (molten glass in this case) and forcing the

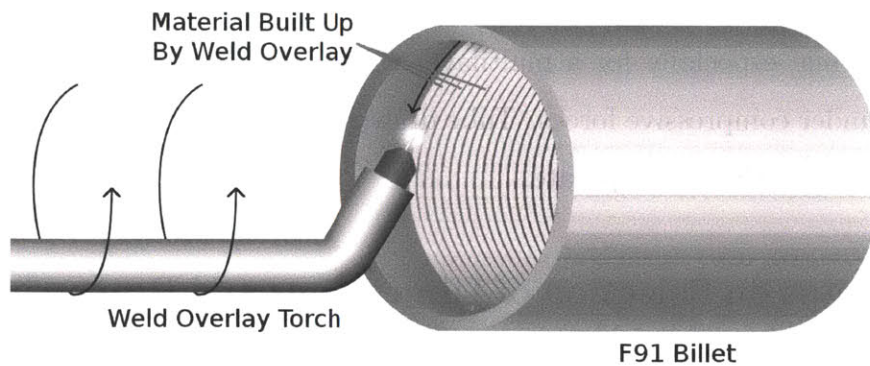


Figure 2-33: Diagram showing how weld overlaying works. To weld overlay the ID of a billet, a TIG torch is rotated inside the bore, or the billet turns around the torch. It deposits a spiral layer of material, with adjacent weld beads overlapping each other. The billet is turned as the torch is slowly retracted. Multiple layers can be deposited on top of each other to increase the thickness of the coating.

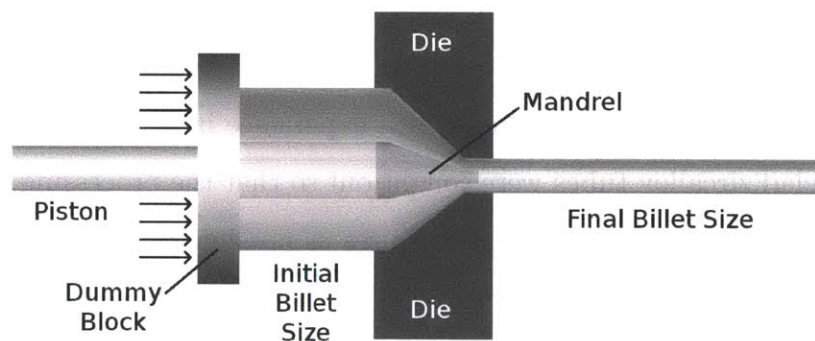


Figure 2-34: Diagram showing how extrusion works. A piston pushes the billet through a mandrel and die using a dummy block and hundreds of tons of force. This reduces the dimensions of the billet drastically. The ratio of diameter reduction to cross sectional area reduction is referred to as the extrusion ratio.

billet through a die and mandrel. This reduces the dimensions very rapidly, in a matter of seconds. By controlling the billet size, the weld overlay coating thickness, and the size & shape of the die and mandrel, the ratio of area reduction to diameter reduction (often referred to as the extrusion ratio) can be controlled, and therefore the end thickness of each layer can be predetermined. A diagram of how extrusion works is shown in Figure 2-34.

After extrusion, pilgering was chosen as the method to further reduce the diameter of the composite to its coolant piping form. Pilgering involves compressing a tube

through successive conic sectional dies. This method is favorable to others such as tube drawing, especially for a multilayer tube, because pilgering puts the entire composite under compressive forces. Tube drawing would apply tension to the layers, which could cause them to separate.

#### **2.4.7 Notes on Selection of Dimensions and Processing Steps**

It should be noted that the dimensions and steps listed above were estimates. The actual dimensions after each step were solely functions of existing commercial domestic capabilities. The dimensions were subject to change, for if a vendor already had a set of dies close to requested dimensions, they would be used to avoid paying extra tooling costs, which can be in the tens of thousands of dollars. Actual extrusion ratios, pilgering parameters, weld overlay parameters and final tolerances could not be accurately specified until the processing step is finished, as this composite has never been made before. Commercial vendors with experience in dealing with F91 as well as zirconium-clad zircalloy tubes were sought out so that the processing steps for the FGC would be as similar to existing procedures as possible.



# Chapter 3

## Experimental Methods

In this section all the methods and parameters used for performing the experiments and subsequent analysis will be described. Each analysis method and the information obtained will be discussed.

### 3.1 Material Procurement and Initial Testing

#### 3.1.1 Material Procurement

Two 25.4 cm (10") diameter, 2.54 cm (1") thick slices of F91 were purchased from Metalmen Sales, Inc. in Long Island City, NY in the quenched and tempered condition. One 200 g custom melt of Fe-12Cr-2Si was also supplied by Metalmen, but the samples used in the remainder of the tests ultimately came from a slice of the weld wire forging billet as described in Section 3.4.1. Ultra pure (99.999%) lead and bismuth were supplied in 34 kg (75 lb.) buckets by Surepure Chemicals, Inc. in Florham Park, NJ.

#### 3.1.2 Initial Testing

Microstructural analysis was performed on the F91 material to ensure that it arrived properly quenched and tempered. Samples of the F91 billet were sectioned by wire electrical discharge machining (EDM), mounted in Buehler Epoxicure epoxy and

Sample	Fe	Cr	Si	W	Mo	Cu			
F91	88.0147	9.4351	0.3478	0.0717	0.9606	0.1388			
Fe-12Cr-2Si	84.6493	13.1086	1.9975	0.1736	0.0006	0.0002			
Sample	Ni	Mn	V	S	P	Al			
F91	0.2797	0.5088	0.1918	0.0243	0.0173	0.0094			
Fe-12Cr-2Si	0.0058	0.0190	0.0004	0.0029	0.0005	0.0416			
Sample	Pb	Bi	As	Fe	Sb	Sn	Cu	Ni	Cr
Lead	95.9336	4.0661	0	0.0003	0	0	0	0	—
Bismuth	0	99.9974	0	0	0	—	0	—	0.0026

Table 3.1: Compositions of F91, Fe-12Cr-2Si, lead and bismuth in weight percent used in this study as verified by ICP-MS. Oxygen concentrations were subtracted, as they were subject to change by the cover gases during the experiments.

polished using SiC lapping paper, diamond paste and alumina suspension to 50 nm. Samples were then etched in 2% nital (2 wt. % highly concentrated nitric acid and pure ethanol) for up to five minutes. If that etch was insufficient, the samples were stained using a diluted Kalling's reagent (25 mL 18 M HCl, 25 mL pure ethanol, 0.2 g CuCl<sub>2</sub>) to uniformly add contrast to the material. Vickers hardness tests were also performed on the material to confirm that the hardness was in the properly tempered range for F91, which is described in Vallourec & Mannesmann's T91 book [19]. Finally, ICP-MS was performed on the F91, Fe-12Cr-2Si, pure lead and pure bismuth to test for any impurities that might exist. Elemental compositions as verified by inductively coupled plasma mass spectroscopy (ICP-MS) are shown in Table 3.1. Oxygen concentrations were subtracted from this analysis, as oxygen would either be consumed or added depending on the cover gas used in each experiment.

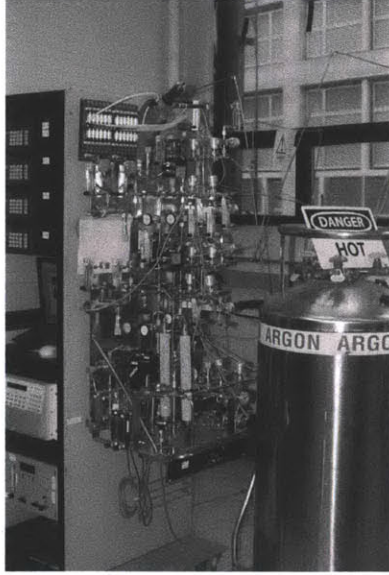
## 3.2 Static LBE Corrosion Testing

The goal of this sub-project was to test the corrosion response of each individual alloy at a range of times, temperatures and environments. The custom Fe-12Cr-2Si alloy was tested to establish its overall corrosion rates and mechanisms, and the same tests were performed on F91 in order to fill a gap in high temperature data for this alloy. This second set of tests was done to evaluate what would happen to the composite

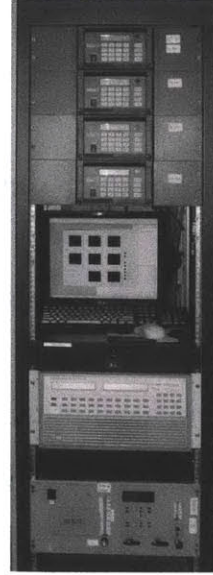
should the Fe-12Cr-2Si cladding layer be completely violated.

### 3.2.1 Experimental System Description

The experimental system was designed to deliver a different, precisely controlled cover gas to each of two heat treatment furnaces. This study made modifications to an existing gas delivery and monitoring system built for heat treatment of electromagnetic coils. Tanks of industrial grade argon and hydrogen were mixed to provide a hydrogen concentration of 0.25%, or 2,500 ppm. This gas mixture was chosen to provide enough of a reducing atmosphere to preclude the formation of fast-forming iron oxides. The argon gas passed through an oxygen trap consisting of an Oxy-Gon OG-120M gettering furnace outfitted with an Oxy-Gon C41-0008 titanium oxygen-trapping cartridge. Gas flow through the gettering furnace was partially diverted into a built-in oxygen meter at a flow rate of 0.1 LPM. This meter was read manually; measured oxygen levels remained at or below 120 ppb (parts per billion) throughout the test. The hydrogen was passed through dual redundant Middlesex Gases 6210-10 palladium catalytic converters that joined any oxygen present in the stream with hydrogen to form H<sub>2</sub>O. This was followed by flowing through dual redundant Middlesex Gases 8040-4 moisture traps to remove all moisture. The two gases were then mixed using Sierra Instruments Side-Trak mass flow controllers to a hydrogen concentration of 0.25%. This mixed gas stream was then analyzed using Panametrics Moisture Monitor 3 H<sub>2</sub>O/O<sub>2</sub> monitors outfitted with GE M9LR-Z moisture sensors and Delta-F SF3X555 oxygen sensors. The moisture sensors had a range of 0.001 - 10,000 ppmV (parts per million by volume), while the oxygen sensors had a range of 0.05 - 50 ppmV. All moisture and oxygen sensors in this project were sent back to their manufacturers for recalibration immediately before this study. This mixed gas stream was then fed directly to one furnace to provide the reducing atmosphere, and pumped through a water bath at a controlled temperature of 12.0°C ±0.1°C that provided a nominal inlet moisture concentration of 13,150 ppm for the oxidizing atmosphere. This vapor



(a) Gas mixing system with gas conditioners and sensors



(b) H<sub>2</sub>O/O<sub>2</sub> monitors, HP data acquisition system, oxygen gettering furnace and data logging computer

Figure 3-1: Gas mixing, delivery and analysis system used in the static corrosion experiments

pressure was determined from the Antoine equation [134]:

$$P_{sat} = 10^{\left[8.07131 - \frac{1730.63}{233.426 + T}\right]} \quad (3.1)$$

where  $P_{sat}$  is the saturation pressure for water at temperature  $T$  in °C. This equation is valid in the range of 1 - 100°C. The actual vapor pressure was measured to be lower by a factor of two, as the gas had to flow through the water bath at a sufficient rate to run the moisture and oxygen sensors. Therefore, the vapor pressure was not able to reach saturation before entering the oxidizing furnace. Separate gas outflows were collected and reanalyzed for H<sub>2</sub>O and O<sub>2</sub> content. Pictures of the gas delivery and analysis system are shown in Figure 3-1. A schematic of the system is shown in Figure 3-2.

Two Mellen upright cylindrical furnaces were outfitted with Honeywell K-type thermocouple temperature controllers to perform the heat treating. Custom-built stainless steel autoclaves were manufactured in-house at the Massachusetts Institute

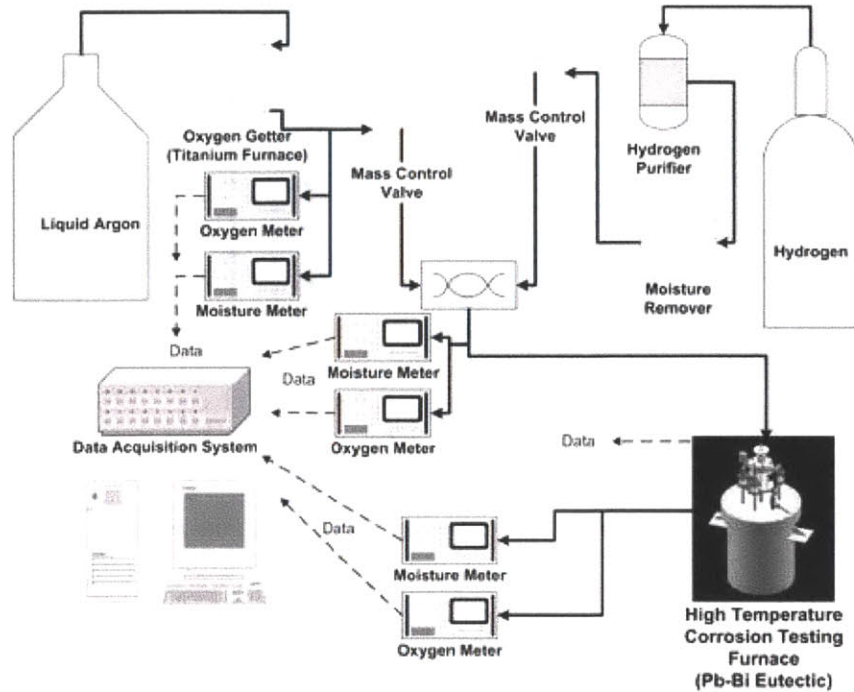
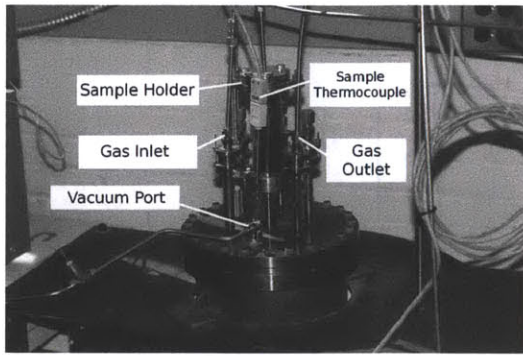
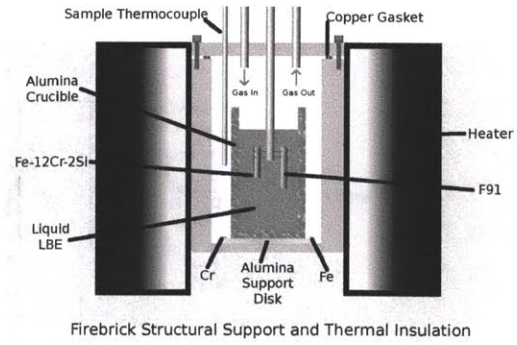


Figure 3-2: Schematic of LBE static corrosion test setup [7]

of Technology (MIT) to house the test setup and LBE. The autoclaves were built using copper gasket seals with knife edges, and previous studies had them helium leak tested to  $10^{-7} \frac{\text{cc}}{\text{sec}}$  [7]. The top of each autoclave was fitted with multiple bellows: one for a gas inlet, one for a gas outlet, one for applying a vacuum, two for alumina sheathed K-type thermocouples and one large adjustable bellows in the center for raising and lowering samples. This allowed the LBE to be melted and mixed before introducing the samples. It also allowed the samples to be lowered into the LBE at a known time and removed before the LBE solidified at the end of the test. The furnaces' temperatures were monitored with dedicated thermocouples inside the heating coils, while sample temperatures were measured with a thermocouple outside, but directly adjacent to, the LBE. The actual LBE was housed in McDanel Advanced Ceramic ACN3768 alumina crucibles. Samples were attached to a titanium rod coated with TiCN. By drilling 1.27 mm holes through the sample and the holding rod, it was possible to thread two short lengths of pure 1 mm thick molybdenum wire through the holes to avoid sample rotation and ensure their secure attachment to the holding rod. This ensured that the samples remained immersed in the LBE. Previous attempts



(a) Photograph of LBE test setup, showing bellows and gas tubing



(b) Cut-away of one LBE furnace showing placement of the LBE, samples and thermocouples

Figure 3-3: Picture and cut-away drawing of LBE furnaces used in this study

to dunk samples using tie wire resulted in the samples floating on top of the LBE. A picture of the test setup along with a cross sectional drawing of one furnace is shown in Figure 3-3.

### 3.2.2 Sample Preparation, Experimental Procedures and Test Matrix

Samples of F91 and Fe-12Cr-2Si were cut from a 2.54 cm (1") slice of their respective billets (as will be described below in Section 3.4.1) by wire EDM. Samples of F91 were 30 mm on a side, while samples of Fe-12Cr-2Si were 20 mm on a side. All samples were 2 - 3 mm thick. Two 1.27 mm holes were drilled in each sample for attachment to the sample holders as described in Section 3.2.1. Samples of each metal were then bound to a plate fitted for a Buehler EcoMet 3000 polisher equipped with an AutoMet 2 automatic polishing head and planed flat on one side using 120 grit SiC Carbimet sandpaper. Once flat, the samples were ground with the following grits of sandpaper for three minutes each: 320, 600, 800 and 1,200 grit. Samples were then polished using 3  $\mu\text{m}$  and 1  $\mu\text{m}$  MetaDi polycrystalline diamond suspensions for 2 minutes each, followed by a final polish using MasterPrep 50 nm alumina suspension for 3 minutes. All samples were polished using a force of 1.36 - 1.82 kg (3 - 4 pounds) per sample using counter-rotation at a speed of 130 RPM on a 20 cm (8 inch) platen. They were then

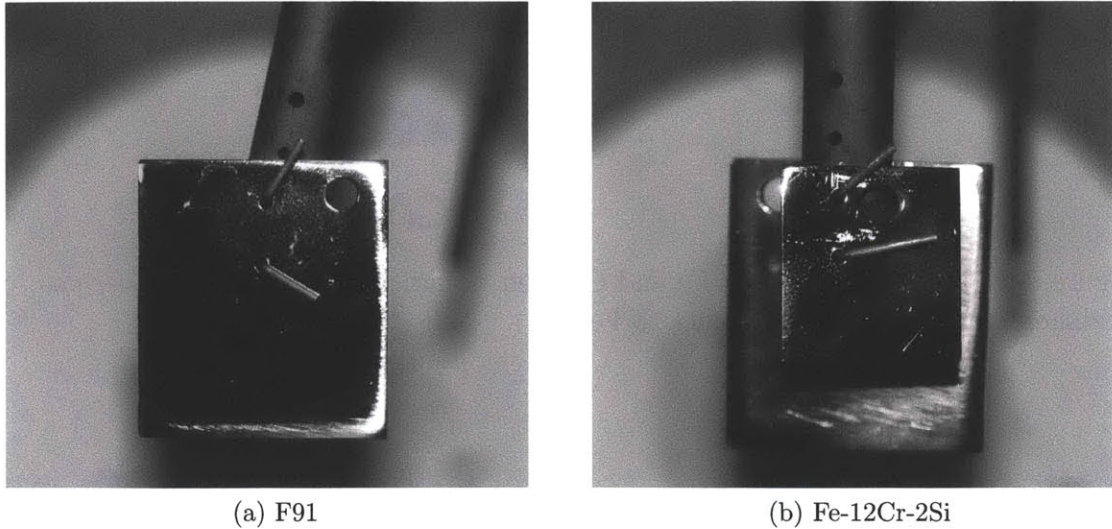


Figure 3-4: Polished and cleaned samples ready for exposure to LBE

scratched on the other side with 120 grit sandpaper to aid in identifying the polished surface following exposure to LBE. Samples were first sonicated in acetone, then in ethanol, for two minutes each to remove any residue from fingerprints and/or polishing solutions. Finally, they were cleaned with Kimwipes and 99.9% pure ethanol. A photograph of samples prepared for the LBE exposure experiments is shown in Figure 3-4.

Once the samples were affixed to the test setup, the autoclaves were closed and evacuated with a vacuum pump. The Ar/H<sub>2</sub> mixture was pumped in as a backfill, and this procedure was repeated three times. Backfilling ensures that the vacuum does not suck air into the furnaces through any small leaks that may exist. During this time the vacuum tightness of the setup was checked, and if any leaks were found, they were closed with the aid of leak detector solution and the backfilling procedure was repeated. The furnaces were then heated up to 400°C for a bakeout of 8 - 12 hours, and were held at the final test temperature until the gas levels inside them equilibrated. This was done to allow the hydrogen to consume any available oxygen in the system, a process which would be detected as a rise in the moisture levels in the gas outlet stream. The moisture level in the outlet stream of the reducing atmosphere was kept to a minimum, below 25 ppm, so that the H<sub>2</sub>/H<sub>2</sub>O ratio was maintained

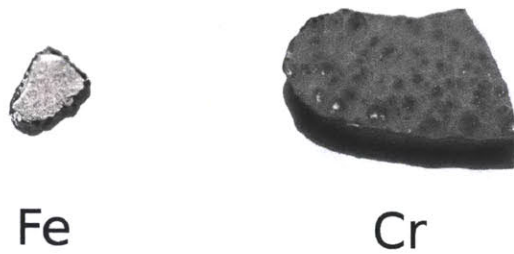
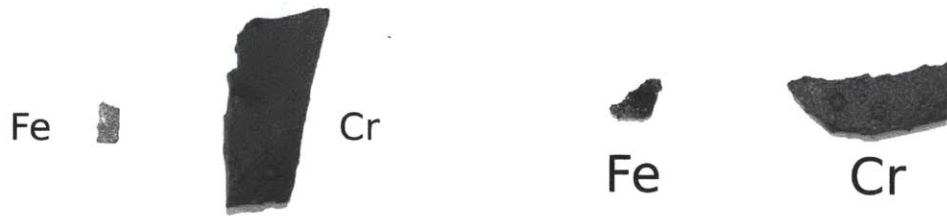


Figure 3-5: Test pieces of pure Fe and Cr used to indicate whether the cover gas was oxidizing or reducing with respect to  $\text{Fe}_3\text{O}_4$



(a) Test pieces after exposure to reducing environment (b) Test pieces after exposure to oxidizing environment

Figure 3-6: Test pieces of pure Fe and Cr after exposure to the cover gas in each environment, indicating the rough oxygen potential present during each experiment

between  $\frac{1}{100}$  and  $\frac{1}{1,000}$ . This established the oxide formation potential between that of  $\text{Fe}_3\text{O}_4$  and  $\text{FeCr}_2\text{O}_4$ , ensuring that any fast-growing iron oxides could not form. The moisture level in the outlet stream of the oxidizing atmosphere was maintained between 3,000 and 7,000 ppm, which corresponds to a  $\text{H}_2/\text{H}_2\text{O}$  ratio of between 0.83 and 0.36. This is above the formation potential of  $\text{Fe}_3\text{O}_4$  and  $\text{FeO}$ , but well below the formation potentials for lead and bismuth oxides. The oxygen levels were kept below 0.1 ppm on the  $\text{O}_2$  monitors. This reading is below the minimum rated range of the detectors. Therefore the measured oxygen levels only served to ensure a potential below the formation of  $\text{PbO}$  and  $\text{Bi}_2\text{O}_3$ , and to indicate if any leaks had formed. There were no leaks throughout the duration of the tests. A second definitive indicator of oxygen concentration was created by putting samples of highly pure, unoxidized iron and chromium in each furnace during each test. Examples of these test pieces before exposure can be seen in Figure 3-5, while test pieces after exposure to each environment can be seen in Figure 3-6. This served to confirm whether the oxygen concentration for each test was below or above the oxide formation potentials for

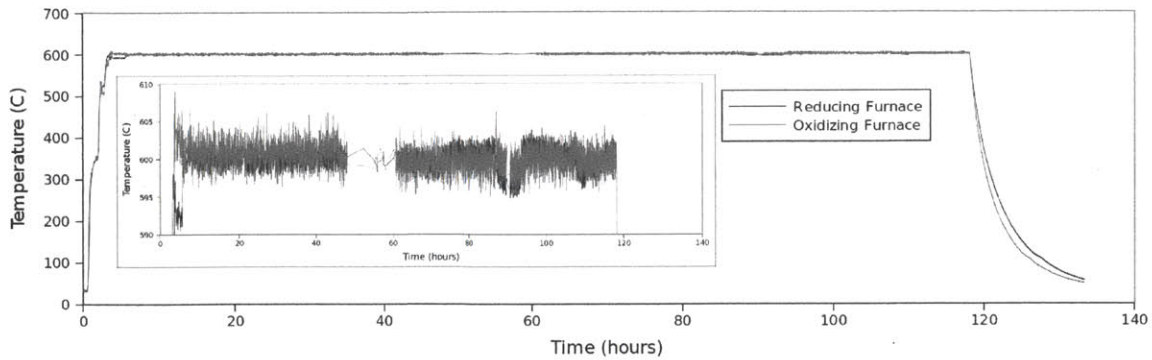


Temperature (°C)	600	700
Control Samples	0	0
Aging Time (hours)	124	70
	257	245
	504	506

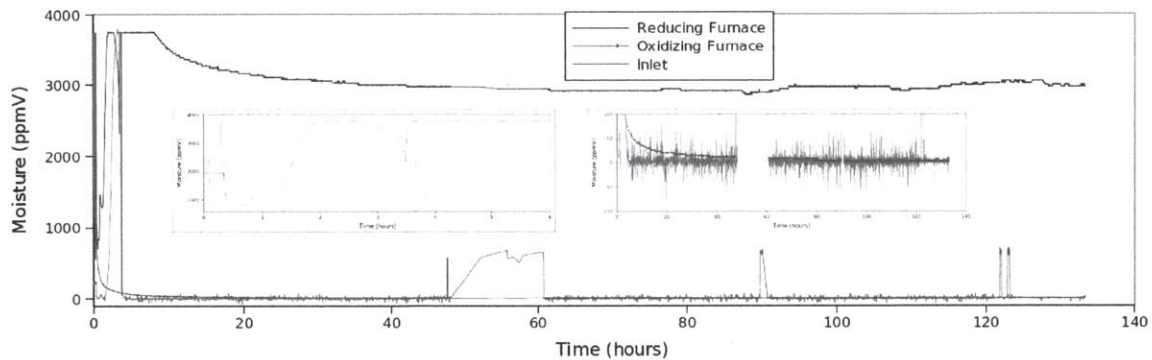
Table 3.2: Sample test matrix for static corrosion experiments showing actual aging times

Fe<sub>3</sub>O<sub>4</sub> and Cr<sub>2</sub>O<sub>3</sub>, which were the two most important O<sub>2</sub> potential boundaries in this study. Note that both samples exhibit a thick coating of black oxide (Fe) or blue oxide (Cr) in the oxidizing environment. In the reducing environment, the piece of Fe remains unoxidized, while the piece of Cr is once again oxidized. An example of the temperatures, moisture levels and oxygen levels recorded in these experiments is shown in Figure 3-7. In this example, one can see the backfilling process as spikes and dips in the moisture level of the inlet at the start of the test, as flow is started and as flow is stopped three times. The temperature rises to 400°C, then plateaus to 838°C in order to heat the furnaces to 700°C. This was done because the tops of the autoclaves were left without thermal insulation. This allows for cooling so as to avoid any over-temperature events. Therefore, the furnaces had to be heated above the test temperature to ensure that the samples reached the desired temperature setpoint.

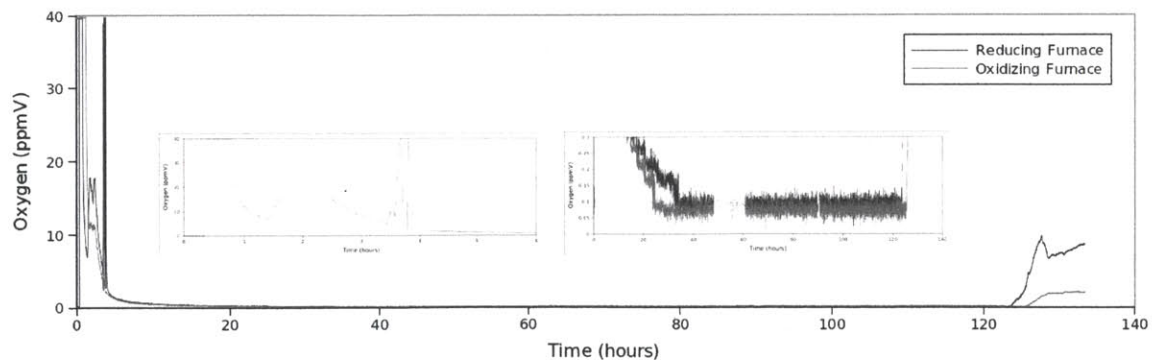
Samples of both F91 and Fe-12Cr-2Si were tested at 600°C and 700°C ( $\pm 2^\circ\text{C}$ ) for different times to obtain corrosion rate laws. The actual aging times are recorded in the sample matrix, shown in Table 3.2. After exposure, the samples were removed from the LBE via the bellows and the furnaces were shut off. Natural cooling was allowed to take place through the top of the autoclave. The cover gases were run and monitored continuously during cooldown to avoid any additional oxidation during this period. The cooldown process continued until a temperature of 40°C was reached. This took 18 hours to complete. When the cooldown process was complete, the samples were extracted and photographed.



(a) Temperature values recorded in this experiment. Note that a temperature of  $700^{\circ}\text{C} \pm 2^{\circ}\text{C}$  had to be maintained at the furnace coils to keep the samples at  $600^{\circ}\text{C}$  due to heat loss through the top of the experimental setup.



(b) Moisture levels recorded in this experiment. The zoomed-in portions show the moisture levels at startup and a closeup of the moisture levels during the test. The spikes in inlet moisture as well as noise on all lines are due to electronic noise; reading the actual moisture monitors showed far more stable results.



(c) Oxygen levels recorded in this experiment. The zoomed-in portions show the oxygen levels at startup and a closeup of the oxygen levels during the test. The thicker bands on the oxygen lines are due to electronic noise; reading the actual oxygen monitors showed far more stable results.

Figure 3-7: Example of the temperatures, moisture and oxygen levels recorded for the  $600^{\circ}\text{C}$  124 hour experiment

### 3.2.3 Analysis Procedures

The goals of analyzing the static corrosion samples were:

- Determine corrosion rates for both alloys as functions of time, temperature and environment.
- Determine corrosion mechanisms for both alloys at both temperatures (600°C & 700°C) and environments (oxidizing and reducing with respect to magnetite).
- Measure elemental depth profiles for the thin oxides on the Fe-12Cr-2Si samples.
- Determine oxide binding energies, and therefore oxidation numbers, for oxides on the Fe-12Cr-2Si samples.

#### 3.2.3.1 Post-Experimental Sample Preparation

Samples were sectioned into three pieces using a Leco VC-50 low speed diamond saw with an IsoCut wafering blade. This was done to produce three parts of each sample for different analyses: one to mount for optical and electron microscopy, one to send out for secondary ion mass spectroscopy (SIMS), and one for x-ray photoelectron spectroscopy (XPS) surface analysis. The first piece was mounted in Bakelite using a Struers Prestopress-3 and polished as in Section 3.2.2. The hot press used to mount the samples was sufficiently hot to melt some of the LBE that adhered to the samples during the LBE exposure tests. The other two pieces of each sample were sonicated first in acetone, then ethanol, in order to clean the surfaces for SIMS and XPS analyses. A photograph of a sample divided in this way is shown in Figure 3-8.

#### 3.2.3.2 Optical Microscopy

Mounted sections of each sample were analyzed on a Zeiss metallograph equipped with a Zeiss AxioCam MRc digital camera. These samples were left unetched in order to highlight any zones of LBE attack, porosity or difference in reflectivity from the oxide layers. Micrographs were taken at 50× and 200×.

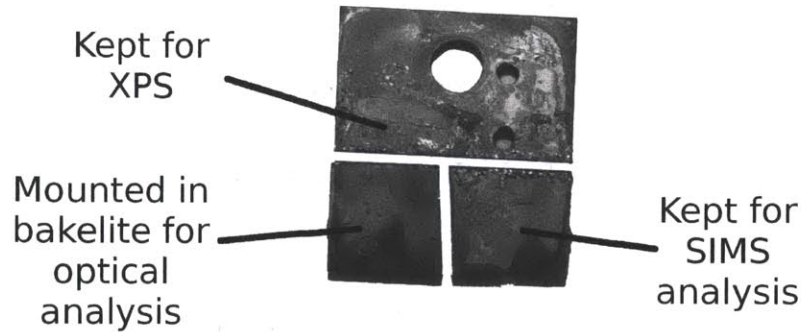


Figure 3-8: Photograph showing how samples were sectioned for analysis

### 3.2.3.3 SEM and EDX Analysis

Samples of F91 exposed to LBE were analyzed on a Topcon ABT-150 scanning electron microscope (SEM) equipped with a LaB<sub>6</sub> filament. The accelerating voltage was 29 kV, the emission current was 120  $\mu$ A, and a 50  $\mu$ m physical aperture was used. SEM photographs were taken using an Orion digital capture system. Energy dispersive x-ray spectroscopy (EDX) elemental maps were acquired to measure the thickness and the rough composition of the oxide layers that developed on the F91 samples. The oxide layers were too thin (on the order of hundreds of nanometers) to be measured accurately with the available SEM, so they were reserved for SIMS analysis.

### 3.2.3.4 XPS Surface Analysis

Samples of Fe-12Cr-2Si exposed to 700°C LBE for 506 hrs were analyzed on a Kratos x-ray photoelectron spectrometer equipped with a monochromatic aluminum x-ray source emitting x-rays at 1,486 eV and an emission current of 0.1 mA. Multiple locations were analyzed on these samples, as many regions were coated in a film of LBE, making surface analysis of the oxides difficult. The samples were also coated in a thin (on the order of tens of angstroms) layer of hydrocarbons and new oxides as a result of exposure to the air and cleaning agents. Any samples found in this condition were sputtered using an argon ion beam in the XPS to a depth of 10 - 20 Å. Once suitable locations for analysis were found, low resolution (1 eV) survey spectra were taken to identify which elements existed on the surface, and high resolution (0.1 eV) spectra

were taken near  $2p$  and  $2p^-$  orbital emission lines for iron, chromium and silicon in order to determine the exact binding energies of these metal ions. This allowed for the rough determination of oxidation states and oxide compositions on the surface. A high resolution spectrum for carbon (graphite) was taken to evaluate the amount of shift in the spectra, as even a shift of 0.2 eV can be the determining factor between two similar oxides. F91 samples were not analyzed by XPS, as available time on the instrument was scarce and knowledge of the surface composition of these samples was not deemed to be as important to this study.

### 3.2.3.5 SIMS Depth Profiles

Samples of Fe-12Cr-2Si were sent to the Evans Analytical Group in East Windsor, NJ for SIMS analysis. A beam of argon ions was used to sputter through the oxide layers to a depth of  $17\ \mu\text{m}$ . It was quickly determined that even the most highly oxidized ( $700^\circ\text{C}$ , 506 hours exposure, oxidizing environment) sputtered through all the oxide layers or elemental enrichment zones after less than 500 nm through the surface. Thus, future samples were sputtered to that depth or less at the highest spatial resolution possible. Samples exposed to LBE at  $700^\circ\text{C}$  for 506 hrs were first analyzed to determine the maximum thickness of the oxide layers on all samples, and the rest of the samples were sputtered to that depth. SIMS analysis was performed for the following elements: Fe, Cr, Si and O. F91 samples were not analyzed by SIMS, as the oxide layers were up to  $150\ \mu\text{m}$  thick. Instead SEM, EDX and the literature were used to estimate which oxides were present on the F91 samples.

## 3.3 Diffusion Studies

The goals of the diffusion studies were:

- To determine the diffusion coefficients of the two alloys in the composite.
- To identify and explain any microstructural changes incurred by diffusion.

- To develop a model that explains the shape and magnitude of concentration profiles as a function of time and aging temperature.
- To determine the diffusional stability of the composite.

### **3.3.1 Experimental System Description**

The experimental system for diffusion studies consisted of a Lindberg open air furnace fitted with MoSi<sub>2</sub> high temperature heating elements and R-type thermocouples for furnace control. Extra K-type thermocouples were used to monitor the temperature directly next to the samples. A chart recorder was used to record the temperature throughout the test.

### **3.3.2 Sample Preparation, Experimental Procedures and Test Matrix**

Samples of F91 and Fe-12Cr-2Si were sectioned from the initial materials in Sections 3.1.1 and 3.4.1, respectively. These samples measured 20 mm × 15 mm × 3 mm in size. These samples were mounted to a backing plate and planed using 180 grit sandpaper. They were then flipped, mounted with the flat side on the platen, and polished to a mirror finish as in Section 3.2.2. This was done to ensure that the two materials not only had mirror-flat faces, but also that the sides were parallel to avoid mismatch and slipping during manufacture of the diffusion couples. Samples were sent to Bodycote PLC, Inc. in Andover, MA for hot isostatic pressing (HIPing) in order to form a thin diffusion bond between the two materials that would be relatively free of porosity. Samples were sealed in stainless steel foil, vacuum canned in 3.2 mm (1/8") carbon steel to lock out oxygen, and HIPed at 1,050 - 1,100°C for 4 hours at a pressure of 96.5 MPa. These diffusion couples were then sealed in quartz ampoules under an inert argon atmosphere by Allen Scientific Glass in Boulder, CO. Upon return to MIT, the samples were then aged at 700°C, 750°C and 800°C in a Lindberg Model 51333 furnace in open air for different times as shown in Table 3.3. Control samples of each lot from the HIPing process were kept as references to compare to the

Aging Temperature (°C)	700	750	800
Control Samples	0 <sup>1</sup>		0
Aging Time (hours)	282	299	274
	556	597	495
	1,160	— <sup>2</sup>	1,220

<sup>1</sup>One control sample was taken from the lot that made both the 700°C and 750°C samples.

<sup>2</sup>Cells marked with “—” were not tested

Table 3.3: Test matrix for diffusion study samples

aged samples. Two batches of HIPing were carried out: one for the 800°C samples and one for the rest of the samples. One control sample from each of the two batches was kept for comparison to the aged samples.

### 3.3.3 Analysis Procedures

The goals of analyzing the diffusion couples were:

- To measure concentration profiles of iron, chromium and silicon across the interface.
- To monitor and explain any microstructural changes observed at or near the interface.
- To measure the hardness across the interface as an indirect measure of carbon diffusion and microstructural change.

#### 3.3.3.1 Post-Experimental Sample Preparation

Samples were sectioned into three pieces using the low speed diamond saw. One piece was reserved for mounting and polishing for optical microscopy, one was polished without mounting for EMPA and nanohardness analysis, and one piece was kept as a spare for future experiments.

The first piece of each sample was mounted and polished using the same procedure as in Section 3.2.2. Etching diffusion couples proved to be rather difficult. This is because both the diffusion bond and the carbon steel created galvanic couples that caused the more chemically active metal to become overetched, leaving the other metal

relatively untouched. To improve the etching process, samples were first carefully swabbed with 2% nital, taking care to only wet the sample while avoiding the can. If nital proved insufficient, samples were reswabbed with a concentrated solution of aqua regia by adding one drop each of highly concentrated HCl and HNO<sub>3</sub> to a cotton swab. The entire sample was then etched/stained using diluted waterless Kalling's reagent as described in Section 3.1.2.

The second piece of each sample was required to be less than 5 mm thick and as narrow as possible in preparation for both EMPA and nanohardness analysis. The stainless steel can was ground off, and the samples were planed flat, using 180 grit sandpaper. Next, they were mounted one at a time on a precision South Bay Technologies polishing rig intended for crystal planing. The samples were then carefully polished to a roughness of 50 nm so that the exposed face was both smooth and parallel to the other face. The parallel faces are necessary for nanohardness analysis, as the diamond tip moves across the sample only 30  $\mu\text{m}$  from the surface. An angle of even a few degrees could result in a raised section of the sample, which could damage or knock off the diamond indenter. Samples were then sonicated, first in acetone and then in ethanol, for one minute each before analysis.

### **3.3.3.2 Optical Microscopy**

Mounted diffusion couples were analyzed at 50 $\times$  and 200 $\times$  after etching. Polarizing filters were added to the light path in the microscope to add contrast to anisotropic phases (such as martensite), and regions selectively etched or stained by waterless Kalling's reagent.

### **3.3.3.3 Electron Microprobe Analyzer (EMPA) Concentration Profiles**

A JEOL JXA-733 Superprobe EMPA equipped with five wavelength dispersive spectrometer (WDS) detectors was used to measure the concentration profiles of iron, chromium, silicon and molybdenum across the interface of the diffusion couples. First, standard samples of each element were used to calibrate the WDS detectors. X-rays were counted for five minutes at each point. The grid of points was chosen to ensure



Aging Temp. (°C)	700/750	700			750		800			
Aging Time (hrs)	0	282	556	1,160	299	597	0	274 <sup>1</sup>	495 <sup>1</sup>	1,220
Coarse Grid (μm)	10	12			10		10	20	40	
Fine Grid (μm)	4	6			2.5		—	—	20	

<sup>1</sup>Only one point spacing was used for these samples

Table 3.4: Point spacings for diffusion couples analyzed by EMPA

not only that the majority of the points fell in the interface region, but also that the asymptotic ends of the concentration profiles, which become apparent as one moves further away from the interface, would still be measured. The center region of the analysis grid consisted of fifty finely spaced points (2.5 - 6 μm apart, depending on the aging time) followed by ten more widely spaced points on either side. A list of point spacing values for each sample analyzed is shown in Table 3.4. The minimum spacing was limited to 2 μm, as the beam was 1 μm wide.

### 3.3.3.4 Micro- and Nanohardness Profiles

Vickers hardnesses of each material in each diffusion couple were acquired on a Leco LM-247AT microhardness tester equipped with a Paxcam-2. Measurements were taken 2 mm away from the interface to provide an indication of carbon diffusion and microstructural change as a result of aging. The Vickers hardness measurements served to chronicle the diffusion of carbon into the cladding during aging. It was also used to gather information about carbon diffusion out of the F91 and microstructural changes induced by both carbon diffusion out and silicon diffusion in.

Nanohardness profiles were performed on a Micro Materials NanoTest 600 nanoindenter. Relevant parameters for all the tests are shown in Table 3.5. Successive linescans of indentations were made across the interface of each sample, resulting in a grid of indentations. These were averaged to obtain a more confident picture of how hardness varied across the interface. The total acquisition time for each point was five minutes. Scans were not begun until the machine had been kept in thermal isolation and equilibrium at 26°C ±0.1°C for five hours.

Parameter	Init. Load	Load Rate	Max Load	Max Depth	Dwell	Velocity		
Value	0.1 mN	0.2 mN/sec	19 N	1,000 nm	10 sec	0.3 $\mu\text{m}/\text{sec}$		
Aging Temp. (C)	700			800				
Aging Time (hrs)	0	282	556	1,160	0	274	495	1,220
# of Indents per Scan	20	10		10	10			
Indent Spacing ( $\mu\text{m}$ )	10	200		5	10			

Table 3.5: Relevant parameters and grid spacings for nanohardness tests on diffusion couples

### 3.4 Commercial Feasibility Study

The goal of this study was to demonstrate the immediate commercial viability for this composite. Unlike other materials developed to resist LBE corrosion, this composite is uniquely ready to be scaled up to the commercial production level. This was accomplished by:

- Identifying domestic vendors capable and willing to process this material
- Identifying possible processing steps for the composite and selecting the best ones
- Developing first order estimates for parameters for these processes based on the literature, static corrosion studies and diffusion studies in this thesis
- Processing the actual material as weld wire, F91 based pipe/tube production and FGC based pipe/tube production
- Analyzing the end results of each processing step, and tailoring the parameters of the next step to better ensure success
- Suggesting revisions to the processing schedule for the next iteration of composite fabrication

#### 3.4.1 Material Procurement

Three billets of quenched and tempered F91 were purchased from Metalmen Sales, Inc. in Long Island City, NY. Two billets were 30.5 cm (one foot) long, while one was

Element	Fe	Cr	Si	S	P	Ni	C	N
Spec.	Bal.	12 ±0.5	2 ±0.25	<0.008	<0.008	<0.01	<0.01	<25 ppm

Table 3.6: Specified chemistry in weight percent for Fe-12Cr-2Si weld wire

61 cm (two feet) long. All were 25.4 cm (10 inches) in diameter. Two 136 kg (300 lb.) billets of Fe-12Cr-2Si were custom melted at Metalwerks, Inc. in Aliquippa, PA. These billets were joined and remelted in a vacuum arc remelting (VAR) furnace to further remove impurities. Materials were tested by ICP-MS to verify their compositions as described in Section 3.1.2. This analysis was compared to the specifications set by this project for the Fe-12Cr-2Si alloy, as shown in Table 3.6. The chromium and silicon ranges were chosen to allow for compositional changes while still remaining highly protective against LBE attack. Sulfur and phosphorus levels were kept at very low levels, below 250 ppm, because these elements can segregate on grain boundaries, especially during welding, severely weakening the material. In addition, Müller et al. have demonstrated highly accelerated LBE attack on FeCrAl alloys whose grain boundaries were enriched in sulfur [104]. However, a small amount of sulfur does aid in weldability and flow by keeping the coefficient of surface tension in the weld bead positive [135]. A sulfur content of less than 70 ppm results in a negative coefficient of change in surface tension, producing a concave weld bead with a high width-to-depth ratio. Therefore sulfur was not entirely eliminated in this melt. Nickel was kept to a reasonable minimum of 0.01 wt. % to avoid dissolution of the alloy in LBE, as has been explained in Section 2.1.2. Carbon was also kept to a reasonable minimum of 0.01 wt. % so the effects of LBE on only one phase (ferrite) of this material could be studied. Finally, nitrogen was kept to a very low level, as nitrogen stabilizes austenite and reduces its ability to form martensite [136]. The manganese was added to consume any remaining sulfur by forming very small, well dispersed MnS precipitates [137].

### 3.4.2 Material Processing Procedures

A summary of the processing steps undertaken to manufacture this composite from raw materials is shown in Figure 3-9. Each step will be described below in terms of

## Procure three F91 billets

Three billets, 10" OD, 1' (x2) Long, 2' (x1) Long, Quenched & Tempered  
 F91 (9Cr, 0.1Ni, 1Mo, 0.2V, 0.4Mn, 0.075Nb, 0.4Si, 0.1C, Bal. Fe)

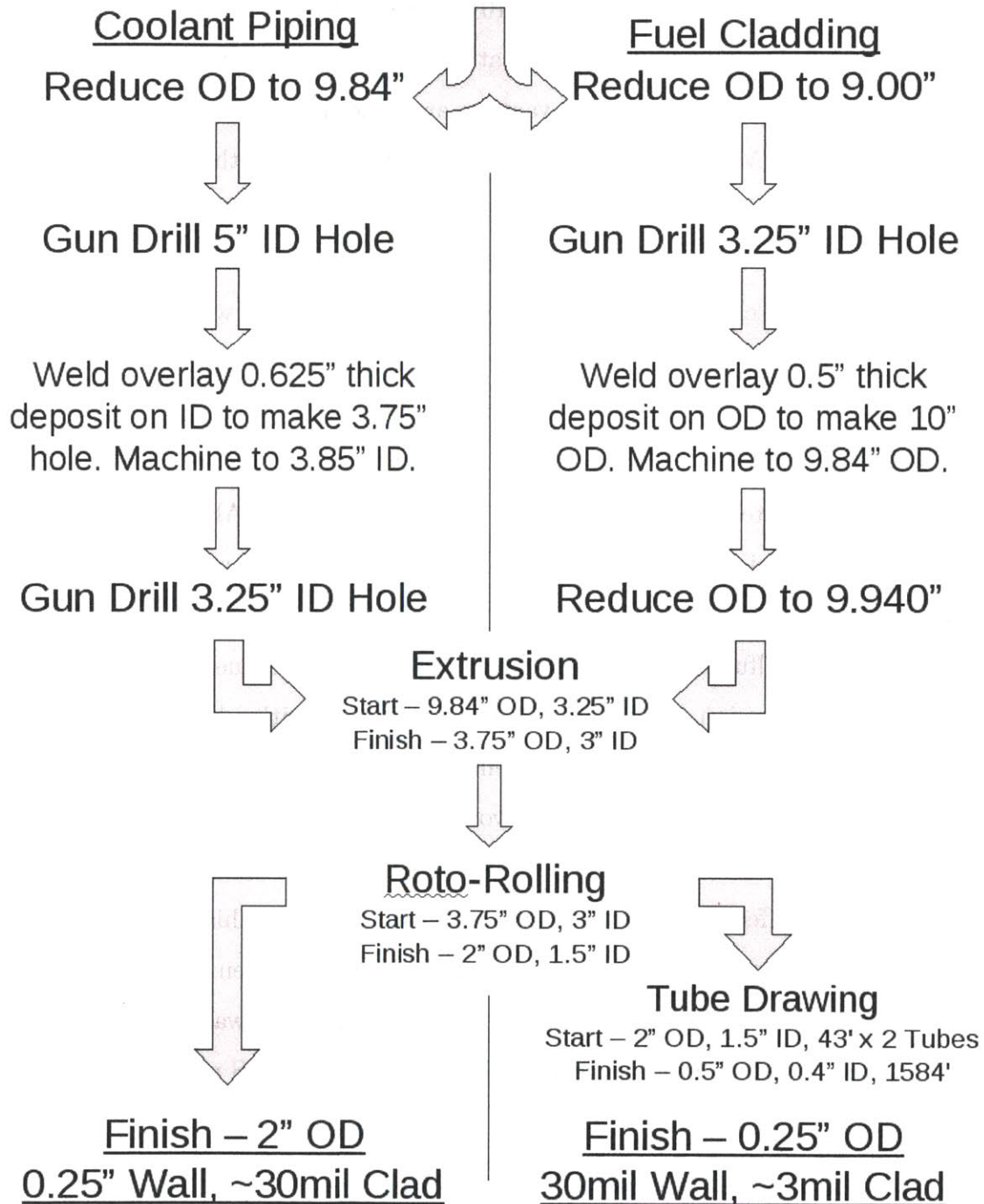


Figure 3-9: Processing schedule for the FGC developed in this study



Figure 3-10: Billets of F91 as machined, ready for weld overlaying. The long billet on the right (#1) has been drilled to a 12.7 cm (5") ID to become coolant piping. The billet at the back right (#2) has been lathe-turned down to a 22.9 cm (9") OD to become fuel cladding. The third billet (#3) is to become bare F91 fuel cladding for another project.

the process and relevant parameters.

It should be noted that significant research and work was done to ensure that the end product from each processing step would both have a high yield and be compatible for insertion into the next processing step. Simultaneous research while working between multiple vendors with an unfamiliar material was necessary to ensure success through this multi-step processing schedule.

#### 3.4.2.1 Initial Machining of Alloy F91 Billets

Billets of F91 were machined down by Deep Hole Specialists, Inc. in Chagrin Falls, OH to accommodate existing tooling available for future processing steps, specifically for the hot extrusion. The billets as-machined are shown in Figure 3-10. The available die and mandrel for extrusion called for an OD of 25 cm (9.84") and an ID of no less than 8.26 cm (3.25"). The billets were machined as follows: the two foot billet (#1) was destined to become coolant piping, so its outer diameter was lathe-turned

down to 25 cm (9.84") while its inner diameter was gun-drilled to 12.7 cm (5.00") to accommodate an ID cladding layer. The one foot billet destined to become fuel cladding (#2) was gun drilled to an ID of 8.26 cm (3.25") and lathe turned down to 22.9 cm (9.00") OD to allow for deposition of an outer layer of Fe-12Cr-2Si alloy. The third billet (#3) was machined to fit the mandrel and die dimensions, as it was not destined to be weld overlaid. In Figure 3-10, the billet on the right is the coolant piping billet, the billet on the back left is the fuel cladding billet, and the bare F91 billet is visible in the front left.

### **3.4.2.2 Weld Wire Fabrication**

The forging billet of Fe-12Cr-2Si, now 1.68 m (66 inches) long by 10.2 cm (4 inches) in diameter, was processed by Special Metals, Inc. in Huntington, WV in their bar and wire mill. Reduction down to 12.7 mm (1/2") in diameter proceeded smoothly, until the material became cobbled (bent and tangled) between two steps. This material was then cut out of the bar and wire mill, partially straightened, and sent to Haynes International, Inc. to be friction welded back together. This resulted in 6.35 mm (1/4") wire rod, which was sent down to Electrode Engineering in Harrington, TN to be drawn into 0.89 mm (0.035") solid core weld wire. The smaller weld wire dimension was chosen to allow a tighter bending radius for the automatic welding robot to use during weld overlay in the next step. A photograph of the weld wire at each stage of production is shown in Figure 3-11. It should be noted that the manufacturers described this material as very forgiving during processing, with no cracking whatsoever. This led to the high (nearly 100%) yield of this processing step.

### **3.4.2.3 Weld Overlay**

The weld wire and F91 billets were sent to Arc Applications in York, PA for weld overlaying. Billets were first fitted with carbon steel endcaps to allow the weld overlay process to run past the end of each billet, thereby increasing the yield of the process. A Bor-Tech automatic spiral welding machine outfitted with a GTAW electrode and a 61 cm (24") stroke length was used to apply a uniform, spiral coating of Fe-12Cr-

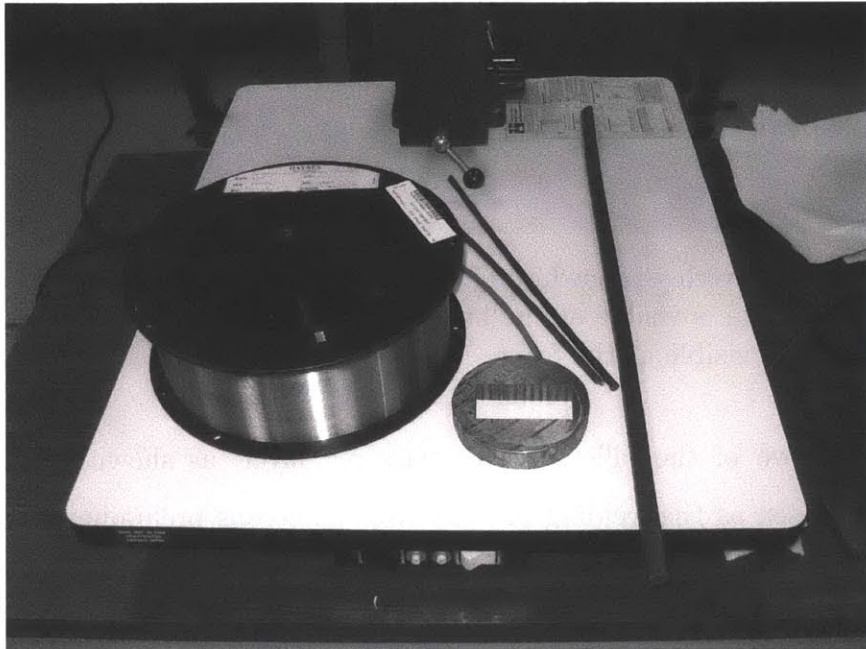


Figure 3-11: Photographs of weld wire in various stages of production. First a forging billet was made, a slice of which is visible at the front of the figure. It was then drawn in a bar-and-wire mill to 12.7 cm (1/2") OD rod (on the right), and then to 6.35 mm (1/4") OD wire rod (at the back). Finally, it was wire drawn to 0.89 mm (0.035") solid core MIG weld wire (at the front-left).

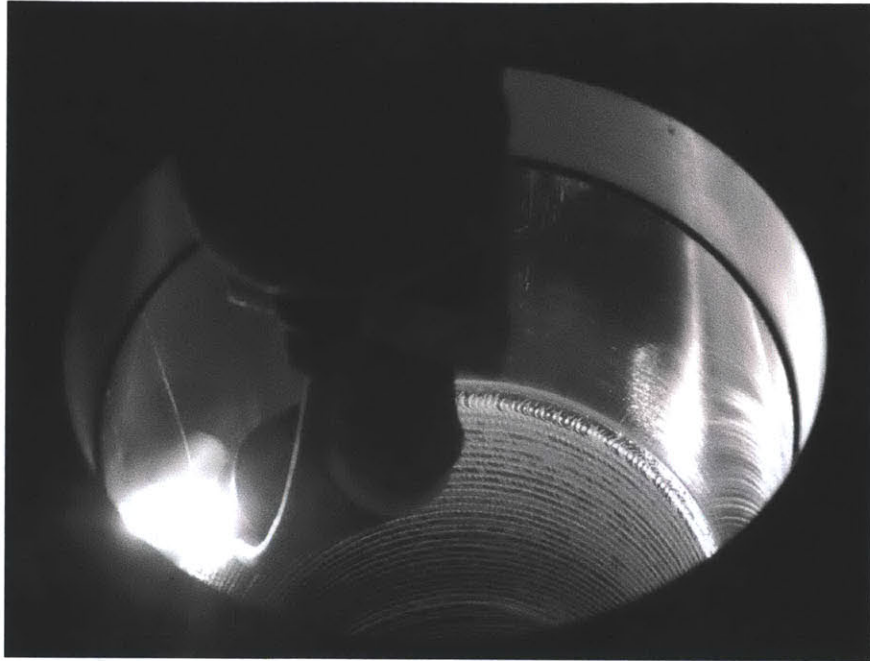


Figure 3-12: Weld overlay procedure of the ID-clad billet in process. The first pass of deposited material is visible at the back of the billet, while bare metal waiting to be weld-overlaid is visible at the front.

2Si alloy onto two of the billets in one pass per layer, as shown in Figure 3-12. GTAW was chosen as the welding process after numerous preliminary TIG welding studies (detailed below in Section 3.5.1) and after experimentation by the vendor with different processes. The welder used a zig-zag motion so that the thickness of material deposited during each pass was larger than the diameter of the weld wire. The billets were preheated to 400°C before welding, and the interpass temperature was maintained between 200°C and 400°C. After welding, the billets underwent a post-weld heat treatment (PWHT) at 600°C for 4 hours. A photograph of the finished ID-clad billet is shown in Figure 3-13. The endcap can clearly be seen; its function is to allow the weld overlay process to extend beyond the length of the actual billet in order to increase the yield of the process.

#### **3.4.2.4 Co-Extrusion**

Weld-overlaid billets were then sent to H. C. Starck in Coldwater, MI for extrusion. The billets were cleaned, and a 2.54 cm (1") fillet was turned on the OD of each



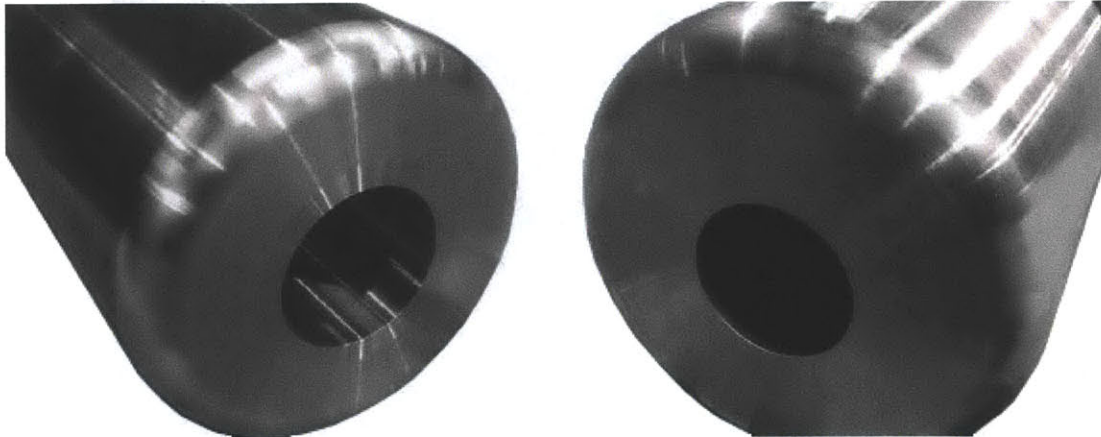


Figure 3-13: Finished ID-clad weld overlaid billet

billet to allow for easier insertion into the extrusion die, as shown in Figure 3-14. The billets were then preheated to 816°C (1,500°F) in a reducing gas furnace for one hour, followed by an induction preheat to between 1,193 and 1,224°C (2,180 - 2,236°F) for 15 minutes. The billets were then immediately rolled out of the furnace and onto a fiberglass blanket. Glass lubricant was poured into the inner diameter, glass endcaps were melted on, and the billet was extruded within 15 seconds. A full extrusion report is provided in Appendix B. This shows the time and temperature information, the extrusion force as a function of time, and the speed at which the billet moved through the press. The billets were then allowed to air cool in still air to room temperature. A 2.54 cm (one inch) section from the back end of each extruded billet was removed using a hot chop saw attached to the outlet of the extrusion press for further analysis.

#### 3.4.2.5 Pilgering and Tube Drawing

As of the date of submission of this thesis, the tubes are currently undergoing pilgering and tube drawing at Haynes International, Inc. in Arcadia, LA. The coolant piping tubes will be pilgered in a two step process down to the modified Schedule 80 dimensions as previously described (3.81 cm ID, 5.08 cm OD with a 1.27 mm thick



(a) ID-clad billet, ready for extrusion. The Fe-12Cr-2Si layer is visible as a shinier layer on the ID of the billet.

(b) OD-clad billet, ready for extrusion

Figure 3-14: Billets with fillets, ready for extrusion. The 1" radius fillets allow for easier insertion of the billets into the die, reducing the force necessary to begin extrusion.

cladding layer on the ID, or a 1.50" ID, 2.00" OD with a 0.05" thick cladding layer). The fuel cladding tubes will be processed down to an OD of 6.35 mm with a 1 mm wall thickness as specified in the design for the MYRRHA accelerator driven reactor at SCK-CEN in Belgium.

### 3.4.3 Testing Procedures and Analysis Techniques

The purposes of the analysis steps in this project were:

- To evaluate the effects of each processing step on the microstructure and properties of the composite
- To adjust the next processing step based on results from the previous step
- To make recommendations as to how to further improve processing
- To explain any and all microstructural features observed after each step

### **3.4.3.1 Post-Experimental Sample Preparation**

Samples of each billet from each step were sectioned, mounted and polished in the same manner as in Section 3.2.2. Samples were immersed in dilute waterless Kalling's reagent for five seconds, then immediately rinsed in flowing water to avoid overetching. Ultrasonic testing (UT) scans were performed in-house on the slices of the extrusion billets to check for deformities or gaps. None were found.

### **3.4.3.2 Optical Microscopy**

Samples of each billet from each step were analyzed by optical microscopy in the same manner described in Section 3.2.2, with the aim of identifying microstructural features that were different from the idealized diffusion and static corrosion experiments. Changes in the bulk microstructure were tracked, as was the microstructure of the interface. Both radial and axial cross sections of each extrusion billet were analyzed to look for any directionality in the microstructure due to extrusion or pilgering.

### **3.4.3.3 Microhardness Testing**

Samples of the as-received metals, the weld overlaid billets, and the extruded billets underwent Vickers hardness testing. This was done to link hardnesses of observed phases to their microstructures. It is then possible to explain how processing affected the composite and to suggest any extra additional annealing, quenching or tempering steps that would be necessary to improve fabrication. Vickers indentations were performed with either a 10 g or a 500 g deadweight and a dwell time of 15 seconds. The squareness of the indent was used to judge its quality. Any indentation whose diagonals differed in length by more than 5% was rejected.

## **3.5 Auxiliary Tests**

The overall goal of these studies was to understand more about how the composite evolved and how it could be used by employing laboratory scale methods to gain new

insights.

### **3.5.1 Initial Welding Study**

The initial welding study consisted of welding lines of Fe-12Cr-2Si weld wire in 1, 2 and 3 passes on coupons of F91 under controlled voltage and current settings. The goals of this test were to demonstrate the weldability of the system (before undertaking the weld overlay composite processing step) and to see how the first few layers would mix and evolve during weld overlaying.

#### **3.5.1.1 Experimental Procedure**

Three coupons of F91 were sectioned and polished using the procedure in Section 3.2.2. A partially rolled spool of Fe-12Cr-2Si weld wire was sent to us from Electrode Engineering in Harrington, TN to test the actual material in this study that would be used in weld overlaying. An in-house manual GTAW welder was used to deposit lines of Fe-12Cr-2Si onto the F91. If a coupon received more than one welding pass, then the passes were laid on top of each other to simulate the weld overlaying procedure. A welding current of 50 ADC and a negative electrode were used with pure argon cover gas at a flow rate of 20 cubic feet per minute (CFM) with 20 seconds of post weld flow to avoid oxidation. No preheat or postheat treatments were performed.

#### **3.5.1.2 Post-Experimental Sample Preparation**

Samples of each weld were sectioned both perpendicular to and in parallel with the welding direction. This was done to check for any differences. Samples were then mounted in epoxy, polished and etched for 10 seconds in Kalling's reagent as in Section 3.1.2.

#### **3.5.1.3 Optical Microscopy**

Samples were analyzed using optical microscopy on a Zeiss metallograph equipped with a Zeiss AxioCam MRc digital camera to evaluate microstructural changes and

mixing due to the welding procedures. Photographs were taken at 50× and 200×, and photo montages were created to show a high-resolution overall picture of the entire weld and heat affected zones. No image processing was performed, except for stitching the pictures together using the GIMP image processor software package.

### **3.5.2 Commercially Certified FGC Welding Study**

In order to demonstrate actual weldability in accordance with ASME standards, an ASME-certified weld was performed on the as-extruded composite in accordance with B31.1 boiler code welding procedure. The goals of this study were to demonstrate the code-certified weldability of the composite and to identify any microstructural changes that resulted from the welding process. This would allow for further development of the welding procedure based on initial commercial welding experience with this composite.

#### **3.5.2.1 Sample Procurement**

One foot sections of the two as-extruded clad tubes were removed from the processing schedule by a horizontal bandsaw for this study. Samples were taken from the back of each extruded tube to ensure that any regions of inhomogeneity (usually found at the front of the extrusion) would not be used. The preparation and welding of these two test sections is described in Figure 3-15. First, each sample was sliced in half axially. Next, two grooves were ground through the middle of the billet as shown in Figure 3-15 to accommodate the two different types of weld wire. The ID clad billet was then filled to 2.5 mm (0.1") with Fe-12Cr-2Si weld wire. Then the remaining 7 mm (0.275") was filled with F91 weld wire. The OD clad billet was filled to 7 mm (0.275") with F91 weld wire, followed by the remaining 2.5 mm (0.1") with Fe-12Cr-2Si weld wire. A preheat of at least 204°C (400°F) was applied to the billets before welding, and the interpass temperature did not exceed 371°C (700°F). This preheat temperature was maintained throughout the welding procedure, followed by a post weld heat treatment at 746°C (1,375°F) for two hours, and was finished by slow cooling

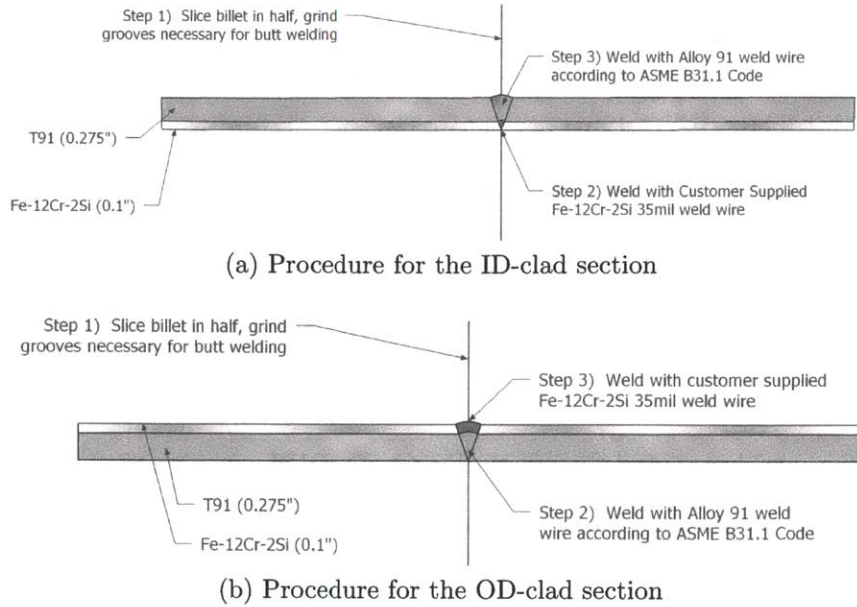


Figure 3-15: Welding procedure for samples in the ASME-certified welding study

in ambient still air to room temperature. This was followed by the normalization, quench and temper procedure for alloy F91 as outlined in the T91 book [19], which consisted of normalization at 1,050°C for 30 minutes, followed by cooling in air (which is effectively a quench for alloy F91 according to its TTT diagram, shown in Figure 3-16), followed by tempering at 750°C for one hour and slow cooling in air to room temperature. The full welding and certification report can be found in Appendix C.

### 3.5.2.2 Post-Experimental Sample Preparation

Samples were cut from each test section perpendicular to the welding direction. Samples were extracted to show at least the midpoint of the weld, as well as one inch beyond its outer boundary, to ensure that any heat affected zone was captured by this analysis. The sectioning, mounting, polishing and etching procedure was the same as that described in Section 3.1.2.

### 3.5.2.3 Optical Microscopy

Optical micrographs were taken on a Zeiss metallograph equipped with a Zeiss Axio-Cam MRc digital camera at 50× and 200×. The photographs at 50× were stitched

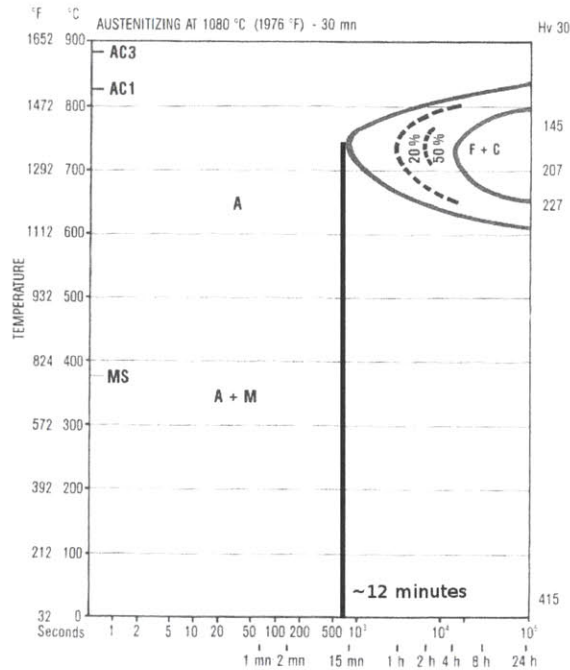


Figure 3-16: TTT Diagram for F91, showing that even slow cooling in air to  $T_M$  for 12 minutes still forms 100% martensite [19]

together to make a photo montage showing the entirety of the weld and the surrounding HAZ as described in Section 3.5.1.3.

### 3.5.2.4 Microhardness Profiles

Vickers hardness profiles were acquired using a 10 g weight and a grid spacing of  $50 \mu\text{m}$ . The fine features and variability required this relatively light load in order to create smaller indents. Vickers hardness measurements are normally carried out using heavier loads, between 100 and 500 gf. A larger uncertainty in point measurement was therefore accepted in order to vastly increase the spatial resolution of the analysis. These profiles were acquired in order to match regions of observed microstructure to their hardnesses. In addition, quantification of the size and severity of any HAZ present was of the utmost importance, as the HAZ is the most likely site for unexpected cracking in F91 welds due to Type IV cracking. Type IV cracking is defined as preferential failure in the fine-grained region of the HAZ due to creep-induced damage, often on the boundary between the finer grained HAZ and the base metal [138].

This occurs after thousands to tens of thousands of hours of service, as a result of a high hardness in the HAZ due to an improper post-weld heat treatment [139, 138].

### **3.5.3 Composite Breach Corrosion Study**

The goal of this study was to evaluate how liquid metal attack would proceed should the cladding layer of the composite be entirely breached. This consisted of manually breaching the cladding by drilling holes and performing LBE static corrosion experiments to simulate the effects that LBE exposure would have on this composite in the event of total cladding failure.

#### **3.5.3.1 Experimental System Description**

The experimental system used was identical to that used in the static corrosion experiments described in Section 3.2.1.

#### **3.5.3.2 Sample Preparation & Experimental Procedure**

Two samples of each product form were removed from the as-extruded billets with a hacksaw. The test coupons were 19 mm (3/4") square and 9.5 mm (3/8") thick with an inner radius of curvature of 38 mm (1.5"). 22.6 mm (0.89") holes were drilled through the cladding well into the F91 layer to allow LBE to accumulate and become depleted in oxygen. One sample of each product form (ID-clad & OD-clad) was exposed to static LBE at 700°C for 98 hours in both oxidizing and reducing environments with respect to the formation potential of magnetite.

#### **3.5.3.3 Post-Experimental Sample Preparation**

Samples were sectioned so that the three holes were coplanar on the face of the samples. Samples were mounted in epoxy, as mounting in Bakelite would have melted the LBE and changed the observed morphology of the areas inside the holes. Samples were then polished using the same procedure as in Section 3.1.2. These samples were



left unetched to allow for high contrast imaging of any oxides and/or LBE present inside the material.

#### **3.5.3.4 Optical Microscopy**

Optical micrographs were taken on a Zeiss metallograph equipped with a Zeiss Axio-Cam MRc digital camera at 50× and 200×.

#### **3.5.3.5 SEM and EDX Analysis**

SEM images of the samples were acquired to show finer features of oxidation and liquid metal attack. EDX elemental maps were also acquired to show the depth of any oxidation or liquid metal penetration into the materials.

### **3.6 Descriptions of Analysis Methods**

Quick descriptions of what each method of analysis is, what it measures, and how it can be used to find unique information are presented here for further clarification of the experimental processes used in this study.

#### **3.6.1 Sample Preparation**

The goal of proper sample preparation is to give an unobstructed, unchanged view of a flat cross section of material. Mounting methods are chosen to maximize edge retention and contrast while still taking into account factors such as conductivity (for SEM analysis), temperature (for Bakelite, as it melts solid LBE), and polishing quality (epoxy tends to hold onto polishing particles, producing more scratches). The goal of each polishing step is to erase all the scratches from the previous step while removing as little material as possible. Polishing multicomponent samples with different hardnesses such as this composite can result in far more scratches than usual, due to carbides dislodging from F91 and scratching Fe-12Cr-2Si. This is evident in many micrographs, in which the path of carbides dislodged near the interface can

be tracked along scratches that are found only in Fe-12Cr-2Si while the F91 remains perfectly polished. It has been found that applying relatively light loads (1.36 - 1.82 kg, or 3 - 4 lbs, per sample) and lower polishing speeds (120 - 150 revolutions per minute (RPM)) results in fewer particle dislodgements and thus fewer scratches in Fe-12Cr-2Si, the softer phase. Careful cleaning of all polishing machine parts and sonication of the samples in water for one minute between steps also drastically reduced the scratches present on each sample. One additional step that helps to further alleviate this problem is to continue polishing on a grit that is just above the average size of the carbides that dislodge. Polishing at finer grits will not be able to remove the scratches if the sandpaper grit size is smaller than the size of the scratching agent. Finally, it is important to check that the polishing wheels themselves do not contain any particles. Carbides from F91 are especially prone to lodging in cloth-based polishing wheels. Pouring some 2 - 5% nital (2 - 5% concentrated nitric acid in pure ethanol) on the polishing wheel both reveals the presence of carbides and dissolves them. Any lodged carbides will become visible as circles of orange rust. This rust is then washed off, and the process is repeated until no more carbides are present.

### **3.6.2 Sample Etching**

The choice of which etchant to use and for how long makes a large difference in the observable microstructure of a sample. Etchants such as nital can attack certain phases faster, preferentially attacking ferrite, grain boundaries and ferrite-carbide interfaces in higher carbon steels [140]. This is the case for F91, and this is manifested as an initial time when no etching appears to take place. In reality, certain phases are dissolving faster than others. Etching with waterless Kalling's reagent tends to stain each phase differently. Staining pure ferrite, as in Fe-12Cr-2Si, results in similar grains being differently shaded. This is believed to be due to varying surface energies between differently oriented grains, and it also allows for much easier identification of grain size and shape in a normally difficult to etch material. Care must also be taken when dealing with samples that form galvanic couples, as is the case with all forms of the

composite in this study. Improper or careless etching can leave one alloy overetched or stained while leaving the other untouched. Therefore careful masking or swabbing is sometimes required to properly etch all regions of a multicomponent sample. It has been found in this study that waterless Kalling's reagent provides excellent contrast for the entire composite when preceded by etching for 1 - 2 minutes in 2% nital to dissolve some of the carbides in F91. This reduces the sizes of the galvanic zones created due to etching with waterless Kalling's solution. Just applying waterless Kalling's alone can result in zones of underetching surrounding larger carbides.

### **3.6.3 Optical Microscopy**

Optical microscopy allows the visual identification of the different microstructures present in the sample. This can be further enhanced using digital cameras with high contrast, as high quality cameras can provide better contrast than the human eye. Crystallographically anisotropic materials have the property of polarizing incident light, so the addition of a polarizing filter in the path of the light can add further contrast to polycrystalline materials, such as the tempered martensite present in F91.

### **3.6.4 SEM and EDX**

Scanning electron microscopy rasters (scans back and forth, across & down) a beam of electrons across the sample, where secondary electrons are ejected and counted by a secondary electron detector. The detector is held at a 31° angle with respect to the sample, so variations in both height and secondary electron emissivity are picked up as differences in contrast by the SEM. Tightly focusing the electrons onto a very small point (typically a few microns) and at a very low angle with respect to the beam allows for a much higher depth of field as compared to optical microscopy. This allows for far larger variations in sample height without losing focus during analysis. The electrons in an SEM have the theoretical ability to resolve features sized on the

order of their de Broglie wavelength, which is given by the following equation:

$$\lambda = \frac{h}{p} = \frac{h}{m_e v} = \frac{h}{\sqrt{2m_e eV}} \quad (3.2)$$

where  $\lambda$  is the de Broglie wavelength of the electron,  $h$  is Planck's constant,  $p$  is the relativistic momentum of the electron,  $m_e$  is the rest mass of the electron,  $v$  is its velocity,  $e$  is the charge of an electron and  $V$  is the accelerating voltage in the SEM. The electrons in an electron microscope can travel at a significant fraction of the speed of light, so relativistic effects cannot be neglected. The relativistic corrected wavelength of a particle traveling close to the speed of light is given by the following equation:

$$\lambda = \frac{h}{\sqrt{2m_e eV}} \times \frac{1}{\sqrt{1 + \frac{eV}{2m_e c^2}}} \quad (3.3)$$

where the second term is the relativistic wavelength correction factor. The de Broglie wavelength of an electron (here accelerated with a 29 kV potential) is 0.000168 nm, while the wavelengths of visible light lie between 400 and 700 nm. This resolution is not actually achievable due to beam spreading, sample charging, etc. However, the SEM used in this study has a realistic maximum resolution of 50 nm under ideal conditions.

Factors that affect the signal and resolution of an SEM image include vacuum pressure, working distance, accelerating voltage, physical apertures, spot size, vibration isolation, and sample preparation. Better vibration isolation, lower pressures, and higher quality sample preparation all increase both the signal and the resolution of the image. A shorter working distance generally results in a better image, as the electrons travel through less space with less of a chance of interacting with air molecules. A working distance of 25 mm is required to allow x-rays to enter the detector in the SEM used in this study. Higher accelerating voltages can increase the resolution of the sample; however, too high a voltage can damage some samples. Shrinking the physical and electronic apertures improves resolution at the cost of beam signal.

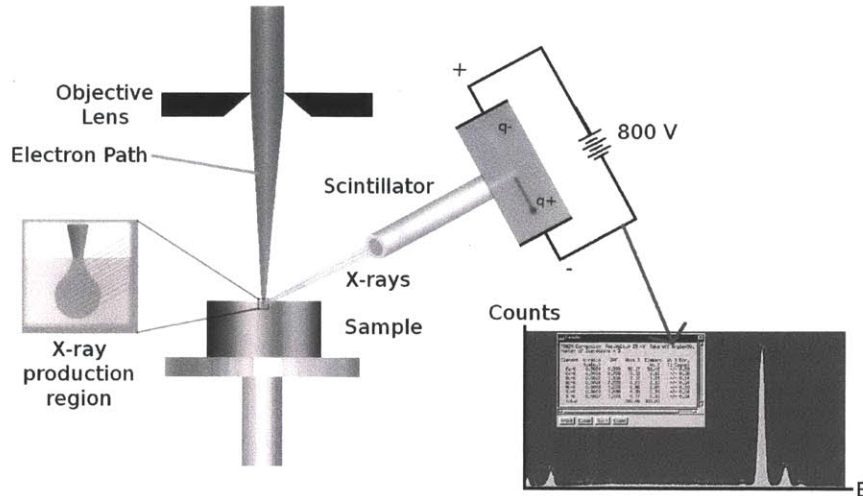


Figure 3-17: Diagram showing how EDX works in an SEM. X-rays generated by electron transitions in the sample enter the detector and are counted by energy.

EDX tallies the number of x-rays at each energy as they are emitted from the sample due to the interactions between the sample surface and the electron beam. When electrons from the beam strike the sample, they excite electrons in the sample, which then decay to their ground states by releasing characteristic x-rays. These x-rays can be counted using a high voltage biased detector to acquire an area x-ray spectrum for compositional analysis, or by rastering the beam in either a line or across an area to produce elemental linescans or elemental maps, respectively. The accelerating voltage of the beam must be at least 2.5 times the highest energy x-ray that is to be excited for compositional analysis. For example, if the copper  $K_{\alpha}$  line (8.048 keV [141]) is to be measured, the accelerating voltage of the beam must be at least 20 kV to get an accurate quantitative measurement of the copper percentage in the sample. A diagram explaining how EDX works is shown in Figure 3-17.

### 3.6.5 EMPA Concentration Profiling

An EMPA functions as a high precision SEM with individual WDS detectors tailored to individual elements, rather than as one detector that is used for all elements. This results in far higher quantitative accuracy, and allows for the acquisition of higher resolution linescans and elemental maps. This instrument is used when a conventional

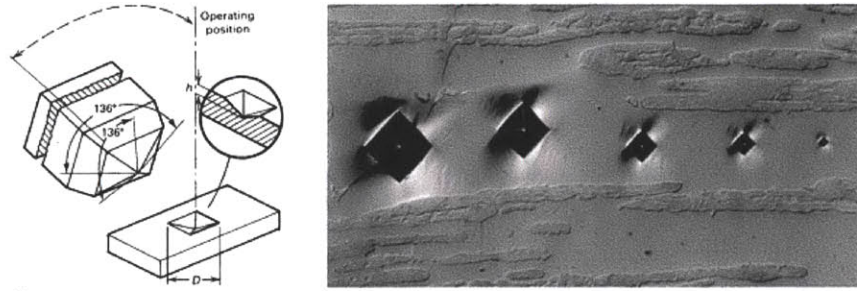


Figure 3-18: Diagram of the Vickers indenter and example indents [20]

SEM does not have the ability to resolve small differences in elemental composition, as is the case with the diffusion couple samples in this study. This is due to the far smaller size of the beam in an EMPA (typically less than one micron), which allows for higher spatial resolution when acquiring elemental maps and EDX linescans.

### 3.6.6 Micro- and Nanohardness Analysis

Micro- and nanohardness testing evaluate the resistance of a sample to small scale plastic deformation. In both types of analysis, a tip with a known geometry is applied to the sample using a fixed load, allowed to dwell so that time effects are not present, and released. The size of the indentation is then measured, either by measuring the width of the indentation (Vickers) or the depth to which the tip penetrated (Berkovich nanohardness) to obtain hardness data. The Vickers hardness of an indentation is measured by the following formula:

$$HV = \frac{1,854.4F}{d^2} \quad (3.4)$$

where  $F$  is the force in grams and  $d$  is the length of a diagonal in microns [20]. This hardness is usually reported as “xxxHV”, where HV stands for “Hardness Vickers,” denoting the type of hardness test. Ideally, the lengths of the diagonals would be equal; in reality, they should not differ by more than a few percent. A diagram of a Vickers hardness test, along with the tip used, is shown in Figure 3-18. Strain hardening takes place during these indentations. Therefore nearby indentations must be well separated to avoid interference of two localized areas of strain hardening,

which would produce an artificially high hardness measurement. For nanohardness testing, the indents must be separated by at least ten times the depth of each indent to be completely clear of the strain hardening zone. For Vickers hardness, a conservative estimation is to keep neighboring indents at least five times their width away from each other. This is because the Vickers indenter has a  $135^\circ$  angle tip, so the indentations are shallower than they are wide. Hardness values can correlate directly or indirectly to physical properties, such as tensile strength and yield stress. The hardness of known alloys can correlate to when and where cracking will likely occur, as harder regions typically cannot store as much energy before crack propagation takes place. Hardness mapping provides an excellent way to image a HAZ next to a weld where traditional microstructural analysis, such as optical microscopy or SEM, cannot resolve any distinguishing features.

### **3.6.7 XPS Surface Analysis**

XPS uses a monochromatic x-ray source to eject photoelectrons from the outer orbitals of the atoms in a sample. Because the source emits x-rays that are relatively low in energy (1 - 2 keV), the penetration depth of this technique is limited to a few atomic layers, making this a surface technique only. It is able to resolve the ejected photoelectrons at a very high resolution, typically on the order of tenths to hundredths of electron volts. This allows for the precise measurement of the binding energies of those ejected photoelectrons. Comparison of observed binding energies with known values allows the experimenter to determine the binding state that atom is in, and subsequently the oxidation state and oxide composition on the surface.

XPS does have a number of limitations due to the nature of the process. Photoelectrons are ejected with low kinetic energies. This kinetic energy is the x-ray source energy minus the binding energy of the photoelectron. Electrons with higher energies, such as in iron, leave with a lower kinetic energy than those with low binding energies, such as in silicon. As a result, electrons with higher kinetic energies escape the sample from a greater depth, resulting in larger peak weights for elements whose photoelectrons are more weakly bound. This can result in an inability to distinguish

whether an element is present on the surface or to a depth of tens of nanometers beneath. In addition, peaks for similar oxides (especially those of iron) can differ by only tenths of eV, which can be the resolving power of the XPS system. Care must be taken when interpreting XPS spectra based on sample geometry, surface preparation, possible contamination and which elements are being measured.

### **3.6.8 SIMS Depth Profiling**

SIMS involves using a beam of ions to sputter atoms from the surface of a sample into a mass spectrometer, where particles are separated by their mass-to-charge ratios by an electric field and counted. SIMS is unique in that it can sputter atoms to a great depth of tens of microns, and resolve both heavy and light elements. However, its quantitative resolution is very low. Therefore, it is more suitable to showing elemental concentration trends as a function of depth, rather than for purposes of exact concentration quantization.



# Chapter 4

## Results

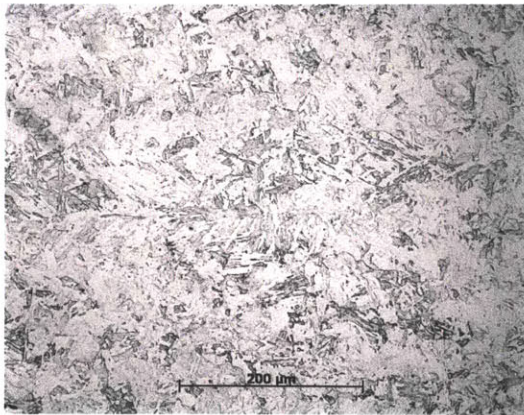
In this chapter the actual results for each test will be summarized, organized by alloy and type of analysis for ease of comparison. Only one or two micrographs will be shown to illustrate the features observed on each sample for the sake of brevity. Additional processing details and other data are included in the appropriate appendices.

### 4.1 Initial Testing

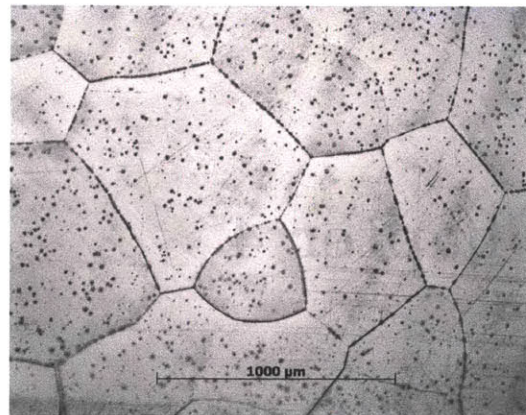
Before showing the results of all the tests performed on the alloys and the composite, it is helpful to understand what the starting materials look like compared to the reference materials, if they exist. Therefore, optical micrographs and hardnesses of the as-received materials will be shown for comparison with the post-experimentation samples.

#### 4.1.1 Optical Microscopy

Micrographs of the materials as they were received are shown in Figure 4-1. F91 exhibited a typical microstructure of tempered martensite and bainite, as can be seen from the highly elongated grains in Figure 4-1a. The grain size was 25 - 75  $\mu\text{m}$  in the long direction and 5 - 25  $\mu\text{m}$  in the short direction. This is typical of tempered F91's typical microstructure of plate-like grains of martensite as shown in the literature



(a) F91 as-received, 200 $\times$ . This is a typical quenched and tempered ferritic/martensitic microstructure, with a grain size between 25 - 75  $\mu\text{m}$  in the long direction and 5 - 25  $\mu\text{m}$  in the short direction.



(b) Fe-12Cr-2Si, 50 $\times$ . Large grains of ferrite are visible, whose size varies from 0.5 to 2.0 mm. Most small carbides are concentrated on grain boundaries, while some are evenly dispersed throughout the grains. The size of the carbides has been exaggerated by etching.

Figure 4-1: Photographs of F91 and Fe-12Cr-2Si as received from the manufacturer. Samples were mounted in Bakelite, polished to 50 nm and swabbed with waterless Kalling's reagent for three seconds.

[142]. The cross sections of plate-like grains appear as laths in the micrographs. Fe-12Cr-2Si, shown in Figure 4-1b, exhibits a typical cast microstructure for nearly pure ferrite. This material was taken from a slice of the forged billet, which was hot forged from 15.25 cm (6") in diameter to 10.15 cm (4"). The grains were typically shaped ferrite grains, with sizes of 0.5 - 2.0 mm. Small carbides are visible as black dots both inside the grains and on grain boundaries. This is expected, as there exist temperature regions on the Fe-C binary phase diagram (shown in Figure 4-2) where this alloy's 0.01 wt. % carbon content results in a phase separation into  $\alpha$ -Fe with dissolved carbon and  $\text{Fe}_3\text{C}$  (iron carbide). These temperatures were likely encountered during forging. Therefore, these carbides precipitated out of solid solution.

#### 4.1.2 Microhardness Tests

F91 as-received had a Vickers hardness of 258 HV  $\pm$ 3 HV, while Fe-12Cr-2Si had a Vickers hardness of 161 HV  $\pm$ 8 HV. Uncertainties are given as 95% confidence intervals, or twice the standard error, throughout this thesis for each set of data. A

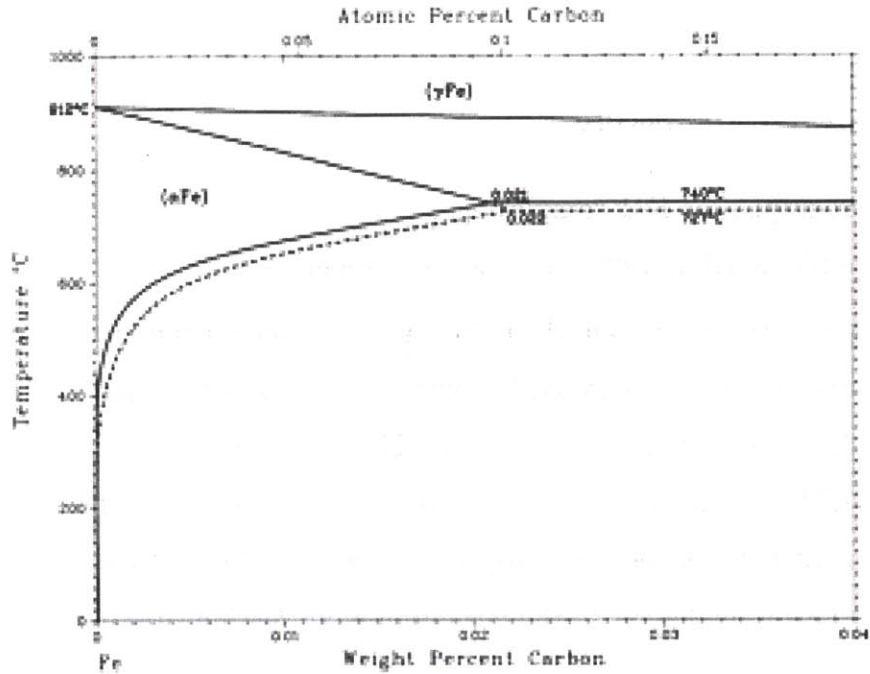


Figure 4-2: Fe-C binary phase diagram, showing two-phase regions ( $\alpha$ -Fe & Fe<sub>3</sub>C) for this alloy (shaded) [5]

hardness of 258 HV corresponds to a quench and temper heat treatment for F91. This hardness is too high for deployment in the field, as F91 possesses the best balance of ductility and strength between 190 HV and 220 HV [143, 144]. The hardness of Fe-12Cr-2Si is softer than fully annealed F91, and thus it will always be the softer material throughout the processing schedule.

## 4.2 Static LBE Test Results

The results of the static corrosion tests will be documented here, organized by alloy and method of analysis. SIMS was not performed on the F91 samples. XPS was not performed on the F91 samples, as the surface oxide composition for this alloy is well documented in the literature [68]. Otherwise, the alloys were analyzed in identical fashions for purposes of comparison.

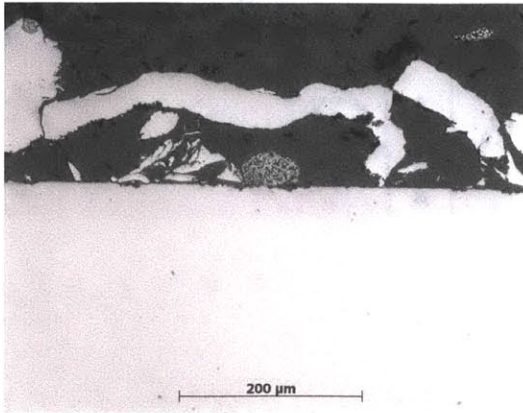
## 4.2.1 Results for F91

### 4.2.1.1 Optical Microscopy

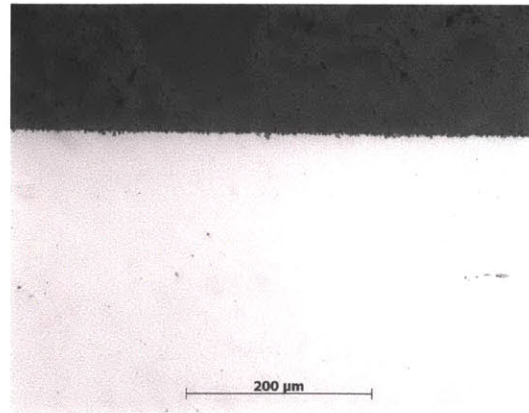
Optical micrographs for F91 samples aged at 600°C are shown in Figure 4-3, while those for samples aged at 700°C are shown in Figure 4-4.

Samples exposed at 600°C in the reducing environment experienced fairly uniform dissolution from the LBE, as would be expected for a material that has not formed a protective film against liquid metal attack. These samples appear to form regions of accelerated LBE attack, as in the 124 hour sample exposed to reducing LBE. Here, small regions of LBE penetration appear to spread outwards across the surface of the sample. This is analogous to the formation of nucleation sites, which then trigger further LBE liquid metal attack to spread radially outwards across the exposed surface of the sample. The sample exposed for 257 hours to reducing LBE appears to have been more uniformly corroded, with slightly thicker regions of attack existing close to larger clumps of adhered liquid metal. The sample exposed for 504 hours to reducing LBE shows accelerated LBE attack underneath a detached clump of LBE, spreading outwards across the surface. In all these samples, the heat of the Bakelite mounting process partially melted LBE on the surface, causing it to appear detached from the sample. The LBE adhered to the samples quite well before mounting.

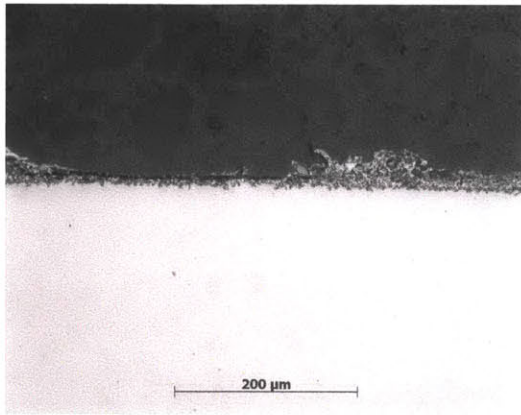
Samples exposed at 600°C in the oxidizing environment did not experience such extreme dissolution as the samples in the reducing environment. However, in all samples exposed to oxidizing LBE at this temperature, considerable surface roughening was observed along with occasional sites of accelerated LBE attack. This is indicative of the fact that the oxides formed on bare F91 are insufficient to keep LBE from damaging it. The sample exposed for 124 hours to oxidizing LBE exhibited fairly uniform attack with some small regions of accelerated, deeper corrosion. F91 exposed for 257 hours to oxidizing LBE appeared fairly similar to the previous one, with the exception of one site of more accelerated corrosion. This is thought to originate from deeper areas of corrosion as seen in the 124 hour sample. F91 exposed to oxidizing LBE for 504 hours showed more zones of accelerated corrosion, showing that the oxides



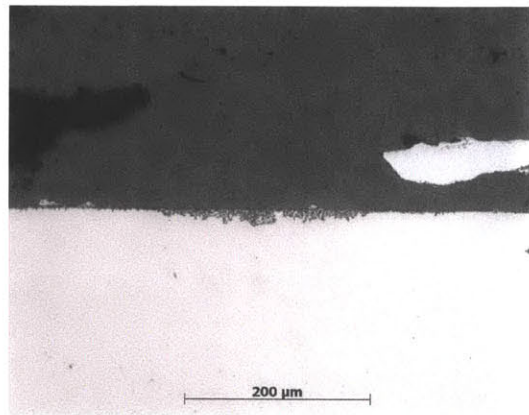
(a) After 124 hrs in reducing LBE



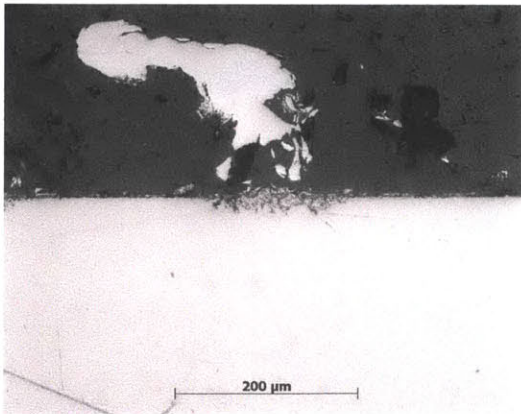
(b) After 124 hrs in oxidizing LBE



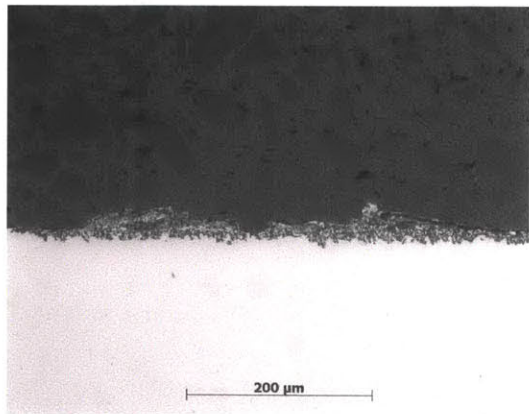
(c) After 257 hrs in reducing LBE



(d) After 257 hrs in oxidizing LBE

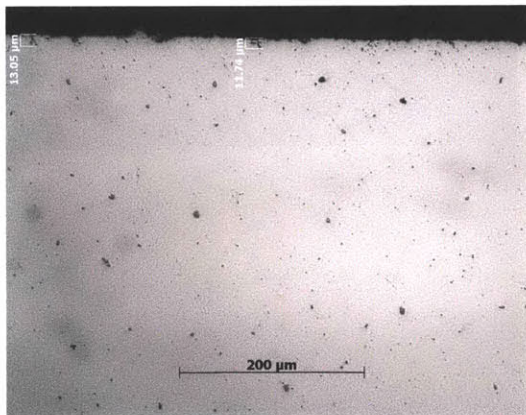


(e) After 504 hrs in reducing LBE

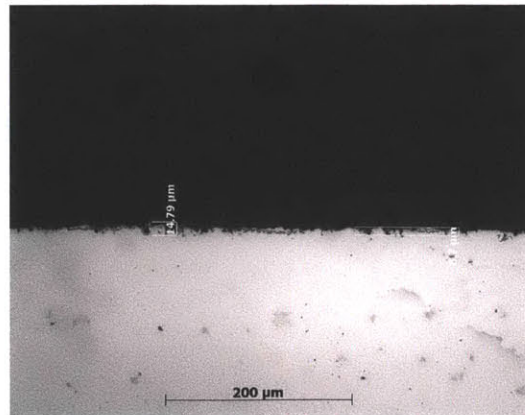


(f) After 504 hrs in oxidizing LBE

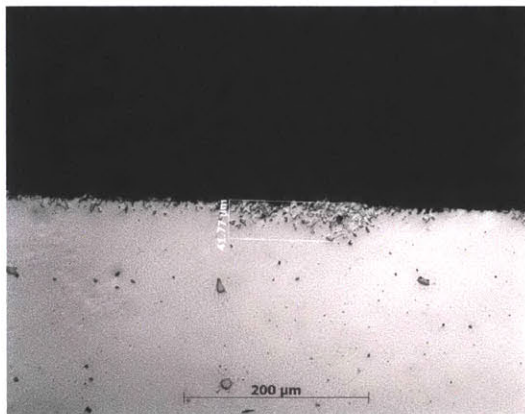
Figure 4-3: Optical micrographs of F91 samples exposed to 600°C LBE at 200 $\times$ . Samples exposed to reducing LBE show evidence of liquid metal attack channels, while those exposed to oxidizing LBE exhibit more uniform oxidation characteristics.



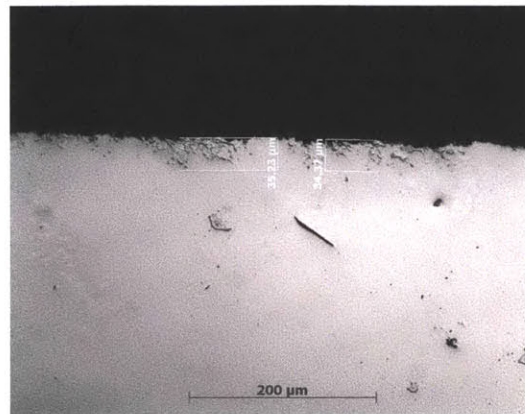
(a) After 70 hrs in reducing LBE



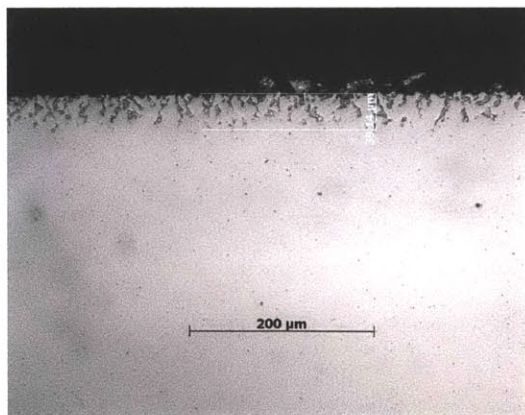
(b) After 70 hrs in oxidizing LBE



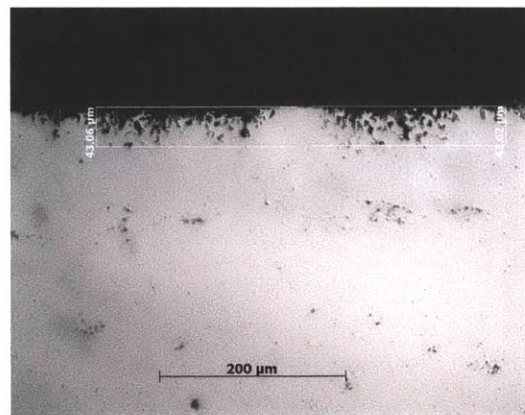
(c) After 245 hrs in reducing LBE



(d) After 245 hrs in oxidizing LBE



(e) After 506 hrs in reducing LBE



(f) After 506 hrs in oxidizing LBE

Figure 4-4: Optical micrographs of F91 samples exposed to 700°C LBE at 200 $\times$ . Samples exposed to reducing LBE show evidence of liquid metal attack channels, while those exposed to oxidizing LBE exhibit more uniform oxidation characteristics. Large internal oxidation zones are visible on the oxidized samples.

formed are unable to prevent LBE penetration through the oxide into the base metal.

Samples exposed at 700°C to reducing LBE showed severe degradation due to the formation of channels of LBE liquid metal attack. The sample exposed for 70 hours exhibited between one and three sites every 200  $\mu\text{m}$ , at which LBE appeared to be attacking the metal at a very fast rate compared to the rest of the sample. After 245 hours in reducing LBE, these zones continued to grow considerably while merging with new LBE attack channels. At this time, the sample exhibited between 15 and 25 channels of accelerated LBE attack every 200  $\mu\text{m}$ . After 506 hours the surface of the sample was more uniformly covered in LBE attack channels, while the space between channels was rough, making accurate determination of the original surface location of the sample difficult. It is highly likely that the space between the accelerated LBE attack channels underwent dissolution, removing what was the original surface of the sample.

Samples exposed at 700°C to oxidizing LBE exhibited some features reminiscent of LBE dissolution in addition to significant surface roughening and internal oxidation. The sample exposed for 70 hours underwent fairly uniform surface roughening, with a few deeper pits or channels observed every 200  $\mu\text{m}$ . No LBE was observed inside these channels. After 245 hours this roughening continued, doubling in depth. LBE was observed inside these channels, though it is not known whether dissolution was taking place or whether capillaries formed by the oxides drew LBE towards the surface. Surface roughening continued even more after 504 hours, with LBE being observed inside a few pits. In addition, a new layer was observed that terminated 150  $\mu\text{m}$  below the surface of the 504 hour sample. This is likely an internal oxidation layer, a fact which will be confirmed in the SEM/EDX analysis below.

Overall, samples exposed to reducing LBE exhibited dissolution and areas of liquid metal attack, whose number and depth increased with both time and temperature of the LBE. Samples exposed to oxidizing LBE exhibited less dissolution but more general surface roughening, sometimes accompanied by an internal oxidation layer. This is consistent with the literature for F91 [145], as well as with other alloys that do not form protective scales at this temperature. Table 4.1 summarizes the maximum

Aging Temperature (°C)	600					
Environment (w.r.t. Fe <sub>3</sub> O <sub>4</sub> )	Oxidizing			Reducing		
Aging Time (hours)	124	257	504	124	257	504
Max. Corrosion Depth (μm)	8	12	22	9	20	23
Corrosion Mechanism(s) <sup>1</sup>	OX, DIS			LMA		
Aging Temperature (°C)	700					
Environment (w.r.t. Fe <sub>3</sub> O <sub>4</sub> )	Oxidizing			Reducing		
Aging Time (hours)	70	245	506	70	245	506
Max. Corrosion Depth (μm)	15	35	43	12	42	39
Corrosion Mechanism(s) <sup>1</sup>	OX, IOX			DIS, LMA		

<sup>1</sup>OX stands for oxidation, IOX stands for internal oxidation,  
LMA stands for liquid metal attack, DIS stands for dissolution

Table 4.1: Maximum corrosion distances for F91 samples exposed to static LBE

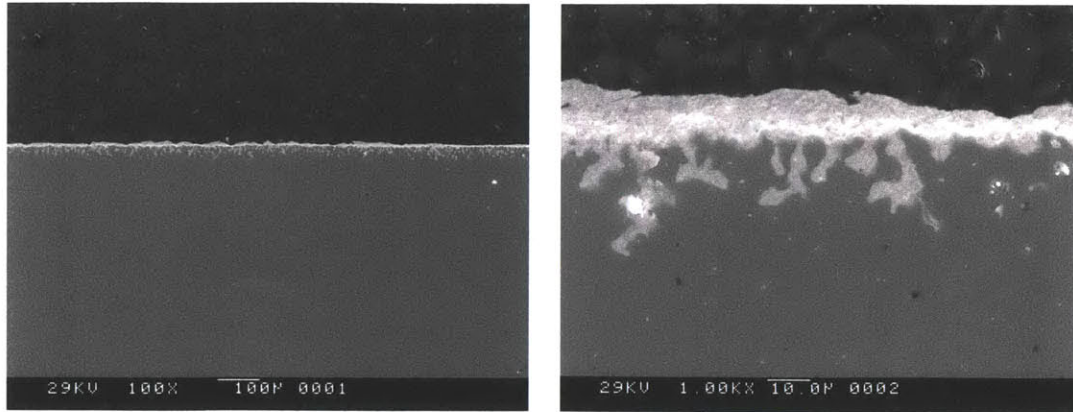
penetration distances of either LBE attack or internal oxidation for each of the F91 samples.

#### 4.2.1.2 SEM and EDX Analysis

Analysis of the F91 samples by SEM and EDX served two main purposes: to verify the observations from optical microscopy, and to catalog any zones of elemental depletion or enrichment. EDX elemental maps were therefore used in place of SIMS analysis for reasons cited in Section 4.2.

SEM images of F91 exposed to 700°C reducing LBE for 506 hours are shown in Figure 4-5. A layer of LBE can be seen adhering to the surface of the metal, while channels of LBE penetration are seen progressing via liquid metal attack. These channels correspond to the attack channels observed during optical microscopy analysis of the same sample. EDX elemental maps were acquired in this region of liquid metal attack, as it is believed that the main method of LBE corrosion on this alloy in a reducing environment is dissolution (see Section 2.1.2). These elemental maps are shown in Figure 4-6. The most interesting feature is the depletion of chromium throughout the region of LBE attack, suggesting selective dissolution of chromium as the dominant attack mechanism. Silicon is present on the surface from the mounting medium, not from the sample. No oxide layers were observed on the surface or inside the sample. This is expected, as the oxygen potential was far too low to form





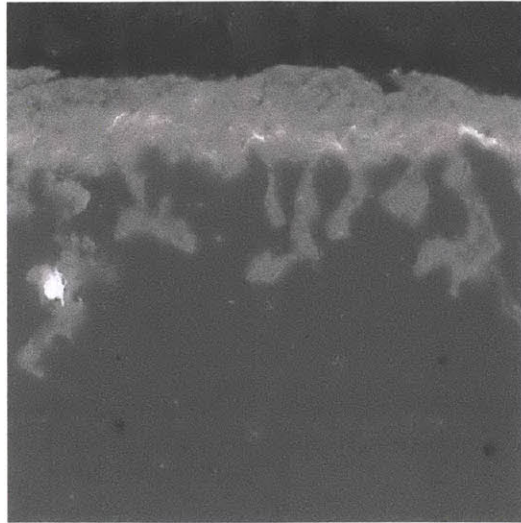
(a) F91 exposed to 700°C reducing LBE for 506 hours, 100× (b) F91 exposed to 700°C reducing LBE for 506 hours, 1,000×

Figure 4-5: SEM images of F91 exposed to 700°C reducing LBE for 506 hours. The lighter layer and channels beneath are LBE. A layer of LBE can be seen adhering to the surface of the metal, while channels of LBE penetration are seen progressing via liquid metal attack.

iron oxides, and F91 does not contain enough chromium to form a protective layer of chromia.

An SEM image of F91 exposed to 700°C oxidizing LBE for 506 hours are shown in Figure 4-7. No layer of LBE can be seen adhering to the surface of the metal, in contrast to samples exposed to reducing LBE. In addition, the surface of the oxidized sample is significantly rougher than the samples exposed to reducing LBE. This suggests selective dissolution or removal of oxides, such as wüstite, as the dominant mode of attack. Any wüstite formed would float away, as it is nonstructural. This would leave open capillaries for LBE penetration and further oxidation. This penetration of LBE deeper and deeper would allow oxygen to diffuse further into the sample, creating a layer of internal oxidation.

EDX elemental maps are shown in Figure 4-8. The most interesting feature once again is the depletion of chromium throughout the region of LBE attack, suggesting selective dissolution of chromium as the dominant attack mechanism. Silicon is present on the surface from the mounting medium, not from the sample. Light oxidation can be observed between the channels of LBE attack. The lack of LBE adhered to the surface combined with these capillary channels of LBE attack suggest



(a) SEI, 1,000×



(b) EDX map - Bi

(c) EDX map - Cr

(d) EDX map - Fe



(e) EDX map - O

(f) EDX map - Pb

(g) EDX map - Si

Figure 4-6: EDX elemental maps of F91 exposed to 700°C reducing LBE for 506 hours, 1,000×. The channels penetrating into the surface of F91 are confirmed to be LBE. A chromium depletion region was present throughout the region of LBE attack, suggesting that selective dissolution of chromium was the dominant attack mechanism. Silicon is present on the surface from the mounting medium, not from the sample. No oxide layers were observed.

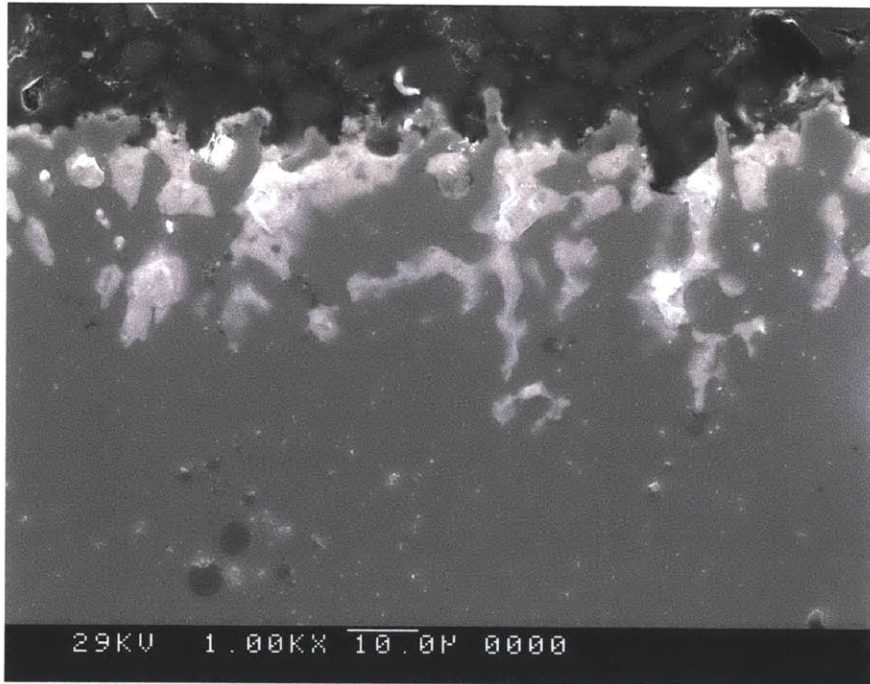
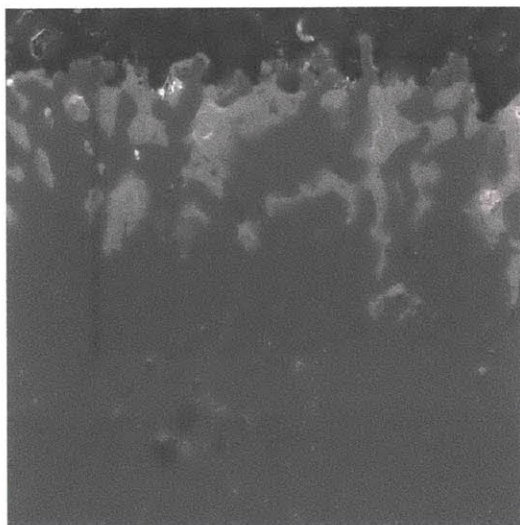


Figure 4-7: SEM image of F91 exposed to 700°C oxidizing LBE for 506 hours, 1,000 $\times$ . The lighter channels beneath the surface of the sample are LBE. No layer of LBE can be seen adhering to the surface of the metal. The surface of this sample is significantly rougher than those exposed to reducing LBE, suggesting that selective dissolution or removal of oxides, such as wüstite, was the dominant mode of attack.



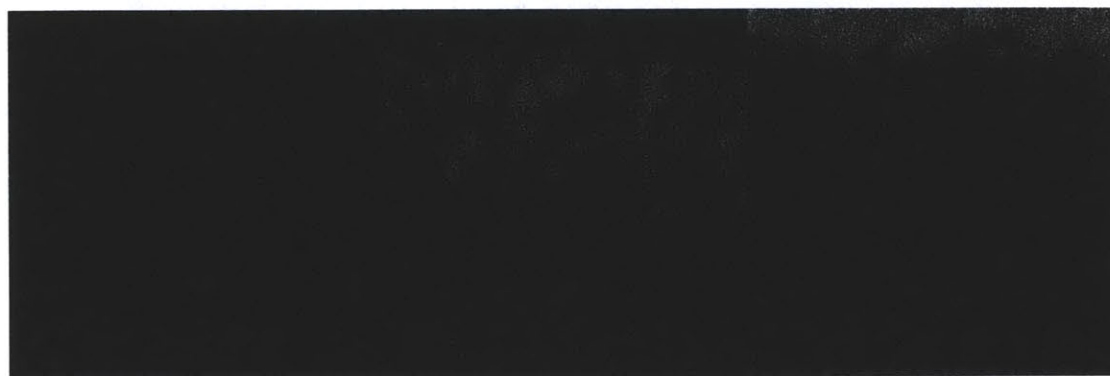
(a) SEI, 750 $\times$



(b) EDX map - Bi

(c) EDX map - Cr

(d) EDX map - Fe



(e) EDX map - O

(f) EDX map - Pb

(g) EDX map - Si

Figure 4-8: EDX elemental maps of F91 exposed to 700°C oxidizing LBE for 506 hours, 750 $\times$ . The channels penetrating into the surface of F91 are confirmed to be LBE. A chromium depletion region was present throughout the region of LBE attack, suggesting that selective dissolution of chromium was one attack mechanism. Silicon is present on the surface from the mounting medium, not from the sample. Light oxidation can be seen between channels of LBE attack. The lack of LBE adhered to the surface also suggests the surface is an oxide, as LBE cannot adhere as well to oxides as to clean metals.

that a combination of oxidation, chromium dissolution and wüstite formation are the mechanisms of attack in oxidizing LBE.

## **4.2.2 Results for Fe-12Cr-2Si**

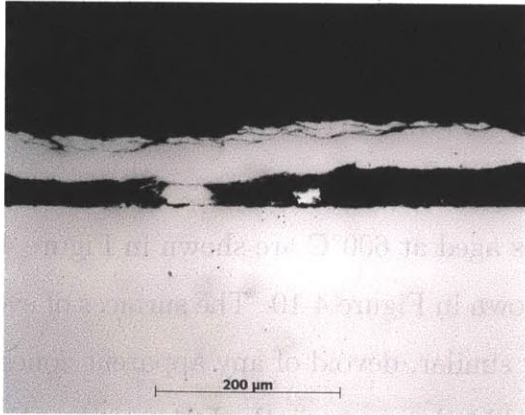
### **4.2.2.1 Optical Microscopy**

Optical micrographs for Fe-12Cr-2Si samples aged at 600°C are shown in Figure 4-9, while those for samples aged at 700°C are shown in Figure 4-10. The surfaces of every single one of these samples were remarkably similar, devoid of any apparent zones of oxidation, dissolution or liquid metal attack, like those seen in the F91 samples. Each sample had a measurable surface roughness of between 1 and 4  $\mu\text{m}$ . This roughness could just as easily be due to sample preparation as it could be due to uniform LBE attack. Most samples had LBE residue that had either adhered directly to the surface (as in the 600°C 257 hr reducing and oxidizing samples) or separated due to Bakelite mounting (as in the 600°C 504 hr oxidizing sample). Either way, the presence of LBE on the surface did not visibly change the material under the optical microscope. It is likely that oxide layers do exist, but that they were too small to be resolved with an optical microscope. Therefore, their detection and measurement will be left to XPS and SIMS analyses.

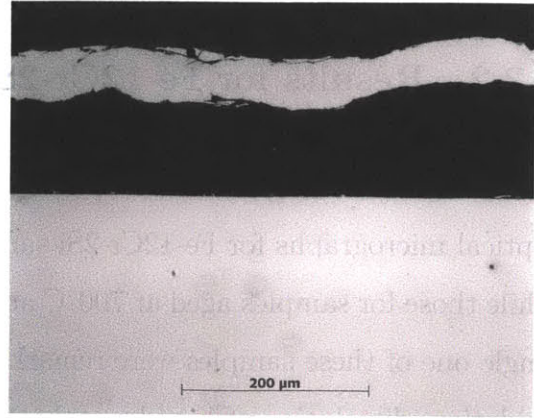
One interesting feature was observed on the sample exposed to reducing LBE at 700°C for 245 hours. This consisted of a small area of adhered LBE accompanied by a porous layer that appears to have grown outwards, as can be seen in Figure 4-11. A table of maximum penetration distances is not given here, because whatever corrosion depth was reached is too small to be measured accurately using the optical microscope.

### **4.2.2.2 SEM and EDX Analysis**

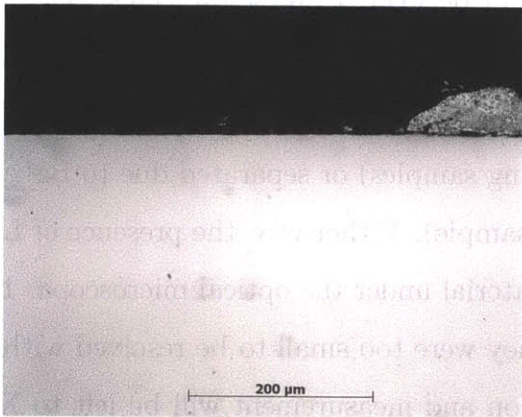
There were two main purposes of SEM and EDX analysis. The first was to use EDX elemental maps to catalog any zones of elemental enrichment or depletion as they correspond to the SIMS data (given below in Section 4.2.2.4). The second was to use



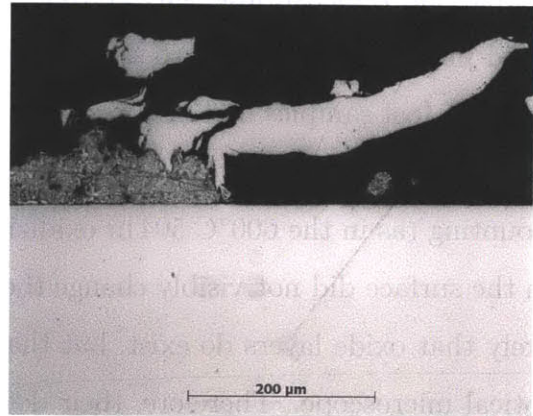
(a) After 124 hrs in reducing LBE



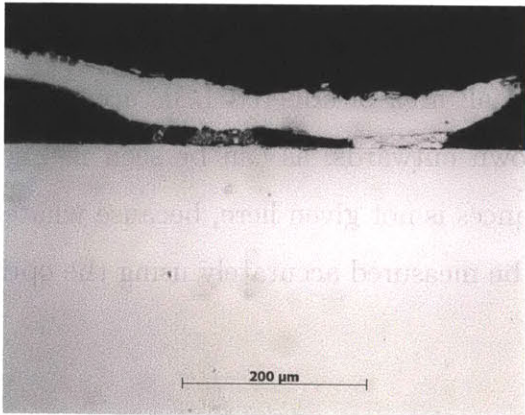
(b) After 124 hrs in oxidizing LBE



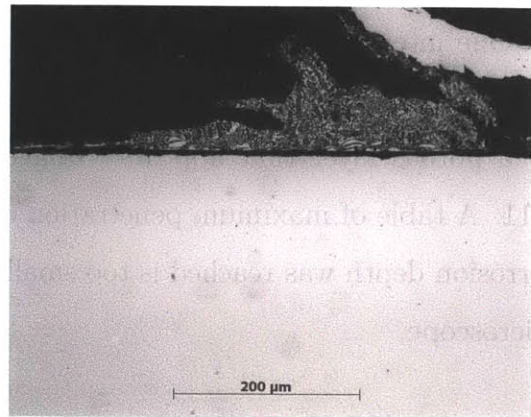
(c) After 257 hrs in reducing LBE



(d) After 257 hrs in oxidizing LBE

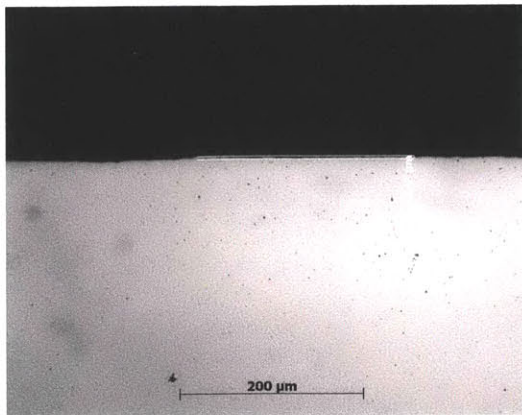


(e) After 504 hrs in reducing LBE

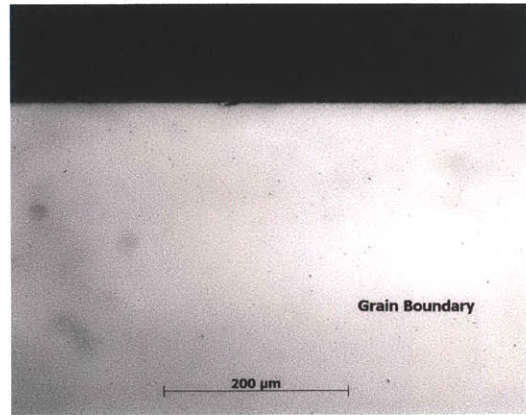


(f) After 504 hrs in oxidizing LBE

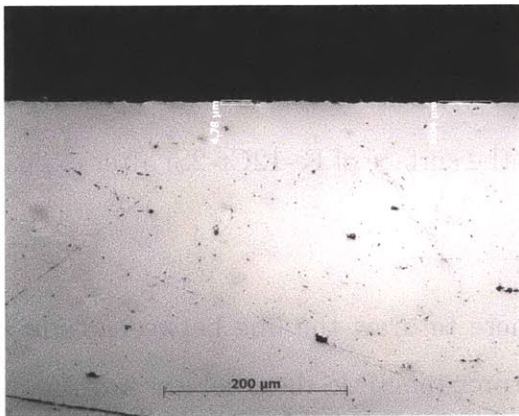
Figure 4-9: Optical micrographs of Fe-12Cr-2Si samples exposed to 600°C LBE at 200 $\times$ , showing no appreciable attack from either reducing or oxidizing LBE



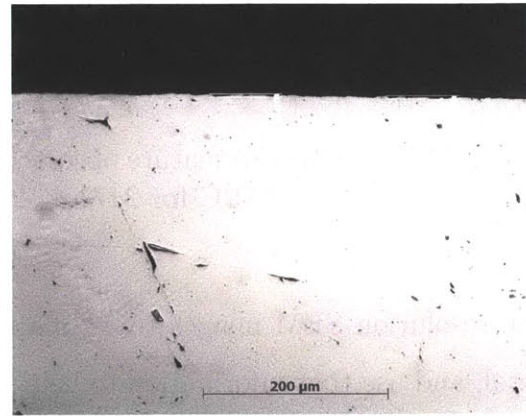
(a) After 70 hrs in reducing LBE



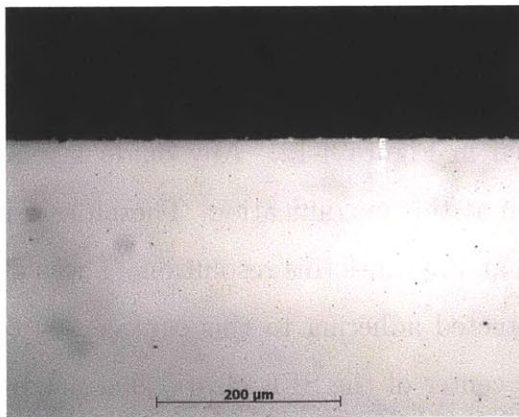
(b) After 70 hrs in oxidizing LBE



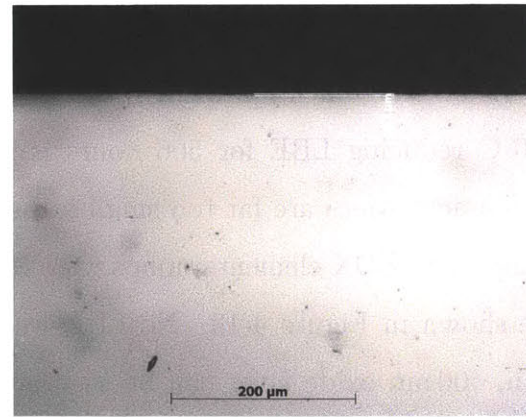
(c) After 245 hrs in reducing LBE



(d) After 245 hrs in oxidizing LBE



(e) After 506 hrs in reducing LBE



(f) After 506 hrs in oxidizing LBE

Figure 4-10: Optical micrographs of Fe-12Cr-2Si samples exposed to 700°C LBE at 200 $\times$ , showing no appreciable changes after exposure to either reducing or oxidizing LBE

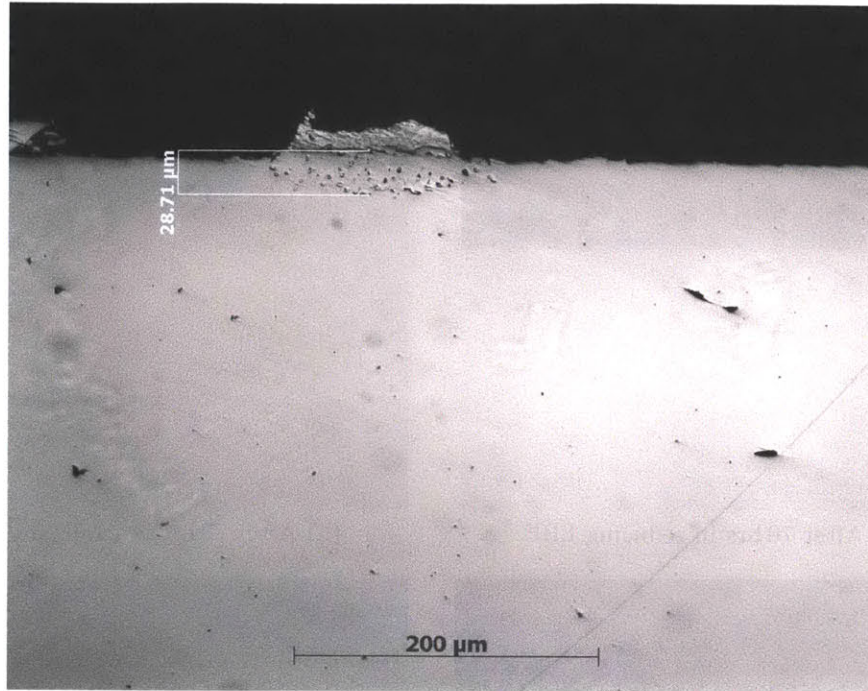


Figure 4-11: Anomalous feature observed on the surface of Fe-12Cr-2Si after exposure to reducing LBE at 700°C for 247 hrs, 200×

high-resolution SEM images to estimate where to draw the line between oxide and metal, and use that information to help interpret the SIMS data below. Additionally, silicon is present in the mounting medium, so its presence should only be compared to regions inside the sample in the corresponding SEI.

A low magnification SEM image of the surface of Fe-12Cr-2Si after exposure to 700°C reducing LBE for 506 hours is shown in Figure 4-12. Any oxide layers or enrichment zones are far too small to be seen at this magnification. Therefore, SEM images and EDX elemental maps were taken at 100 times this resolution. These data are shown in Figure 4-13. No LBE was detected adhering to this sample. A very thin, 400 nm oxide layer can be seen at the center of the SEI, clearly distinct from the bare metal below. The oxide layer in the middle of the SEI is enriched in silicon and depleted in iron. Features on the chromium map cannot be distinguished. This is because the magnification of these images is at the maximum resolution for this particular SEM. Nevertheless, enrichment of silicon and depletion of iron are clearly visible.



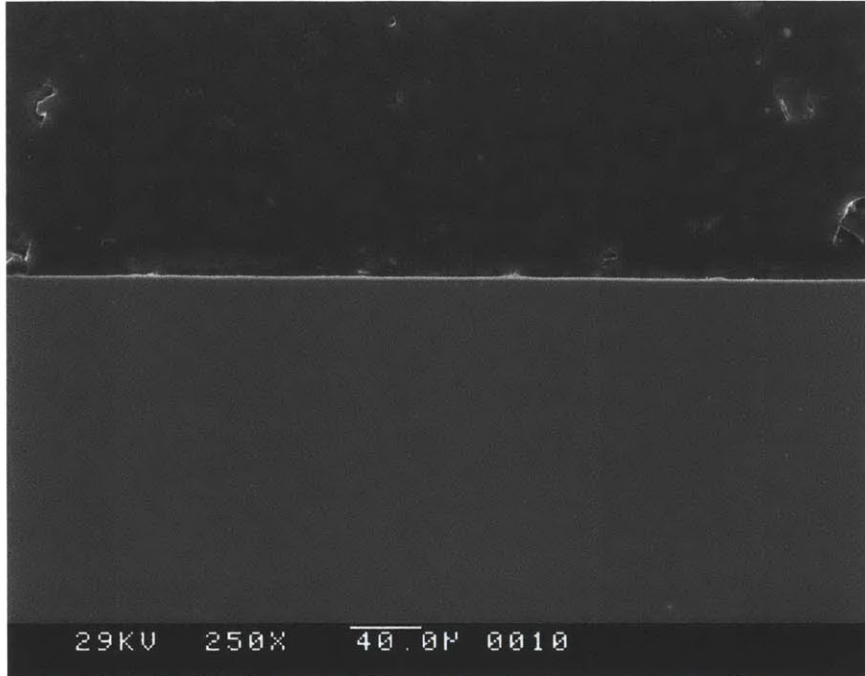
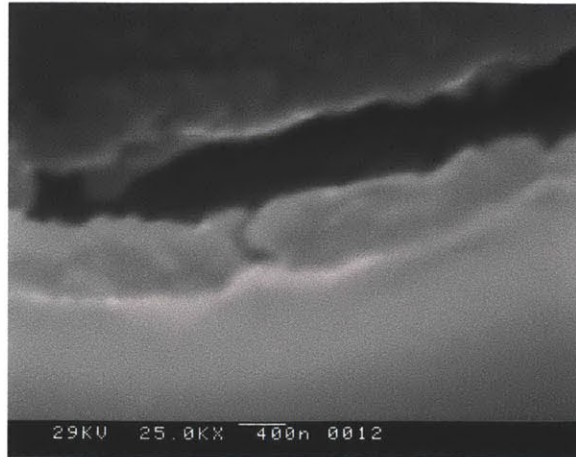


Figure 4-12: Fe-12Cr-2Si after exposure to 700°C reducing LBE for 506 hours, 250 $\times$ . Note the absence of any visible oxide layers, due to the fact that those present are too thin to be seen at this magnification.

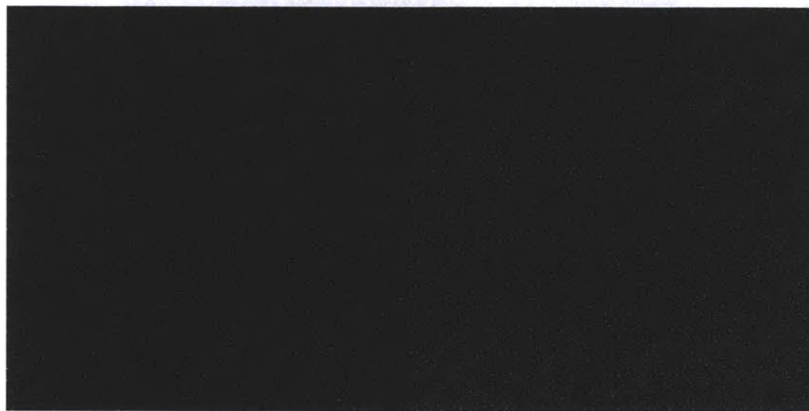
A low magnification SEM image of the surface of Fe-12Cr-2Si after exposure to 700°C oxidizing LBE for 506 hours is shown in Figure 4-14. Any oxide layers or enrichment zones are far too small to be seen at this magnification. Therefore, SEM images and EDX elemental maps were taken at 50 times this resolution. These data are shown in Figure 4-15. No LBE was detected adhering to this sample. A very thin, 400 nm dark region can be seen on some of the surface, clearly distinct from the bare metal below. The elemental maps show that the dark layer in the middle of the SEI is an oxide layer, enriched in silicon and chromium, and depleted in iron. The layer shown here is the thickest oxide layer observed on the sample.

#### 4.2.2.3 XPS Surface Analysis

Before presenting the XPS results, the reader should be aware that XPS is not a technique that can definitively identify specific oxide chemistries for all elements. Iron and its oxides are especially difficult to identify, because the XPS peaks can differ by as little as 0.1 eV. In addition, the escape probability for iron oxides is

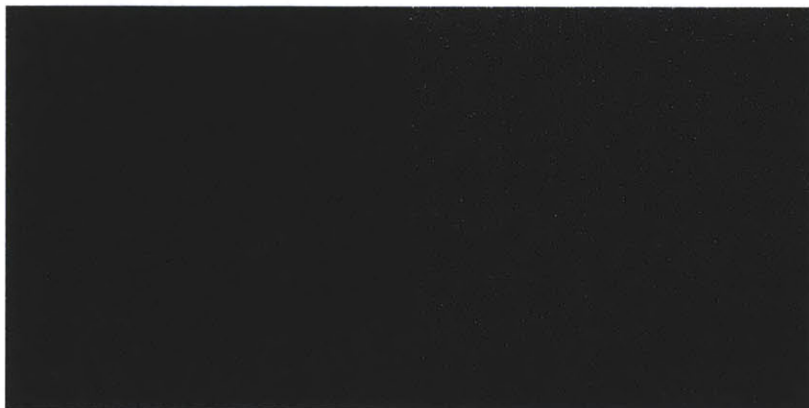


(a) Fe-12Cr-2Si after exposure to 700°C reducing LBE for 506 hours, 25,000×



(b) EDX map - Cr

(c) EDX map - Fe



(d) EDX map - O

(e) EDX map - Si

Figure 4-13: EDX elemental maps of Fe-12Cr-2Si exposed to 700°C oxidizing LBE for 506 hours, 25,000×. A very thin, 400 nm oxide layer can be seen, clearly distinct from the bare metal below. No LBE was detected adhering to this sample. The contrast on the EDX maps has been enhanced to make distinguishing features visible. The oxide layer in the middle of the SEI is enriched in silicon and depleted in iron.

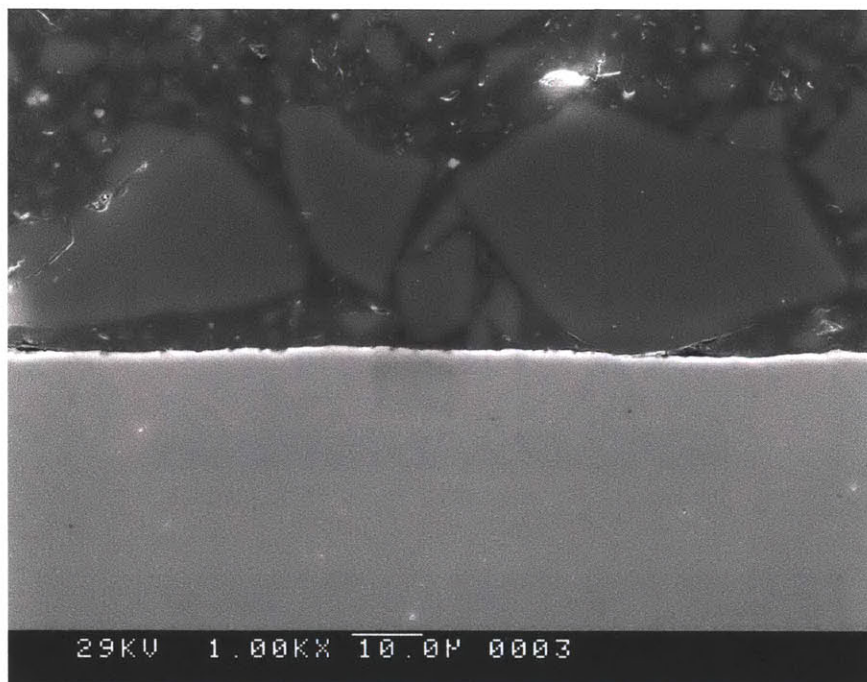
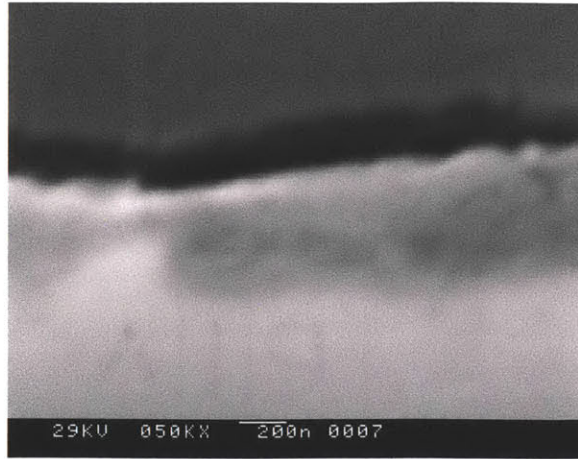


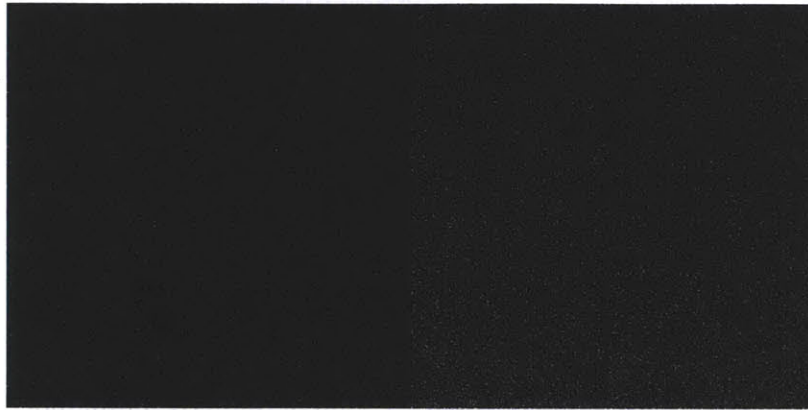
Figure 4-14: Fe-12Cr-2Si after exposure to 700°C oxidizing LBE for 506 hours, 1,000 $\times$ . Note the absence of any visible oxide layers, due to the fact that those present are too thin to be seen at this magnification.

lower than those of chromium and silicon. This is because the kinetic energy the photoelectrons escape with is lower when they have higher binding energies, because the x-ray source emits at a fixed energy. Careful sample preparation and analysis of not only the peak locations, but also the widths and shape of the overall spectrum envelope, are required for qualification of oxide chemistries.

**Fe-12Cr-2Si Exposed to 700°C LBE for 70 Hours** XPS analysis was carried out for samples of Fe-12Cr-2Si, which were exposed to LBE in both environments for 70 hours. Survey spectra were first taken on each sample in order to find suitable points for analysis which were not covered in LBE. These are shown in Figure 4-16. Both samples exhibit weak iron 2p and 2p<sup>-</sup> peaks, which will be the key to determining the oxidation state(s) of iron present on the samples. Much stronger Cr 2p & 2p<sup>-</sup> and Si 2p & 2p<sup>-</sup> peaks were visible on the sample exposed to oxidizing LBE compared to the analogous peaks for the sample exposed to reducing LBE. This is thought to be due to the inability to find a suitable uncovered spot for analysis,



(a) Fe-12Cr-2Si after exposure to 700°C oxidizing LBE for 506 hours, 50,000×



(b) EDX map - Cr

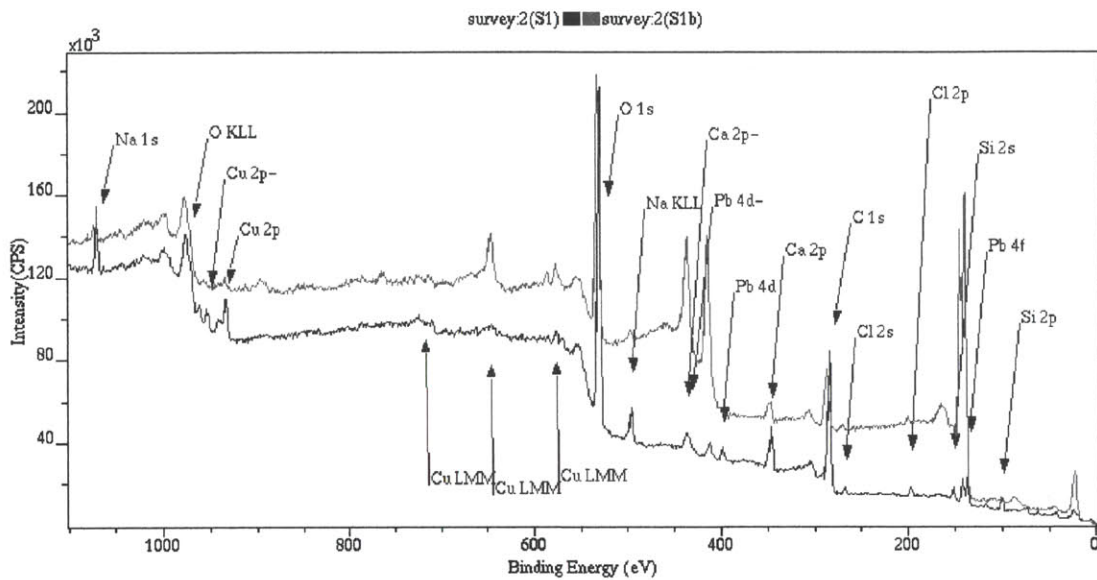
(c) EDX map - Fe



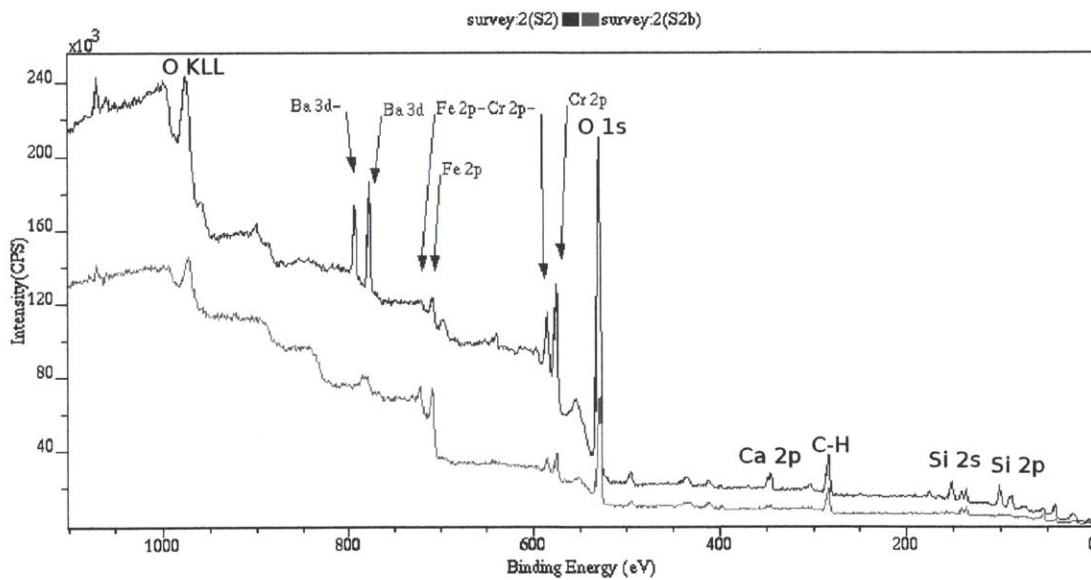
(d) EDX map - O

(e) EDX map - Si

Figure 4-15: EDX elemental maps of Fe-12Cr-2Si exposed to 700°C oxidizing LBE for 506 hours, 50,000×. No LBE was detected adhering to this sample. A very thin, 400 nm darker region can be seen on some of the surface, clearly distinct from the bare metal below. The contrast on the EDX maps has been enhanced to make distinguishing features visible. The elemental maps show that the dark layer in the middle of the SEI is an oxide layer, enriched in silicon and chromium, and depleted in iron.



(a) XPS survey spectrum for Fe-12Cr-2Si exposed to reducing LBE



(b) XPS survey spectrum for Fe-12Cr-2Si exposed to oxidizing LBE

Figure 4-16: XPS survey spectra of Fe-12Cr-2Si samples exposed to LBE at 700°C for 70 hrs. Note how the iron, chromium and silicon peaks are much stronger on the sample exposed to oxidizing LBE.

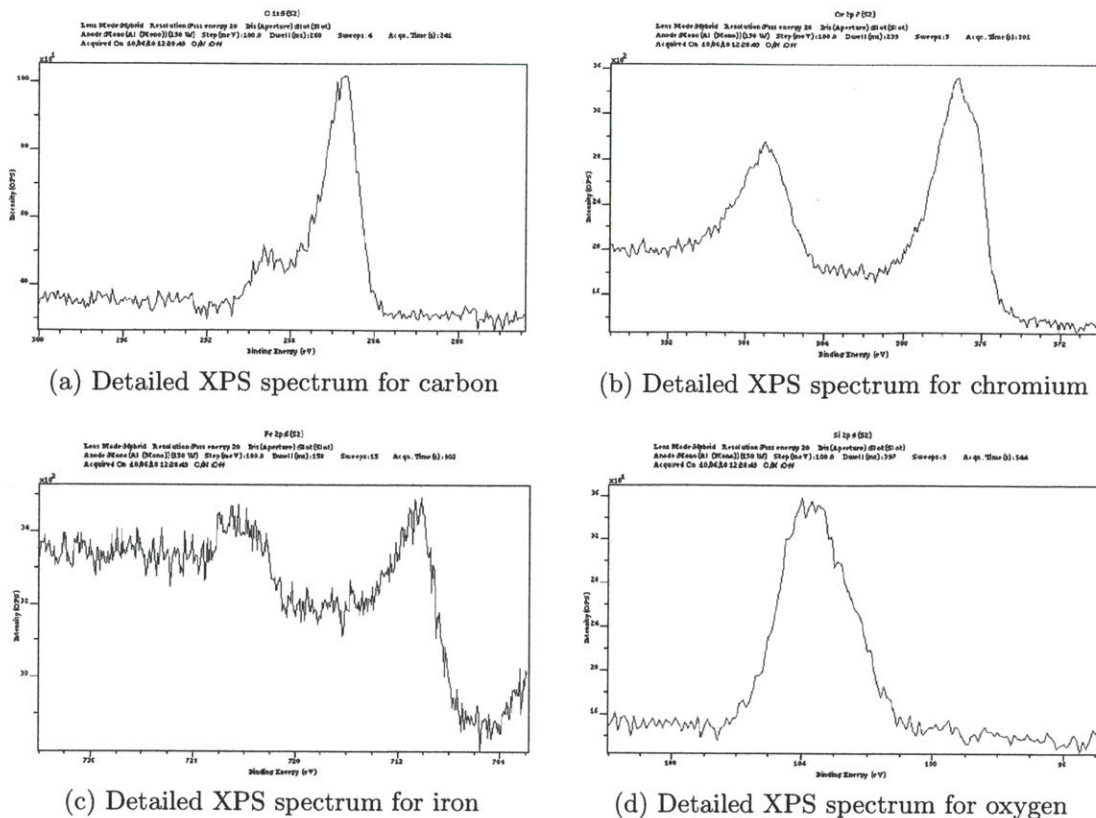


Figure 4-17: Detailed XPS spectra around the 2p and 2p<sup>-</sup> lines for C, Fe, Cr and Si on the Fe-12Cr-2Si sample exposed to 700°C oxidizing LBE for 70 hours

as many unexpected elements were found on the two samples. The copper present is likely due to vapor pressure from the copper gaskets used to seal the furnaces, as the vapor pressure of copper at 830°C is  $3 \times 10^{-7}$  torr [146] (the furnace had to be kept at 830°C to keep the samples at 700°C due to heat loss out the top of the experimental setup). This is very small, but significant enough that a small amount of copper could deposit onto the samples during the test. Sodium, chlorine and calcium are likely a result of human contamination. It is not known why barium was found on the oxidizing-LBE sample.

The spot S2 on the oxidizing-LBE sample was chosen from detailed XPS analysis to determine the precise binding states of iron, chromium and silicon. Detailed spectra from this location are shown in Figure 4-17. These spectra have varying signal-to-noise ratios due to differences in the strengths of each atom's signals. Better signal-to-noise ratios are indicative that more of an element is present on the sample surface.

Elements with stronger signals required fewer ‘sweeps,’ or scans, to fully define the peaks present. A sweep consisted of a scan over a small range (typically 20 - 40 eV) at a resolution of 0.1 eV for 30 seconds. For many peaks, especially iron, chromium and silicon, multiple oxide phases can be present on one area of the sample, leading to splitting of the peaks. For excellent samples this manifests as two peaks separated by 0.1 - 3.0 eV. In realistic samples such as these, it merely alters the shape of the peak so that it has a shoulder on one side. This is likely the sum of two Gaussian functions with different heights and peak locations. In addition, the entire spectrum is often shifted by -2.0 to 2.0 eV due to charging on the sample. Less conductive samples accumulate greater static charge, and their peaks get shifted to a higher energy. Therefore, a reference peak (in this case the C-H bond in hydrocarbons) must be acquired in order to determine that shift. The reference peak for the C-H bond is 284.4 eV, obtained by averaging the five reference values on the NIST XPS database version 3.5 [147]. The measured peak energy for the C-H bond on this sample was 285.6 eV, and was obtained by finding the energy of the midpoint of the full width at half maximum (FWHM) line for the carbon peak. This indicated that a correction shift of -1.2 eV should be applied to all of the peaks acquired on these two samples.

Based on this shift, the estimated positions of the peaks for iron, chromium and silicon were calculated by finding the x-coordinate of the FWHM for each peak and subtracting 1.2 eV. These peaks are summarized in Table 4.2, along with a list of possible matches and their positions. Data from the National Institute of Standards and Technology (NIST) database were averaged when a large number of references existed. These instances are marked in the table. A single reference was selected for compounds which had very few references; this one was chosen based on its data collection method, its quality and its peak energy uncertainty.

The XPS data show that iron could exist as either  $\text{Fe}_3\text{O}_4$  or  $\text{FeO}$ , as both of these compounds’  $2p^{3/2}$  lines are 0.2 eV from the measured value. It is likely that  $\text{Fe}_3\text{O}_4$  does exist, as two peaks were measured to be within 0.1 eV of  $\text{Fe}_3\text{O}_4$ ’s  $2p$  peaks. Chromium likely exists as a mixture of  $\text{Cr}_2\text{O}_3$  and mixed Fe-Cr spinel oxides, the

Element & Orbital	Peak Energy (eV)	Possible Matches	Ref. Energy (eV)
C	285.6 (before shift)	<b>C-H bond (reference)</b>	<b>284.4 (avg. of 5)</b>
Cr 2p <sup>1/2</sup>	585.9	<b>FeCr<sub>2</sub>O<sub>4</sub></b>	<b>585.8</b>
		<b>Cr<sub>2</sub>O<sub>3</sub></b>	<b>586.0</b>
Cr 2p <sup>3/2</sup>	576.4	Fe <sub>1.4</sub> Cr <sub>1.6</sub> O <sub>4</sub>	576.2
		FeCr <sub>2</sub> O <sub>4</sub>	576.0
		<b>Fe<sub>2</sub>CrO<sub>4</sub></b>	<b>576.4</b>
		<b>Cr<sub>2</sub>O<sub>3</sub></b>	<b>576.55 (avg. of 21)</b>
		Fe <sub>2.4</sub> Cr <sub>0.6</sub> O <sub>4</sub>	576.6
Fe 2p <sup>1/2</sup>	723.6	<b>Fe<sub>3</sub>O<sub>4</sub></b>	<b>723.5</b>
Fe 2p <sup>3/2</sup>	709.6	<b>Fe<sub>3</sub>O<sub>4</sub></b>	<b>709.7 (avg. of 7)</b>
		FeO	709.8 (avg. of 7)
Si 2p <sup>3/2</sup>	102.6	<b>SiO</b>	<b>102.7</b>
		<b>SiO<sub>2</sub>/Si</b>	<b>102.9</b>
		<b>SiO<sub>2</sub></b>	<b>103.0</b>
	101.6	<b>SiO<sub>x</sub></b>	<b>101.5 (avg. of 2)</b>
		<b>SiO</b>	<b>101.7</b>
		<b>SiO<sub>x</sub>/Si</b>	<b>102.0</b>

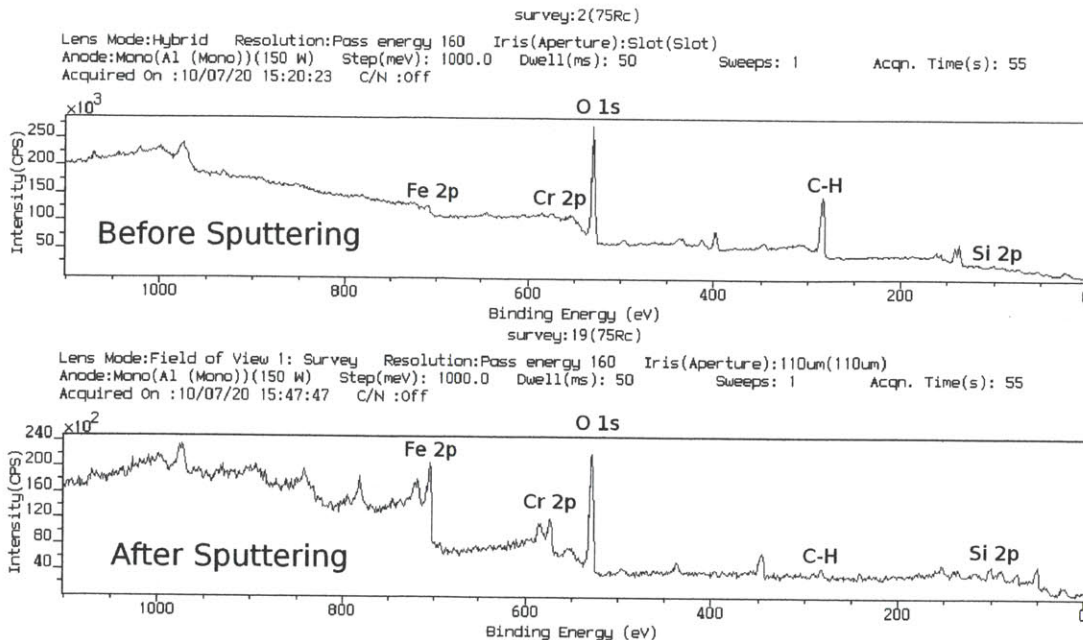
Table 4.2: XPS binding energy peaks for C, Cr, Fe and Si on the sample of Fe-12Cr-2Si exposed to oxidizing LBE at 700°C for 70 hrs. All measured peak energies have been shifted down by 1.2 eV except for carbon, which was used as the reference. The most likely matches are in bold.



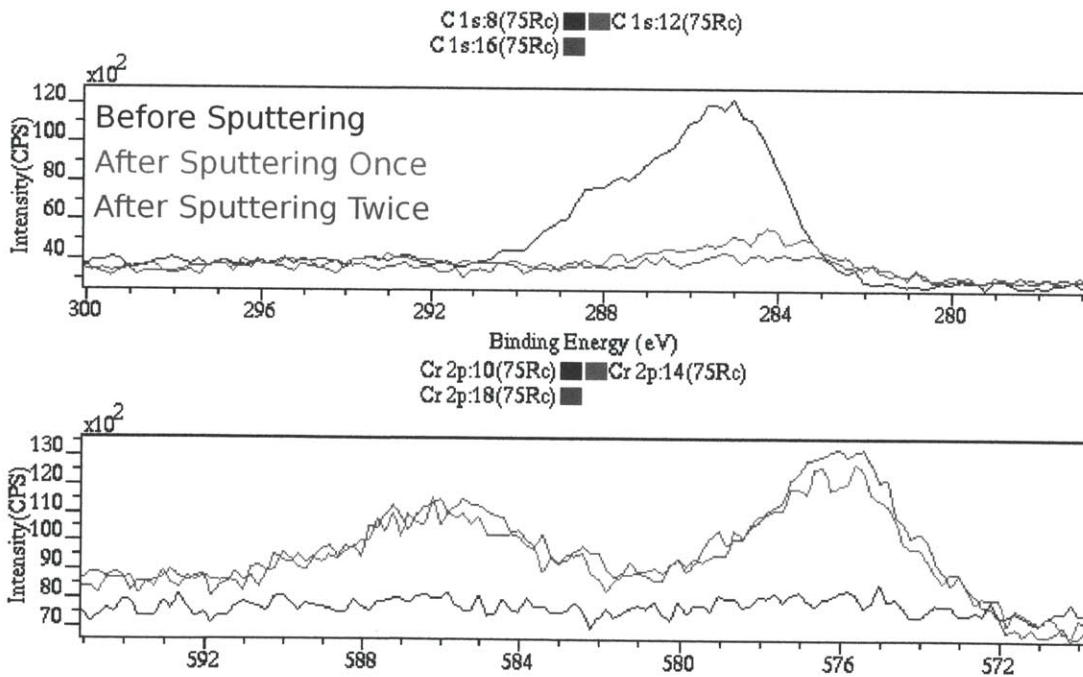
closest of which seems to be  $\text{Fe}_2\text{CrO}_4$ . However, due to the proximity of the peaks for all three spinel oxides, the existence of any one of them is a possibility.  $\text{Cr}_2\text{O}_3$  is also likely present on this sample, but it would exist beneath Fe-Cr spinel oxides. The faster growing oxides are the iron oxides, and iron tends to diffuse outwards to the surface during the initial oxide layer formation. The silicon peak was too weak to measure accurately. Its presence would not be expected on the surface of the sample, as previous studies have shown that it tends to form oxides beneath faster-growing iron and chromium oxides [7]. The most likely form of silicon oxide present is  $\text{SiO}_x$  from the match in binding energies. Oxygen levels are low enough that silicon oxide formed may not be stoichiometric  $\text{SiO}_2$ .

**Fe-12Cr-2Si Exposed to 700°C Reducing LBE for 506 Hours** Upon first analyzing these samples, it was clear that they possessed a small amount of surface contamination. This was due to a lack of peaks besides oxygen and carbon. XPS is a technique whose penetration depth is on the order of angstroms. Therefore, any layer of surface contamination completely obscures the actual samples. A built-in argon ion gun was used to sputter a  $2\text{ mm} \times 2\text{ mm}$  area on each of the two samples to remove this surface contamination. Survey spectra were then reacquired to confirm that removal of the surface contamination took place. Spectra acquired before and after sputtering are shown in Figure 4-18 for comparison. Sputtering caused the thin layer of surface hydrocarbon contamination to disappear, while peaks for iron, chromium, silicon, lead and bismuth grew much stronger. This contamination was a result of exposure to open air.

A survey spectrum of the Fe-12Cr-2Si sample exposed to 700°C reducing LBE for 506 hours after two sputtering sessions is shown in the lower half of Figure 4-18a, while detailed XPS peak spectra for carbon, chromium, iron and silicon are shown in Figure 4-19. The Kratos XPS software package was used to subtract background signal and fit Gaussian curves to the envelope created by the data, which is always shown in pink. The dominant peak for carbon is that of the C-H hydrocarbon bond, shown in blue. This peak was used as the reference for all other peaks on this sample.

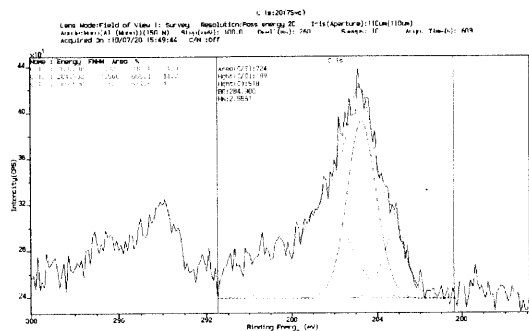


(a) Comparison of XPS survey spectra before and after sputtering. Note how peaks for iron, chromium and silicon become visible after sputtering, while the C-H bond peak nearly disappeared.

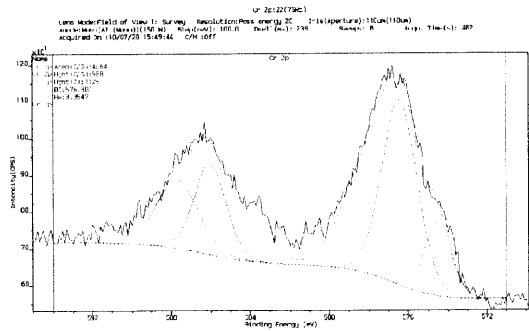


(b) Comparison of carbon and chromium XPS peak heights before and after sputtering. The spectra before sputtering are in red, while spectra after one and two sputtering sessions of 120 seconds each are shown in green and blue, respectively. Note how the C-H bond peak nearly disappears, while the dual peak for chromium becomes very strong.

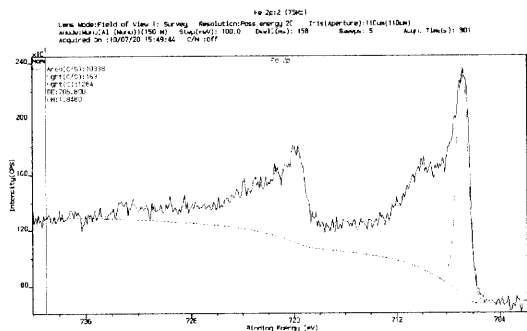
Figure 4-18: Comparison of XPS spectra of Fe-12Cr-2Si exposed to reducing LBE for 506 hours before and after sputtering. Sputtering to a depth of 10 - 20 Å almost completely removed hydrocarbon surface contamination, uncovering the actual surface of the sample.



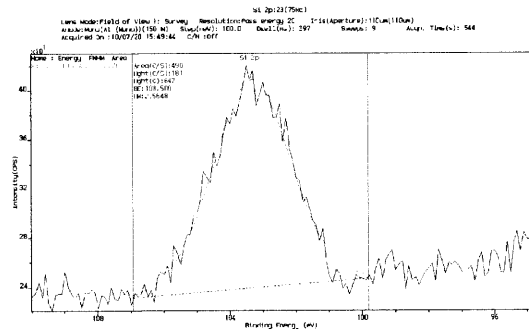
(a) Detailed XPS spectrum for carbon. The dominant peak is that of the C-H hydrocarbon bond, shown in blue. This peak was used as the reference for all other peaks on this sample.



(b) Detailed XPS spectrum for chromium. Three chromium oxide chemistries were noticed, each with a corresponding 2p and 2p<sup>-</sup> peak.



(c) Detailed XPS spectrum for iron. One strong peak was noticed for iron. Its location and its small FWHM indicates that it is the peak for metallic iron. The shoulder on the left corresponds to a weak peak for wüstite.



(d) Detailed XPS spectrum for silicon. Only one chemistry, SiO<sub>2</sub>, was observed for silicon.

Figure 4-19: Detailed XPS spectra around the 2p and 2p<sup>-</sup> lines for C, Cr, Fe and Si on the Fe-12Cr-2Si sample exposed to 700°C reducing LBE for 506 hrs. The Kratos XPS software package was used to subtract background signal and fit Gaussian curves to the envelope created by the data. This envelope is always shown in pink.

Its energy fell within 0.3 eV of the reference for this peak (284.4 eV [147]), so a shift of -0.3 eV was applied to all peak energies for this sample. The small shift is due to less charging, which in turn is due to the high conductivity of the sample. The reducing environment inhibited the formation of thick oxide layers, keeping iron in its metallic state and raising the conductivity of the sample surface. Three chromium oxide chemistries were noticed, each with a corresponding  $2p$  and  $2p^-$  peak. The most dominant chromium oxide chemistry was that of  $\text{Cr}_2\text{O}_3$ . One strong peak was noticed for iron. Its location and its smaller FWHM indicates that it is the peak for metallic iron, rather than an iron oxide. The shoulder to the left of the metallic iron peak corresponds to wüstite. Only one chemistry,  $\text{SiO}_2$ , was observed for silicon. A summary of XPS data for this sample is shown in Table 4.3.

**Fe-12Cr-2Si Exposed to 700°C Oxidizing LBE for 506 Hours** A survey spectrum of the Fe-12Cr-2Si sample exposed to 700°C oxidizing LBE for 506 hours after two sputtering sessions is shown in Figure 4-20, while detailed XPS peak spectra for carbon, chromium, iron and silicon are shown in Figure 4-21. The Kratos XPS software package was used to subtract background signal and fit Gaussian curves to the envelope created by the data, which is always shown in pink. The only peak present for carbon after sputtering is that of the C-H hydrocarbon bond, shown in pink. This peak was used as the reference for all other peaks on this sample. Its energy fell within 2.3 eV of the reference for this peak (284.4 eV [147]), so a shift of -2.3 eV was applied to all peak energies for this sample. This higher shift is due to more charging on the sample, which in turn is due to the lower conductivity of the oxides present on the surface. Only one oxide chemistry,  $\text{Cr}_2\text{O}_3$ , was observed for chromium. No peaks were found for iron, proving that it does not exist in the outermost oxide layer on this sample. Only one chemistry,  $\text{SiO}_2$ , was observed for silicon. In addition, its high signal-to-noise ratio of this peak suggests that it is one of the two dominant oxides present on this sample. These data suggest that only chromia and silica exist on the surface of this sample, and thus the iron oxides present on earlier samples (see samples aged for 70 hours above) have either dissolved or been reduced away. In

Element & Orbital	Peak Energy (eV)	Possible Matches	Ref. Energy (eV)
C	284.7 (before shift)	<b>C-H bond (reference)</b>	<b>284.4 (avg. of 5)</b>
	282.9	<b>Cr/(-C<sub>6</sub>H<sub>2</sub>(CH<sub>3</sub>)<sub>2</sub>O-)<sub>n</sub></b>	<b>282.90</b>
		Cr <sub>2</sub> C <sub>3</sub>	282.94
	286.2	<b>(-CH<sub>2</sub>CH<sub>2</sub>-)<sub>n</sub></b>	<b>286.17</b>
		CH <sub>3</sub> CH <sub>2</sub> OH	286.30
Cr 2p <sup>1/2</sup>	583.5	<b>Cr (metal)</b>	<b>583.50</b>
	585.8	<b>FeCr<sub>2</sub>O<sub>4</sub></b>	<b>585.80</b>
		<b>Cr<sub>2</sub>O<sub>3</sub></b>	<b>586.00</b>
		<b>Fe<sub>1.4</sub>Cr<sub>1.6</sub>O<sub>4</sub></b>	<b>586.00</b>
587.4	Cr(OH) <sub>3</sub>	586.80	
Cr 2p <sup>3/2</sup>	574.2	<b>Cr (metal)</b>	<b>574.19 (avg. of 7)</b>
	576.1	Fe <sub>2</sub> CrO <sub>4</sub>	576.40
		Cr <sub>2</sub> O <sub>3</sub>	576.55 (avg. of 21)
		<b>Fe<sub>1.4</sub>Cr<sub>1.6</sub>O<sub>4</sub></b>	<b>576.20</b>
		<b>FeCr<sub>2</sub>O<sub>4</sub></b>	<b>576.00</b>
578.0	CrO <sub>3</sub>	578.30	
Fe 2p <sup>3/2</sup>	707.4	<b>Fe (metal)</b>	<b>707.38 (avg. of 4)</b>
	709.7	<b>FeO</b>	<b>709.56 (avg. of 5)</b>
Si 2p <sup>3/2</sup>	103.0	SiO <sub>2</sub> /Si	102.90
		<b>SiO<sub>2</sub></b>	<b>103.00</b>
		SiO	102.70

Table 4.3: XPS binding energy peaks for C, Cr, Fe and Si on the sample of Fe-12Cr-2Si exposed to reducing LBE at 700°C for 506 hrs. All measured peak energies have been shifted down by 0.3 eV except for carbon, which was used as the reference. Most likely matches are in bold.

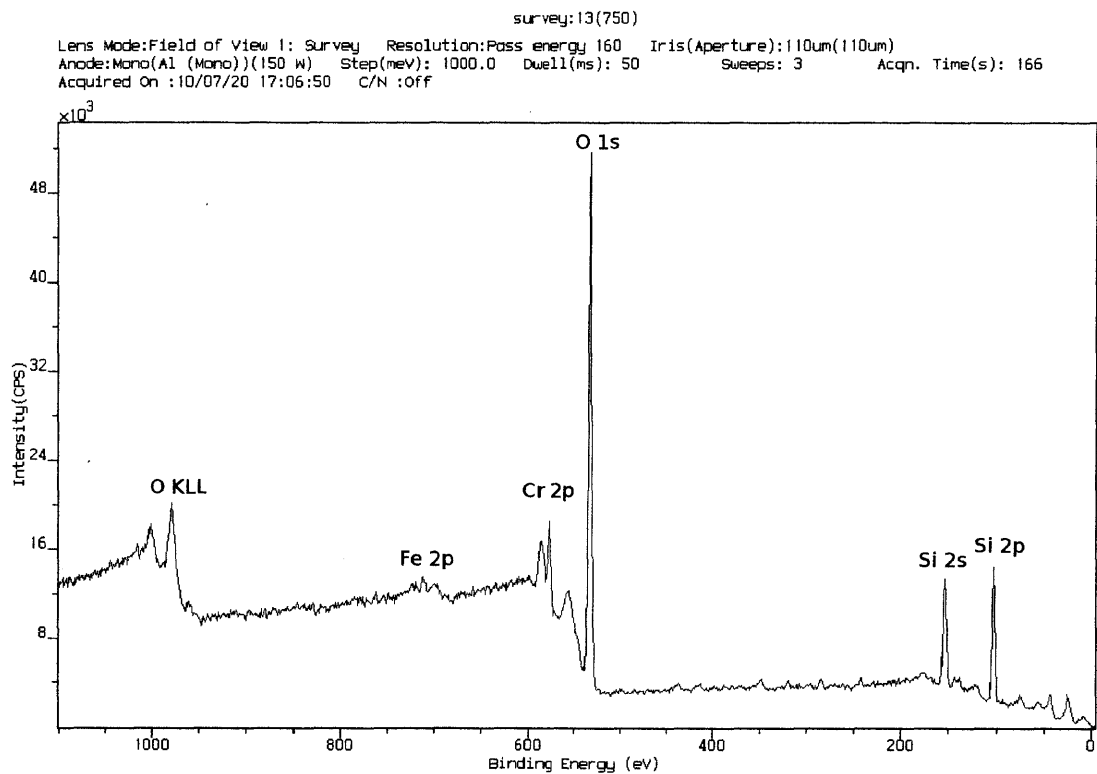
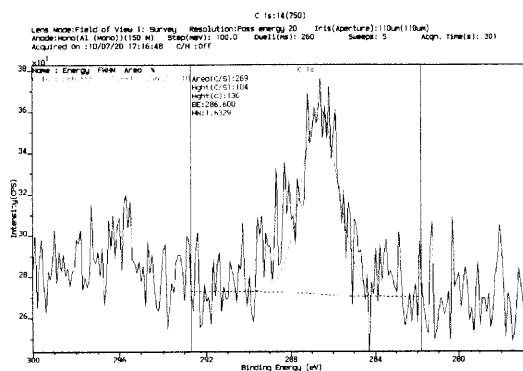
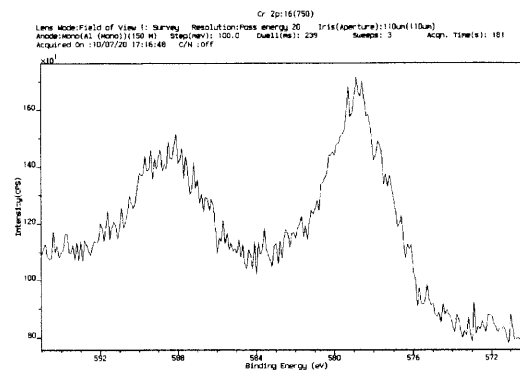


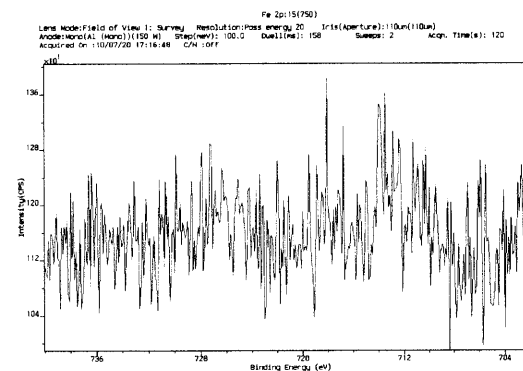
Figure 4-20: XPS survey spectrum for Fe-12Cr-2Si after exposure to 700°C oxidizing LBE for 506 hours. Note that the iron peak is not present on this sample.



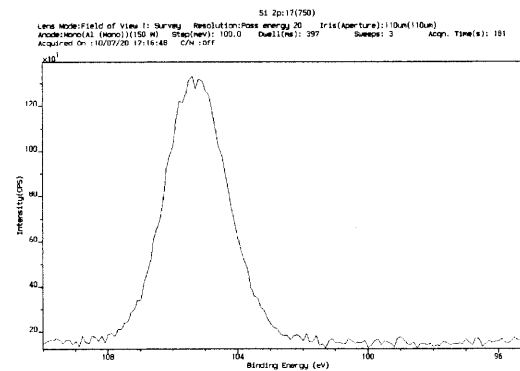
(a) Detailed XPS spectrum for carbon. The only peak is that of the C-H hydrocarbon bond, shown in pink. This peak was used as the reference for all other peaks on this sample.



(b) Detailed XPS spectrum for chromium. Only one oxide chemistry,  $\text{Cr}_2\text{O}_3$ , was observed for chromium. It is one of only two oxide chemistries found on this sample.



(c) Detailed XPS spectrum for iron. No peaks were found for iron, proving that it does not exist in the outermost oxide layer on this sample.



(d) Detailed XPS spectrum for silicon. Only one chemistry,  $\text{SiO}_2$ , was observed for silicon. In addition, the high signal-to-noise ratio of this peak suggests that it is one of the two dominant oxides present on this sample.

Figure 4-21: Detailed XPS spectra around the  $2p$  and  $2p^-$  lines for C, Cr, Fe and Si on the Fe-12Cr-2Si sample exposed to  $700^\circ\text{C}$  oxidizing LBE for 506 hrs. The Kratos XPS software package was used to subtract background signal and fit Gaussian curves to the envelope created by the data. This envelope is always shown in pink.

Element & Orbital	Peak Energy (eV)	Possible Matches	Ref. Energy (eV)
C	284.7 (before shift)	<b>C-H bond (reference)</b>	<b>284.4 (avg. of 5)</b>
Cr 2p <sup>1/2</sup>	586.2	<b>Cr<sub>2</sub>O<sub>3</sub></b>	<b>586.00</b>
Cr 2p <sup>3/2</sup>	576.5	Fe <sub>2</sub> CrO <sub>4</sub>	576.40
		<b>Cr<sub>2</sub>O<sub>3</sub></b>	<b>576.55 (avg. of 21)</b>
		Fe <sub>1.4</sub> Cr <sub>1.6</sub> O <sub>4</sub>	576.20
		FeCr <sub>2</sub> O <sub>4</sub>	576.00
Fe	<b>No Peaks Found</b>		
Si 2p <sup>3/2</sup>	103.0	SiO <sub>2</sub> /Si	102.90
		<b>SiO<sub>2</sub></b>	<b>103.00</b>
		SiO	102.70

Table 4.4: XPS binding energy peaks for C, Cr, Fe and Si on the sample of Fe-12Cr-2Si exposed to oxidizing LBE at 700°C for 506 hrs. All measured peak energies have been shifted down by 2.3 eV except for carbon, which was used as the reference. Most likely matches are in bold.

addition, the chromium oxides present have been reduced from iron-chrome spinel to pure chromia. A summary of XPS data for this sample is shown in Table 4.4.

#### 4.2.2.4 SIMS Concentration Depth Profiles

The nature of SIMS allows for excellent spatial resolution of elements versus sputtering distance. However, its quantitative abilities are very limited, as a beam of argon atoms will cause different elements to be ejected at different rates. This depends on the relative amounts and binding states of each element. Elements in oxides yield very different signals than do free elements. Therefore, the SIMS data should not be interpreted quantitatively. The relative amounts of one element at different depths, and subsequent comparisons between these profiles for different elements, yields the most useful information. Surface contamination due to both LBE and oxidation in air can skew the results. Thus, the outer oxide layer will be said to begin at or near the highest measured oxygen value. Exact determination of this location is not possible with this data. The estimated bounds for the actual oxide layers are shown on the graphs with gray dashed lines.



**Control Samples** The SIMS concentration profiles for control samples are shown in Figure 4-22. These samples were exposed to the cover gas conditions, one in the oxidizing environment and one in the reducing environment. This was done to know what the elemental profiles looked like for the other samples at the start of each test. These samples were heated from room temperature to the test temperature over a period of 4 - 8 hours, and allowed to remain at the test temperature (700°C) for between 12 - 18 hours as the gas levels equilibrated. Doing so ensured that the control samples and the test samples had received identical treatment up to the point of experimentation.

These concentration profiles both show iron depletion coexisting with oxygen enrichment, suggesting that the oxides present are either poor or completely lacking in iron. In both profiles, the chromium peak is closer to the outer edge of the sample than the silicon peak. The outermost oxides likely formed first, so this suggests that either an iron-chromium spinel oxide or chromium oxide formed rapidly. This could have happened even in the reducing sample, as it took up to 18 hours for the oxygen levels to stabilize. The total thickness of the entire oxide layer for both samples is 200 nm. No elemental depletion was observed beneath the oxide layers in either sample, due to the very thin oxide layer formed.

**700°C, 70 Hour Samples** The SIMS concentration profiles for samples exposed to 700°C LBE for 70 hours are shown in Figure 4-23. The oxide layers in the reducing condition remained in the same order as in the control samples, but the size of each decreased. In addition, a new iron peak is coexistent with the chromium peak, while the silicon peak is still behind the other two. This again suggests that silicon rich oxides, either an iron-silicon mixed oxide or silica, exist behind the faster growing iron-chromium oxides. The total oxide layer thickness was 130 nm.

The oxide layers in the oxidizing condition both grew with respect to the control sample and changed locations. In this sample, the silicon peak coexists with the iron peak at the outside of the sample, while a chromium peak is visible underneath the iron and chromium peaks. This suggests the existence of an iron-silicon spinel oxide

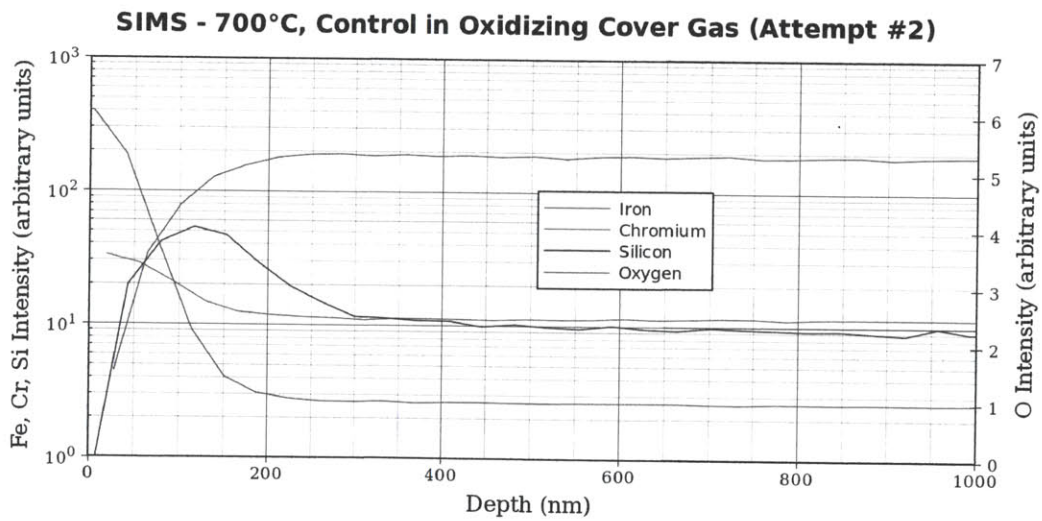
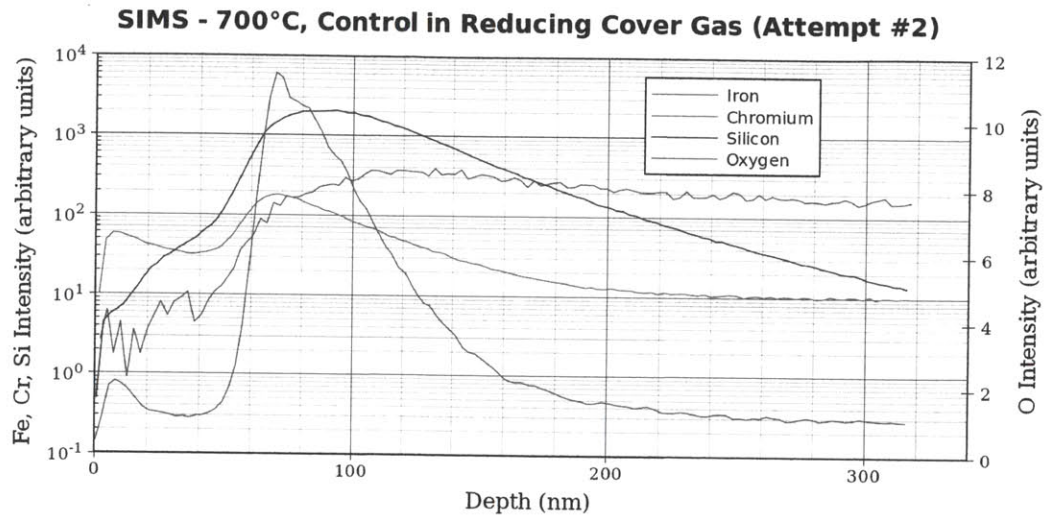


Figure 4-22: SIMS concentration profiles for samples exposed to the cover gas conditions at 700°C

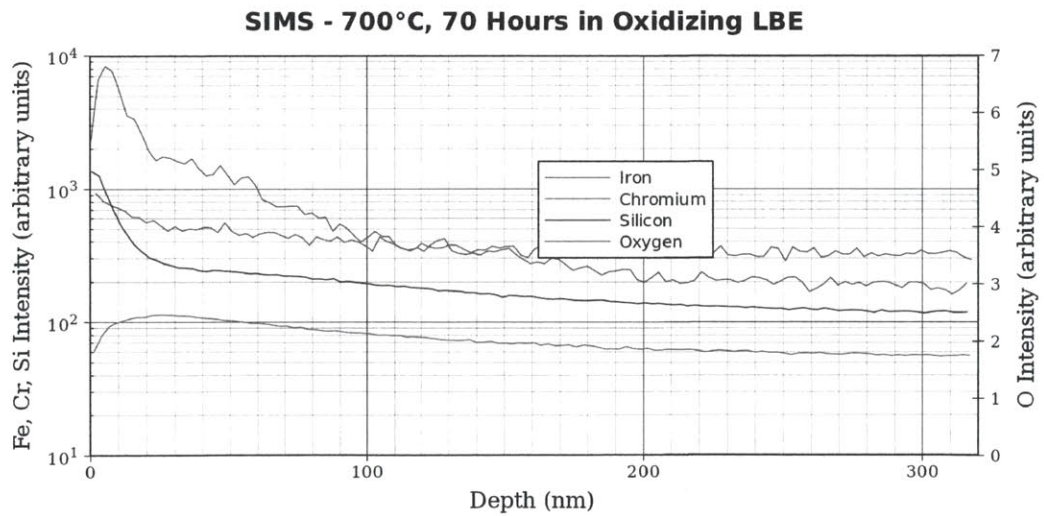
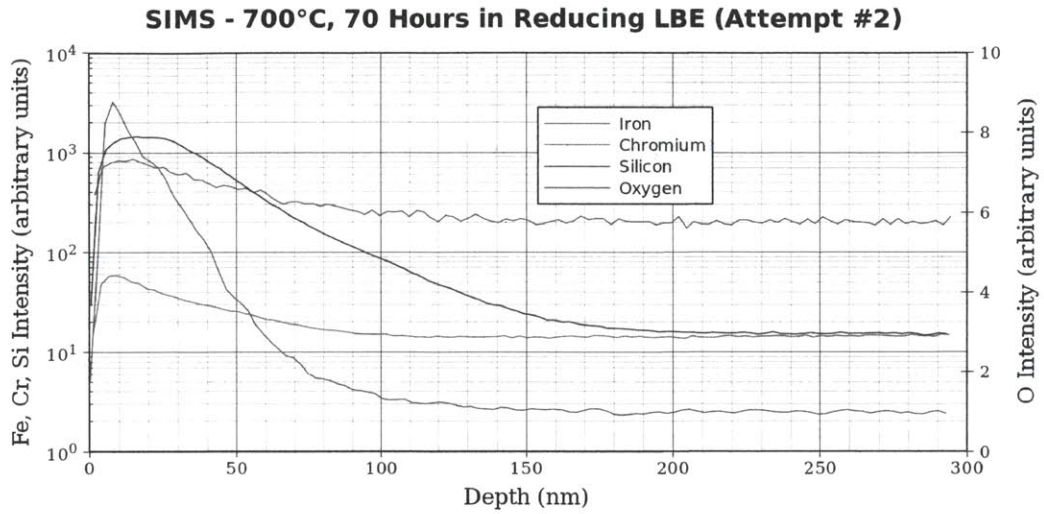


Figure 4-23: SIMS concentration profiles for samples exposed to 700°C LBE for 70 hours

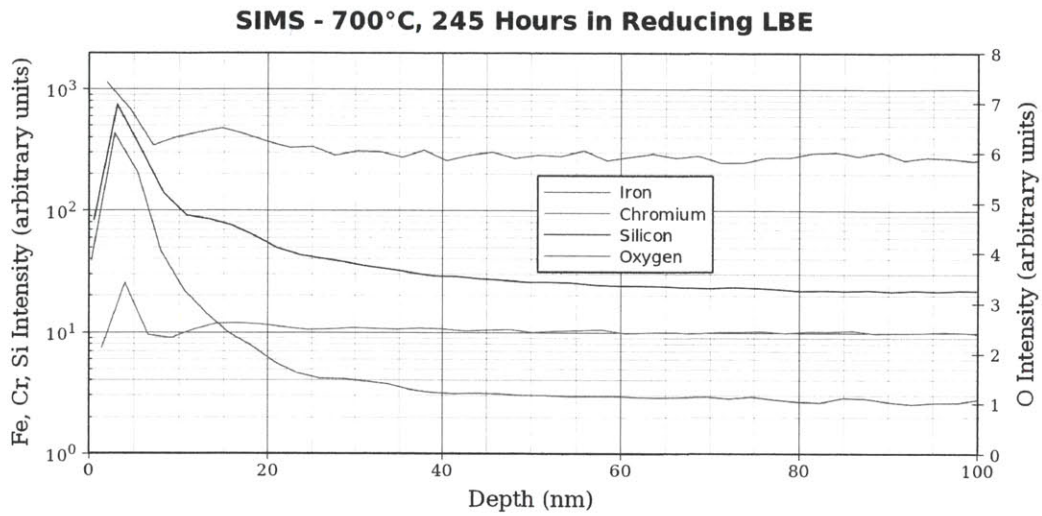
with a layer of either chromia or iron-chrome spinel underneath. The total thickness of the oxide layer was 250 nm. No elemental depletion was observed on either sample beneath the oxide layers.

**700°C, 245 Hour Samples** The SIMS concentration profiles for samples exposed to 700°C LBE for 245 hours are shown in Figure 4-24. The sample exposed to reducing LBE exhibited oxide peak strengths and locations very similar to the sample aged for 70 hours, but at a drastically reduced thickness. Again peaks for iron and silicon are coexistent at the outside of the sample, while a strong silicon peak is present just below the other two. The total thickness of all the layers present was determined to be 80 nm by judging when the silicon and oxygen signals flat-lined.

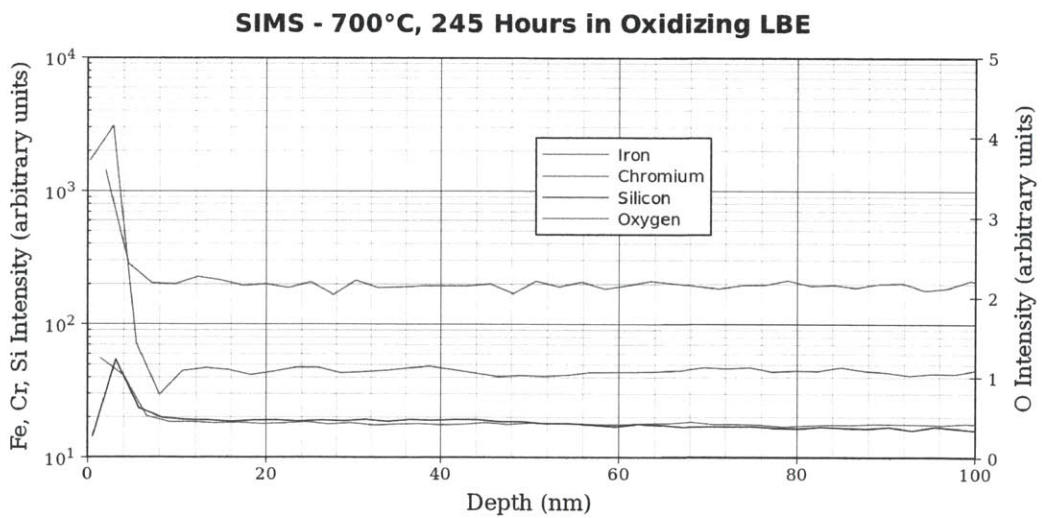
The sample exposed to oxidizing LBE exhibited oxide layers more reminiscent of the control and 70 hour-aged sample in the oxidizing condition. The outermost layers consisted mainly of iron and chromium, while a strong silicon peak was present underneath the other two. The total thickness of the oxide layers was 20 nm. No elemental depletion was observed on either sample for any element.

**700°C, 506 Hour Samples** The SIMS concentration profiles for samples exposed to 700°C LBE for 506 hours are shown in Figure 4-25. The sample exposed to reducing LBE exhibited a depletion in chromium coexistent with an enrichment in iron and silicon. This could be due to a much higher solubility of chromium in LBE as compared to iron and silicon. A slight depletion in silicon was observed beneath the silicon peak; however, the magnitude of this depletion was extremely small. The total depth of the oxidation/enrichment zone is estimated at 120 nm.

The sample exposed to oxidizing LBE showed continued evolution in line with all the other samples exposed to oxidizing LBE and cover gas. However, this time the chromium peak was coexistent with an order of magnitude depletion in iron. This strongly suggests that the outer oxide layer is chromia, and not iron-chromium spinel. The oxygen peak is also coexistent with the chromium peak. The silicon peak is only 15 nm behind the chromium peak, and oxygen levels are still high at this location.



(a) Reducing environment



(b) Oxidizing environment

Figure 4-24: SIMS concentration profiles for samples exposed to 700°C LBE for 245 hours

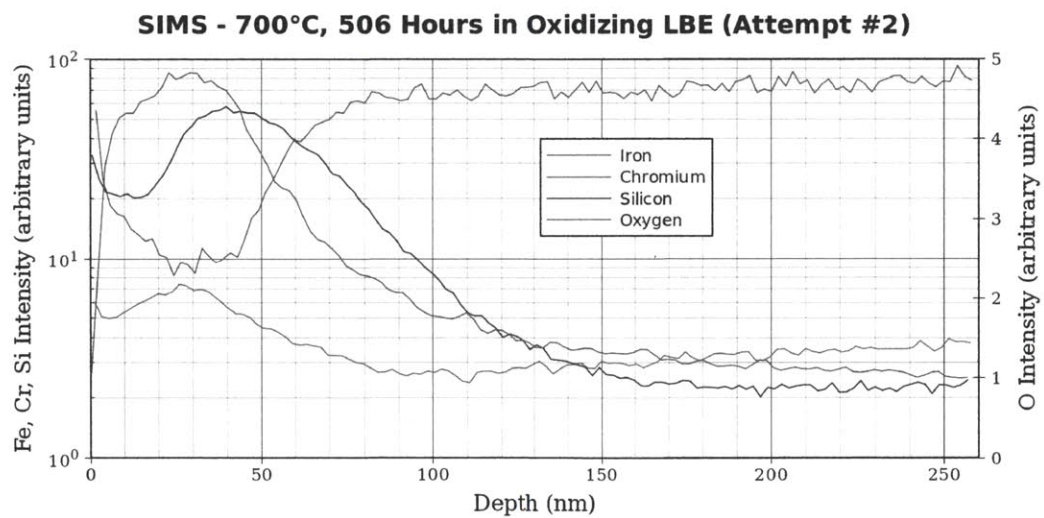
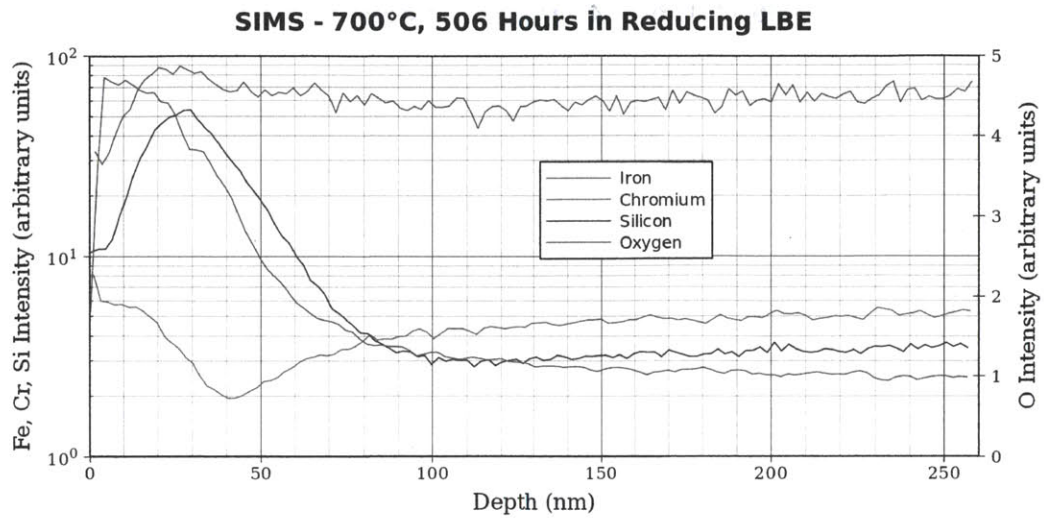


Figure 4-25: SIMS concentration profiles for samples exposed to 700°C LBE for 506 hours

Env.	Temp. (°C)	Time (hrs)	Interaction Layer (nm)	Mechanisms <sup>1</sup>	Peak Order	Depleted Elements
RED	600	504	80	ENR, DIS	Si & O, Fe, Cr	—
		0	200	OX	Cr & O, Si	—
	700	70	130	OX	Cr & Fe & O, Si	—
		245	80	ENR	Fe, Si & O, Cr	—
		506	120	ENR, DIS	Cr & O, Fe, Si	<b>Cr, Si</b>
OX	600	504	250	OX	Cr & O, Si	—
		0	200	OX	Cr & O, Si	—
	700	70	250	OX, DIS	Fe & Si, O, Cr	—
		245	20	ENR, OX	Cr & O, Si	—
		506	180	OX	Cr & O, Si	Cr

<sup>1</sup>ENR - Enrichment; DIS - Dissolution; OX - Oxidation

Table 4.5: Summary of SIMS data, showing total interaction layer thickness, proposed interaction mechanisms, enrichment zone order and any depletion zones present. Peak locations are listed in order starting with the outer surface of the sample. Peaks found together are marked with ampersands. Stronger depletion zones are marked in bold.

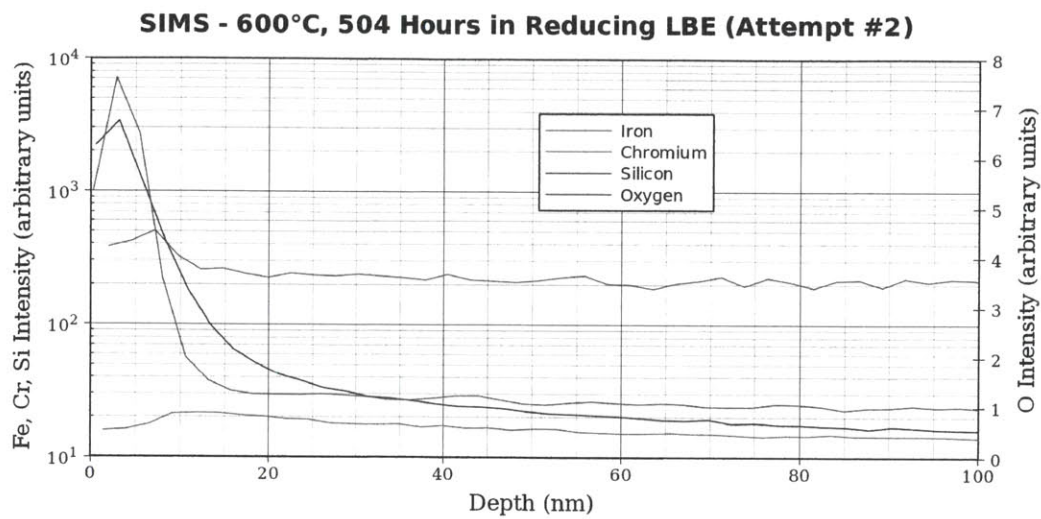
A slight depletion in chromium is observed beneath the chromium oxide layer. The total thickness of the oxidation layer is estimated at 180 nm.

**600°C, 504 Hour Samples** The SIMS concentration profiles for samples exposed to 600°C LBE for 504 hours are shown in Figure 4-26.

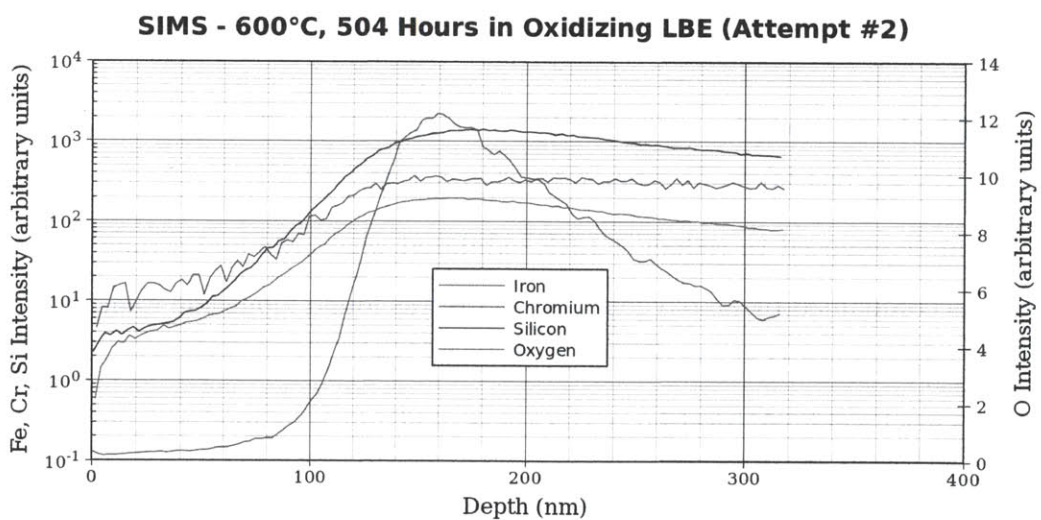
The sample exposed to reducing LBE exhibited weak iron and strong silicon enrichment, accompanied by an oxygen peak. This was found alongside weak chromium depletion. Further inside the metal silicon enrichment was found together with slight chromium enrichment. A total layer thickness of 80 nm is estimated from flat-lining of all signals except for silicon.

The sample exposed to oxidizing LBE exhibited features typical of this alloy in oxidizing LBE, with a chromium peak at the outer surface of the metal followed by a silicon peak tens of nanometers further inside. The sputtering depth for this sample was not sufficient to tell where the concentrations flattened out, so an exact determination of both layer thickness and the presence of any depletion was not possible. The total layer thickness is estimated at 250 nm based on similar samples.

Data from SIMS analysis are summarized in Table 4.5. These include total inter-



(a) Reducing environment



(b) Oxidizing environment

Figure 4-26: SIMS concentration profiles for samples exposed to 600°C LBE for 504 hours



action layer thickness, proposed interaction mechanisms, enrichment zone order and any depletion zones. Zones of stronger depletion are marked in bold. Peaks found together are indicated together with ampersands. Otherwise the peaks are listed in order from outer surface to the inside of the sample.

## **4.3 Diffusion Study Results**

The goal of this analysis was to track and explain changes in microstructure and composition as a function of distance from the original interface. Optical micrographs showed the thickness of the phase change region(s), while also indicating whether any major microstructural changes would have affected the results of the tests. EMPA concentration profiles provided detailed composition as a function of distance, and the shapes of these profiles gave insight into coupling of diffusion coefficients in this system. Finally, hardness profiles gave an indirect measure of carbon diffusion, as the amount of carbon relates to the hardness of the material.

### **4.3.1 Optical Microscopy**

A macro photograph of one diffusion couple as-received is shown for reference in Figure 4-27. In the figure, the carbon steel jacket can be seen surrounding the two metal coupons that make up the diffusion couple. The jacket has rusted due to etching in nital.

#### **4.3.1.1 Control Samples**

One diffusion couple from each lot was kept unaged to track any compositional and microstructural changes as a result of manufacturing the samples. Figures 4-28a & 4-29a show the as-HIPed control samples for comparison to the aged samples. The microstructure of F91 in the control samples is typical of its quenched and tempered form, very similar to that observed for the as-received material in Figure 4-1a. No noticeable amount of microstructural coarsening or other changes have taken place, suggesting that the HIPing process did not noticeably change the microstructure of



Figure 4-27: Optical macrograph of a diffusion couple as-received from Bodycote, Inc. The carbon steel jacket can be seen surrounding the two metal coupons that make up the diffusion couple. The jacket has rusted due to etching in nital.

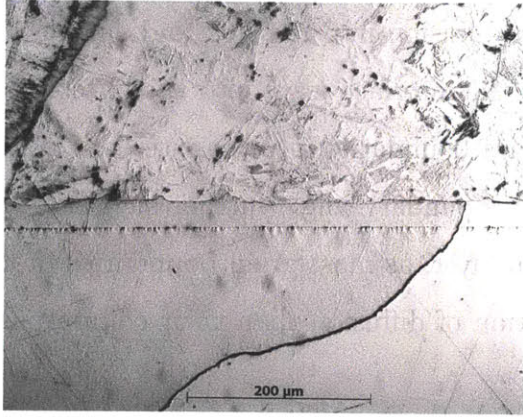
F91 and therefore would not have significantly affected the diffusion coefficients of elements in F91. It is highly possible that coarsening of the typically small vanadium and niobium carbonitrides did take place, as the HIPing temperature was very close to the normalization temperature for alloy F91 (1,050 - 1,080°C [19]). The microstructure of Fe-12Cr-2Si exhibits large grains of ferrite typical of the cast structure for similar alloys. Intragranular carbides are evenly dispersed throughout the grains, as even the 0.01 wt. % carbon specified for this alloy would have formed two phases during periods of slow cooling the diffusion couples (see the Fe-C binary phase diagram in Figure 4-2).

A 20 - 25  $\mu\text{m}$  thick interaction layer is clearly visible between the two alloys. The small bubbles at the bottom of this layer mark the original interface between the two polished metals. This fact was confirmed by following the interface to the edge of the sample, where a slight positional mismatch between the metals indicated that the bubbles did mark the original interface. No “bowing” or curvature of the interface was observed, which would have indicated that vacancy diffusion had been moving

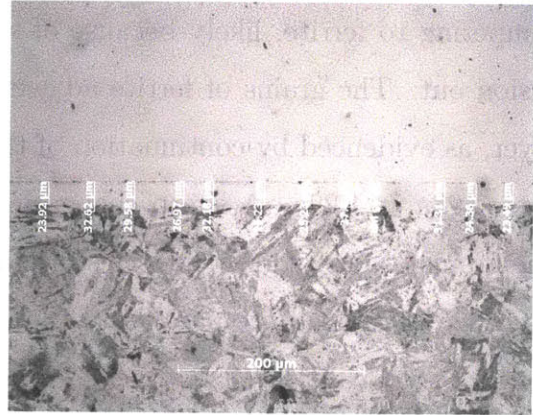
the bubbles away from the original interface. Inside the interaction layer, what was formerly martensite or bainite underwent a combination of phase transformation and tempering to ferrite, likely because of silicon diffusion into the F91 and carbon diffusion out. The grains of ferrite adjacent to the interface grew into this interaction layer, as evidenced by continuation of the grain boundaries into the interface in Figures 4-28a & 4-29a. A sharp change in grain boundary angle further suggests that the grains of ferrite grew into this interaction layer, as most grain boundaries in the interface were far more parallel to the direction of diffusion than their counterparts in the Fe-12Cr-2Si layer.

#### **4.3.1.2 700°C & 750°C Aged Samples**

Representative micrographs of the diffusion couples aged at 700°C and 750°C are shown in Figure 4-28. In each of these samples, the F91 layer is visible as its typical lath-like structure, exhibiting highly anisotropic grains. The Fe-12Cr-2Si layer is visible as the relatively smoother half, as the grains of Fe-12Cr-2Si are so big that only between one and three fit in the image. Note that in some micrographs, like the 700°C 1,160 hr sample, the waterless Kalling's reagent appears to have stained different grains of Fe-12Cr-2Si to different degrees, again suggesting that the crystallographic orientation of each grain determines the degree of etching to which it is subjected. In each of these samples, the interaction layer can be seen to grow slightly with increased aging time and temperature. Diffusion rates at these temperatures are still very slow. A large number of measurements of the interfacial thickness were taken using the Axiovision software package; these results are summarized in Table 4.6. The large number of data points taken ensures that the small differences observed are statistically significant, and not due to random variation. In all these samples, the F91 layer was not observed to coarsen noticeably. If it had, then it would have indicated that the aging took place at or above the original tempering temperature for F91, which has been shown to vary significantly with small changes in composition.



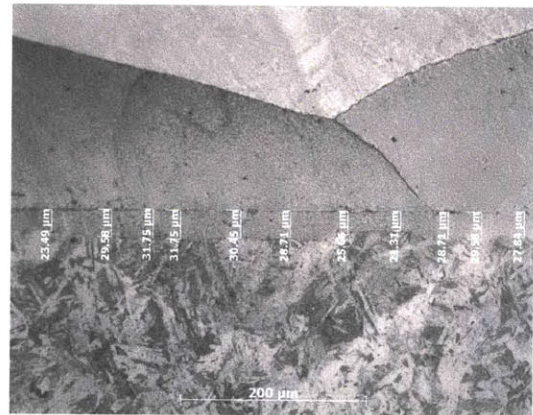
(a) 700/750°C control sample, 200×



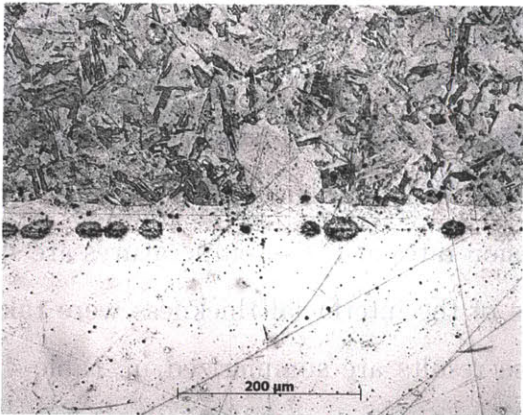
(b) Aged 282 hrs at 700°C



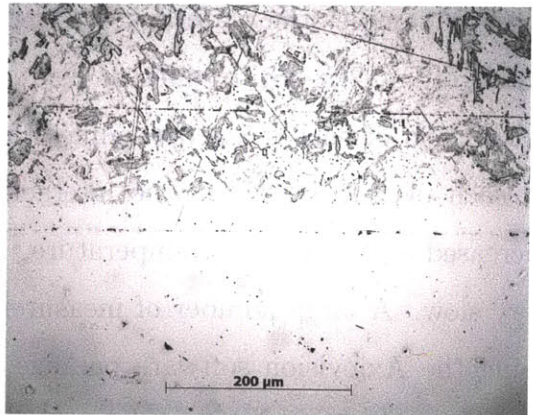
(c) Aged 556 hrs at 700°C



(d) Aged 1,160 hrs at 700°C



(e) Aged 299 hrs at 750°C



(f) Aged 597 hrs at 750°C

Figure 4-28: Optical micrographs of diffusion couples aged at 700°C and 750°C, 200×. All of these samples experienced little microstructural change beyond growth of the single interaction layer, likely due to silicon and carbon diffusion through the system.

Aging Temp. (°C)	Aging Time (hrs)	Avg. Thickness ( $\mu\text{m}$ )	Max. Thickness ( $\mu\text{m}$ )
700 / 750	0	27.7 $\pm$ 1.6	34.8
700	282	27.6 $\pm$ 1.0	32.6
	556	30.0 $\pm$ 1.1	37.4
	1,160	28.1 $\pm$ 1.0	31.8
750	299	29.2 $\pm$ 2.1	43.5
	597	31.8 $\pm$ 2.7	40.0

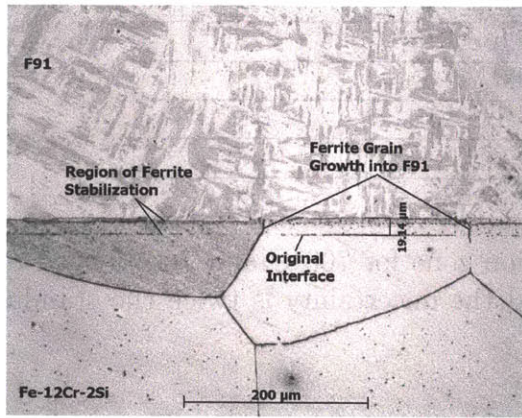
Table 4.6: Average thickness of the interaction zone for 700°C and 750°C aged diffusion couples. Many points were taken, and the uncertainty is twice the standard error of each sample's measurements.

#### 4.3.1.3 800°C Aged Samples

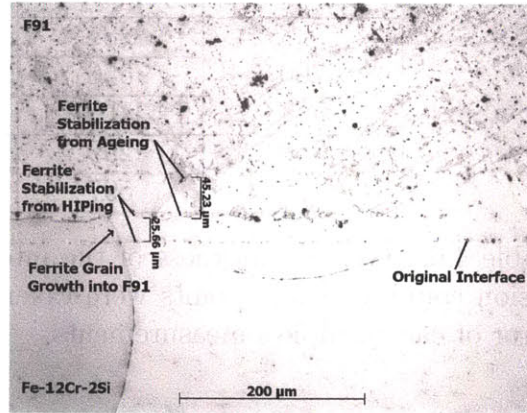
Representative micrographs of the diffusion couples aged at 800°C are shown in Figure 4-29. In all of these samples, two interaction layers were visible between what was clearly F91 and Fe-12Cr-2Si. The first interaction layer, or the one closest to the Fe-12Cr-2Si layer, appears to be ferrite stabilization and growth into the F91 layer. This is especially evident in the 274 hr and 495 hr aged samples, as grain boundaries formerly confined to Fe-12Cr-2Si can be seen to grow into the F91 layer across the line of bubbles demarcating the original interface. The second interaction layer appears to contain many small, ferritic grains, though not as small as the grains of F91.

The F91 in each successive sample appears to contain larger and larger carbides, seen as black particles in the F91 layer. In addition, the F91 layer in each sample appears to get more ferritic, less martensitic and etches similar to the ferrite where different grains appear to be preferentially stained by orientation. All three of these signs point to overtempering of F91, where too much martensite and bainite have been allowed to relax and form equilibrium phases of ferrite and carbides. The decreasing number and increasing size of carbides as the samples age are further indications that overtempering has taken place. Below the tempering temperature, carbides in F91 should remain stable without agglomerating into fewer, larger particles.

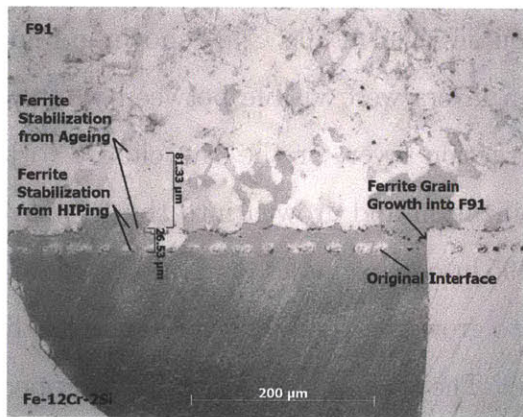
Interaction zones thicknesses were still measured. The data from these measurements is summarized in Table 4.7. Because of the much more elevated diffusion temperature, zone thicknesses grew at a more easily measurable rate. The lines of



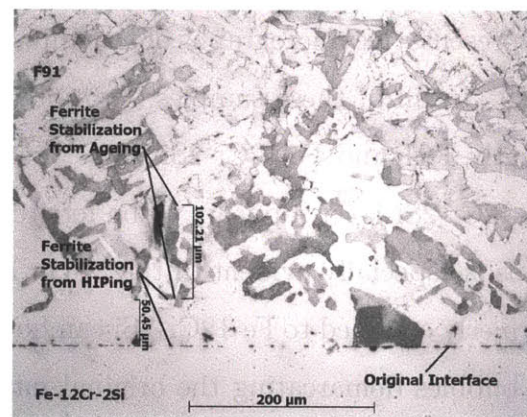
(a) 800°C control sample, 200×



(b) Aged 274 hrs at 800°C



(c) Aged 495 hrs at 800°C



(d) Aged 1,220 hrs at 800°C

Figure 4-29: Optical micrographs of diffusion couples aged at 800°C, 200×. All of these samples experienced significant microstructural changes. The growth of the interaction layers can be attributed to diffusion, while the coarsening of the F91 suggests that the aging temperature for these samples was above the tempering temperature for F91.

Aging Time (hrs)	0	270	495	1,220
Zone 1, Ferrite Growth ( $\mu\text{m}$ )	33.03	33.0	32.6	56.5
Zone 2, F91 Coarsening ( $\mu\text{m}$ )	—	46.2	119.6	119.6

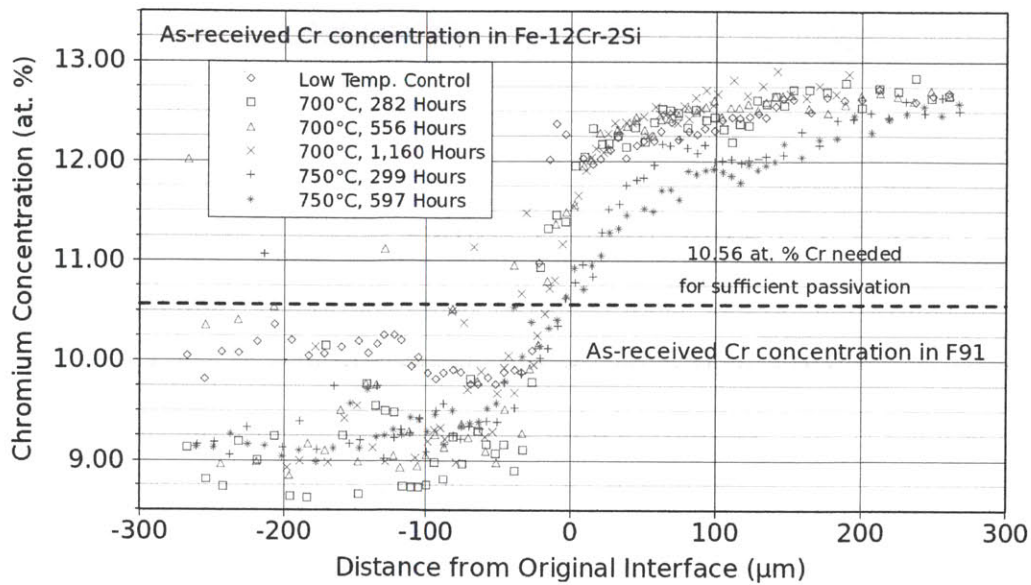
Table 4.7: Maximum interaction zone thicknesses for diffusion couples aged at 800°C. Samples that did not exhibit one or more zones are marked out with “—”

demarcation for the two zones were inferred from regions of differing microstructure, which only varied in the dimension parallel to diffusion. This is most apparent in the 1,220 hr sample, where there are two clearly distinct zones of differing microstructure. The first zone is where the Fe-12Cr-2Si microstructure continues into the interaction layer, and the second is where the F91 appears coarser than the bulk.

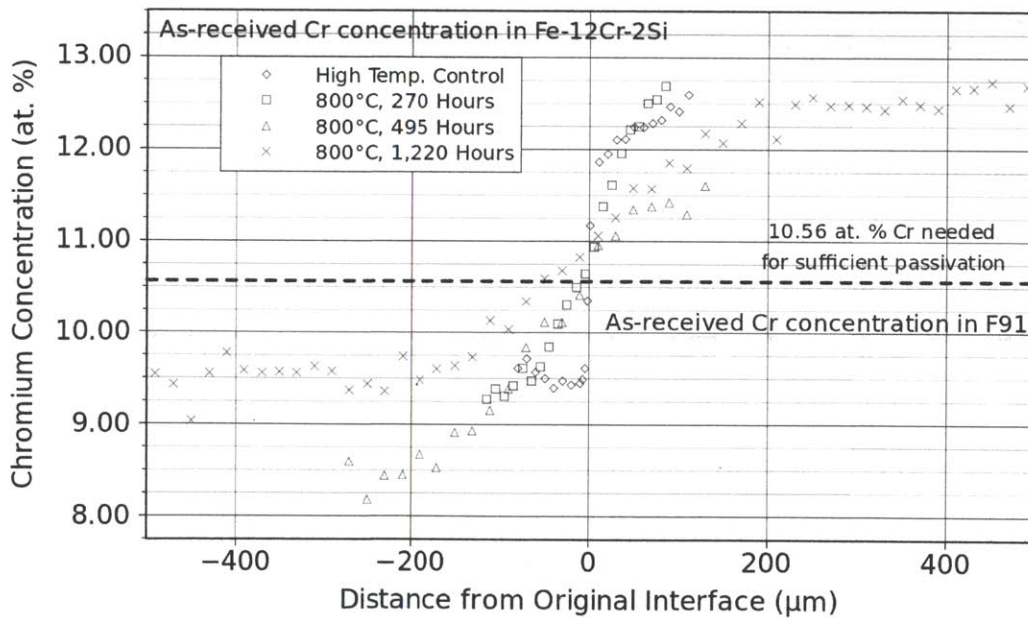
### 4.3.2 EMPA Concentration Profiles

EMPA concentration profiles were collected using the line of bubbles marking the original interface as the  $x=0$  point on the graphs. Iron and molybdenum curves were acquired, but they are omitted from this discussion because the concentration of molybdenum is so low (no more than 1 wt. %) and iron is the base element. Therefore, a complete description of phenomena can be inferred from just the chromium and silicon concentration profiles.

The EMPA concentration profiles for chromium are shown in Figure 4-30, separated into low and high temperature aged diffusion couples. Obvious outliers which mainly consisted of points outside the concentration bounds for the two alloys have been removed for clarity's sake. However, these points are likely not machine errors, but rather different phases in the material. The concentration profiles for chromium in Fe-12Cr-2Si were very smooth compared to those for F91, as is especially apparent in the 700°C aged samples. This is because F91 contains a relatively large amount of carbon, and chromium is known as a carbide former in similar steels [148]. Therefore any  $M_xC_y$  carbides that are captured by the EMPA analysis beam will be greatly enriched in chromium. No points of chromium depletion were observed, further suggesting that this is due to analysis of other phases and not machine error. No sudden discontinuities in slope were observed, suggesting that no phase boundaries significantly impeded chromium diffusion, whether or not they actually existed. It should also be noted that the curves were significantly steeper in the F91 region, suggesting that diffusion is slower in F91 than in Fe-12Cr-2Si. Finally, it should be noted that the only place that the chromium concentration is clearly outside the bounds of the original alloy concentrations is in the F91 region. This is likely due to chromium en-



(a) Cr EMPA profiles for 700°C & 750°C aged samples



(b) Cr EMPA profiles for 800°C aged samples

Figure 4-30: Chromium EMPA concentration profiles for diffusion couples in this study. Obvious outliers that did not fit the overall curves have been removed to improve the clarity of the overall shape of the curves.

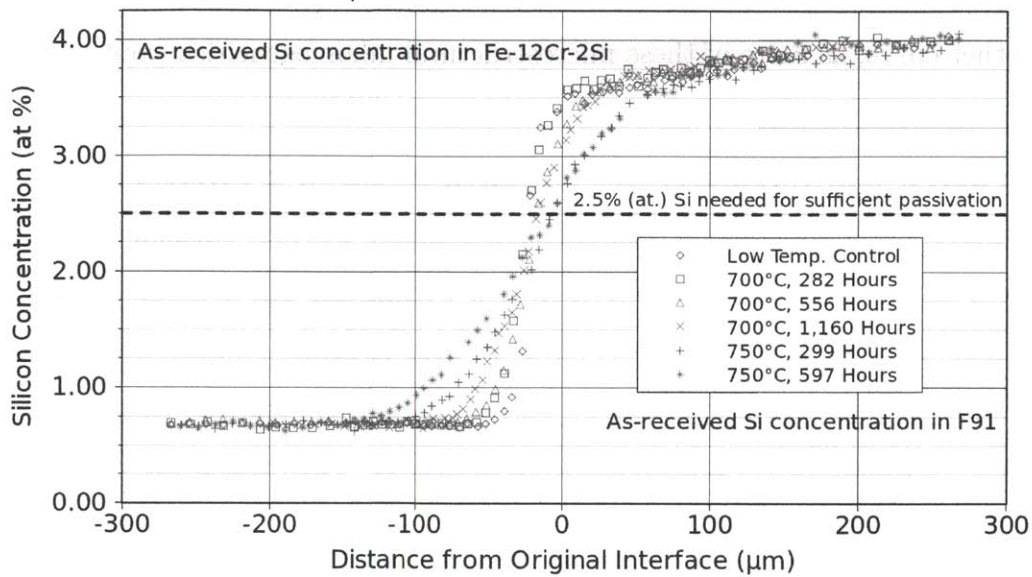


richment in the numerous small carbides interspersed throughout the microstructure of F91, and the baseline chromium concentration is likely due to slight depletion of chromium in the matrix surrounding carbides. A wider beam would have produced a smoother curve, as more of these microstructural inhomogeneities would have been averaged out.

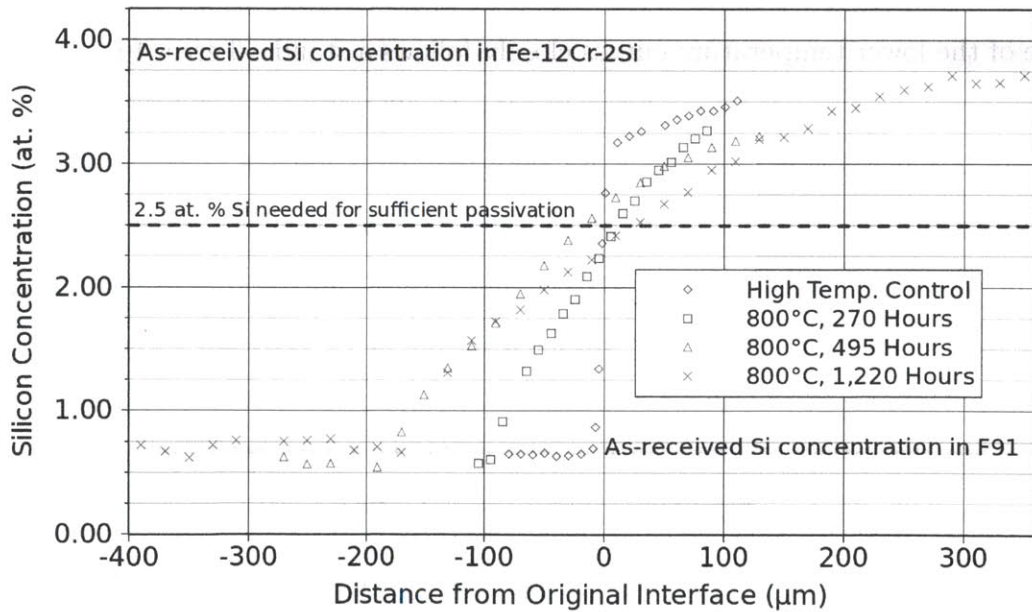
The EMPA concentration profiles for silicon are shown in Figure 4-31, separated into low and high temperature aged diffusion couples. Obvious outliers which mainly consisted of points outside the concentration bounds for the two alloys have been removed for clarity's sake. However, nowhere near as many outliers existed in these profiles as did in the chromium profiles. This is due to silicon mainly existing as a substitutional impurity in the matrix for both materials. This causes the concentration profiles to be much smoother.

In both the lower temperature and the higher temperature samples, the curves are very smooth, and they decrease in steepness with aging time and temperature. The shape of the lower temperature curves closely follows a standard error function in the F91 layer, while it is more complicated in the Fe-12Cr-2Si layer. This indicates that diffusion is much faster in Fe-12Cr-2Si than in F91. Diffusion is most likely slower in F91 because of the large amount of other alloying elements, very fine carbides and carbonitrides, and the more stressed martensitic microstructure present. This slower diffusion in F91 causes the diffusion profile in Fe-12Cr-2Si to be made up of two components: a fast diffusion region dominating far from the interface, and a slow region near the interface. This slow region is due to solute "pile-up" as that solute diffuses towards the interface, but cannot enter the F91 at the same rate it arrives.

In the higher temperature samples, regions of slope discontinuity were observed at the boundary between the first (closer to Fe-12Cr-2Si) and second (middle) interaction zones. These regions of slope discontinuity match up very well with observed regions of differing microstructure. Examples of correlation between concentration and microstructure are shown in Figure 4-32, one for the lower temperature samples showing one interaction layer, and one for the high temperature samples showing two interaction layers. The low temperature samples exhibited smooth concentration

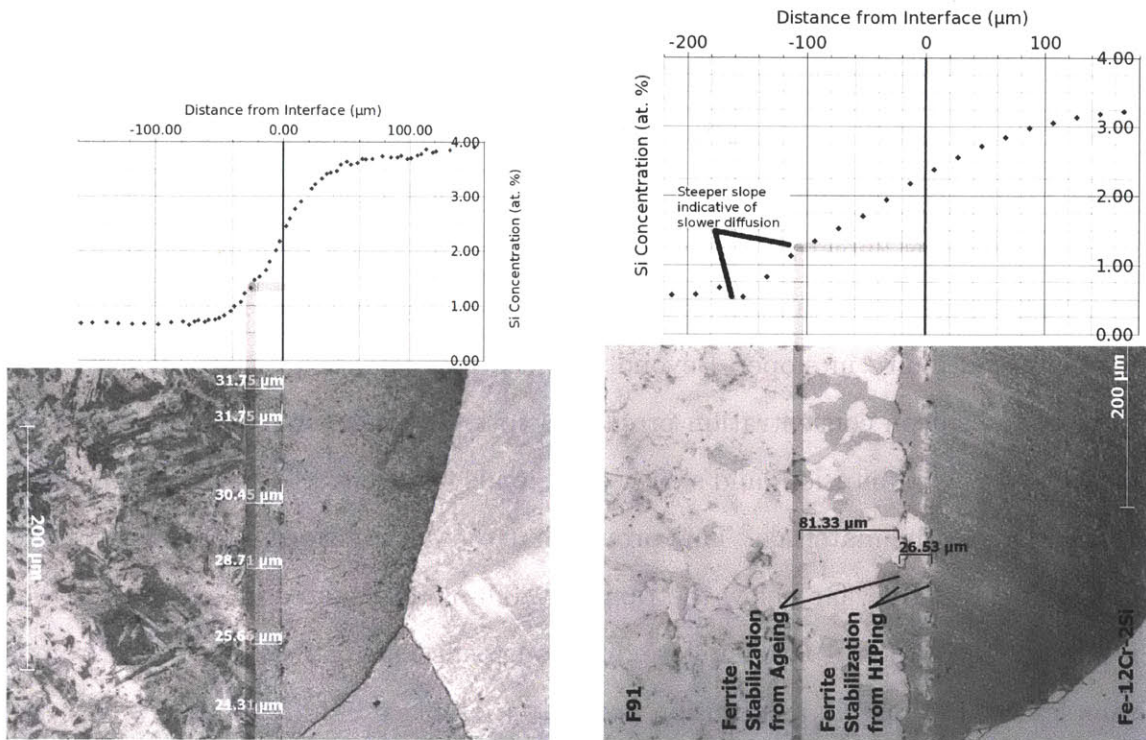


(a) Si EMPA profiles for 700°C & 750°C aged samples



(b) Si EMPA profiles for 800°C aged samples

Figure 4-31: Silicon EMPA concentration profiles for diffusion couples in this study. Obvious outliers that did not fit the overall curves have been removed to improve the clarity of the overall shape of the curves.



(a) Correlation between EMPA silicon concentration and microstructural features in the diffusion couple aged at 700°C for 556 hrs, 200×. Note that bainite abruptly gives way to ferrite at a silicon concentration of 0.6 wt. %.

(b) Correlation between EMPA silicon concentration and microstructural features in the diffusion couple aged at 800°C for 495 hrs, 200×. Note that bainite abruptly gives way to ferrite at a silicon concentration of 0.6 wt. %. Also note that at that point the slope of the concentration profile steepens considerably, indicating that the F91 underwent the A1 phase transformation. Diffusion of many solutes is 1 - 2 orders of magnitude slower in FCC iron than BCC iron at the same temperature [22].

Figure 4-32: Correlation between regions of slope discontinuity, certain Si concentrations and microstructure for aged diffusion couples. On all samples, ferrite became the dominant phase at a silicon concentration of 0.6 wt. %. This is likely due to silicon's role as a bainite destabilizer and a ferrite stabilizer [21].

profiles, with no discontinuities in slope observed on any samples. This indicates that the material did not undergo a phase change at these temperatures, which would have been marked by drastically slower diffusion. The diffusion coefficients for solutes such as carbon and silicon are 1 - 2 orders of magnitude lower in FCC iron than in BCC iron near the transformation temperature, as can be seen in Figure 4-33 [22]. In all samples at the two lower temperatures, a sharp line marked the sudden change in phase dominance from bainite to ferrite. This line was observed at a silicon concentration of 0.6 wt. %. The specified silicon concentration for F91 is no higher than 0.4 wt. % because silicon is known to act as a ferrite stabilizer and a bainite destabilizer [21]. The high temperature samples exhibited three main interaction zones, but only one major discontinuity in slope. Beyond a silicon concentration of 0.6 - 0.7 wt. %, the slope of the silicon concentration profile abruptly gets steeper. A steeper slope is indicative of slower diffusion, and slower diffusion is indicative of a phase change having taken place in the materials. This proves that the A1 transformation temperature is indeed below 800°C, far below the range of 830 - 850°C quoted in Vallourec & Mannesmann's T91 book [19]. Therefore diffusion coefficients cannot be derived from the samples aged at 800°C, as diffusion partially took place in a different crystal system that would never be experienced even during an accident in a properly designed LBE reactor.

### 4.3.3 Micro- and Nanohardness Profiles

Vickers hardness data were acquired on each diffusion couple at least 2 mm away from the interface to ensure that the hardness of the base metal and not the interaction zone was being measured. These data are summarized in Table 4.8. The data show that the hardness values for metal diffusion couples aged at 800°C did tend to approach each other with increasing aging time. This indicates that both F91 tempering and significant carbon diffusion took place, as tempering would tend to soften F91 while increased carbon content would harden Fe-12Cr-2Si. Hardness levels for the lower temperature samples did not experience such a dramatic change, staying closer to their as-received values. This indicates that significant tempering did not

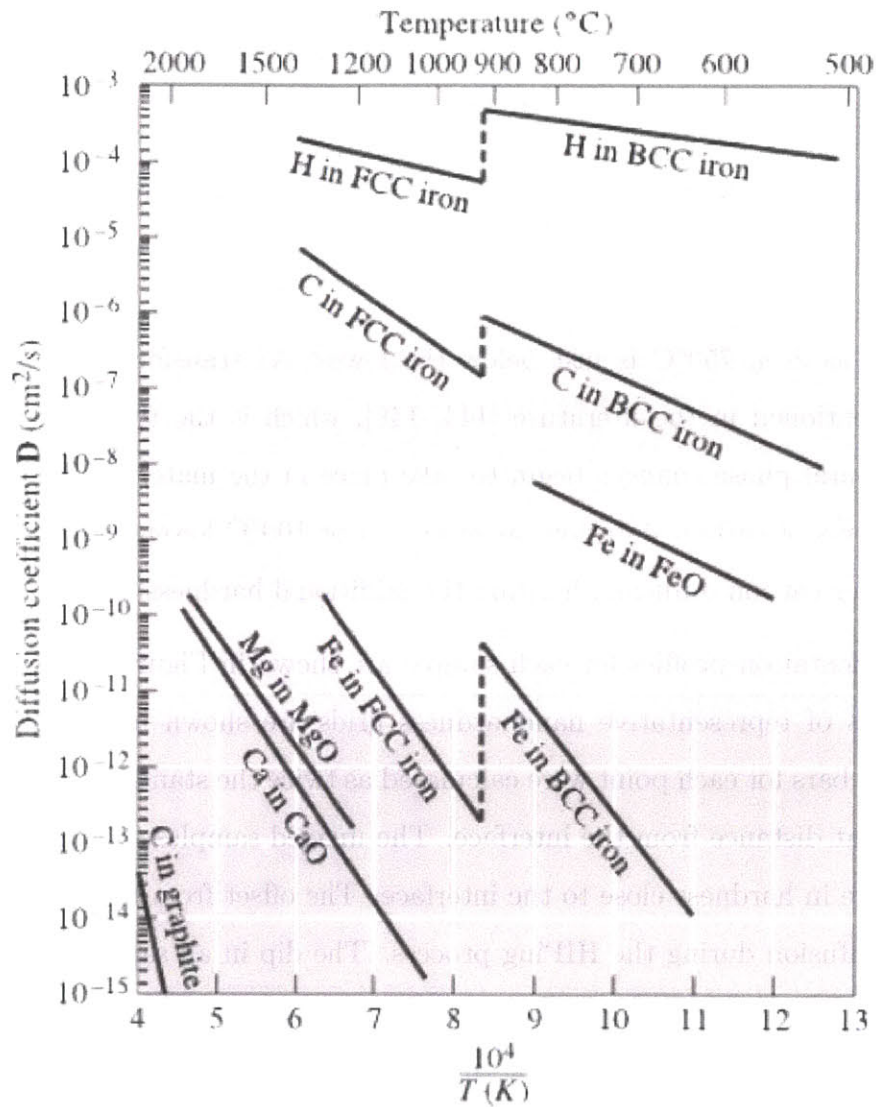


Figure 4-33: Diffusion coefficients of selected solutes in iron, showing a sudden drop in diffusion at the BCC-FCC phase transition temperature [22]

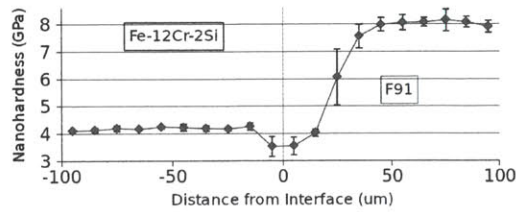
Aging Temp. (°C)	As-Rec'd	700/750	700			
Aging Time (hrs)	—	0	282	556	1,160	
HV <sup>1</sup> - F91	258 ±3	429 ±3	208 ±2	213 ±2	197 ±2	
HV <sup>1</sup> - Fe-12Cr-2Si	161 ±8	168 ±2	161 ±2	157 ±2	176 ±2	
Aging Temp. (°C)	750		800			
Aging Time (hrs)	299	597	0	274	495	1,220
HV <sup>1</sup> - F91	172 ±2	179 ±2	220 ±2	187 ±6	157 ±8	176 ±14
HV <sup>1</sup> - Fe-12Cr-2Si	180 ±2	179 ±2	128 ±20	177 ±6	155 ±4	181 ±13

<sup>1</sup>Hardness Vickers

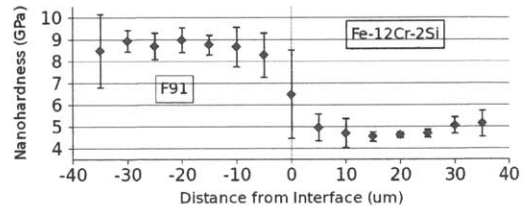
Table 4.8: Vickers hardness data for base materials in diffusion couples. Data were taken at least 2 mm from the interface on either side to track any tempering (in F91) or hardening (in Fe-12Cr-2Si) that took place.

take place, as even 750°C is just below the lowest A1 transformation temperature (756°C) mentioned in the literature [144, 149], which is the temperature at which microstructural phase changes begin to take place in the material. This also makes sense in terms of carbon diffusion, as either 50 or 100°C lower temperatures would see far slower carbon diffusion, limiting the additional hardness of Fe-12Cr-2Si.

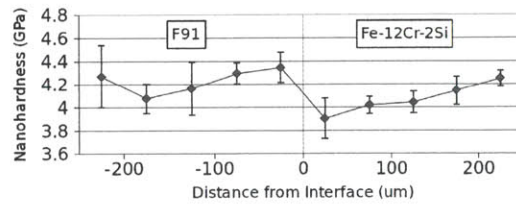
Nanoindentation profiles for each sample are shown in Figure 4-34, while optical micrographs of representative nanohardness grids are shown in Figure 4-35. The uncertainty bars for each point were calculated as twice the standard error for all data taken at that distance from the interface. The unaged samples show a characteristic steep change in hardness close to the interface. The offset from the original interface is due to diffusion during the HIPing process. The dip in all samples' hardnesses at the interface, especially in the 700°C unaged diffusion couple and the 800°C 274 & 495 hr samples, is due to porosity at the original interface between the two metals. This is because the formation of a diffusion bond cannot remove 100% of the porosity present due to initial sample roughness. The high standard deviation whenever a drop in hardness is present at the interface further supports this, as there would be large differences between the hardness of a void and that of sound metal. The 700°C diffusion couple nanohardnesses start out differing by a factor of two for the unaged sample. After 556 and 1,160 hrs, the samples were much closer in nanohardness. The 700°C 282 hr sample does not show any meaningful data, probably because that



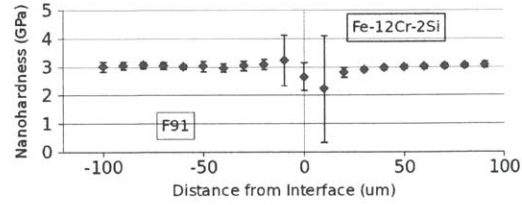
(a) 700°C 0 hour diffusion couple



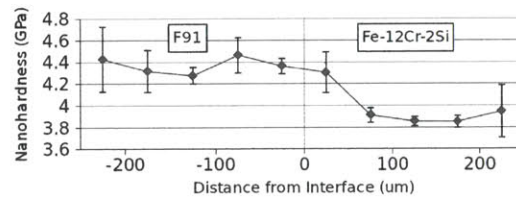
(b) 800°C 0 hour diffusion couple



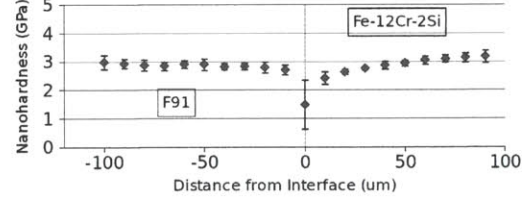
(c) 700°C 282 hour diffusion couple



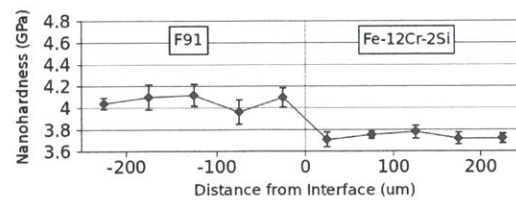
(d) 800°C 495 hour diffusion couple



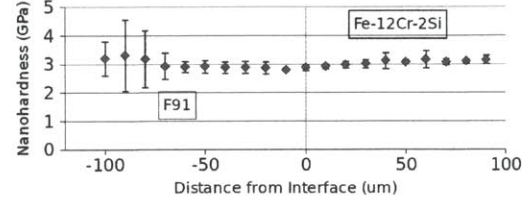
(e) 700°C 556 hour diffusion couple



(f) 800°C 495 hour diffusion couple

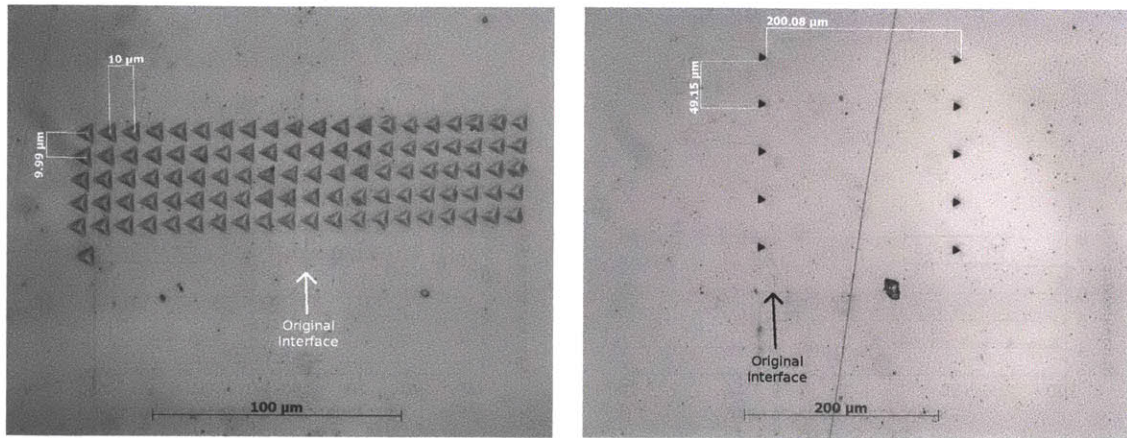


(g) 700°C 1,160 hour diffusion couple



(h) 800°C 1,220 hour diffusion couple

Figure 4-34: Nanohardness profiles for 700°C and 800°C diffusion couples. The overall hardness values for the unaged samples are higher because a lower indent depth was used. Scaling down by a factor of two provides a sufficient comparison with the rest of the data.



(a) Nanohardness grid from unaged diffusion couple from 700°C/750°C lot, 500× (b) Nanohardness grid taken on diffusion couple aged at 700°C for 300 hours, 200×

Figure 4-35: Optical micrographs of representative nanohardness grids taken on diffusion couples

sample was more scratched than the rest. Scratches on the order of the indenter size can drastically affect the results. The 800°C diffusion couples show almost equal nanohardnesses even after 274 hrs, suggesting that carbon diffusion was extremely rapid. The 800°C unaged sample showed a similarly steep drop-off in hardness, while the two metals in the aged samples are nearly equal in nanohardness. This can be partly attributed to carbon diffusion and carbide precipitation in Fe-12Cr-2Si as well as tempering and softening in F91. This further suggests that 800°C is above the A1 transformation temperature for this lot of F91. Finally, while one may be concerned that the point spacing on the control samples' nanohardness grids is too fine, the point spacing was calculated as ten times the indentation depth. The depth of the indentation is almost ten times as shallow as it is wide, leading to a very small plastically deformed zone around the indentation. This is not expected to have significantly altered the nanohardness profiles. If it had, it would have been visible as one softer point at the start of each control sample's nanohardness profile. Given that in all cases the first indent was made in Fe-12Cr-2Si and no dip in nanohardness is visible on that side, plastic deformation between indents did not make a difference in these samples.



## 4.4 Commercial Feasibility Results

Here the microstructural and hardness results after each test will be presented, along with any comments from the manufacturers pertaining to the ease and quality with which the material behaved.

### 4.4.1 Weld Wire Fabrication

Formation of the initial forging billet (seen as the 10.15 cm (4") diameter slice with the middle missing in Figure 3-11) did not encounter any problems. The largest contributing factor is the quality of chemistry control employed in making the melt. Highly pure metal powders were used rather than other sources, such as ferro-chrome scrap. This enabled far more strict controls to be placed on unwanted elements, such as phosphorus, sulfur and nickel. The manganese level was chosen by estimating the sulfur content and adding a sufficient amount to bind it up in the form of MnS inclusions. Typically this is done at 10 - 20× the sulfur concentration, which in this case would have corresponded to a manganese concentration of 0.08 - 0.16 wt. %. However, because we didn't want to completely remove the sulfur, less than this was added. The value of 0.019 wt. % from ICP-MS of the weld wire (see Table 3.1) may or may not include MnS inclusions.

Reduction of the forging billet in Special Metals' bar and wire mill proceeded very well until it was 12.7 mm (1/2") in diameter (seen as the 12.7 mm (1/2") straight rods in Figure 3-11). At that point the material cobbled between steps. A bar and wire mill typically uses a number of dies in series at once to reduce a billet by a large amount through multiple passes. The speed of the rolls in each step must be inversely proportional to the square of the diameter, as the mass flow rate through each step must remain constant. Therefore the speed of each subsequent roll must be faster than the previous one. Even a short transient drop in roll speed on one step could cause the rod to bend, and once it starts to bend there is no stopping it. This required all of the cobbled wire to be cut out of the mill. Luckily the lack of carbon in the material made friction welding it back together very easy, as no cracking

occurred at friction welded joints. Further processing down to 6.35 mm (1/4") wire rod (the thinner straight rods in Figure 3-11) and then 0.89 mm (35 mil) weld wire (the spool of wire in Figure 3-11) went smoothly. The manufacturers indicated that the material worked very easily and without significant resistance, again due to the very low concentration of carbon.

#### 4.4.2 Weld Overlaying

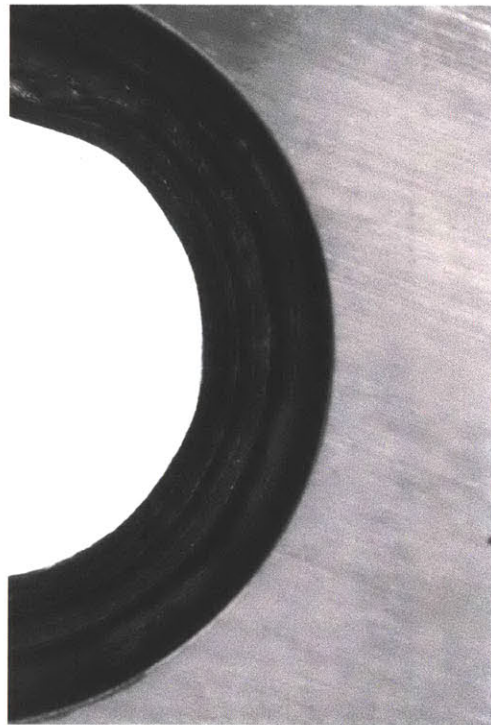
Photographs of the cut surfaces as well as the weld beads of slices of billets described in Section are shown in Figure 4-36. In each billet slice, no incomplete fusion between the overlay and the F91 base layer was observed. The weld beads appeared as nearly perfect layers of "stacked coins," indicating the regularity and precision of the automated welding process. The width and thickness of each pass was much higher than the thickness of the weld wire, showing how the zig-zag welding procedure increases both of these parameters. The weld wire was extremely cooperative and easy to weld. In the words of the project manager at the weld overlay shop, "We tried to be as careful as possible but that much welding without any problems even impresses me."

A photograph of the interface as weld overlaid from the ID-clad billet is shown in Figure 4-37. The visible mixing layer in this billet is very small, less than the thickness of one pass. Mixing is visible as what appears to be martensitic F91 grains poking into a light grain of ferrite near the center of the picture. The curvature present in the interface is centered around the location of one weld bead. It is possible that the mixing zone is thicker than it appears, as carbon mixing and diffusion during melting could turn much of the first overlay pass into martensite and bainite upon fast cooling. The large thermal mass of the billet would have ensured that cooling after the melt zone had passed occurred very rapidly, as heat would have been sucked out into the rest of the billet.

The thickness of the mixing zone on the OD-clad billet was too large to fit in one micrograph, so a montage showing the entire zone is shown in Figure 4-38. The actual mixing zone, which consists of mostly bainite, is likely confined to the first pass.



(a) ID-clad overlaid billet, cut face



(b) ID-clad overlaid billet, weld bead



(c) OD-clad overlaid billet, cut face



(d) OD-clad overlaid billet, weld bead

Figure 4-36: Slices of weld-overlaid extrusion billets. In each billet, the Fe-12Cr-2Si layer is visible as a region of different reflectivity either on the ID or the OD, and is demarcated with dotted black lines.



Figure 4-37: Layer interface on the ID-clad weld overlaid billet, 100 $\times$ . Some mixing is present, seen as fingers of martensite poking into a grain of ferrite at the center of the photograph. Overall the interface and mixing layer was very thin.

However, a large amount of fast carbon diffusion along grain boundaries is visible as carbides decorating most grain boundaries out to a distance of 3 mm. In addition, it appears that fast carbon diffusion is taking place through close-packed directions in the grains of Fe-12Cr-2Si. This is evidenced by the presence of sharp, well-defined lines of carbides at 90° angles to each other inside each grain. This is clearly visible in the two long grains (one light, one dark) at the center of the micrograph. The light grain's fast carbon diffusion can be seen in the middle of the grain, starting on the right side. The same phenomenon can be seen near the bottom left of the dark grain. This accelerated carbon diffusion ends abruptly at a distance of 3 mm. Beyond this distance, the Fe-12Cr-2Si takes on its more typical microstructure with finely dispersed carbides throughout the grains. It is of particular note that the grains of Fe-12Cr-2Si in the fast carbon diffusion zone are devoid of intragranular carbides.

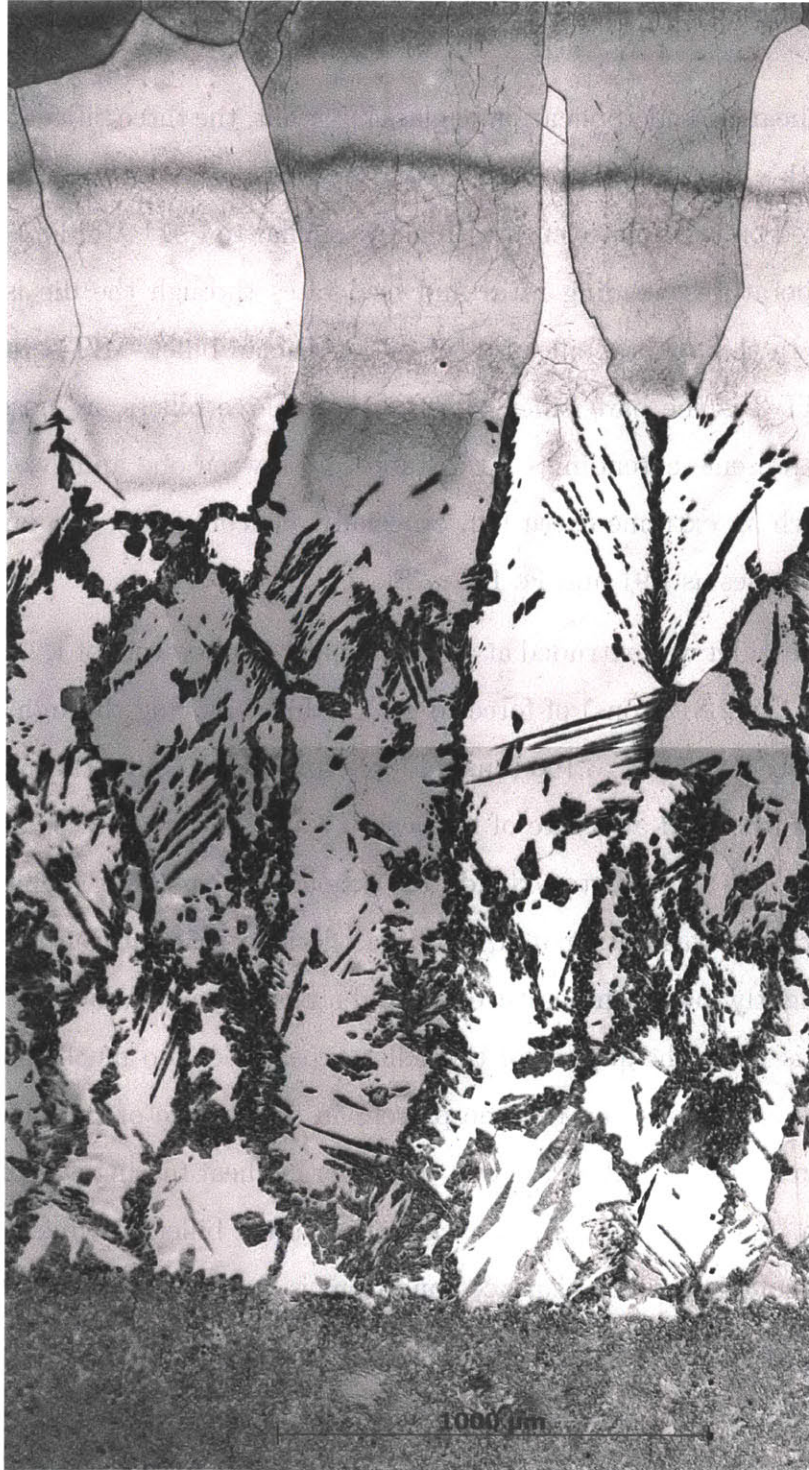


Figure 4-38: Layer interface on the OD-clad weld overlaid billet, 50 $\times$ . Some mixing from the melt zone is present, but more striking is the presence of carbides along grain boundaries. Grains of Fe-12Cr-2Si grow in columns perpendicular to the interface. Spears of carbon diffusion can also be seen in close-packed directions inside these grains, visible as black lines at 90 $^{\circ}$  angles to each other.

### 4.4.3 Extrusion

Following preheating and application of glass lubricant, the three billets were extruded on H. C. Starck's 4,545 MT (5,000 ton) extrusion press using temperatures, forces and feed rates based on their experience with alloys similar to F91. A full extrusion report showing temperatures, loading rates and feed rates through the die is attached as Appendix B. In this report, billet MIT-1 is the ID-clad billet, MIT-2 is the OD-clad billet and MIT-3 is the bare billet of F91. In all three billets, a "nose" of warped material was present, extending to a distance of between one and two feet. This is normal for such an extreme extrusion, especially one containing two layers of vastly differing hardnesses as F91 and Fe-12Cr-2Si.

The ID clad billet was extruded at an initial billet temperature of 1,224°C (2,236°F), it took 2,556 MT (2,812 tons) of force to get the billet moving through the mandrel, and it took up to 2,905 MT (3,196 tons) of force to move the billet through to the end. The billet was extruded at a rate of between 9.7 and 18.5 cm/sec (3.83 - 7.3 in/sec), taking five seconds in total to extrude the whole 59.7 cm (23.5") billet. This was slightly faster than was anticipated, so it was decided that future extrusions would be run at a slightly lower temperature to avoid a phenomenon known as heat tearing. Heat tearing is when the surface of the billet experiences too much force when it is too soft, and grooves or tears become present in the surface of the billet. This was only a concern for the Fe-12Cr-2Si layer. However, no heat tearing was present during this extrusion. A photograph of the back section of the billet showing the initial and final diameters along with the surface conditions is shown in Figure 4-39a.

The OD-clad billet was extruded at an initial billet temperature of 1,207°C (2,205°F) to lower the risk of heat tearing. It took 3,085 MT (3,393 tons) of force to get the billet moving through the mandrel, and it took up to 3,183 MT (3,501 tons) of force to move the billet through to the end. This is likely because the inner diameter of the ID-clad billet was 9.78 cm (3.85") as compared to 8.26 cm (3.25") for the other two, leading to less force necessary to send it through the same die and mandrel. This is further supported by the larger extrusion ratio of 15.28, compared to the ratio of



(a) Back end of the ID-clad extrusion billet. Note the regular surface finish, indicating that no heat tearing took place. This is because the cladding (visible as a reddish ring in the cross section) underwent much less deformation being on the ID.



(b) Back end of the OD-clad extrusion billet. The axial grooves present throughout the outer surface of the billet are the beginnings of heat tearing. This is because the cladding (visible as a reddish ring in the cross section) was on the outside, and it clearly was deformed far more in being forced through the mandrel and die during extrusion.

Figure 4-39: Back sections of the extrusion billets after extrusion, showing the post-extrusion reductions in diameter, area and the surface conditions. The black crusty material is burned glass used as a lubricant during the extrusion process.

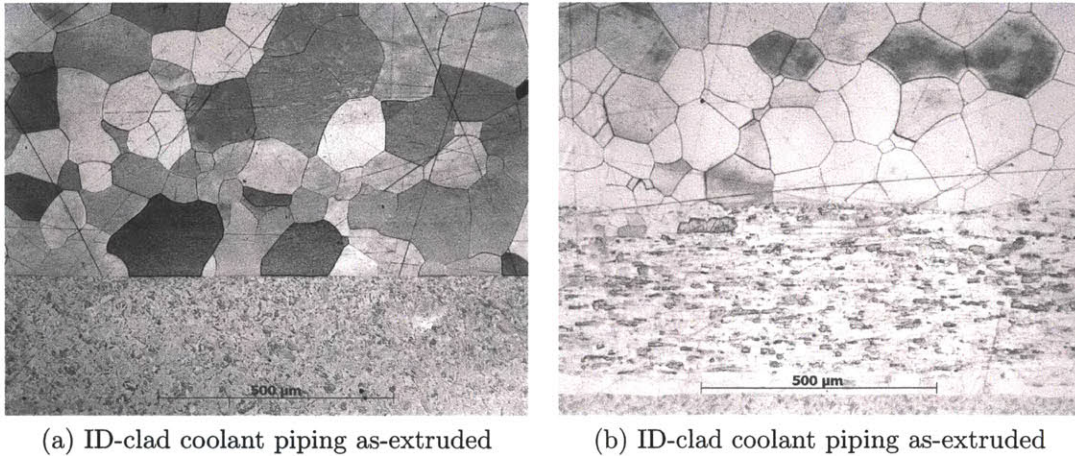


Figure 4-40: Optical micrographs of as-extruded product forms immediately prior to welding, 100 $\times$ . Note the sharp interface between the two metals present in the ID-clad sample. Also note the relatively small grain size in both materials, and the ferritic grain shape of Fe-12Cr-2Si.

12.66 for the ID-clad billet. The billet was extruded at a rate of between 9.9 and 14.0 cm/sec (3.9 - 5.5 in/sec), taking 2.5 seconds in total to extrude the whole 29.2 cm (11.5") billet. A photograph of the back section of the billet showing the initial and final diameters along with the surface conditions is shown in Figure 4-39b. In this photograph, the beginnings of heat tearing are visible as axial streaks along the surface of the extrusion billet, forming near the very beginning of the extrusion process. This occurred only on the OD-clad billet because the softer Fe-12Cr-2Si layer was present on the outside rather than the inside of the billet. This resulted in a far higher deformation rate for this layer than the innermost layer of F91, exposing the softer cladding to a much higher flow stress.

Optical micrographs of the as-extruded tubes are shown in Figure 4-40 for reference. The ID-clad sample exhibited a very sharp interface, a typical martensitic F91 microstructure and very cubic grains of Fe-12Cr-2Si, which were slightly smaller than in previous forms due to a lack of annealing after extrusion. The interface was thin, but present. Ultrasonic testing showed no visible porosity on the interface. The OD-clad sample exhibited much of the same with the addition of an interfacial layer with stretched-out grains of Fe-12Cr-2Si. These are due to the fast carbon diffusion that took place during weld overlaying (see Figure 4-38). This layer of carbon diffusion



was stretched out axially and compacted radially, leading to the smaller, elongated grains on the interface. Further annealing and heat treatment would eliminate this layer of elongated grains.

#### **4.4.4 Pilgering**

As of this writing, pilgering is still in progress at Haynes Tubular Products in Arcadia, LA. It will be discussed in the future work section.

#### **4.4.5 Tube Drawing for Fuel Cladding**

As of this writing, tube drawing into the final fuel cladding form is still in progress at Haynes Tubular Products in Arcadia, LA. It will be discussed in the future work section.

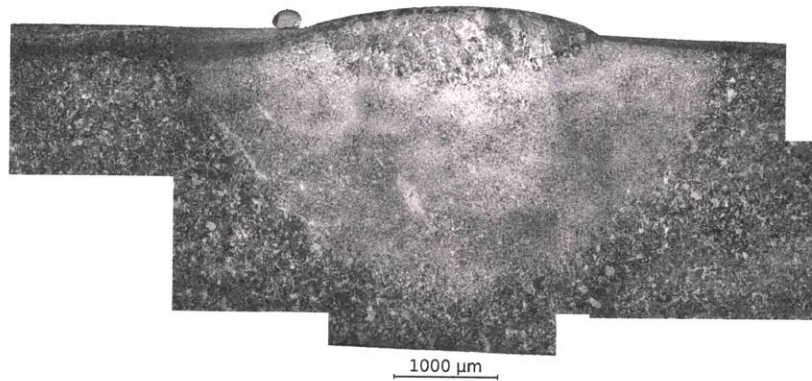
### **4.5 Auxiliary Studies**

Here data will be presented from small experiments that shed additional insight on the major tests performed in this study. These data either demonstrate the effects and characteristics of parts of individual processing tests, or further demonstrate how the composite would perform in scenarios more likely to be found in the field than in the laboratory.

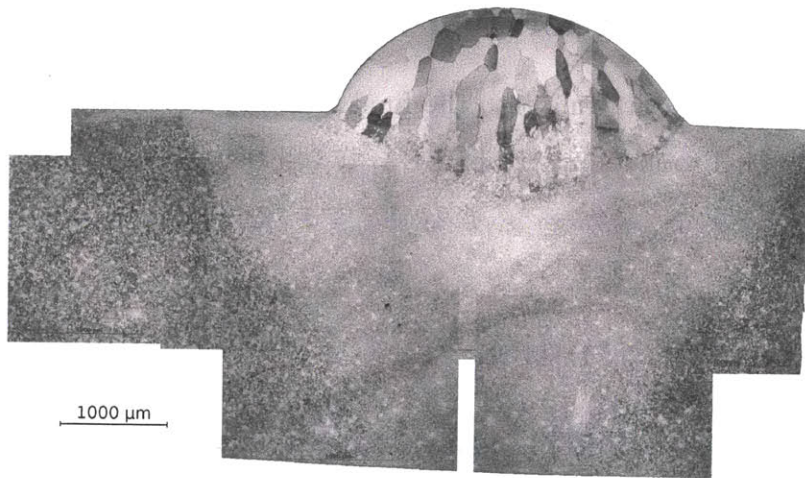
#### **4.5.1 Initial Welding Study**

##### **4.5.1.1 Optical Microscopy**

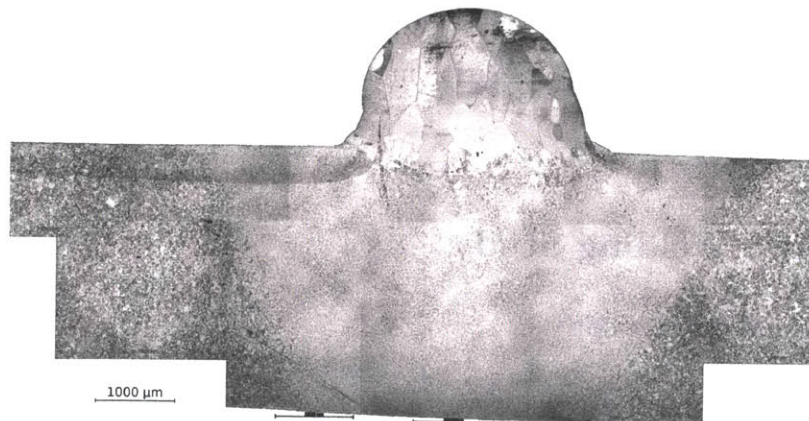
A number of optical micrographs were taken from cross sections of each weld test specimen mentioned in Section 3.5.1. These were stitched together to form a photo montage that shows all important characteristics of each weld at once. These montages are shown in Figure 4-41. Transverse sectional images were also taken, but these are not shown because they did not differ noticeably from the cross sections. The one-pass sample shows nearly complete mixing in the weld, as this entire layer



(a) One pass



(b) Two passes



(c) Three passes

Figure 4-41: Optical micrograph montages of initial TIG-welded specimens. Individual photographs were taken at 50 $\times$ . No post-processing was performed on any images except for stitching them together. Note that only the first pass undergoes significant mixing in all three samples. Each sample has a HAZ that is 1.5 mm thick. This shows what an F91 weld would look like without applying the proper post weld heat treatment.

would have been melted along with some F91 beneath. This caused the weld layer, formerly devoid of carbon, to become enriched and form more carbides, bainite and even martensite upon fast cooling. The two-pass sample shows a mixing layer beneath a layer of large, columnar grains of Fe-12Cr-2Si. This indicates that the columnar region is still lacking in carbon, indicating that the second pass diluted the mixing zone of the first pass. Also note that the mixing zone is now beneath the base metal surface, where in the one-pass sample it was above. In the three-pass sample, this mixing zone does not shrink or move compared to the two-pass sample, indicating that significant melting and mixing only occurs to a depth of one layer, or 1 - 2 mm. In all three samples, the weld bead can be seen to increase in height by this distance. This increase in thickness would be expected to increase during the actual weld-overlaying procedure, as material will build up from adjacent beads as well as the weld wire deposition technique, which usually involves welding in a small zig-zag pattern to deposit more thickness per pass.

## **4.5.2 Commercially Certified FGC Welding Study**

Complete documentation of the entire weld, including any heat affected zones, is necessary to properly characterize the quality and success of the weld. Optical image montages of the entire weld zone for each product form will be given here along with comprehensive 2D Vickers hardness maps for the purposes of correlating hardness with observed microstructure.

### **4.5.2.1 Optical Microscopy**

Images of the as-extruded tubes before any welding procedures took place are shown in Figure 4-40 for reference. The ID-clad sample exhibited a very sharp interface, a typical martensitic F91 microstructure and very cubic grains of Fe-12Cr-2Si, which were slightly smaller than in previous forms due to a lack of annealing after extrusion. The OD-clad sample exhibited much of the same with the addition of an interfacial layer with stretched-out grains of Fe-12Cr-2Si.

Montages of the welds are shown in Figures 4-42 and 4-43. In the ID-clad weld, the Brinell hardness indent was made by the welding shop for internal quality control. More detailed Vickers hardness maps will serve that function in this study. In both sections of the weld, grains can be seen to grow in the direction of heat conduction away from the weld, especially near the weld-base metal boundary. The grain size in these zones gets smaller and smaller with proximity to the base metal, but not so much so that a smooth grain size gradient is observed. It is of particular interest that the ID-clad Fe-12Cr-2Si weld region did not uniformly solidify into large, columnar grains as it did in Section 4.5.1.1. The best explanation for this fact is that the Fe-12Cr-2Si weld layer was deposited first, with many passes of F91 weld wire deposited directly on top. This would have caused the Fe-12Cr-2Si layer to be at a very high temperature during nearly the entire welding process. Being held at a higher temperature accelerates diffusion processes greatly, especially carbon, as it is an interstitial impurity. The prolonged time at high temperature would have allowed plenty of carbon to diffuse in from the F91 melted zone above as well as the surrounding base metal. This would increase the carbon content to the point that martensite and bainite were stable, precluding the formation of large grains of Fe-12Cr-2Si present with less carbon. No HAZ was observed, which would have been marked by a region of smaller, more uniform grains directly adjacent to the weld. The grain size distribution of both F91 and Fe-12Cr-2Si next to the weld is very similar to that of the base material far from the weld.

In the OD-clad weld, the Fe-12Cr-2Si weld region exhibits large, columnar grains growing in the direction of heat conduction out of the weld. However, part of the Fe-12Cr-2Si weld region close to the F91 weld region looks more like the entire Fe-12Cr-2Si weld region in the ID-clad sample. Otherwise microstructural features are very similar. The F91 weld zone shows a mixture of martensite and bainite (stained darker). There is no HAZ observed. This is most easily determined by looking at the grain size in both layers of base metal close to the weld. The grain size close to the weld is similar to that far from the weld, indicating that a proper post-weld heat treatment took place. The most likely reason that this sample's Fe-12Cr-2Si weld

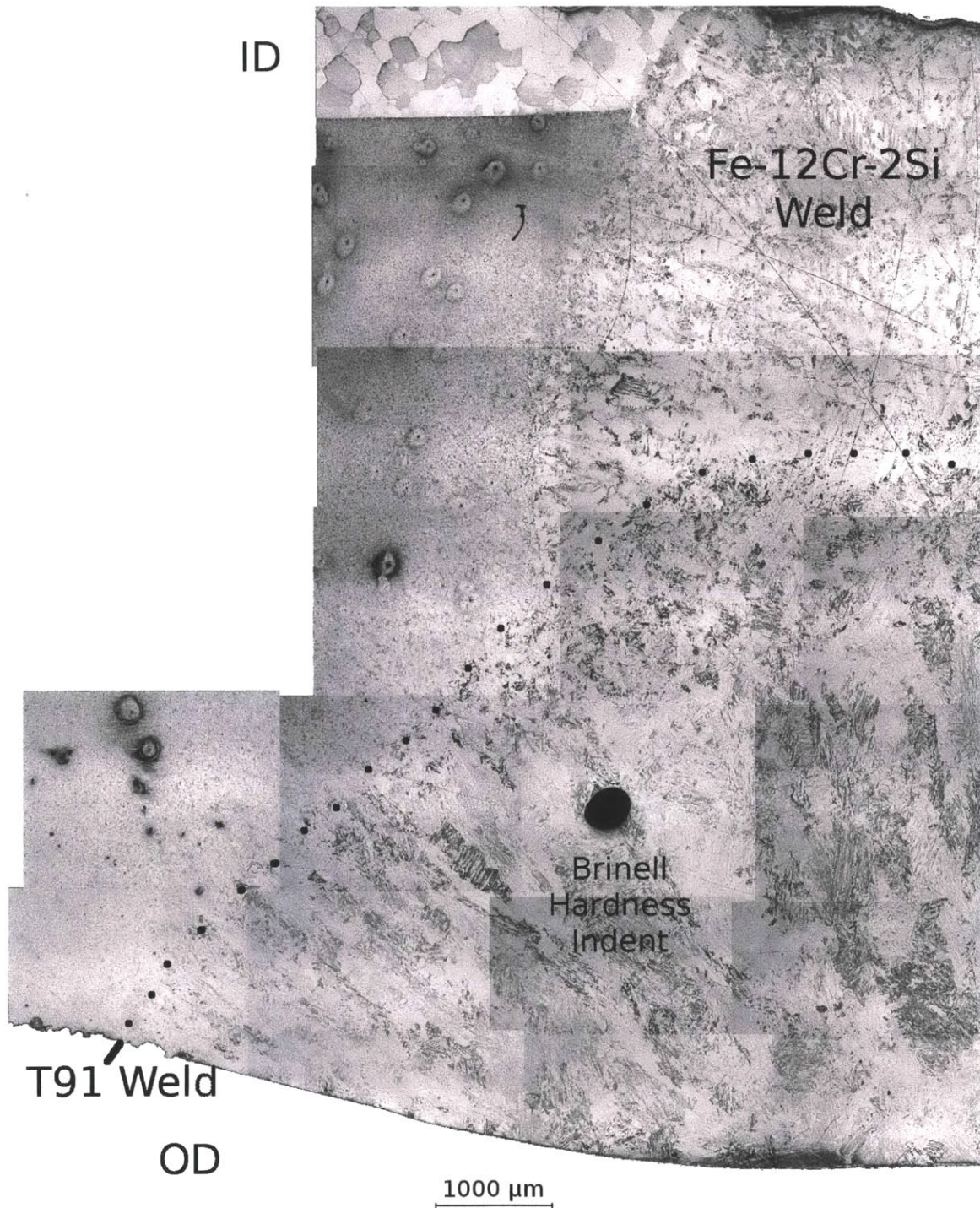


Figure 4-42: Photo montage of the ASME-certified ID-clad weld, made by grinding a double bevel, filling the weld to 2.5 mm (0.1") with Fe-12Cr-2Si and finally backfilling the weld with F91 weld wire. The boundary between the two welds has been delineated with black dots. Note the lack of any appreciable HAZ, showing that the proper quench and tempering heat treatment for F91 was performed. Individual images were taken at 50 $\times$ .

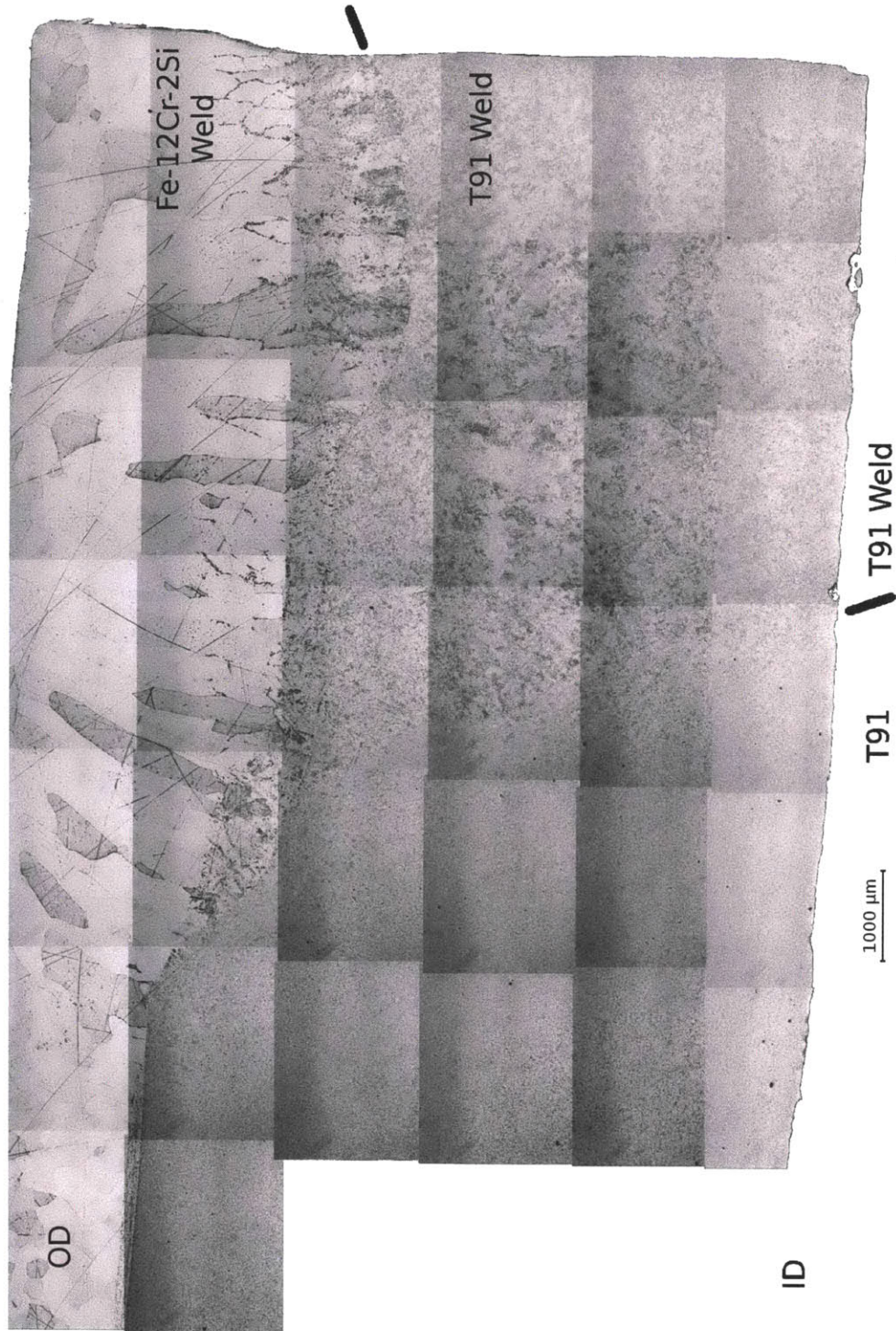


Figure 4-43: Photo montage of the ASME-certified OD-clad weld, made by grinding a double bevel, filling the weld to 7 mm (0.275") with F91 weld wire and finally back-filling the weld with Fe-12Cr-2Si. Note the lack of any appreciable HAZ, showing that the proper quench and tempering heat treatment for F91 was performed. Individual images were taken at 50 $\times$ .

zone is far more ferritic in nature is that it was welded last, so it spent comparatively little time at a high enough temperature for accelerated carbon diffusion to take place. This lower amount of carbon kept the stable phase as ferrite, so the microstructure upon cooling would be large, columnar grains of Fe-12Cr-2Si with finely interspersed carbides throughout, rather than martensite or bainite.

#### **4.5.2.2 Microhardness Profiles**

An extensive microhardness study was performed with the aim of matching regions of varying hardness with corresponding changes in microstructure. A grid of over 2,000 indents was acquired, mapped showing increasing hardness with redder colors, and superimposed on the optical montage of the ID-clad weld. This image is shown in Figure 4-44. The Brinell hardness indent was used as an anchor point to align the hardness indentations with the optical montage. The F91 weld zone is clearly visible as a region of higher hardness in the lower right quadrant of the image. In addition, zones of higher amounts of bainite and carbides (darker regions) correspond directly to regions of higher hardness in this zone. The Fe-12Cr-2Si weld zone is visible above the F91 weld as a softer, blue-purple region. To the left is the original composite material, which is harder than the optimal range for quenched and tempered F91 (180 - 220 HV) [143, 144]. This is likely due to the post-weld heat treatment applied to this part, specifically to the tempering time. Tempering the weld for longer times will remove the HAZ next to the weld, as well as soften the weld itself. This can prevent Type IV cracking from occurring, which has been a growing problem when using F91 weldments [139, 138].

### **4.5.3 Composite Breach Corrosion Study**

#### **4.5.3.1 Optical Microscopy**

Optical micrographs of each product form after exposure to 700°C LBE for 98 hours with a simulated cladding breach are shown in Figure 4-45. In all cases, there is no evidence of preferential LBE attack at the interface between the two metals. This

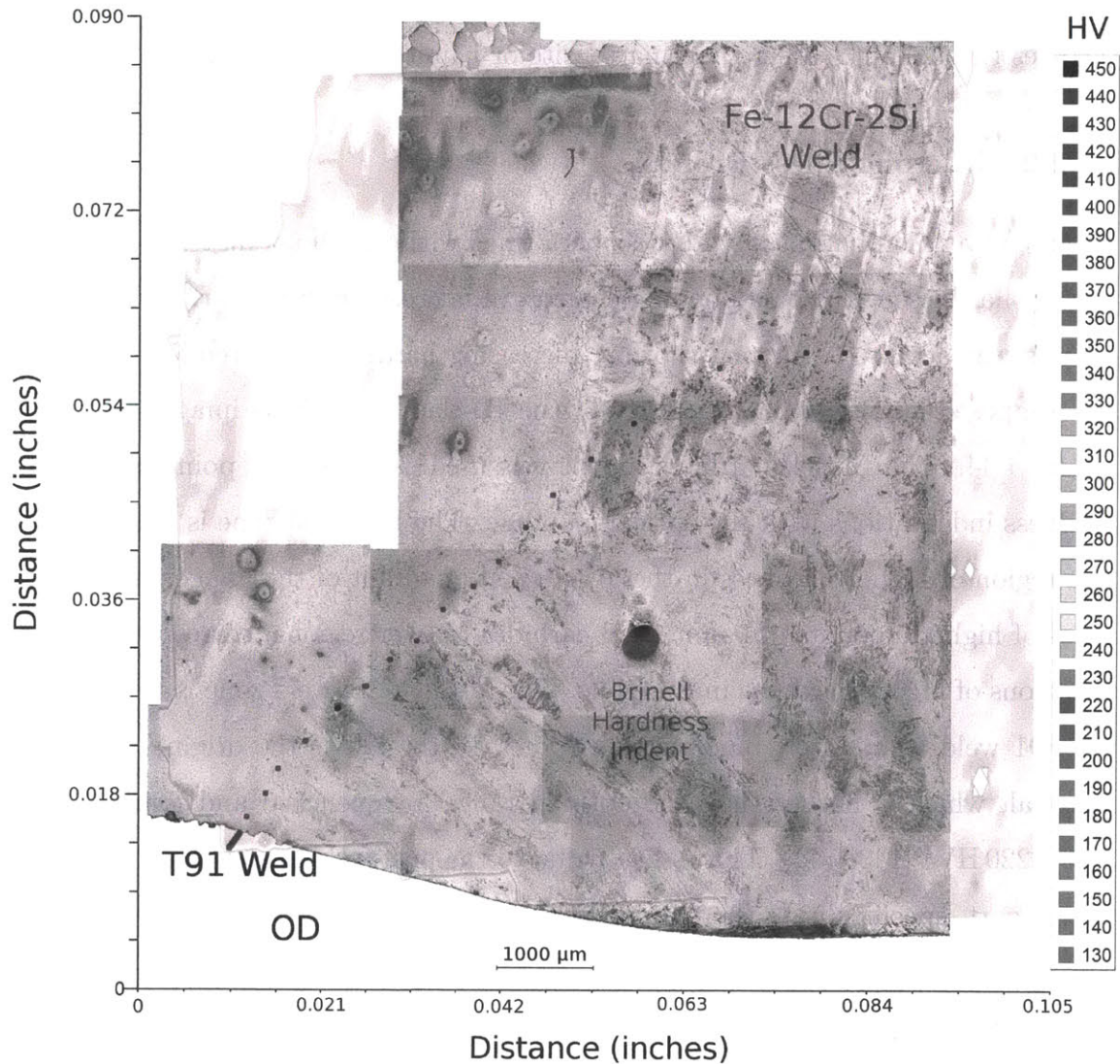
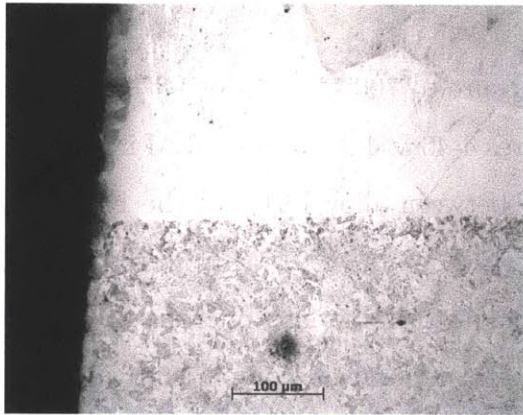
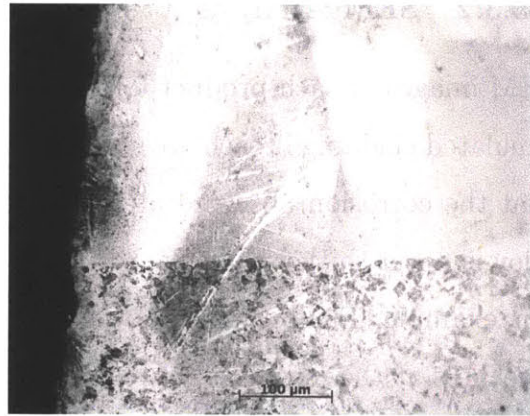


Figure 4-44: Superposition of the ID-clad optical montage with a 2-D Vickers hardness map of its surface. Regions of differing microstructure correspond directly to changes in hardness. The hardest area is the F91 weld, which approaches 400 HV at some locations. The Fe-12Cr-2Si portion of the weld is softer than the surrounding microstructure, due to a lack of carbon in that weld wire. There is a mild HAZ extending 2.5 mm (0.1") from the weld boundary. This will likely disappear after further tempering according to the proper PWHT for F91.

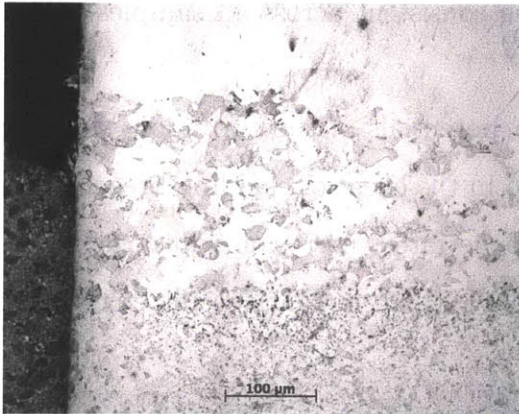




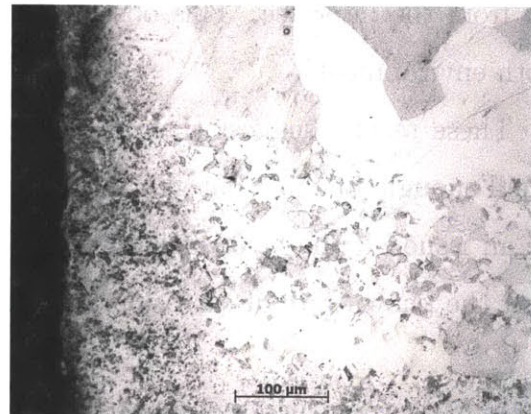
(a) ID-clad FGC exposed to reducing LBE



(b) ID-clad FGC exposed to oxidizing LBE



(c) OD-clad FGC exposed to reducing LBE



(d) OD-clad FGC exposed to oxidizing LBE

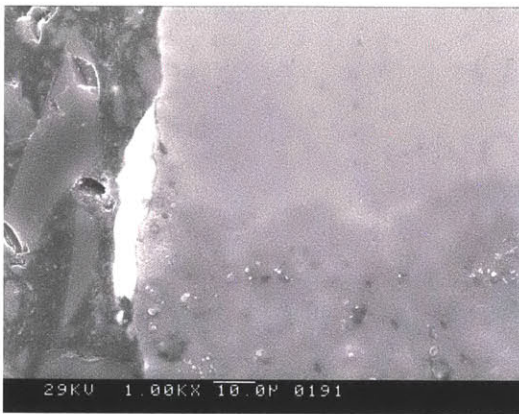
Figure 4-45: Optical micrographs of ID and OD-clad as-extruded composite forms after exposure to 700°C LBE for 98 hours, 200×. In all cases, no preferential LBE attack sites were noted at the interface between the two metals. This suggests that galvanic corrosion will not be an issue should the cladding be completely breached in an accident.

suggests that their corrosion potentials are very close, such that there is no concern of galvanic corrosion occurring in the event of cladding breach. The underlying F91 will still be subject to faster attack than the Fe-12Cr-2Si alloy, but not at levels accelerated beyond normal corrosion of F91 in LBE.

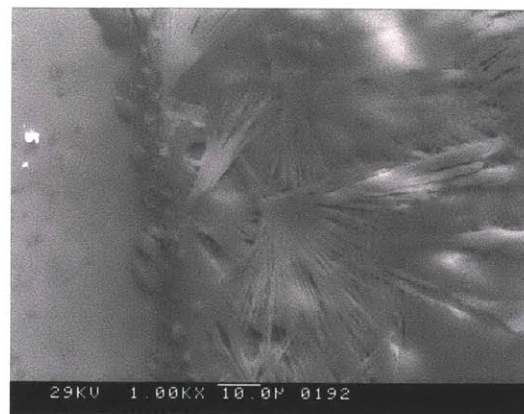
#### **4.5.3.2 SEM Analysis**

SEM images of each product form after exposure to 700°C LBE for 98 hours with a simulated cladding breach are shown in Figures 4-46 & 4-47. These SEM images show that the corrosion observed at the interface between alloy F91 and the Fe-12Cr-2Si alloy is never thicker than the corrosion observed on alloy F91 far from the interface. For example, Figure 4-46c shows what appears to be twenty microns of corrosion thickness at the interface between the two metals. However, comparison with Figure 4-46d shows that this corrosion thickness is observed on alloy F91 on the same sample, far from the interface. This observation was consistent across all samples tested in both environments.

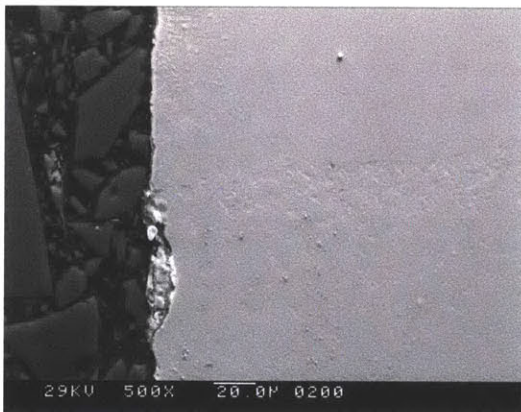
These results suggest that the corrosion potentials of the two alloys differ by a small enough amount that galvanic corrosion in the event of cladding breach will not be an issue. If the layer of Fe-12Cr-2Si is penetrated, corrosion will continue at or near the known rate of corrosion for alloy F91 by LBE in that specific environment.



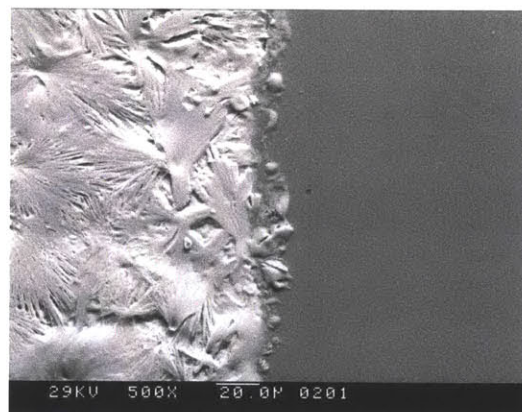
(a) ID-clad FGC exposed to reducing LBE at the bimetal interface, 1,000 $\times$ . The interface is visible in the middle of the metal, with LBE adhered to its surface.



(b) ID-clad FGC exposed to reducing LBE far from the interface on the F91 side, 1,000 $\times$ . Crystals of LBE have solidified on the surface of alloy F91, growing radially from nucleation points.



(c) ID-clad FGC exposed to oxidizing LBE at the bimetal interface, 500 $\times$ . The interface is clearly visible as the line where the small grains of F91 end (bottom half), and the smoother surface of Fe-12Cr-2Si begins (top half). Fifteen microns of corrosion thickness is visible in alloy F91.

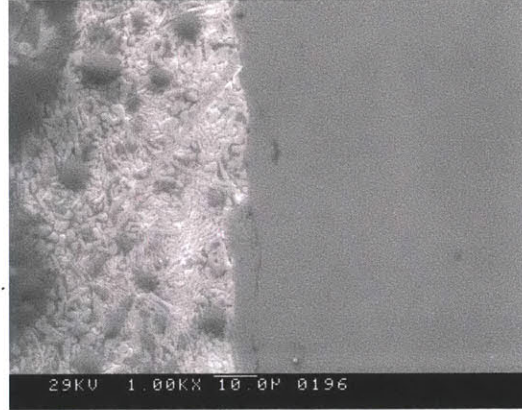


(d) ID-clad FGC exposed to oxidizing LBE far from the interface on the F91 side, 500 $\times$ . The same 15 - 20  $\mu\text{m}$  LBE penetration is observed far from the interface in this sample as in (c).

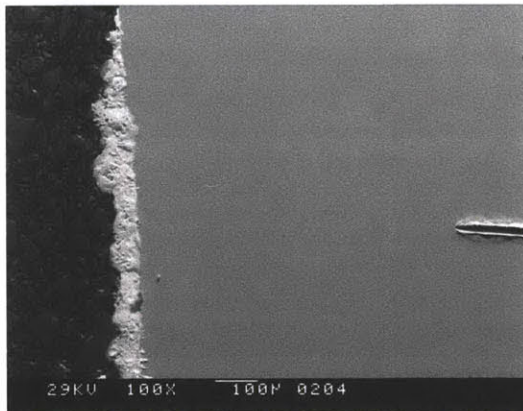
Figure 4-46: SEM images of the ID-clad as-extruded composite after exposure to 700°C LBE for 98 hours. In all cases, no preferential LBE attack sites were noted at the interface between the two metals. This suggests that galvanic corrosion will not be an issue should the cladding be completely breached in an accident. The corrosion thickness noted at the interface between alloy F91 and the Fe-12Cr-2Si alloy is very similar to that of alloy F91 far from the bimetal interface.



(a) OD-clad FGC exposed to reducing LBE at the bimetal interface, 100 $\times$ . Ferritic grains of Fe-12Cr-2Si are visible on the upper right of the figure. Their termination near the scratch on the right marks the interface.



(b) OD-clad FGC exposed to reducing LBE far from the interface on the F91 side, 1,000 $\times$ . LBE has penetrated up to 10  $\mu\text{m}$  into alloy F91.



(c) OD-clad FGC exposed to oxidizing LBE at the bimetal interface, 100 $\times$ . The bimetal interface is visible as a line of differing brightness 200  $\mu\text{m}$  above the scratch mark.



(d) OD-clad FGC exposed to oxidizing LBE far from the interface on the F91 side, 500 $\times$ . LBE has penetrated 20  $\mu\text{m}$  into alloy F91.

Figure 4-47: SEM images of the OD-clad as-extruded composite after exposure to 700°C LBE for 98 hours. In all cases, no preferential LBE attack sites were noted at the interface between the two metals. This suggests that galvanic corrosion will not be an issue should the cladding be completely breached in an accident. The corrosion thickness noted at the interface between alloy F91 and the Fe-12Cr-2Si alloy is very similar to that of alloy F91 far from the bimetal interface.

# Chapter 5

## Discussion

The results of this study show that the FGC developed is immensely successful at increasing the potential feasibility and efficiency of lead- and LBE-cooled reactors and systems. This is due to the following measures of success, which will be thoroughly discussed in this chapter:

- The FGC protects against LBE corrosion in all expected environments so well, that corrosion is no longer a concern for lead- or LBE-cooled systems that use it. Extrapolated corrosion rates based on the experiments in this study are less than  $1 \frac{\mu\text{m}}{\text{yr}}$ , which is negligible in terms of reactor design, even assuming a 60 year reactor lifetime. The corrosion mechanisms, growth rates and oxides present differ significantly from the existing body of literature for comparable Fe-Cr-Si alloys.
- The FGC is diffusionally stable. The diffusional dilution zone will not exceed  $17 \mu\text{m}$  for fuel cladding (three year life) or  $33 \mu\text{m}$  for coolant piping (sixty year life), both assumed to operate at  $700^\circ\text{C}$ . These numbers decrease with decreasing temperature.
- The FGC can be manufactured in the U.S. on a commercial scale today. Each manufacturing step was performed domestically with great success. This demonstrates the potential for immediate deployment should the demand arise.

- The FGC can be welded according to ASME code using existing procedures and standards. Welding according to existing procedures coupled with the prescribed quench-and-temper heat treatment for alloy F91 produces a sound weld with little to no heat affected zone (HAZ). Any remaining HAZ can be removed by further tempering, eliminating the possibility for Type IV cracking on a properly heat treated part.
- Because of the performance gains above, the FGC represents an enabling technology for lead- and LBE-cooled reactors and systems. A temperature increase of up to 150°C is possible, provided that suitable structural materials exist. This allows reactor designers to increase the power density and/or increase the output of their reactors, as well as to build in larger safety margins in case of an accident.
- This FGC is ready for immediate deployment in non-irradiated or low-dose applications. The corrosion resistance has been demonstrated, and will be verified pending longer length experiments. However, based on the materials choices made, there is no reason to believe that these experiments will not be successful. New ASME codes do not have to be developed, as joining this FGC falls within existing ASME certified welding procedures. Further work is required to investigate the properties of the FGC under irradiation, especially at temperatures below 450°C where mechanical properties can be adversely affected by fast neutron irradiation [16].

## 5.1 Corrosion Resistance of the FGC

The FGC promises to be extremely corrosion resistant in liquid lead or in LBE. The corrosion rate is so small that the old coolant temperature limitation of 550°C due to corrosion concerns is no longer valid. Corrosion rates in the Fe-12Cr-2Si layer are less than  $1 \frac{\mu\text{m}}{\text{yr}}$ , which is negligible in terms of reactor design, even assuming a 60 year reactor lifetime. The corrosion rates for the F91 layer follow a fractional power law,

and can easily be found as functions of time and temperature. A lack of depletion layers underneath very thin oxides in Fe-12Cr-2Si ensures that should the passivating layer be breached, enough chromium and silicon will be present to reform the layer. Any localized depletion will quickly be alleviated by diffusion from the rest of the metal, which proceeds very quickly at high temperatures and such small (hundreds of nanometers) depletion layers. If the cladding layer is breached entirely, corrosion in alloy F91 is highly predictable as a function of time and temperature. Finally, galvanic corrosion at the interface is not an issue, as a corrosion tests of the as-extruded composite showed no preferential attack at the exposed material interface. Therefore the composite as a whole is highly corrosion resistant.

### **5.1.1 Performance of the Fe-12Cr-2Si Cladding Layer**

As shown in Figures 4-9 & 4-4, the thickness of the corrosion layer is not visible even in optical micrographs at  $200\times$ . The surface of the metal appears to remain unchanged before and after the tests. SIMS analysis (see Section 4.2.2.4) has shown that the oxides present do not exceed a thickness of 250 nm, which is smaller than all wavelengths of visible light. Therefore, optical microscopy cannot detect the oxides present. Even an oxide layer several hundred nanometers thick acts as an excellent diffusion barrier against oxygen ingress or metal dissolution. This is because the diffusion coefficients are orders of magnitude lower in oxides than in metals, and are especially low for  $\text{Cr}_2\text{O}_3$  and  $\text{SiO}_2$  as shown in Figure 2-3. Oxygen potentials too low to form magnetite do result in the formation of chromium and silicon oxides on the surface. This ensures that the metal stays protected at all oxygen potentials that would be encountered in a reactor.

The corrosion rates, mechanisms and oxides present differ significantly from comparable alloys, such as EP-823 as discussed in Section 2.3.2. Existing similar Fe-Cr-Si alloys (such as EP-823, Fe-12Cr-1.8Si-NbWV) exhibit square root growth laws, indicative of continued diffusional growth of the oxides through the existing oxide layer [14]. By contrast, Fe-12Cr-2Si is marked by the dissolution of the iron-rich oxides in high-temperature LBE, resulting in a much thinner, less porous and more protective

oxide scale. The main difference between Fe-12Cr-2Si and EP-823 (aside from minor deviations in composition) is the crystal structure. EP-823 and other Russian Fe-Cr-Si alloys developed for service in LBE are martensitic, while Fe-12Cr-2Si is ferritic. Martensite is a highly stressed phase of iron carbide. Metals under a high internal stress state have been shown to corrode faster, because it takes less energy for oxidation to occur on a high-energy stressed surface [150, 151]. This is because stressed areas act as nucleation sites for corrosion to begin more easily [150]. This indicates that the choice of ferrite as opposed to martensite for the cladding layer could be a large factor in its superior corrosion resistance.

The poor corrosion resistance of martensitic alloys similar to Fe-12Cr-2Si highlights the need for a composite material, rather than a single alloy. An alloy that resists creep and deformation better will be inherently less corrosion-resistant in LBE, because the properties of a creep-resistant, strong steel imply a large number of nucleation sites for corrosion to begin.

The results from these experiments are verifications of short-term behavior, and are also indications of expected long-term behavior. Longer length experiments, ranging from 1,000 to 50,000 hours, must be undertaken at a range of oxygen potentials and temperatures in order to verify the intermediate and long-term behavior of the corrosion resistance of Fe-12Cr-2Si. However, there is no reason to believe that the long-term behavior will not be very good, based on the fact that the corrosion thickness reaches an equilibrium level after short-term (up to 500 hour) experiments.

#### **5.1.1.1 Oxidizing Environments**

Fe-12Cr-2Si protects itself extremely well against corrosion in oxidizing environments. Optical micrographs show that any interaction layer present is too small to be detected using visible wavelengths of light. SEM images show that a layer hundreds of nanometers thick is formed, which was confirmed by SIMS depth profiles. This layer is enriched in chromium and silicon, as any iron oxides that form would be wüstite, which is nonstructural and unstable in LBE. Iron would quickly become depleted, leaving nothing but chromia and silica. This evolution of oxides has been



confirmed by XPS measurements, which show that iron oxides are present after aging for 70 hours, but disappear after aging for 506 hours. These iron oxides give way completely to  $\text{Cr}_2\text{O}_3$  and  $\text{SiO}_2$ . Any iron-chrome spinel oxides present after 70 hours exposure either dissolved or were reduced to pure  $\text{Cr}_2\text{O}_3$ . Charging from the XPS measurements also indicated that the metal surface is covered in less conductive oxides, rather than bare metal, showing that these oxides adhered to the metal surface. The absence of LBE adhered to the sample surface as seen in the SEM shows that an oxide is indeed present. LBE adheres well to exposed metal, but not to an oxide layer.

Careful analysis of the SIMS concentration profiles shows coexisting peaks for chromium and oxygen closest to the surface of the metal, followed by a smaller peak for silicon. This behavior was found in all samples exposed to oxidizing LBE or cover gases except for the 245 hour,  $700^\circ\text{C}$  aged sample. The extremely small oxide thickness also indicates that the spot analyzed on this sample by SIMS could be an outlier, and should not be counted towards the overall trend. This is due to the variability in the thickness of the oxide, and the fact that there was only enough time to analyze one spot per sample.

The presence of chromium peaks together with oxygen enrichment and severe iron depletion on the 506 hour,  $700^\circ\text{C}$  aged sample suggests that a thin film of  $\text{Cr}_2\text{O}_3$  or  $\text{FeCr}_2\text{O}_4$  evolved over time. This is consistent with XPS analysis, which strongly suggested the presence of both  $\text{Cr}_2\text{O}_3$  and  $\text{FeCr}_2\text{O}_4$  on the surface of the same sample. The sample aged for 504 hours at  $600^\circ\text{C}$  behaved in a very similar way. This layer of chromium-rich oxide evolved from a layer of more iron-rich oxides, as could be seen in the  $700^\circ\text{C}$  sample aged for 70 hours. On this sample, iron and silicon were found to be enriched at the surface with a corresponding drop in chromium concentration. This is due to a much higher solubility of chromium in  $700^\circ\text{C}$  LBE (43 ppm wt. [94]) as compared to iron (32 ppm wt. [94]) and silicon (7 ppm wt. [95]), as was discussed in Section 2.1.1.2.

The evolution of the interaction layer in oxidizing environments therefore proceeds as follows. Upon initial exposure to the cover gas, a thin layer of iron oxide

immediately forms at the surface of the metal. This simulates what would happen in an actual LBE reactor very well, because an initial peak in oxidation will occur when the LBE is first heated. The surface of the lead and bismuth will oxidize in air, and this oxygen transient will cause the same behavior that was observed in the cover gas condition. Upon first exposure to LBE, some of the chromium dissolves, leaving a layer enriched in iron and silicon. These elements quickly oxidize. However, the phase transformation temperature between magnetite and wüstite is highly dependent on chromium content, as was shown in Figure 2-14. Iron oxides depleted in chromium will exist as wüstite. These will dissolve into the LBE, leaving a thin layer of silicon enrichment. Meanwhile, chromium diffuses towards the metal surface, where its high affinity for oxygen causes chromium-rich oxides to form. This layer of chromia or chromium-rich spinel oxide acts as a diffusion and dissolution barrier, preventing further oxygen ingress or metal dissolution. The oxygen that had already diffused into the base metal quickly interacts with silicon, which has the highest affinity for oxygen as shown in the Ellingham diagram in Figure 2-2. This only allows the formation of silica, as the oxygen potential at such low concentrations is too low for other compounds to form. Of all the oxides and metals present, silica acts as the strongest barrier to diffusion, as has been shown in the graphs of diffusion coefficients in Figure 2-3. Therefore, after the layers have stabilized after 500 hours at 600 or 700°C, further growth is severely inhibited by a thin, but powerful barrier to further interaction. EDX results of this layer show the existence of some iron and chromium in the oxide, but it is predominantly silicon-based.

Existing models for corrosion in LBE show some differing results. Models developed by Epstein [152] and He et al. [153] involve solving diffusion and mass transport equations to solve for the local corrosion rate in a non-isothermal LBE loop. Epstein's results show an equation as follows:

$$q = 0.023 \frac{D}{d} Re^{0.8} Sc^{0.4} \frac{dS}{dT} \Delta T \quad (5.1)$$

where  $q$  is the species flux for one element (which can be extended to the corrosion

rate),  $d$  is the diameter of the tube,  $D$  is the diffusion coefficient,  $Re$  is the Reynolds number (defined as  $\frac{vd}{\nu}$ , where  $v$  is the coolant velocity and  $\nu$  is the kinematic viscosity),  $Sc$  is the Schmidt number (defined as  $\frac{\nu}{D}$ ),  $\Delta T$  is the temperature difference across the loop and  $\frac{dS}{dT}$  is the change in solubility with temperature [152]. This corrosion rate is an average across the loop. By contrast, the results of He et al.'s model yield the following equation:

$$q = \frac{\partial c}{\partial y} = 0.608 \frac{D}{d} Re^{0.6} Sc^{\frac{1}{3}} \left( \frac{d}{L} \right)^{\frac{1}{3}} \sum_k c_k k^{\frac{1}{3}} e^{(2\pi i k \xi + i \frac{\pi}{6})} \quad (5.2)$$

where  $c$  is the concentration of species  $k$ ,  $x$  and  $y$  are coordinates in the axial and transverse directions, respectively,  $L$  is the length of the loop, and  $\xi$  is defined as  $\frac{x}{L}$  [153].

It should be noted that these models rely on a constant and significant mass flux through the system, with dissolution in the hot leg and precipitation in the cold leg. These models would be noticeably different for the FGC developed in this study. The presence of thin, dense oxide layers and enrichment zones that act as diffusion barriers would shift the dominant mode of corrosion from mass transport to others, such as erosion-corrosion from inclusions in the coolant or oxide layer spalling from differences in thermal expansion or high stresses.

### 5.1.1.2 Reducing Environments

In reducing LBE, Fe-12Cr-2Si still forms its superbly protective passivating oxide layer. SEM and EDX have confirmed the presence of an oxide layer on the surface of the metal, enriched in chromium and silicon, and depleted in iron. XPS spectra show the possible presence of both  $Cr_2O_3$  and  $SiO_2$ , along with metallic iron. The oxygen potential was far too low to form magnetite or other iron oxides. SIMS concentration profiles show enrichment zones of chromium and silicon at the surface, corresponding directly to the oxide layer observed in the SEM and in the XPS spectra. This proves that the film formed by Fe-12Cr-2Si is extremely stable, and that the metal will be able to remain passive even in extremely low oxygen environments, such as in crevices.

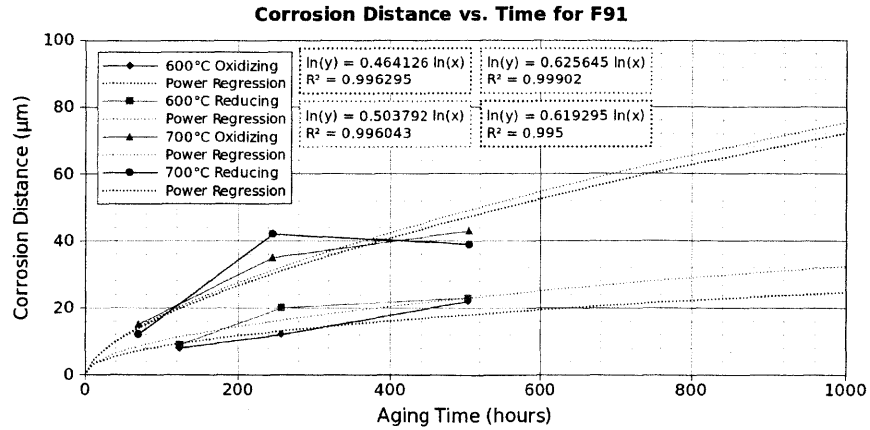


Figure 5-1: Corrosion distances for alloy F91 exposed to LBE at both temperatures and environments. The exponents show that corrosion of alloy F91 in LBE follows close to a standard  $\sqrt{t}$  law in a range of environments and temperatures. This behavior is typical of diffusion-limited corrosion processes.

### 5.1.2 Performance of the F91 Base Layer

Alloy F91's performance was more typical of a material that cannot adequately protect itself against internal oxidation or liquid metal attack. Corrosion distances and power law regression fits are shown for F91 at both temperatures in both environments in Figure 5-1. These curves generally followed close to a square root law typical of diffusion-limited corrosion processes [11]. Corrosion at 600°C took place more slowly than at 700°C, which was expected, as diffusion based corrosion follows an Arrhenius law based on Equation 5.3:

$$N = N_0 e^{\left[\frac{-E_A}{RT}\right]} \quad (5.3)$$

Here,  $E_A$  is the activation energy of the process (diffusion in this case),  $R$  is the universal gas constant, and  $T$  is the absolute temperature.

At 600°C, corrosion by liquid metal attack in the reducing environment took place faster than corrosion by oxidation in the oxidizing environment. This is because the oxide layers that formed, while not technically passivating, do provide a diffusion barrier to further oxygen ingress. The oxygen layers formed on the surface of alloy F91 consist mainly of magnetite ( $\text{Fe}_3\text{O}_4$ ) and iron-rich mixed spinel oxides, as has been shown in the literature [154]. It has also been shown in Table 2.1 that the diffusion coefficients of iron and oxygen in  $\text{Fe}_3\text{O}_4$  are three to four orders of magnitude

higher than their counterparts in  $\text{Cr}_2\text{O}_3$ . This means that while the oxide layers are somewhat protective, diffusion still allows enough oxygen to enter the base metal in order to continue the formation of an internal oxidation layer.

In the reducing environment with respect to the formation of  $\text{Fe}_3\text{O}_4$ , there is no barrier present to prevent LBE from dissolving the base metal. It has already been shown in Chapter 2 that steels need a minimum of 10 - 11 wt. % chromium to be self-passivating [11], and the specification for alloy F91 calls for a minimum of 8.50 wt. % and a maximum of 9.50 wt. % chromium [19]. This means that F91 contains too little chromium to form oxides that are rich enough in chromium to resist both diffusion and liquid metal attack. Consequently, as soon as LBE forms a small crevice or channel at a weak point in the metal surface, the oxygen potential drops drastically. This further precludes the formation of any oxides, allowing accelerated liquid metal attack to take place at those locations. This behavior was observed on the F91 samples exposed to 600°C LBE in the oxidizing environment. Figure 4-3 shows locations where LBE adhesion has formed localized sites of attack, which are seen to spread out as the aging time increases.

At 700°C, similar mechanisms cause corrosion to occur as in the samples exposed to 600°C LBE. Samples in the reducing condition at 700°C corroded twice as quickly as those at 600°C. This is well below the expected factor for Arrhenius rate processes, where every 10 - 15°C multiplies the corrosion rate by a factor of two. If corrosion in the reducing LBE followed an Arrhenius law, such as that in Equation 5.3, then the corrosion depth would have proceeded 60 - 500 times more quickly. The fact that it only proceeded twice as quickly suggests that the diffusion of soluble species away from the region of corrosion is the limiting process in liquid metal attack in the absence of a passivating layer. Liquid metal attack inside crevices or channels is limited by the dissolution rate into the LBE and the solubility of different elements in the LBE. In this case, iron and chromium, the two major alloying elements in F91, have very low solubilities in 700°C LBE (32 ppm and 43 ppm, respectively) as was shown in the phase diagrams and solubility curves in Chapter 2. Very small volumes of LBE are present in any given channel, so the liquid metal quickly reaches saturation

levels of the solute concentrations. The limiting step in the process once steady state has been reached is therefore diffusion of the solute atoms out of the channels. Even so, diffusion of iron and chromium in liquid LBE has been shown to be very fast (see Figure 2-3). EDX elemental maps also confirmed a layer of chromium depletion along with LBE penetration. This is expected, as the solubility of chromium in LBE is higher than that of iron.

Samples in the oxidizing environment undergo accelerated oxidation while protecting themselves from internal liquid metal attack. Those in the reducing environment are subject to accelerated liquid metal attack. As can be seen in Figure 5-1, oxidation proceeds three times faster at 700°C than at 600°C. Again, if this followed a purely Arrhenius law, oxidation would have happened 60 - 500 times faster with a 100°C difference in temperature. This means that the oxidation processes do not follow an Arrhenius law, and other processes (such as diffusion through the oxide layer) are likely the limiting processes in oxide growth.

As the oxide layers grow thicker they continue to act as better diffusion barriers, not because of a change in chemistry, but because of an increase in thickness. The oxides that form on F91 are not nearly as protective as those on true stainless steels (such as Fe-12Cr-2Si). Diffusion processes proceed more slowly in Fe<sub>3</sub>O<sub>4</sub> as compared to iron or to Fe-Cr alloys. Diffusion coefficients for metal atoms are a factor of 2 - 5 lower, while those for oxygen are four orders of magnitude lower. This is mainly due to a higher activation energy for diffusion in oxides, which are more tightly bound due to ionic bonding, than in covalently bonded metals. Finally, the highly accelerated corrosion observed in F91 at 700°C after 506 hours exposure to oxidizing LBE is due to an internal oxidation layer, which is not technically an oxide. In this layer, particles of oxide form amidst a matrix of base metal. This internal oxidation layer thus is subject to much faster diffusion than in Fe<sub>3</sub>O<sub>4</sub>, and corrosion is expected to continue at a rapid rate once the Fe<sub>3</sub>O<sub>4</sub> layer reaches a critical thickness. This internal oxidation layer is severely weakened compared to the base metal, and must be considered structurally unsound. Data at longer aging times is required to accurately understand how this phenomenon will progress and affect the long-term structural

integrity of F91.

### **5.1.3 Performance of the FGC in the Event of Total Cladding Breach**

As seen in Figure 4-45, there is no preferential attack at the interface for samples exposed to 700°C LBE for 98 hours in either environment. This shows that there is no concern that galvanic corrosion will take place during an accidental cladding breach, which is very good from a standpoint of safety. Should the cladding be breached, the remaining wall thickness will corrode at the well-understood rate of F91 corrosion in reducing LBE. This is because a cladding breach will create a thin region like a crevice, which will quickly consume any oxygen locally present in the LBE, precluding the formation of a passive film.

The underlying F91 will then be subject to dissolution and liquid metal attack at known corrosion rates, making the system highly predictable. A comparison of the LBE corrosion thicknesses and penetration depths from the FGC composite breach study (15 - 20  $\mu\text{m}$ , see Figure 4-46) with the equations fit to corrosion of bare alloy F91 in LBE (see Figure 5-1) shows that F91 in the FGC during a cladding breach corrodes at the same rate that would be expected for bare alloy F91. This shows that accelerated corrosion will not occur at the interface between the two metals. If the cladding is penetrated, the region of LBE ingress will rapidly form a channel of highly reducing LBE as oxygen is quickly consumed. The corrosion rate through the composite will then proceed at the rate for F91 in reducing LBE.

## **5.2 Diffusional Stability of the FGC**

The FGC is highly stable from a diffusion standpoint. Silicon is the only element that is a concern, because the average chromium concentration (10.5 wt. %, which is required for sufficient passivation) will always be found in the Fe-12Cr-2Si layer. The diffusion thickness that must be accounted for is well below the thickness of the

cladding layer.

## 5.2.1 Calculated Diffusion Coefficients

### 5.2.1.1 Silicon Diffusion in F91

In order to study the diffusion of silicon in F91 in the diffusion couples (see Figure 4-27 for an example photograph), a program was written in C in order to fit an error function to the complete data set. Experiments at 700°C and 750°C were used in this data set, as it has been shown that aging at 800°C exceeded the phase transformation temperature for alloy F91, as can be seen in the 1,220 hour aged diffusion couple in Figure 4-29. This code and an example input file is attached for reference in Appendix D. The data for silicon in F91 were assumed to follow a standard one dimensional error function:

$$c(x, t) = c_{avg} + \frac{\Delta c}{2} \operatorname{erf} \left[ \frac{x}{\sqrt{4\tilde{D}_{Si}t}} \right] \quad (5.4)$$

where  $c(x, t)$  is the concentration as a function of distance  $x$  and time  $t$ ,  $\Delta c$  is the difference between  $c_L$  (the silicon concentration in F91) and  $c_R$  (that in Fe-12Cr-2Si),  $c_{avg} = \frac{c_L + c_R}{2}$ ,  $\operatorname{erf}$  is the error function and  $\tilde{D}_{Si}$  is the diffusion coefficient for silicon in alloy F91[155].  $\tilde{D}_{Si}$  is an Arrhenius-based diffusion coefficient, and it is given by the following formula:

$$\tilde{D}_{Si} = D_0 e^{\left(\frac{-E_A}{RT}\right)} \left[ \frac{m^2}{sec} \right] \quad (5.5)$$

where  $D_0$  is the temperature-independent diffusion constant,  $E_A$  is the activation energy of the process in  $\frac{J}{mol}$ ,  $R$  is the universal gas constant ( $8.314 \frac{J}{mol-K}$  [156]), and  $T$  is the absolute temperature in Kelvin. The two parameters  $D_0$  and  $E_A$  uniquely identify diffusion of one solute in one crystal system of one alloy. In this case, the solute is silicon, and it diffuses through BCC F91.

A pseudocode flowchart explaining how the program works is shown in Figure 5-2. First, the user supplies the input file along with a range of independent diffusion parameters ( $D_0$ , the diffusion constant, and  $E_A$ , the activation energy). Next, “equivalent aging times” for the HIPing process (the control sample) are calculated



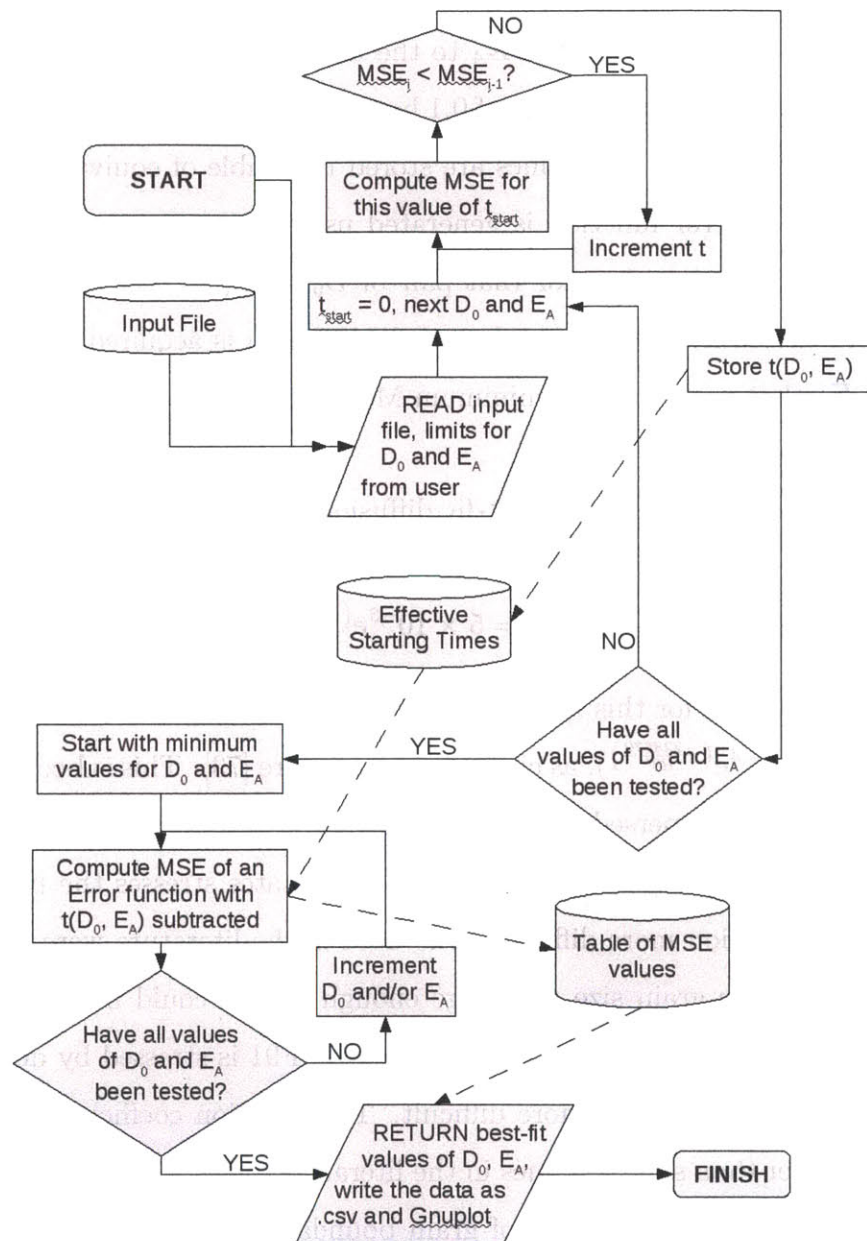


Figure 5-2: Flowchart explaining how the diffusion data fitting code works. First, the user supplies the input file along with a range of independent diffusion parameters ( $D_0$ , the diffusion constant, and  $E_A$ , the activation energy). Next “equivalent aging times” for the HIPing process (the control sample) are calculated using each pair of diffusion parameters,  $D_0$  and  $E_A$ . Next, an error function is generated using each parameter trio of  $D_0$ ,  $E_A$  and the equivalent aging time for that pair of  $D_0$  &  $E_A$ . These error functions are compared to the entire data set, and a total mean squared error (MSE) sum is acquired. Finally the pair of  $D_0$  and  $E_A$  that produced the minimum MSE sum is chosen as the best fit.

using each pair of diffusion parameters,  $D_0$  and  $E_A$ . This is done by fitting an error function using each pair of  $D_0$  and  $E_A$  to the unaged sample's concentration profile, stepping through time in increments of 0.1 hours until a minimum mean squared error (MSE) sum is reached. These values are stored in a table of equivalent aging times. Following this, an error function is generated using each parameter trio of  $D_0$ ,  $E_A$  and the equivalent aging time for that pair of  $D_0$  &  $E_A$ . These error functions are compared to the entire data set, and a total MSE sum is acquired. Finally the pair of  $D_0$  and  $E_A$  that produced the minimum MSE sum is chosen as the best fit.

This program found that the best-fit diffusion coefficient for silicon in BCC F91 is:

$$\tilde{D}_{Si\ in\ BCC\ F91} = 5 \times 10^{-3} e^{\left(\frac{-253969}{RT}\right)} \left[ \frac{m^2}{sec} \right] \quad (5.6)$$

The activation energy for this system is higher than that for silicon diffusion in pure BCC iron ( $1.7 \times 10^{-4} e^{\left(\frac{-228670}{RT}\right)}$ ), as cited in the literature [73]. This is because alloy F91 has numerous finely dispersed carbides and carbonitrides both inside the grains and on the grain boundaries [19]. Each of these precipitates stresses the matrix around them, making diffusion more difficult. The data in the literature were performed on pure ferrite, and the grain size was large enough that it could be approximated as single crystals. Any retained martensite present in F91 is stressed by definition, and diffusion through it would be more difficult. The diffusion coefficient is an order of magnitude higher than similar values in the literature for BCC ferrite materials. This is because F91 has a high amount of grain boundary volume, due to its very small grain size of 5 - 100  $\mu\text{m}$ . Diffusion at any temperature would therefore proceed with more fast diffusion paths than in single crystal ferrite.

The overall effect of the results of silicon diffusion in F91 shows that while more fast diffusion paths are present at all temperatures (accounting for the higher diffusion constant in F91 compared to in  $\alpha\text{-Fe}$ ), the lattice is more stressed by martensite and precipitates, requiring a higher temperature overall for diffusion to occur (accounting for the higher activation energy in F91 compared to in  $\alpha\text{-Fe}$ ).

### 5.2.1.2 Silicon Diffusion in Fe-12Cr-2Si

The calculation of a single silicon diffusion coefficient in Fe-12Cr-2Si is impossible, as the diffusion profiles in Figure 4-31 show. A solute with one diffusion coefficient means that it diffuses via only one mechanism. Instead, the silicon concentration profile appears to have both slow and fast components. It appears to be the sum of two error functions. It therefore requires a more complex function to fully define it, consisting of two or more diffusion coefficient. One diffusion coefficient would be required for each unique diffusion process.

A mathematical representation illustrates this point more succinctly. The diffusion of one solute through one solid solvent via one mechanism can be fully modeled by Fick's diffusion law:

$$J = D \frac{\partial c}{\partial x} \quad (5.7)$$

where  $J$  is the mass flux of solute  $i$ ,  $D$  is the diffusion coefficient and  $x$  is the distance along the sample [155]. By contrast, a solute whose diffusion coefficient is a function of temperature cannot always be solved mathematically:

$$J = \nabla \cdot [D(C)\nabla c] \quad (5.8)$$

where  $D(c)$  is the diffusion coefficient as a function of concentration. Adding more than one diffusing solute further complicates this scenario, as the interdiffusivity becomes a matrix with diagonal and cross terms [155]:

$$\begin{bmatrix} J_1 \\ J_2 \end{bmatrix} = -\underline{\tilde{D}}\nabla \begin{bmatrix} c_1 \\ c_2 \end{bmatrix}; \quad \underline{\tilde{D}} = \begin{bmatrix} \tilde{D}_{11} & \tilde{D}_{12} \\ \tilde{D}_{21} & \tilde{D}_{22} \end{bmatrix} \quad (5.9)$$

This is the representation for a three component system (two solutes) with diffusivities independent of concentration. Adding time dependence of the system and concentration dependence of the diffusion coefficients further complicates things, but

fully realizes the complexity of diffusion in the Fe-Cr-Si system [155]:

$$\frac{\partial}{\partial t} \begin{bmatrix} c_1 \\ c_2 \end{bmatrix} = \frac{\partial}{\partial x} \left\{ \begin{bmatrix} \tilde{D}_{11}(c_1, c_2) & \tilde{D}_{12}(c_1, c_2) \\ \tilde{D}_{21}(c_1, c_2) & \tilde{D}_{22}(c_1, c_2) \end{bmatrix} \frac{\partial}{\partial x} \begin{bmatrix} c_1 \\ c_2 \end{bmatrix} \right\} \quad (5.10)$$

These equations cannot be solved mathematically; they must be solved numerically given adequate data. However, it is known that the  $D_0$  of silicon in dilute Fe-Si alloys is linearly dependent on the silicon concentration [83].

Only a simulation that takes all of these factors into account can accurately describe the diffusion of silicon in this FGC. Because diffusion in F91 was observed to be so much slower than in Fe-12Cr-2Si, a single error function fits the data very well, as the Fe-12Cr-2Si acts as a silicon source to the F91 layer. No standard function fits the silicon concentration profile in Fe-12Cr-2Si. Advanced multiphase diffusion software was not available to the author during this study. Instead, a function describing the distance at which the silicon falls to a critical level of 1.25 wt. % was derived from the data. This function and its implications will be described in the next section.

## 5.2.2 Extrapolations to the End-of-Life for a Typical LBE-Cooled Reactor at 700°C

### 5.2.2.1 Diffusion Characteristics

Based on the data and diffusion coefficient calculated above, the only limiting element from a diffusional point of view is silicon. The data are best summarized by showing the distance at which silicon will drop to the previously mentioned minimum level of 1.25 wt. % in the interdiffusion zone of the composite. Figure 5-3 shows this graph, along with an logarithmic regression equation that allows for extrapolation to longer times. Data points from diffusion couples aged at 700°C and 750°C were scaled using an Arrhenius relation to equivalent aging times at 700°C in order to provide a single comparison. By using an activation energy of  $250,000 \frac{\text{J}}{\text{mol}}$  and  $R$  as given above in the Arrhenius equation (see Equation 5.3), a factor of 22.08 was applied to aging times at 750°C to scale them to equivalent aging times at 700°C.

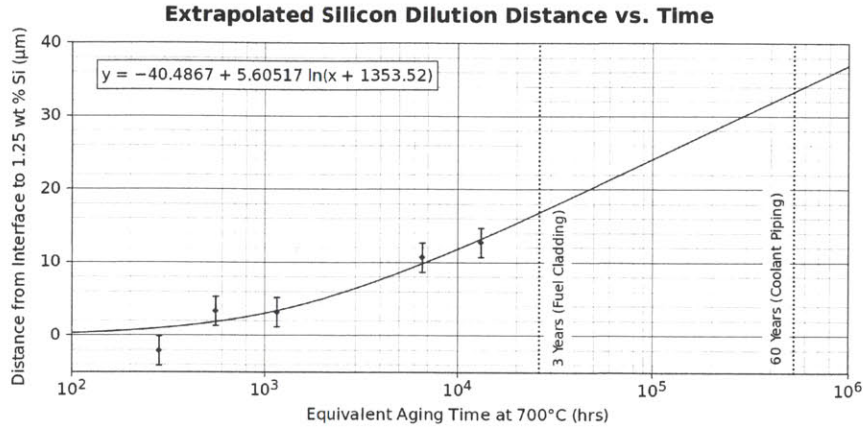


Figure 5-3: A log-linear curve fit to location of minimum silicon content during reactor operation at 700°C

Fuel cladding is expected to reside in the core at a temperature of up to 700°C for three years. Using the equation in Figure 5-3 yields a critical silicon dilution distance of 17 μm from the interface after three years. It would be wise to account for at least twice this distance when designing actual fuel cladding. Therefore, the cladding thickness for fuel cladding could be as thin as 34 μm and still have a two-fold margin of safety from a diffusional point of view. The FGC in this study used five times this distance. Coolant piping in the hottest section of the core could experience temperatures of 700°C for up to 60 years. Using the equation in Figure 5-3 gives a diffusional dilution distance of 33 μm after 60 years. This is negligible compared to the expected cladding thickness of 0.05 inches, or 1,270 μm. These numbers show that diffusion is no cause for concern in the coolant piping.

### 5.2.2.2 Corrosion Resistance

In order to maintain its corrosion resistance, passivating elements must remain at or above a minimum concentration level far from the metal surface. This ensures that if the metal must repassivate, which would cause localized depletion of chromium and silicon, sufficient reserves exist in the underlying base metal that can diffuse into the depletion zones and replace them. A conservative estimate would be that the cladding layer must retain its original levels of chromium and silicon at a distance of twenty times the thickness of the oxide layer, or 5 μm, from the surface of the cladding. The

proposed cladding layer thickness for the fuel cladding, which will see the highest temperatures, is 75  $\mu\text{m}$ . As found above, an extrapolation of diffusion for three years at 700°C would cause the silicon level to drop below 1.25 wt. % at a distance of 17  $\mu\text{m}$  from the F91-cladding interface. This leaves a thickness safety factor of 4.4, which leaves no concern for diffusional dilution of the FGC.

### **5.2.2.3 Physical Properties**

Diffusion is not expected to affect physical properties of the composite. In these diffusion couples, the hardnesses of each alloy equalized after only 300 hours of aging time due to the migration of carbon into the cladding layer (see Section 4.3.3). In the actual composite, the thickness of the cladding layer will be 10 to 20 times thinner than the F91 layer. Equalization of carbon content between the two layers will not decrease the carbon concentration in F91 by more than 10% of its original value. Silicon concentration will only convert up to 5  $\mu\text{m}$  of bainite in F91 to ferrite, which represents a structural thickness reduction of 0.6%. This is a negligible thickness compared to the thickness of the cladding layer.

### **5.2.2.4 Radiation Embrittlement and Radiation Induced Migration**

Radiation embrittlement is not expected to be an issue for the FGC. The F91 layer will not suffer from radiation effects, as radiation at high temperatures (above 450°C) causes no deviation in mechanical properties. This was shown in Section 2.3.1 [16, 15]. The cladding layer could be subject to radiation embrittlement via silicon segregation at grain boundaries and at dislocations, due to its high silicon content. However, two factors help to alleviate this effect: location and crystal structure. As already shown in Section 2.3.1, ferritic alloys undergo almost no radiation induced swelling as compared to austenitic alloys. In addition, the fuel cladding in the core is where the FGC will be exposed to the most radiation, and that is where the cladding layer is the thinnest. Where the cladding layer is thinner, less volume is susceptible to radiation embrittlement due to segregation to dislocations. Diffusion of silicon throughout the alloy will also alleviate some of this radiation induced segregation. The dose received

by the coolant piping outside the core will be far too low to cause significant radiation embrittlement, as can be seen in the low dose (<1 dpa) region of mechanical property curves in Klueh et al. [16].

The cladding layer is not expected to be structural in the FGC. While the corrosion-resistant layer may suffer some damage, it would not affect the structural integrity of the composite at all. This claim needs to be verified by future work, which would involve testing the material after irradiation with fast neutrons or protons at a range of temperatures.

## **5.3 Commercial Feasibility of Producing this FGC**

The key choice to be made was the overall composition of the corrosion resistant layer. This choice was made based on the results of previous research and engineering judgment on the author's part. This judgment has been confirmed at least for short time tests that need to be extended in a future effort. The composition of the alloy not only determined the corrosion resistance of the FGC, but the parameters, dimensions and success of each processing step, detailed below.

### **5.3.1 Feasibility of Each Processing Step**

Production of this FGC has been demonstrated to be commercially feasible using currently available methods. F91 has been a widely used alloy in the fossil fuel industry for the past twenty years and was readily available. The only difficulty in producing Fe-12Cr-2Si was the small quantity requested. A processing order of 273 kg (600 lb.) is far smaller than most facilities are willing to process. Once processing quantities are increased to 9,090 kg (20,000 lb.) or more, sourcing material will not be an issue.

The weld overlay process is a widely used process, employed in a number of situations in which a composite must possess the properties of two very different materials. Weld overlay is used to clad carbon steel reactor pressure vessels with stainless steel and to coat waterwall tubes in fossil fuel plants with a high chromium alloy. Find-

ing a vendor who was comfortable with this process was not difficult. Many weld overlay machines are limited in stroke length; therefore, the sizes of the extrusion billets were limited by this length of 61 cm (two feet). This length will be sufficient to produce commercial amounts of coolant piping and fuel cladding. One two-foot extrusion billet can produce over 1.2 m (40 feet) of finished coolant piping and over 0.8 km (0.5 miles) of finished fuel cladding. These are standard lengths that can be shipped and adapted to any further manufacturing process, such as extrusion. In addition, weld overlaying is the only cost-effective process that can deposit a sufficiently thick cladding layer on the insides of elbows, joints, valves, tubes of varying diameter, and other complex shapes. Using thinner weld wire (such as the 0.89 mm (35 mil) wire used in this project) allows for smaller ID bore welding, as the weld wire can bend through the GTAW torch more easily. The key choice here was to select the proper combination of materials for the composite such that weld compatibility could be maintained. The prospect of ensuring defect free welds influenced the upper boundary for the Cr and Si content.

Co-extrusion is also widely used throughout the nuclear and fossil power production industries. Zircaloy tubes are co-extruded with a liner of pure zirconium to produce fuel cladding, and have been for decades. Locating a vendor that has extruded alloy F91 was not difficult, as many fossil plants have required similar extrusions. The vendor was slightly apprehensive about extruding a clad billet with materials of vastly differing flow stresses. In reality, only the slightest bit of heat tearing took place, and only on the OD-clad billet. A decrease of 25 - 50°C in extrusion temperature should alleviate that problem in the next iteration. The key issue here was ensuring that a sound weld bond was maintained. This was assured by proper choice of composite materials.

Pilgering is used extensively, especially for further reducing the diameter of extruded tubes. The vendors used in this project have a long history of working together to reduce tubing, so each was familiar with the capabilities of the other. Because pilgering puts the entire composite under a hydrostatic, compressive stress, debonding or differing flow stresses do not make a difference in this step.



Cold drawing tubes of F91 has presented problems in the past. This could be due to a number of factors, the most likely of which are thermal history and percent cold work applied to each step. Annealing the clad tubes without quenching or tempering will lead to more success when tube drawing, as dislocations will flow much more easily when carbides are larger and fewer in number. Decreasing the amount of cold work in each step will decrease the probability of cracking. It will, however, increase the cost of this processing step.

### **5.3.2 Effects of Processing on the Performance of the FGC**

The weld overlay process lends itself very well to producing a well-bonded FGC. Much dilution occurs in the first pass, with a smaller amount occurring in the second pass. By the third pass, no more dilution takes place. The dilution that occurs is significant, as can be seen in Figures 4-37 & 4-38. This ensures that even after extrusion, which involves a reduction in thickness by a factor of eight, a thin layer of well-bonded, weld-diluted material exists. This would not occur during co-extrusion of a billet and a sleeve or liner, as the two metals start out separately, and are kept in place by compressive forces. Some diffusion bonding would take place, but the potential for debonding is much higher in co-extruded sleeves than in weld-overlaid material, provided a sound weld was made.

Pilgering helps to keep the bond intact, as radial compressive forces will not result in debonding at the interface. Maintaining this sound interface is crucial to the performance of the FGC, as fuel cladding could be subjected to radial outward pressures of 50 - 100 MPa due to buildup of fission gases. Differences in thermal expansion due to thermal cycling of the reactor also will put stress on the interface. The better the bond is, the less likely it is that debonding will occur.

### **5.3.3 Effects of Each Processing Step on the Next Step**

The weld overlay process ensures that co-extrusion will not separate the two layers as they are pushed through the mandrel and die at a tremendous force. The only way

that weld overlaying could negatively affect the next step is by hydrogen embrittlement. Performing a proper post weld heat treatment and maintaining a sufficiently high interpass temperature completely precludes this from happening.

The fact that co-extrusion is performed at such a high temperature ensures that pilgering goes more smoothly. The tubing arrives in the annealed state with a very sound interface, which makes subsequent deformation easier. After pilgering, a full anneal is required before tube drawing, as this last step is the riskiest of all due to the possibility of F91 cracking.

## 5.4 Reactor Performance Gains and Economic Implications of Using this FGC

The successful creation of the proposed FGC has significant impacts on the design of lead- and LBE-cooled reactors. *This FGC represents an enabling technology for lead- and LBE-cooled reactors*, relaxing previous limits in safety, temperature and flow rate that made the construction and operation of LBE-cooled reactors prohibitively expensive.

### 5.4.1 Performance Gains

The most obvious gain for LBE-cooled reactors as a result of using this FGC is an increased outlet temperature. Aside from increasing the thermodynamic efficiency of the cycle, a high outlet temperature of 650 - 700°C opens the door to vastly higher efficiencies for hydrogen production. A graph showing the efficiency gain of three common high-temperature hydrogen production processes is shown for reference in Figure 5-4 [23]. Increasing the outlet temperature to 700°C moves the efficiency of the HTSE process into an economically viable region, and it makes the Westinghouse and the sulfur-iodine processes possible.

A more subtle but far-reaching gain achieved by using this FGC is an increased coolant flow velocity. Previous designs were limited to 2 - 3  $\frac{\text{m}}{\text{sec}}$  due to coolant shear

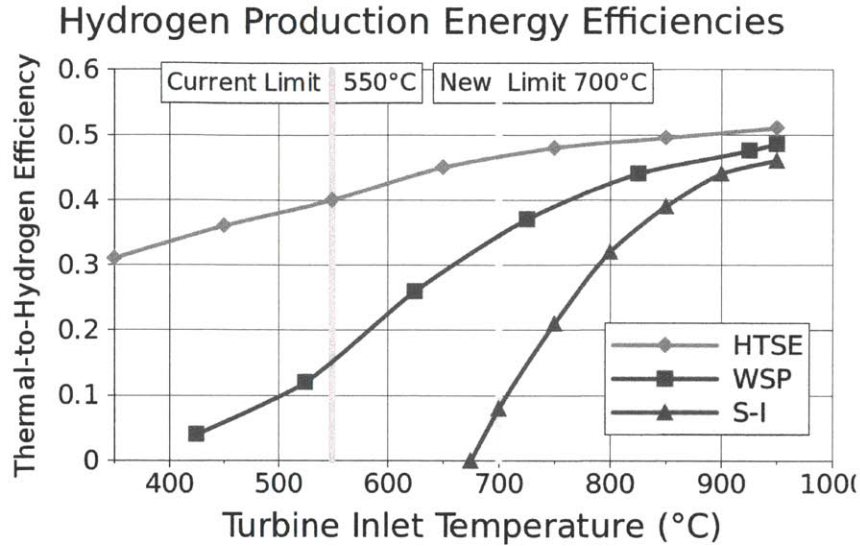


Figure 5-4: Hydrogen production process efficiencies, showing the increase in efficiency by using a higher outlet temperature [23]

force concerns and flow assisted corrosion (FAC). The presence of an extremely effective diffusion and dissolution barrier eliminates the concern for FAC. The strength of fully dense chromia and silica (as compared to more porous iron oxides or iron-chromium spinel oxides) resists shear deformation, adheres to the base metal more effectively and allows the coolant to flow at a higher speed. Given the same size core, increasing the flow velocity allows the pitch-to-diameter ratio of the fuel pins to be decreased, leading to a smaller core and therefore a higher power density. This translates directly into large cost savings in a reactor design.

Calculations were performed to show how moderate performance gains achieved by using this FGC would affect the performance of a typical LBE-cooled reactor. A 2,400 MWTh reactor design by Nikiforova et al. [24] was used as a baseline case. An improved case was compared to this baseline, where the outlet temperature was increased by 50°C to 650°C and the flow rate was tripled to  $6 \frac{m}{sec}$ . Figure 5-5 shows the results of this comparison. If the reactor designer wishes to maintain the same power level while shrinking the core, just increasing the outlet temperature shrinks the P/D ratio from 1.30 to 1.17. It can be further reduced to 1.08 by increasing the coolant flow to a modest  $3 \frac{m}{sec}$ . As of this writing, a larger vessel to accommodate

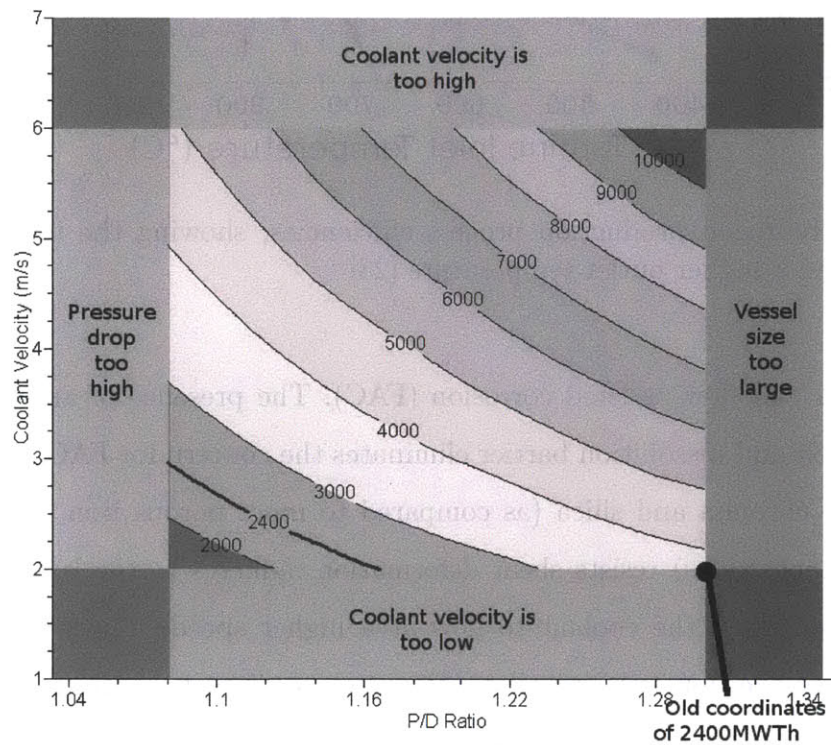


Figure 5-5: Power and P/D ratio performance gains by increasing the coolant flow velocity and outlet temperature, based on the design by Nikiforova et al. [24]. The baseline design point of 2,400 MWth is shown as compared to power contours for the new design. A P/D ratio of over 1.30 was deemed too large due to core size constraints, as the baseline design already filled all available space in the core.

more heat exchangers cannot be made, but with additional manufacturing capabilities more heat exchangers of the same power rating can be added to increase the power level. Increasing the coolant flow rate to  $6 \frac{\text{m}}{\text{sec}}$  and shrinking the P/D ratio to 1.08 yields a reactor with an output capability of 4,800 MWTh, or double the previous capacity. This does not take other considerations into account, such as the secondary side design or accident scenarios.

Such a high coolant velocity may not be achievable due to the increased pumping work necessary to force more coolant through a tighter core. Therefore, the designers of the baseline case placed a pumping work limit of 1,500 kPa on future designs based on current availability of liquid metal pumps [24]. In addition, a power limit of 6,000 MWTh was placed on future designs due to the limited capacity of the heat exchangers to remove heat from the primary coolant loop. Figure 5-6 summarizes the remaining operating regions for future LBE-cooled reactor designs as a result of these design restrictions. While some restrictions do exist, the operating window for LBE-cooled reactors has been dramatically increased from a single feasible point to a wide range of power levels and coolant velocities, adding much more flexibility to lead- or LBE-cooled reactor designs.

### 5.4.2 Economic Gains

The economic implications for these changes are enormous. Depending on which route is chosen by the reactor designer, significant reductions in cost are achieved by using this FGC. If the P/D ratio of the core decreases, the size of the core can become smaller with a higher power density. This both shrinks the reactor's size and its fuel inventory, reducing materials costs. If the designers decide to maintain the core's dimensions, a higher output temperature and higher coolant velocities allow a power increase of 50% to be achieved.

The elimination of flow assisted corrosion makes the reactor much more predictable from the standpoints of corrosion and safety. Material wastage becomes a non-issue, as radioactive crud will no longer build up in the cold leg. This eliminates the possibility of clogging the coolant lines due to dissolution and wastage from the hot leg. Fuel

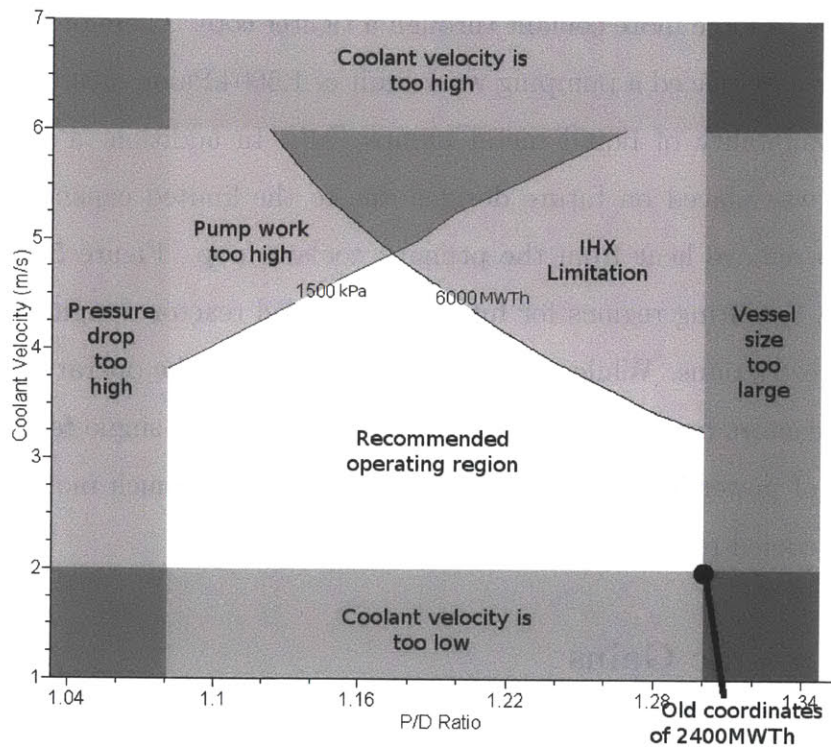


Figure 5-6: Operating regime restrictions based on reasonable design constraints for an LBE cooled reactor. Pumping work, vessel size, pressure drop, heat exchangers and coolant flow velocity were considered when restricting the recommended operation region.

cladding failure probabilities decrease, as does the probability of core damage and early release. This translates into direct financial gains due to lower risk, both from the standpoints of performing a probabilistic risk assessment (PRA) on the reactor and financing it. A lower risk reactor yields a higher expectation value of return per kilowatt-hour of electricity generated, so the interest rates on loans can decrease.

Finally, a smaller core footprint can be achieved by using this FGC. A higher permissible accident temperature during a full 72 hour station blackout means that more safety systems can cool the core passively, and less space is needed for their installation. A smaller reactor footprint reduces the upfront capital construction cost of building the reactor, translating directly into a smaller principal loan with a lower interest rate. All these factors serve to increase the profit margin per kilowatt-hour, decrease the time it takes to repay investors, and decrease the cost of electricity to the public. The added safety that this FGC presents to the design of an LFR or an LBEFR could also make the generation of electricity by nuclear power more acceptable to the general public.





# Chapter 6

## Conclusion & Future Work

The functionally graded composite (FGC) developed in this thesis represents a huge improvement in corrosion performance in Pb and LBE environments. Initial tests, if confirmed by additional tests to determine irradiation performance and long-term corrosion rates, indicate that the FGC system (a corrosion resistant protective layer with a high-strength structural base) constitutes an enabling technology for Pb- and LBE-cooled reactors and systems. This conclusion will be expanded upon below.

### 6.1 Key Result & Contributions

The FGC concept consists of a corrosion resistant layer that faces the liquid metal environment coupled with a structural layer that consists of a high strength material. The corrosion resistant layer is applied at the extrusion billet stage. Two application techniques can be used: (1) a weld overlay, which is the process used in this work, or (2) a machined insert. Further processing to either piping or fuel cladding forms produces a final product. Additionally, the corrosion resistant layer can be applied to complex shapes as a weld overlay. As long as the two components (layer and structure) are ferritic/martensitic steels, the structural layer can be changed as newer alloys are developed. The weld overlay route was chosen as being more versatile but with the potential disadvantage associated with dilution of the welded layer junction during processing and operation.

### 6.1.1 Key Results

The results of this work represent the development of an enabling technology for the Pb- and LBE-cooled reactor system. The FGC removes corrosion as a limitation with the Pb- and LBE-cooled system. Corrosion of liquid metal-facing components has, until now, limited the economic viability of LBE-cooled systems. The enabling technology claim is further reinforced by the following:

1. The modification of an ongoing fuel cycle technology study that had concluded that the sodium cooled system was the most economic fast reactor system. The report now concludes that, assuming that the results of this work are confirmed, the Pb-Bi cooled system is now the best choice going forward [69].
2. The selection of the FGC system developed in this thesis as the preferred system by the Korean team bidding on developing the structural components in SCK-CEN's MYRRHA, a full-size, accelerator-driven, LBE-cooled reactor system.

### 6.1.2 Key Contributions

The key contributions of this thesis are:

1. The development of the FGC concept as it applies to Pb- and LBE-cooled reactor systems.
2. The selection of the layers of the FGC, which includes the selection of the Fe-12Cr-2Si alloy for the cladding layer and the selection of the F91 alloy for the structural layer.
3. The development of processing schedules for and the production of the complete FGC system. This included the production of the corrosion resistant layer as a weld wire, the weld overlay process, the production and processing of F91, the weld overlay process and subsequent processing of the FGC into its final product form.

4. The characterization of the overall system, including corrosion characteristics, welding, and overall system stability at temperature. It is especially important that the corrosion characteristics of Fe-12Cr-2Si, which include an absence of iron oxides, have not been observed on similar alloys in the literature. In addition, little work exists for alloys in LBE at temperatures as high as 700°C.
5. The use of commercial technology to produce commercial quantities of the FGC, which is a demonstration of commercial viability for the FGC.

## 6.2 Overall Conclusions

- **The FGC protects against LBE corrosion in all expected environments, both oxidizing and reducing, such that corrosion is no longer a concern for lead- or LBE-cooled systems that use it.** Extrapolated corrosion rates based on the experiments in this study are less than  $1 \frac{\mu\text{m}}{\text{yr}}$ , which is negligible in terms of reactor design, even assuming a 60 year reactor lifetime for structural components. Extrapolation of the models developed in this thesis lead to a rate of one micron per year as a high estimate of corrosion. The kinetics of the oxide layer growth differ significantly from similar alloys exposed to LBE in the literature.
- **The structural layer/corrosion layer interface as well as the FGC itself are diffusionally stable.** The diffusional dilution zone between the two layers will not exceed  $17 \mu\text{m}$  for fuel cladding (three year life) or  $33 \mu\text{m}$  for coolant piping (sixty year life), both assumed to operate at 700°C. The thickness of the diffusional dilution zone decreases with decreasing temperature. Diffusional dilution of the composite is therefore not a concern, as long as the cladding layer is significantly thicker than the diffusional dilution thickness of tens of microns.
- **The FGC can be manufactured on a commercial scale using existing commercial technology.** Each manufacturing step in this work was performed domestically. This demonstrates the potential for immediate deploy-

ment should the demand arise. Domestic vendors have been identified who are capable of commercial-scale production.

- **The FGC can be welded according to ASME code using existing procedures and standards.** Welding according to existing procedures coupled with the prescribed quench-and-temper heat treatment for alloy F91 produces a sound weld with little to no heat affected zone (HAZ). Any remaining HAZ can be removed by further tempering, eliminating the possibility for Type IV cracking on a properly heat treated part.
- Because of the performance gains above, **the FGC represents an enabling technology for lead- and LBE-cooled reactors and systems.** A temperature increase of up to 150°C beyond the current limitation of 550°C is possible, provided that suitable structural materials exist. This allows reactor designers to increase the power density and/or increase the output of their reactors, and to build in larger safety margins in case of an accident.
- **This FGC is ready for immediate deployment in non-irradiated or low-dose applications.** The corrosion resistance has been demonstrated, and will be verified pending longer length experiments. However, based on the materials choices made, there is no reason to believe that these experiments will not be successful. New ASME codes do not have to be developed, as joining this FGC falls within existing ASME certified welding procedures. Further work is required to investigate the properties of the FGC under irradiation, especially at temperatures below 450°C where mechanical properties can be adversely affected by fast neutron irradiation [16].

### 6.3 Overall Summary of Experimental Results

The results of this study have demonstrated that the FGC corrosion behavior is superior to all other techniques when economics and commercial scalability are considered. The use of this system with currently available methods of system corrosion

control greatly expands the operating window for LBE systems at any temperature up to 700°C. Corrosion rates are below one micron per year, which is classified as outstanding corrosion resistance by most metrics [11].

The corrosion-resistant layer, made of Fe-12Cr-2Si, very rapidly forms iron oxides with a thin layer of chromium oxide beneath when exposed to lead or LBE containing very small amounts of oxygen. These iron oxides soon separate from the metal surface, as can be inferred from the XPS results of 70 hour and 506 hour-aged samples in 700°C LBE in Section 4.2.2.3, in Figures 4-17 & 4-21 (see Tables 4.2 & 4.4 for a detailed comparison of XPS peaks). Left over is a very thin layer of dense chromium oxide on the surface, followed by a region of silicon oxide and/or enrichment (as seen in the SIMS profiles in Section 4.2.2.4, especially in Figure 4-25). This oxide layer's existence, composition and thickness were confirmed by SEM and EDX analysis in Section 4.2.2.2, in Figures 4-13 & 4-15. The presence of this oxide layer imparts superior corrosion resistance to the FGC. It does so by forming a very strong diffusion barrier against oxygen ingress or metal ion migration out of the metal. This was both shown in experiments in this study and simulated in Section 2.1.3.1 (see Figure 2-9). This alloy does not appear to follow conventional models for oxide growth or liquid metal attack, examples of which can be seen in Section 5.1.1 (see Equations 5.1 & 5.2). More data is needed to develop a model to sufficiently describe the kinetics of oxidation growth for this alloy.

The structural layer, made of alloy F91, follows a predictable set of corrosion rates and mechanisms, as has been shown in this work compared to the literature. In reducing environments, the liquid metal adheres to the surface and attacks F91 by dissolution, causing the preferential depletion of chromium as seen in Figure 4-6. These channels of liquid metal attack were confirmed in optical micrographs in Figure 4-4, and the lack of any oxide layer was confirmed by the adherence of LBE to the entire surface of F91, as shown in Figure 4-5. In oxidizing environments, alloy F91 corrodes by the formation of wüstite, which leaves capillary channels for LBE entry into the metal. This is because wüstite is nonstructural and unstable in LBE, and it dissolves readily once it is formed. The presence of these capillary channels inside the

oxide layer, along with corresponding preferential dissolution of chromium (due to its higher solubility in LBE, see Section 2.1.1.2), was shown in Figure 4-8 and confirmed in optical micrographs in Figure 4-4. The fact that an oxide layer is present is evident in Figure 4-7, because no LBE adhered to the surface of the sample.

Static corrosion tests of the fabricated FGC show that no galvanic corrosion takes place in either oxidizing or reducing environments in 700° LBE after 98 hours, as shown in Figure 4-45. This shows that total cladding breach will not cause catastrophic failure by galvanic corrosion, and instead corrosion will follow well understood rates for F91 corrosion, which are summarized in Figure 5-1.

Diffusion studies show that the composite corrosion layer/structural layer interface is diffusionally stable, and that the thickness of the diffusion/dilution layer is not a concern when designing the composite. 17 microns must be accounted for during the three year lifetime of fuel cladding at 700°C, and 33 microns must be accounted for during the 60 year lifetime of coolant piping at 700°C (see Figure 5-3). Beyond these distances, the silicon level will remain above the minimum level of 1.25 wt. % to continue protecting the underlying metal, as was shown by J. Y. Lim [7]. The chromium concentration will always be higher than 10.5 wt. % in the cladding layer, as this is the midpoint concentration between the two alloys in the FGC. Diffusion of silicon in F91 is well understood, and a program written to fit the data to a standard error function model (see Section 5.2.1.1, Figure 5-2) yields a temperature-scalable diffusion coefficient (see Equation 5.6) that is in good agreement with comparable literature [73]. More advanced diffusional modeling is required to fully define the concentration profiles for each element as functions of time and temperature, because the true equations that govern it are highly coupled sets of simultaneous partial differential equations (see Equation 5.10).

This FGC is able to be fabricated (and has been fabricated) on a commercial scale using currently available technology, expertise and domestic vendors. The processing steps selected had to be optimized to improve the yield of each step, to fit the requirements and dimensions of the next steps, and to retain the integrity of the FGC interface, all while processing a new, unfamiliar material. The processing schedule

(see Figure 3-9) was chosen to accommodate existing tooling with vendors willing to work with the small quantities in this study. The availability of vendors will increase as this FGC is made in larger quantities. Each and every processing step yielded new information. Weld overlaying created an excellent interface between the two metals (see Figures 4-37 & 4-38). Hot extrusion refined this interface to a thin, but microstructurally sound, layer, as seen in Figure 4-40. A small amount of heat tearing was observed on the extrusion billets in Figures 4-39a & 4-39b, but this is not expected to be detrimental to the final FGC form. A slight drop in extrusion temperature (15 - 30°C) was suggested by the extrusion vendor in order to eliminate any heat tearing.

Weldability has been demonstrated to existing ASME boiler code B31.1 in Section 4.5.2. Optical micrographs of the dual metal weld (see Figures 4-42 & 4-43) showed typical microstructures for F91 welds, along with a more ferritic structure for the weld portion made of Fe-12Cr-2Si. A 2D Vickers hardness map overlaid onto the ID-clad micrograph montage (see Figure 4-44) shows that the F91 weld zone is harder than the operable range for alloy F91 [143, 144]. There is a relatively small (1 mm) heat affected zone considering the size of the weld. Both the HAZ and the hardness of the F91 weld will be ameliorated by further post-weld heat treatment and tempering.

## 6.4 Future Work

The short-term experiments carried out in this study show very promising results for this FGC. Longer-term studies are now required in order to more fully define and understand corrosion rates, corrosion mechanisms, and microstructural changes in more realistic environments. The studies required consist of the following:

- Long-Term Corrosion Studies - Corrosion studies for times up to 506 hours were immensely successful. Now, this corrosion resistance must be confirmed by a comprehensive testing program, consisting of long-term corrosion tests at periods between 1,000 hours (six weeks) and 50,000 hours (six years). This program is more suited to the national laboratories, and long-term collaboration

between universities and national laboratories will be required to perform these studies.

- Detailed Oxide Characterization - While SEM, EDX, XPS and SIMS give lots of insight into the nature and order of oxide film growth, they do not definitively define which oxides are present. Careful application of low angle x-ray diffraction (XRD) would be the preferred technique to determine exactly which oxides are present by their crystal structures. In addition, TEM images and diffraction pattern analysis would definitively identify any oxides present in the event that low-angle XRD is not sufficient.
- Flowing LBE Corrosion Studies - The static corrosion tests have shown that static LBE does not significantly corrode the FGC. Now, the effect of a flowing coolant in a non-isothermal loop must be tested to simulate deployment in an actual reactor. It is believed that the oxide is very adherent, and that it forms such a good diffusion barrier that flow assisted corrosion will not degrade the FGC. This belief must be rigorously tested in a loop, such as the DELTA loop at Los Alamos, or the HELIOS loop at Seoul National University in South Korea. Doing so will require the construction of a high-temperature test section of the loop, in order to test materials at or above 700°C. This test section could be made out of material from this study. This will also allow for post-mortem analysis of the test section, which will yield long-term flow assisted corrosion information about the FGC. Flowing LBE tests could confirm the belief that this FGC will allow LFR and LBEFR designs to accommodate a higher coolant velocity, and therefore increase the total power output and/or power density.
- Radiation Studies - The corrosion resistance, diffusional stability, mechanical properties and creep properties of the FGC must now be tested under varying doses of fast flux radiation for longer times. Radiation can cause extra diffusion to take place, known as irradiation induced mixing. The radiation resistance of the cladding must also be tested, as it is known that high silicon alloys are susceptible to radiation embrittlement (see Section 2.3.3.2). The database of



information on the properties of F91 under irradiation must be expanded at least to the extent of the property database for HT-9, so that the behavior of F91 under high fast radiation doses is well understood.

- FGC Design Iteration - While the FGC in this study performs its functions very well, it is by no means the best solution. The composite must be redesigned, its composition and processing steps tweaked, and its dimensions refined in order to improve its properties using existing alloys and capabilities. More alloying elements can be added to the cladding to increase its resistances to corrosion, radiation, creep, and its mechanical properties. Its silicon concentration could conceivably be reduced to alleviate some susceptibility to radiation damage while maintaining corrosion resistance. The structural layer can be changed, as Klueh et al. have pointed out that steels are being developed that could exceed the operating temperature and mechanical properties of F91 [124, 16].



# Bibliography

- [1] G. Müller, G. Schumacher, and F. Zimmermann. Investigation on oxygen controlled liquid lead corrosion of surface treated steels. *Journal of Nuclear Materials*, 278(1):85–95, February 2000.
- [2] P. Nash. Binary alloy phase diagrams. In *ASM Handbooks Online, Volume 3 - Alloy Phase Diagrams*, volume 3. ASM, 2004.
- [3] H.A. Wriedt and H. Okamoto. Binary alloy phase diagrams. In *ASM Handbooks Online, Volume 3 - Alloy Phase Diagrams*, volume 3. ASM, 2004.
- [4] R. Olesinski and G. Abbaschian. The Pb-Si (lead-silicon) system. *Journal of Phase Equilibria*, 5(3):271–273, June 1984.
- [5] H. Okamoto. Binary alloy phase diagrams. In *ASM Handbooks Online, Volume 3 - Alloy Phase Diagrams*, volume 3. ASM, 2004.
- [6] Arnulf Muan and E. F. Osborn. *Phase Equilibria Among Oxides in Steelmaking*. Addison-Wesley, 1965.
- [7] J. Y. Lim. *Effects of Chromium and Silicon on Corrosion of Iron Alloys in Lead-Bismuth Eutectic*. PhD thesis, MIT, 2006.
- [8] Idaho National Laboratory. Next generation reactors. Online Article (Accessed at <http://nuclear.inl.gov/gen4/i/lfr-lg.jpg>), Retrieved July 2010.
- [9] F. Balbaud-Célérier and F. Barbier. Investigation of models to predict the corrosion of steels in flowing liquid lead alloys. *Journal of Nuclear Materials*, 289(3):227–242, March 2001.

- [10] R. F. Steigerwals and N. D. Greene. The anodic dissolution of binary alloys. *Journal of the Electrochemical Society*, 109:1026–1034, November 1962.
- [11] Denny A. Jones. *Principles and Prevention of Corrosion*. Prentice Hall, 2nd edition, 1996.
- [12] Michael Schütze. *Protective Oxide Scales and Their Breakdown*. John Wiley & Sons, 1997.
- [13] J. N. DuPont, J. R. Regina, and K. Adams. Improving the weldability of FeCrAl weld overlay coatings. In *Fossil Energy Materials Conference*, pages 131–137, 2007.
- [14] F. Barbier and A. Rusanov. Corrosion behavior of steels in flowing lead-bismuth. *Journal of Nuclear Materials*, 296(1-3):231–236, July 2001.
- [15] R.L. Klueh and J.M. Vitek. Elevated-temperature tensile properties of irradiated 9Cr-1MoVNb steel. *Journal of Nuclear Materials*, 132(1):27–31, May 1985.
- [16] R.L. Klueh and A.T. Nelson. Ferritic/martensitic steels for next-generation reactors. *Journal of Nuclear Materials*, 371(1-3):37–52, September 2007.
- [17] G. Bonny, D. Terentyev, and L. Malerba. On the miscibility gap of FeCr alloys. *Scripta Materialia*, 59(11):1193–1196, December 2008.
- [18] A. M. Babakr, A. Al-Ahmari, K. Al-Jumayyah, and F. Habiby. Sigma phase formation and embrittlement of cast iron-chromium-nickel (Fe-Cr-Ni) alloys. *Journal of Minerals & Materials Characterization & Engineering*, 7(2):127–145, 2008.
- [19] G. Guntz, M. Julien, G. Kottmann, F. Pellicani, A. Pouilly, and J. C. Vaillant. *The T91 Book*. Vallourec Industries, France, 1990.
- [20] George F. Vandervoort. Microindentation hardness testing. *Advanced Materials & Processes*, 154(3):21–25, September 1998.

- [21] E. C. Bain and H. W. Paxton. *Alloying Elements in Steel*. American Society for Metals, 2nd edition, 1966.
- [22] Donald R. Askeland and Pradeep Prabhakar Phule. *The Science and Engineering of Materials*. Cengage Learning, 2006.
- [23] Bilge Yildiz and Mujid S. Kazimi. Efficiency of hydrogen production systems using alternative nuclear energy technologies. *International Journal of Hydrogen Energy*, 31(1):77–92, January 2006.
- [24] Anna Nikiforova, Pavel Hejzlar, and Neil E. Todreas. Lead-cooled flexible conversion ratio fast reactor. *Nuclear Engineering and Design*, 239(12):2596–2611, December 2009.
- [25] USGS World Energy Assessment Team. U.S. geological survey world petroleum assessment 2000 - description and results. Online Article (Accessed at <http://pubs.usgs.gov/dds/dds-060/>), 2000.
- [26] IAEA. Global uranium resources to meet projected demand: Latest edition of "red book" predicts consistent supply up to 2025. Online Article (Accessed at [http://www.iaea.org/NewsCenter/News/2006/uranium\\_resources.html](http://www.iaea.org/NewsCenter/News/2006/uranium_resources.html)), June 2006.
- [27] U.S. Energy Information Administration. World coal data - international energy annual 2006. Online Database (Accessed at <http://www.eia.doe.gov/iea/coal.html>), 2006.
- [28] U.S. CIA. The world factbook - 2009. Online Database (Accessed at <https://www.cia.gov/library/publications/the-world-factbook/>), 2009.
- [29] U.S. IEA. Key world energy statistics. Online PDF (Accessed at [http://www.iea.org/textbase/nppdf/free/2007/key\\_stats\\_2007.pdf](http://www.iea.org/textbase/nppdf/free/2007/key_stats_2007.pdf)), 2007.
- [30] Jefferson W. Tester, Elisabeth M. Drake, Michael J. Driscoll, Michael W. Golay, and William A. Peters. *Sustainable Energy - Choosing Among Options*. The MIT Press, 2005.

- [31] U.S. Energy Information Administration Independent Statistics & Analysis. Nuclear power plants operating in the United States as of December 31, 2008. Online Database (Accessed at <http://www.eia.doe.gov/>), December 2008.
- [32] U.S. DOE Nuclear Energy Research Advisory Committee and the Generation IV International Forum. A technology roadmap for generation iv nuclear energy systems. Technical report, U.S. Department of Energy, 2002.
- [33] U.S. Nuclear Regulatory Commission. Issued design certification - advanced boiling-water reactor (ABWR). Online Article, July 1994.
- [34] Craig F. Smith, William G. Halsey, Neil W. Brown, James J. Sienicki, Anton Moisseytsev, and David C. Wade. SSTAR: The US lead-cooled fast reactor (LFR). *Journal of Nuclear Materials*, 376(3):255–259, June 2008.
- [35] Office of Technology Assessment United States Congress. *Long-lived legacy: managing high-level and transuranic waste at the DOE nuclear weapons complex*. DIANE Publishing, 1991.
- [36] Min-Hwan Kim, Hong-Sik Lim, and Won-Jae Lee. A thermal-fluid assessment of a cooled-vessel concept for a VHTR. *Nuclear Engineering and Design*, 238(12):3360–3369, December 2008.
- [37] N. B. Vargaftik. *Tables on the Thermophysical Properties of Liquids and Gases*. Hemisphere Publishing So., 1975.
- [38] Vitaly Sobolev. Thermophysical properties of lead and lead-bismuth eutectic. *Journal of Nuclear Materials*, 362(2-3):235–247, 2007.
- [39] Pavel Hejzlar, Neil E. Todreas, Eugene Shwageraus, Anna Nikiforova, Robert Petroski, and Michael J. Driscoll. Cross-comparison of fast reactor concepts with various coolants. *Nuclear Engineering and Design*, 239(12):2672–2691, December 2009.

- [40] P. Gierszewski, B. Mikic, and N. Todreas. Property correlations for lithium, sodium, helium, FLiBe and water in fusion reactor applications (PFC-RR-80-12). Technical report, Massachusetts Institute of Technology, Plasma Fusion Center, 1980.
- [41] G. H. Holden and J. V. Tokor. Thermophysical properties of sodium (anl-7323). Technical report, Argonne National Laboratory, 1967.
- [42] J. Buongiorno and P. E. MacDonald. Progress report for the FY-03 Generation-IV R&D activities for the development of the SCWR in the U.S. Technical report, INEEL, September 2003.
- [43] The International Association for the Properties of Water and Steam. *Aqueous Systems at Elevated Temperatures and Pressures*. Elsevier Academic Press, 2004.
- [44] James J. Duderstadt and Louis J. Hamilton. *Nuclear Reactor Analysis*. John Wiley & Sons, 1976.
- [45] Tomohiro Furukawa, Georg Müller, Gustav Schumacher, Alfons Weisenburger, Annette Heinzl, Frank Zimmermann, and Kazumi Aoto. Corrosion behavior of FBR candidate materials in stagnant Pb-Bi at elevated temperature. *Journal of Nuclear Science and Technology*, 41(3):6, 2004.
- [46] G. A. Whitlow, J. C. Cwynar, R. L. Miller, and S. L. Schrock. Sodium corrosion of alloys for fast reactor applications. In *Proceedings of the Symposium on Chemical Aspects of Corrosion and Mass Transfer in Liquid Sodium*, page 1, October, 1971. AIME.
- [47] S. L. Schrock and G. A. Whitlow. Corrosion studies for the sodium cooled fast breeder reactor program. Technical report, Westinghouse Electric, 1974.
- [48] *Proceedings of the Workshop on Utilisation and Reliability of High Power Proton Accelerators*, Mito, Japan, October 1998. pp. 155-156.

- [49] INEEL. Design of an actinide burning, lead or lead-bismuth cooled reactor that produces low cost electricity (ineel/ext-02-01249). Technical report, INEEL, October 2002.
- [50] <http://www.metalprices.com/>, Accessed July 2010.
- [51] Takatsugu Mihara, Yoshiniko Tanaka, Yasuhiro Enuma, Masakazu Ichimiya, and Masashi Nomura. Feasibility studies on commercialized fast breeder reactor systems (3) - HLMC fast reactor. In *Transactions, SMiRT*, Washington DC, August 2001. Paper 1199.
- [52] IAEA. Fast reactor database. Technical report, International Atomic Energy Agency, February 1996.
- [53] Anton Moisseytsev and Diana T. Matonis. Integrated heat balance of STAR-H2 system for hydrogen production. In *Nuclear production of hydrogen: Second Information Exchange Meeting*, pages 277–281, Argonne, IL, USA, October 2003. OECD Nuclear Energy Agency, OECD Publishing.
- [54] P. Alekseev, P. Famichenko, K Mikityuk, V. Nevinitza, T. Shchepetina, S. Subbotin, and A. Vasiliev. RBEC lead-bismuth cooled fast reactor: Review of conceptual decisions. In *Advanced reactors with innovative fuels: second workshop proceedings*, Chester, United Kingdom, October 2001. OECD Nuclear Energy Agency & British Nuclear Fuels Limited, OECD Publishing.
- [55] N. Li. Active control of oxygen in molten lead-bismuth eutectic systems to prevent steel corrosion and coolant contamination. *Journal of Nuclear Materials*, 300(1):73–81, 2002.
- [56] V. Engelko, B. Yatsenko, G. Müller, and H. Bluhm. Pulsed electron beam facility (GESA) for surface treatment of materials. *Vacuum*, 62(2-3):211–216, 2001.



- [57] F.M. Haggag, W.R. Corwin, and R.K. Nanstad. Effects of irradiation on the fracture properties of stainless steel weld overlay cladding. *Nuclear Engineering and Design*, 124(1-2):129–141, November 1990.
- [58] J.J. Kearns. Terminal solubility and partitioning of hydrogen in the alpha phase of zirconium, Zircaloy-2 and Zircaloy-4. *Journal of Nuclear Materials*, 22(3):292–303, June 1967.
- [59] W. J. Reich, R. S. Moore, and K. J. Notz. Distribution of characteristics of LWR spent fuel (ORNL/TM-11670). Technical report, Oak Ridge National Laboratory, January 1991.
- [60] D. F. Wilson, E. C. Beahm, T. M. Besmann, J. H. DeVan, J. R. DiStefano, U. Gat, S. R. Greene, P. L. Rittenhouse, and B. A. Worley. Potential effects of gallium on cladding materials (ORNL/TM-13504). Technical report, Oak Ridge National Laboratory, October 1997.
- [61] A. L. Johnson, D. Parsons, J. Manzerova, D. L. Perry, D. Koury, B. Hosterman, and J. W. Farley. Spectroscopic and microscopic investigation of the corrosion of 316/316L stainless steel by lead-bismuth eutectic (LBE) at elevated temperatures: importance of surface preparation. *Journal of Nuclear Materials*, 328(2-3):88–96, July 2004.
- [62] R. Collins. Factors determining radiation-induced mixing at interfaces. *Radiation Effects*, 98(1):1–20, 1986.
- [63] L. Tan, M.T. Machut, K. Sridharan, and T.R. Allen. Corrosion behavior of a ferritic/martensitic steel HCM12A exposed to harsh environments. *Journal of Nuclear Materials*, 371(1-3):161–170, September 2007.
- [64] Jun Lim, Hyo On Nam, and Il Soon Hwang. Corrosion test of Cr- and Al-containing alloys in static LBE at 550C. In *Proceedings of ICAPP 2008*, pages 632–637, Anaheim, CA, June 2008. ICAPP.

- [65] S. Takaya, T. Furukawa, M. Inoue, T. Fujisawa, T. Okuda, F. Abe, S. Ohnuki, and A. Kimura. Corrosion resistance of Al alloying high Cr ODS steels in stagnant lead bismuth. *Journal of Nuclear Materials*, 398(1-3):132–138, March 2010.
- [66] D. Sapundjiev, S. Van Dyck, and W. Bogaerts. Liquid metal corrosion of T91 and A316L materials in Pb-Bi eutectic at temperatures 400-600°C. *Corrosion Science*, 48(3):577–594, 2006.
- [67] F. Gnecco, E. Ricci, C. Bottino, and A. Passerone. Corrosion behaviour of steels in lead bismuth at 823K. *Journal of Nuclear Materials*, 335(2):185–188, November 2004.
- [68] A. Weisenburger, A. Heinzl, G. Müller, H. Muscher, and A. Rousanov. T91 cladding tubes with and without modified FeCrAlY coatings exposed in LBE at different flow, stress and temperature conditions. *Journal of Nuclear Materials*, 376(3):274–281, June 2008.
- [69] Massachusetts Institute of Technology. The future of the nuclear fuel cycle. Technical report, MIT, 2010.
- [70] A. Bowen and G. Leak. Solute diffusion in alpha- and gamma-iron. *Metallurgical and Materials Transactions B*, 1(6):1695–1700, June 1970.
- [71] W. C. Hagel and A. U. Seybolt. Cation diffusion in Cr<sub>2</sub>O<sub>3</sub>. *Journal of the Electrochemical Society*, 108(12):1146–1152, 1961.
- [72] R. B. McLellan and Margot L. Wasz. Carbon-vacancy interactions in B.C.C. iron. *Physica Status Solidi (a)*, 110(2):421–427, 1988.
- [73] A. Heesemann, E. Schmidtke, F. Faupel, A. Kolb-Telieps, and J. Klower. Aluminum and silicon diffusion in Fe-Cr-Al alloys. *Scripta Materialia*, 40(5):517–522, February 1999.

- [74] J Kucera, B Million, J Ruzickova, V Foldyna, and A Jakobova. Self-diffusion of iron in [alpha]-phase of iron and Fe-Cr alloys. *Acta Metallurgica*, 22(2):135–140, February 1974.
- [75] B. Million. Diffusion of Fe-59 in a-Fe-Si alloys. *Czechoslovak Journal of Physics*, 27(8):928–934, August 1977.
- [76] W. K. Chen and N. L. Peterson. Effect of the deviation from stoichiometry on cation self-diffusion and isotope effect in wustite, Fe<sub>1-x</sub>O. *Journal of Physics and Chemistry of Solids*, 36(10):1097–1103, October 1975.
- [77] L. Himmel, R. F. Mehl, and C. E. Birchenall. Self-diffusion of iron in iron oxides and the wagner theory of oxidation. *Transactions of the AIME*, 197:827–843, 1953.
- [78] A.C.S. Sabioni, A.M. Huntz, F. Silva, and F. Jomard. Diffusion of iron in Cr<sub>2</sub>O<sub>3</sub>: polycrystals and thin films. *Materials Science and Engineering: A*, 392(1-2):254–261, February 2005.
- [79] A. Atkinson and J.W. Gardner. The diffusion of Fe<sup>3+</sup> in amorphous SiO<sub>2</sub> and the protective properties of SiO<sub>2</sub> layers. *Corrosion Science*, 21(1):49–58, 1981.
- [80] Jinsuo Zhang and Ning Li. Review of the studies on fundamental issues in LBE corrosion. *Journal of Nuclear Materials*, 373(1-3):351–377, February 2008.
- [81] A. Bowen and G. Leak. Diffusion in BCC iron base alloys. *Metallurgical and Materials Transactions B*, 1(10):2767–2773, October 1970.
- [82] N. Simon, T. Flament, A. Terlain, and C. Deslouis. Determination of the diffusion coefficients of iron and chromium in Pb<sub>17</sub>Li. *International Journal of Heat and Mass Transfer*, 38(16):3085–3090, November 1995.
- [83] R. J. Borg and D. Y. F. Lai. Diffusion in a-Fe-Si alloys. *Journal of Applied Physics*, 41(13):5193–5200, December 1970.

- [84] Masashi Uematsu, Hiroyuki Kageshima, Yasuo Takahashi, Shigeto Fukatsu, Kohei M. Itoh, Kenji Shiraishi, and Ulrich Gosele. Modeling of Si self-diffusion in SiO<sub>2</sub>: Effect of the Si/SiO<sub>2</sub> interface including time-dependent diffusivity. *Applied Physics Letters*, 84(6):876–878, February 2004.
- [85] N. Hine, K. Frensch, M. Foulkes, M. Finnis, and A. Heuer. Point defects and diffusion in Al<sub>2</sub>O<sub>3</sub>. *APS Meeting Abstracts*, pages 082901–(1–5), March 2010.
- [86] W. Frank, H. J. Engell, and A. Seeger. Solubility and interstitial migration of oxygen in BCC iron. *Transactions of the AIME*, 242:749–750, 1968.
- [87] Z. D. Sharp. Determination of oxygen diffusion rates in magnetite from natural isotopic variations. *Geology*, 19(6):653–656, June 1991.
- [88] S.C. Tsai, A.M. Huntz, and C. Dolin. Growth mechanism of Cr<sub>2</sub>O<sub>3</sub> scales: oxygen and chromium diffusion, oxidation kinetics and effect of yttrium. *Materials Science and Engineering: A*, 212(1):6–13, July 1996.
- [89] M.A. Lamkin, F.L. Riley, and R.J. Fordham. Oxygen mobility in silicon dioxide and silicate glasses: a review. *Journal of the European Ceramic Society*, 10(5):347–367, 1992.
- [90] Y. Oishi, K. Ando, and Y. Kubota. Self-diffusion of oxygen in single crystal alumina. *J. Chem. Phys.*, 73:1410–1412, 1980.
- [91] Shinya Otsuka and Zensaku Kozuka. The diffusivity of oxygen in liquid lead by electrochemical measurements. *Metallurgical and Materials Transactions B*, 6(3):389–394, September 1975.
- [92] S. Honma, N. Sano, and Y. Matsushita. Electrochemical measurement of the diffusivity of oxygen in liquid lead. *Metallurgical and Materials Transactions B*, 2(5):1494–1496, May 1971.
- [93] F. Gromov and B. Shmatko. *Journal of Obninsk*, 4, 1996.

- [94] P. N. Martynov and K. D. Ivanov. Properties of lead-bismuth coolant and perspectives of non-electric applications of lead-bismuth reactor (iaea-tecdoc-1056). Technical report, IAEA, 1997.
- [95] J. R. Weeks. Lead, bismuth, tin and their alloys as nuclear coolants. *Nuclear Engineering and Design*, 15:363–372, 1971.
- [96] J. Berthon, A. Revcolevschi, H. Morikawa, and B. Touzelin. Growth of wustite ( $\text{Fe}_{1-x}\text{O}$ ) crystals of various stoichiometries. *Journal of Crystal Growth*, 47(5-6):736–738, November 1979.
- [97] F. J. Martín, L. Soler, F. Hernández, and D. Gómez-Briceño. Oxide layer stability in lead-bismuth at high temperature. *Journal of Nuclear Materials Science and Engineering*, 335(2):194–198, November 2004.
- [98] H. Steiner and J. Konys. Stresses in oxidized claddings and mechanical stability of oxide scales. *Wissenschaftliche Berichte FZKA*, 7191:1–32, 2006.
- [99] Carsten Schroer and Juergen Konys. Quantification of the long-term performance of steels T91 and 316L in oxygen-containing flowing lead-bismuth eutectic at 550C. *J. Eng. Gas Turbines Power*, 132(8):082901–7, August 2010.
- [100] J. K. Tien and J. M. Davidson. In J. V. Cathcart, editor, *Stress Effects and the Oxidation of Metals - Proceedings of the TMS-AIME Fall Meeting, 1974*, page 200, New York, NY, USA, 1974. TMS-AIME.
- [101] L. Leibowitz and R. A. Blomquist. Thermal conductivity and thermal expansion of stainless steels D9 and HT9. *International Journal of Thermophysics*, 9(5):873–883, September 1988.
- [102] T. H. Bauer, G. R. Fenske, and J. M. Kramer. Cladding failure margins for metallic fuel in the integral fast reactor. In Folker H. Wittmann, editor, *Structural Materials in Reactor Technology, Volume C - Fuel Elements and Assemblies*, pages 31–38, August 1987.

- [103] B. Long and Y. Dai. Investigation of LBE embrittlement effects on the fracture properties of T91. *Journal of Nuclear Materials*, 376(3):341–345, June 2008.
- [104] G. Müller, A. Heinzl, J. Konys, G. Schumacher, A. Weisenburger, F. Zimmermann, V. Engelko, A. Rusanov, and V. Markov. Behavior of steels in flowing liquid PbBi eutectic alloy at 420-600C after 4000-7200 h. *Journal of Nuclear Materials*, 335(2):163–168, November 2004.
- [105] E. Kozeschnik and B. Buchmayr. MatCalc - a simulation tool for multicomponent thermodynamics, diffusion and phase transformation kinetics. *Mathematical Modelling of Weld Phenomena*, pages 349–361, 2001.
- [106] W. D. Manly. Fundamentals of liquid metal corrosion (ornl-2055). Technical report, ORNL, July 1956.
- [107] Alfons Weisenburger, K. Aoto, G. Müller, A. Heinzl, G. Schumacher, and T. Furukawa. Behaviour of chromium steels in liquid Pb-55.5Bi with changing oxygen content and temperature. *Journal of Nuclear Materials*, 358(1):69–76, 2006.
- [108] X. Ren, K. Sridharan, and T.R. Allen. Corrosion of ferritic-martensitic steel HT9 in supercritical water. *Journal of Nuclear Materials*, 358(2-3):227–234, November 2006.
- [109] Eriko Yamaki and Kenji Kikuchi. A stability of oxide layers formed in LBE on HCM12A to external loading. *Journal of Nuclear Materials*, 398(1-3):153–159, March 2010.
- [110] U. Konig and J. W. Schultze. Kinetics of passive layer formation on Fe-20Cr in comparison with Fe. *Materials and Corrosion*, 39(12):595–602, 1988.
- [111] The Institute of Problems in Materials Science. *The Oxide Handbook*. IFI/Plenum, Academy of Sciences of the Ukrainian SSR, Kiev, USSR, 2nd edition, 1982.

- [112] Ning Li. Lead-alloy coolant technology and materials - technology readiness level evaluation. *Progress in Nuclear Energy*, 50(2-6):140–151, March 2008.
- [113] D. J. Littler and E. E. Lockett. The pile neutron absorption cross sections of bismuth. *Proceedings of the Physical Society. Section A*, 66(8):700–704, 1953.
- [114] A. R. Nikolaev, A. A. Kortel', V. P. Karasev, and V. I. Ikonnikov. Reaction of periclase and corundum refractories with killed steel. *Refractories and Industrial Ceramics*, 21(11):635–637, November 1980.
- [115] Yu. I. Matrosov, V. T. Ababkov, and V. P. Kharchevnikov. Aluminum nitride in low-carbon steels. *Metal Science and Heat Treatment*, 12(9):803–808, 1970-09-01.
- [116] George Krauss. *Steels: Processing, Structure, and Performance*. ASM International, 2005.
- [117] Thomas H. Courtney. *Mechanical Behavior of Materials*. Waveland Press, Inc., 2005.
- [118] J. Lim, H. O. Nam, V. S. Rao, and I. S. Hwang. The effect of hydrogen annealing on the corrosion behaviors of FeCrAl alloy (Kanthal-AF) and SS316L in LBE. In *5th International Workshops on Materials for Heavy Liquid Metal Cooled Reactors and Related Technologies (HeLiMeRT-2009)*. NUTRECK, April 2009.
- [119] K. D. Adams and J. N. Dupont. Influence of Ti and C on the solidification microstructure of Fe-10Al-5Cr alloys. *Metallurgical and Materials Transactions A*, 41A:194–201, 2010.
- [120] Bachu N. Singh and Alan J. E. Foreman. Nucleation of helium bubbles at grain boundaries during irradiation. In *Effects of radiation on materials: 14th international symposium*, volume 1, pages 555–571. ASTM International, 1990.
- [121] Ramaswamy Viswanathan, D. Gandy, and K. Coleman. *Advances in Materials Technology for Fossil Power Plants*. ASM International, October 2007.

- [122] F. H. Stott. Influence of alloy additions on oxidation. *Materials Science and Technology*, 5(8):734–740, August 1989.
- [123] W. L. Hu and D. S. Gelles. The ductile-to-brittle transition behavior of martensitic steels neutron irradiated to 26 dpa. In *STP956: Influence of Radiation on Material Properties: 13th International Symposium (Part II)*, page 83, 1987.
- [124] R. L. Klueh and D. R. Harries. *High-chromium Ferritic and Martensitic Steels for Nuclear Applications*. ASTM, 2001.
- [125] K. Suzuki. Two-phase separation of primary MX carbonitride during tempering in creep resistant 9Cr1MoVNb steel. *ISIJ International (Iron and Steel Institute of Japan)*, 43(7):1089–1094, 2003.
- [126] F. A. Garner, M. B. Toloczko, and B. H. Sencer. Comparison of swelling and irradiation creep behavior of FCC-austenitic and BCC-ferritic/martensitic alloys at high neutron exposure. *Journal of Nuclear Materials*, 276(1-3):123–142, January 2000.
- [127] Jan Glowina, Barbara Kalandyk, and Krzysztof Hübner. Delta ferrite predictions for cast duplex steels with high nitrogen content. *Materials Characterization*, 47(2):149–155, August 2001.
- [128] K. Ravindranath and S. N. Malhotra. The influence of aging on the intergranular corrosion of 22 chromium-5 nickel duplex stainless steel. *Corrosion Science*, 37(1):121–132, January 1995.
- [129] W. C. Leslie. *The Physical Metallurgy of Steels*. Hemisphere Publishing Corp., USA, 1981.
- [130] M. K. Miller, K. F. Russell, J. Kocik, and E. Keilova. Embrittlement of low copper VVER 440 surveillance samples neutron-irradiated to high fluences. *Journal of Nuclear Materials*, 282(1):83–88, November 2000.



- [131] A. Kryukov, Yu. Nikolaev, and A. Nikolaeva. Composition effects in the radiation embrittlement of low-alloy steel. *Atomic Energy*, 84(4):304–307, April 1998.
- [132] B. Esmailzadeh, A. Kumar, and F. A. Garner. The influence of silicon on void nucleation in irradiated alloys. *Journal of Nuclear Materials*, 133-134:590–593, August 1985.
- [133] N. Todreas and M. Kazimi. *Nuclear Systems I: Thermal Hydraulic Fundamentals*. Taylor & Francis, 1990.
- [134] C. Antoine. Tensions des vapeurs; nouvelle relation entre les tensions et les températures. *Comptes Rendus des Séances de l'Académie des Sciences*, 107:681–684, 778–780, 836–837, 1888.
- [135] Barbara K. Henon. Specifying the sulfur content of 316L stainless steel for orbital welding. Online Article (Accessed at <http://www.thefabricator.com/article/tubepipefabrication/specifying-the-sulfur-content-of-316l-stainless-steel-for-orbital-welding>), March 2003.
- [136] A. DiSchino, M. Barteri, and J. M. Kenny. Fatigue behavior of a high nitrogen austenitic stainless steel as a function of its grain size. *Journal of Materials Science Letters*, 22(21):1511–1513, November 2003.
- [137] Han Kim, Hae-Geon Lee, and Kyung-Shik Oh. Mns precipitation in association with manganese silicate inclusions in Si/Mn deoxidized steel. *Metallurgical and Materials Transactions A*, 32(6):1519–1525, June 2001.
- [138] J. A. Francis, W. Mazur, and H. K. D. H Bhadeshia. Estimation of Type IV cracking tendency in power plant steels. *ISIJ International*, 44(11):1966–1968, 2004.
- [139] M. Tabuchi, M. Kondo, T. Watanabe, H. Hongo, F. Yin, and F. Abe. Improvement of the Type IV cracking resistance of 9Cr heat resisting steel weldment

by boron addition. *Acta Metallurgica Sinica (English Letters)*, 17(4):331–337, August 2004.

- [140] Joseph R. Davis. *Tool Materials*. ASM International, 1995.
- [141] R. D. Deslattes, E. G. Kessler Jr., P. Indelicato, L. de Billy, E. Lindroth, J. Anton, J. S. Coursey, D. J. Schwab, J. Chang, R. Sukumar, K. Olsen, and R. A. Dragoset. X-ray transition energies. NIST Online Searchable Database (Accessed at <http://www.nist.gov/physlab/data/xraytrans/index.cfm>), June 2010.
- [142] B. Long, Z. Tong, F. Groschel, and Y. Dai. Liquid Pb-Bi embrittlement effects on the T91 steel after different heat treatments. *Journal of Nuclear Materials*, 377(1):219–224, June 2008.
- [143] J. P. Shingledecker, M. L. Santella, and R. L. Klueh. Evaluation of heat-treatment temperature and properties of improperly heat-treated grade 91. In *ETD Conference on T/P91*, London, UK, June 2007.
- [144] J. P. Shingledecker, M. L. Santella, and K. A. Wilson. Evaluation of specification ranges for creep strength enhanced ferritic steels. In *New Developments on Metallurgy and Applications of High Strength Steels*, Buenos Aires, 2008.
- [145] C. Schroer, Z. Voss, O. Wedemeyer, J. Novotny, and J. Konys. Oxidation of steel T91 in flowing lead-bismuth eutectic (LBE) at 550C. *Journal of Nuclear Materials*, 356(1-3):189–197, September 2006.
- [146] The Boeing Company. *Practical Vacuum Systems Design*. Seattle, WA, USA.
- [147] Charles D. Wagner, Alexander V. Naumkin, Anna Kraut-Vass, Juanita W. Allison, Cedric J. Powell, and John R. Rumble, Jr. NIST x-ray photoelectron spectroscopy database - NIST standard reference database 20, version 3.5. Online Database (Accessed at <http://srdata.nist.gov/xps/>), August 2007.
- [148] V. M. Pereverzev. Kinetics and mechanism of carbide formation in chromium steels during carburizing. *Metal Science and Heat Treatment*, 27(11):821–824, November 1985.

- [149] T. Totemeier. Experience with grade 91 steel in the fossil power industry. Presentation, February 2009.
- [150] Roy A. Castelli. *Nuclear Corrosion Modeling*. Butterworth-Heineman, 2010.
- [151] P. Berge. Importance of surface preparation for corrosion control in nuclear power stations. *Materials Performance*, 36(11):56–62, 1997.
- [152] L. F. Epstein. *Liquid Metal Technologies*, 20:67, 1957.
- [153] Xiaoyi He, Ning Li, and Mark Mineev. A kinetic model for corrosion and precipitation in non-isothermal LBE flow loop. *Journal of Nuclear Materials*, 297(2):214–219, August 2001.
- [154] Jinsuo Zhang. A review of steel corrosion by liquid lead and lead-bismuth. *Corrosion Science*, 51(6):1207–1227, June 2009.
- [155] R. W. Balluffi, S. M. Allen, and W. C. Carter. *Kinetics of Materials*. J. Wiley Interscience, 2005.
- [156] P. J. Mohr, B. N. Taylor, and D. B. Newell. CODATA recommended values of the fundamental physical constants: 2006. Technical report, National Institute of Standards and Technology, 2007.



# **Appendix A**

## **Code for Calculation of Resource Depletion**

```

#include <stdio.h>
#include <stdlib.h>
#include <math.h>

// Define constants for the calculations.
#define Increase      0.03

int main(void)
{
    double Consumption, Reserves;
    long Year;

    system("clear");

    printf("Enter the initial consumption (ZJ/yr): ");
    scanf("%lf", &Consumption);
    printf("Enter the total reserves (ZJ): ");
    scanf("%lf", &Reserves);
    printf("Enter the starting year: ");
    scanf("%ld", &Year);
    printf("\n\n");

    do
    {
        Reserves -= Consumption;
        Consumption *= (1 + Increase);
        Year++;
    } while (Reserves > 0);

    printf("\n\nReserves will run out by %ld\n\n\n", Year);

    return 0;
}

```



# Appendix B

## Extrusion Report from H. C. Starck

### Extrusion Production Record Cover Sheet

Customer: Massachusetts Institute of Technology  
Liner: 10.25"  
Date: 2/8/2010  
Job Number: 2099167  
QC Inspector: *AS.*

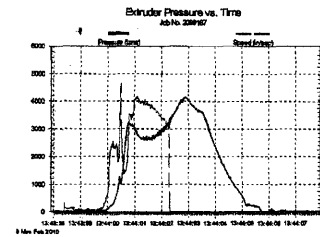
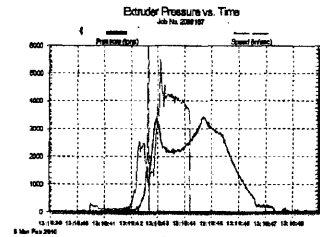
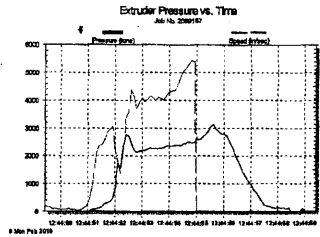
Alloy	Extrusion Size	Quantity
T91	3.750" x 3.000" Tube	3



# Extrusion Production Report

Customer: **Mass. Institute of Technology** Job No. **2099167** Customer PO: **100186** Ass'y **10.25** Date **2/8/2010**  
 Comments | Prod. Order #: \_\_\_\_\_  
 Pushes: **Alloy** Ext OD **3** Ext ID **F (Exp) K (Exp)** Ext Ratio **to 1** Technician: **GLL** Pushes: **1-3** Date: **2/8/2010**

Push No.	Start Time	Billet Heat No.	Fce No.	Billet Temp.	Fce. Load	Tran Time (Sec)	F break (Tons)	F start (Tons)	F end (Tons)	Speed (In/Sec)	Speed end (In/Sec)	K actual (T/In <sup>2</sup> )	Comments	ID	NMR Issued
1	12:44	MIT-1	4	2236°F	12:38	85	2812	2218	3196	3.83	7.3	12.66	Mandrel = 3.05/ 2258 degrees	<input checked="" type="checkbox"/>	<input type="checkbox"/>
Nose Dia.		/	Tail Dia.		/	Length	32'9"	Ext Butt Weight		Die Size (In)		3.795			
2	13:16	MIT-2	4	2205°F	13:06	113	3393	2601	3501	5.5	3.9	15.28	2150 degrees/ rough OD	<input checked="" type="checkbox"/>	<input type="checkbox"/>
Nose Dia.		/	Tail Dia.		/	Length	16'2"	Ext Butt Weight		Die Size (In)					
3	13:43	MIT-3	4	2180°F	13:32	109	3341	3169	3712	5.6	4.35	15.04	2150 degrees	<input checked="" type="checkbox"/>	<input type="checkbox"/>
Nose Dia.		/	Tail Dia.		/	Length	16'7"	Ext Butt Weight		Die Size (In)					



date Insp: 2-8-10  
 part/Alloy: T91  
 quantity: 3  
 inspection: QC

## H.C. STARCK EXTRUSION BILLET INSPECTION & FURNACE LOADING SEQUENCE REPORT

Customer: MIT  
 Job #: 2099167  
 Extr. Date: 2-8-10

Total Weight: \_\_\_\_\_ Form EXT-3 Rev 4

Inner Size: 10.25 Extrusion OD Nom: 3.750 Extrusion ID Nom: 3.000 Fce # 3-Ind Temp: 1350°-2100°

Billet/Casting/Serial No.	Length	Weight	OD	ID	Radius Chamfer	Surface Finish/Remarks	Load	Trans.	Push #	Core Inspected	Coolde Brisco	Liner Lubed
MIT-1	23 1/2	191	9.810	3.850	1"		902	1230	1	1244		
-2	11 1/2	98	9.825	3.255	1"		932	1306	2	1316		
-3	11 1/2	98	9.825	3.260	1"		934	1332	3	1343		

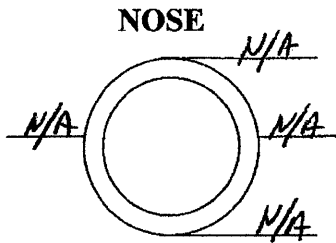
# EXTRUDED HOLLOW DATA RECORD

Job Number: 2099167

QC Tech: GL

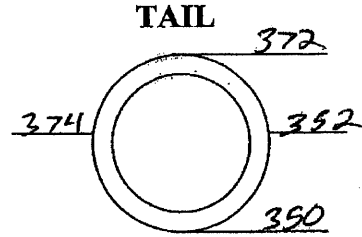
Date: 2-8-10

Customer: Mass. Inst. of Technology Extrusion Size: 3.750" x 3.000" Tube



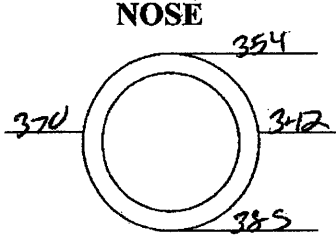
Extrusion Identification #

MIT-1  
32' 9"

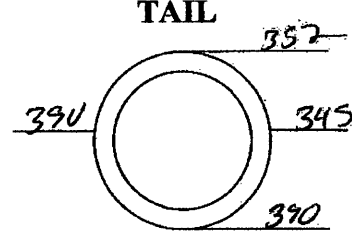


OD 3.780 / 3.730  
ID NOT AVAILABLE

OD 3.725 / 3.735  
ID 2.990 / 2.990

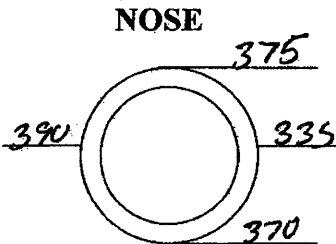


MIT-2  
16' 2"

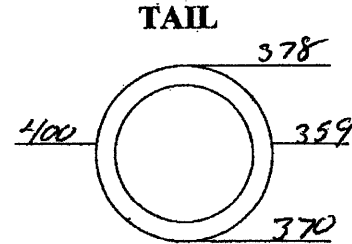


OD 3.72 / 3.725  
ID 3.010 / 3.010

OD 3.735 / 3.735  
ID 3.020 / 3.020

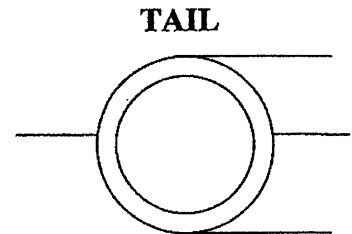
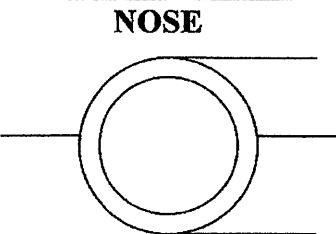


MIT-3  
16' 7"



OD 3.72 / 3.725  
ID 3.010 / 3.005

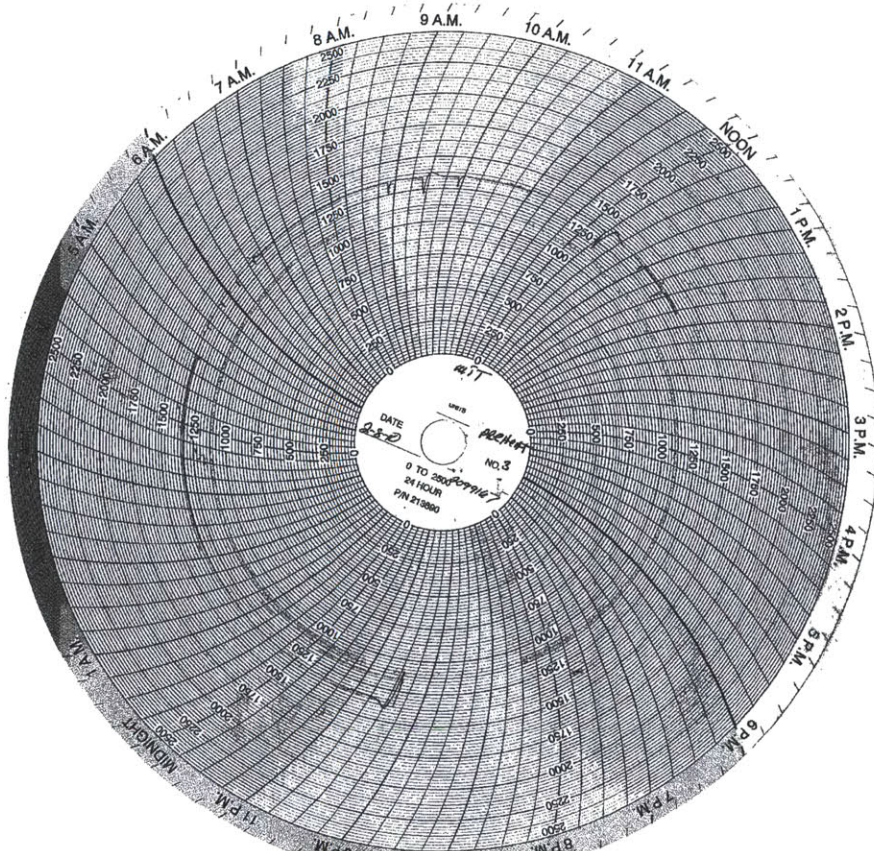
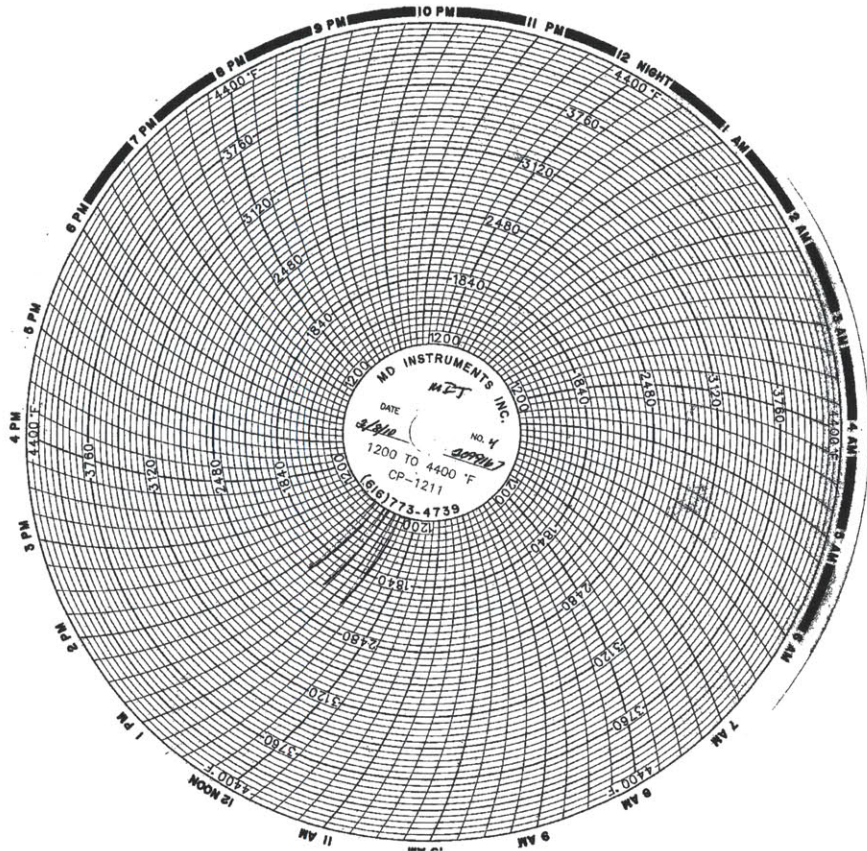
OD 3.73 / 3.735  
ID 3.020 / 3.020



OD \_\_\_\_\_ / \_\_\_\_\_  
ID \_\_\_\_\_ / \_\_\_\_\_

OD \_\_\_\_\_ / \_\_\_\_\_  
ID \_\_\_\_\_ / \_\_\_\_\_

Form - EXT-05 Rev 3





# Appendix C

## ASME-Certified Welding Report from Artisan Industries

Artisan Industries, Inc.  
73 Pond Street  
Waltham, MA 02451-4594

### Welding Procedure Specification (WPS)

WPS No.: 5B-5B-AB Date: 12/5/2007 Rev. No.: 0 Page 1 of 2

Supporting PQR(s): 210[1], 211[1]

Welding Process(es) / Type(s): (1) GTAW / Manual (2) SMAW / Manual

<b>Joint Design (QW-402)</b>					
Weld Type: <u>Groove and fillet welds</u>					
<b>Joint Type</b>	<b>Backing</b>	<b>Root Opening</b>	<b>Groove Angle</b>	<b>Root Face</b>	<b>Groove Radius</b>
Single-bevel groove	No backing	3/16" max	50 deg min	1/8" max	
Double-bevel groove	No backing	3/16" max	45 deg min	1/8" max	
Fillet Welds: All fillet sizes on all base metal thicknesses and all diameters.					
Retainers: <u>None</u>					
WELD JOINT DESCRIPTIONS SHOWN ARE NOT INCLUSIVE OF ALL THOSE FOUND ON A JOB. WELD JOINT DESIGN REFERENCE IN AN ENGINEERING SPECIFICATION OR A DESIGN DRAWING SHALL TAKE PRECEDENCE OVER WELD JOINTS SHOWN IN THIS WPS.					
<b>Base Metals (QW-403)</b>					
P-No. <u>5B</u> Thickness Range: <u>0.1875 in. to 8.0000 in.</u>					
to P-No. <u>5B</u>					
<b>Preheat (QW-406)</b>			<b>Postweld Heat Treatment (QW-407)</b>		
Minimum Preheat Temperature: <u>400</u> °F			PWHT Type: <u>PWHT below lower transformation temperature</u>		
Maximum Interpass Temperature: <u>700</u> °F			PWHT Temperature: <u>1375</u> °F		
Preheat Maintenance: <u>Ceramic electric heaters</u>			PWHT Holding Time: <u>2.0 hr./in. min.</u>		
Once welding starts preheat must be maintained until welding is complete. After welding is complete, post weld bake out at 600 F for 15 min and then slow still air cool to ambient.			Rise and cooling rate over 600 F to be 250 F/Hr. Max.		
			PWHT between 1350 and 1400 F.		
			Hold time 2 Hrs. minimum for less than 2", then 1 Hr./In. thickness over 2".		
Initial and Interpass Cleaning: <u>With wire brush and acetone clean 1 inch (25 mm) on both sides of weld joint</u>					
Method of Back Gouging: <u>When required, grind until all defects are removed.</u>					
48 Hours after PWHT is complete wet Fluorescent MT and 100% RT must be performed.					

We certify that the statements in this specification are correct and in accordance with the requirements of Section IX of the ASME Code.

Prepared By: Rick Moody Date: 12/5/2007

Accepted By: Arthur Hunt Date: 12/5/2007 QC Manager

Artisan Industries, Inc.

Welding Procedure Specification (WPS)

WPS No.: **5B-5B-AB**

Rev. No.: **0**

Page 2 of 2

<b>First Process:</b>	<b>GTAW</b>	<b>Type:</b>	<b>Manual</b>
<b>Filler Metal (QW-404)</b>			
Weld Deposit Limits:	1.0000 in. maximum		
AWS Classification:	ER90S-B9	SFA Specification:	5.28 F-No.: 6
A-No. or Chemical Composition:	5		
Filler Metal Product Form:	Bare (Solid)		
Consumable Insert:	None	GTAW Flux:	None
<b>Position (QW-405)</b>		<b>Technique (QW-410)</b>	
Position of Joint:	All Positions	Stringer or Weave Bead:	Stringer or weave bead
Weld Progression:	Any	Nozzle / Gas Cup Size:	#5 to #10
<b>Gas (QW-408)</b>		Peening:	None
Shielding:	100% Argon / 18-24 CFH	Multiple / Single Pass (per side):	Multipass
Backing:	None / - CFH		
Trailing:	None / - CFH		
<b>Electrical Characteristics (QW-409)</b>			
Current Type and Polarity:	DCEN (straight)		
Pulsed Current:	None		
Tungsten Type:	EWTh-2 Size: 3/32		
Max. Heat Input (J/in):	None		

First Process Welding Parameters

Layer(s) and/or Pass(es)	Filler Metal		Current		Voltage Range	Travel Speed Range (in/min)
	AWS Classification	Size (in.)	Type and Polarity	Amperage Range		
Any	ER90S-B9	1/16	DCEN (straight)	70-175	12-16	1-6
Any	ER90S-B9	3/32	DCEN (straight)	80-200	12-18	2-8
-	-	-	DCEN (straight)	-	-	-
-	-	-	DCEN (straight)	-	-	-

<b>Second Process:</b>	<b>SMAW</b>	<b>Type:</b>	<b>Manual</b>
<b>Filler Metal (QW-404)</b>			
Weld Deposit Limits:	8.0000 in. maximum	No Pass Greater Than 1/2" Allowed	
AWS Classification:	E9015-B9H4	SFA Specification:	5.5 F-No.: 4
A-No. or Chemical Composition:	5		
<b>Position (QW-405)</b>		<b>Technique (QW-410)</b>	
Position of Joint:	All Positions	Stringer or Weave Bead:	Stringer or weave bead
Weld Progression:	Any	Peening:	None
<b>Electrical Characteristics (QW-409)</b>		Multiple / Single Pass (per side):	Multipass
Current Type and Polarity:	DCEP (reverse)		
Max. Heat Input (J/in):	None		

Covered electrode to be low hydrogen and have Manganese + Nickel content <math>\leq 1.5\%</math>.  
Covered electrode Ms/Stratio to be greater than 50.

Second Process Welding Parameters

Layer(s) and/or Pass(es)	Filler Metal		Current		Voltage Range	Travel Speed Range (in/min)
	AWS Classification	Size (in.)	Type and Polarity	Amperage Range		
Any	E9015-B9H4	3/32	DCEP (reverse)	70-110	n/r	Var.
Any	E9015-B9H4	1/8	DCEP (reverse)	90-160	n/r	Var.
Any	E9015-B9H4	5/32	DCEP (reverse)	130-220	n/r	Var.
Any	E9015-B9H4	3/16	DCEP (reverse)	200-300	n/r	Var.
-	-	-	DCEP (reverse)	-	-	-

Artisan Industries, Inc.  
73 Pond Street  
Waltham, MA 02451-4594

Procedure Qualification Record (PQR)

PQR No.: 210 Date: 11/17/2007 WPS No.: \_\_\_\_\_ Page 1 of 2  
Welding Process(es) / Type(s): (1) GTAW / Manual

<b>Joint Design (QW-402)</b> Weld Type: _____ Groove weld Groove Type: _____ Single-V groove Backing: _____ Back-gouged and back welded Root Opening: _____ 1/16 in. Root Face: _____ 0 in. Groove Angle: _____ 30 °		<b>Base Metals (QW-403)</b> Specification Type and Grade: _____ SA-387, Grade 91, Cl. 2 to SA-387, Grade 91, Cl. 2 P-No. <u>5B</u> Group No. <u>2</u> to P-No. <u>5B</u> Group No. <u>2</u> Thickness (in.): _____ 1/2	
		<b>Preheat (QW-406)</b> Minimum Preheat Temperature: _____ 300 °F Preheat Maintenance: _____ Electric ceramic heaters Maximum Interpass Temperature _____ 600 °F Once welding starts preheat must be maintained until welding is complete. After welding is complete slow cool under blankets to ambient.	
		<b>Postweld Heat Treatment (QW-407)</b> Type: _____ PWHT performed below lower transformation temp. PWHT Temperature: _____ 1375 °F PWHT Holding Time: _____ 2 hr. Rise and cooling rate over 600 F to be 250 F/hr max. PWHT hold between 1375 nad 1425. Hold time 2 Hrs. Min., then 1 hrs/in. over 2" thk.	
<b>First Process:</b> _____ GTAW <b>Filler Metals (QW-404)</b> AWS Classification: _____ ER90S-B9 SFA Specification: _____ 5.28 F-No.: _____ 6 A-No. or Chemical Composition: _____ 5 Filler Metal Trade Name: _____ N/R Filler Metal Product Form: _____ Bare (Solid) Consumable Insert: _____ None GTAW Flux: _____ None Weld Deposit 'T' (in.): _____ 1/2		<b>Type:</b> _____ Manual <b>Electrical Characteristics (QW-409)</b> Current Type and Polarity: _____ DCEN (straight) Tungsten Type: _____ EWTh-2 Size: _____ 3/32 Pulsed Current: _____ None <b>Welding Details</b> Filler Metal Size (in.): _____ 1/16   -   - Amperage Used: _____ 80-175   -   - Voltage Used: _____ 12-16   -   - Travel Speed (in/min): _____ 1-4   -   - Max. Heat Input (J/in): _____ N/R	
<b>Positions (QW-405)</b> Position of Joint: _____ 1G - Flat Weld Progression: _____ N/A <b>Gas (QW-408)</b> Shielding: _____ 100% Argon / _____ 20 CFH Backing: _____ None / _____ - CFH Trailing: _____ None / _____ - CFH		<b>Technique (QW-410)</b> Thermal Processes: _____ No Stringer or Weave Bead: _____ Stringer and weave bead Nozzle / Gas Cup Size: _____ #8 Multiple / Single Pass (per side): _____ Multipass	

Artisan Industries, Inc.

Procedure Qualification Record (PQR)

PQR No.: 210 \_\_\_\_\_ Page 2 of 2

Tensile Test (QW-150)

Specimen No.	Width (in.)	Thickness (in.)	Area (in <sup>2</sup> )	Ultimate Total Load (lb)	Ultimate Unit Stress (PSI)	Failure Type and Location
T-1	0.746	0.469	0.350	33500	95700	P5B Ductile
T-2	0.746	0.466	0.348	34200	98300	P5B Ductile

Guided Bend Tests (QW-160)

Type and Figure No.	Result	Type and Figure No.	Result
QW-462.2 Side bend	Satisfactory	QW-462.2 Side bend	Satisfactory
QW-462.2 Side bend	Satisfactory	QW-462.2 Side bend	Satisfactory

Visual Examination: Per QW194 Satisfactory

Welder's Name: Kapinos, John I.D.: 50 Stamp No.: 50

PQR was done and welding of coupon was witnessed by: Artisan Industries, Inc.

Test conducted by: Triangle Engineering Inc. Lab Test No.: ST-6860

We certify that the statements in this record are correct and that the test welds were prepared, welded, and tested in accordance with the requirements of Section IX of the ASME Code.

Prepared By: \_\_\_\_\_  \_\_\_\_\_ 11/16/07 QC Manager  
Date

Procedure Qualification Record (PQR)

PQR No.: 211 Date: 11/17/2007 WPS No.: Page 1 of 2  
Welding Process(es) / Type(s) (1) SMAW / Manual (2) GMAW / Semiautomatic

<b>Joint Design (QW-402)</b> Weld Type: Groove weld Groove Type: Double-V groove Backing: Back-gouged and back welded Root Opening: 1/16 in. Root Face: 0 in. Groove Angle: 30°		<b>Base Metals (QW-403)</b> Specification Type and Grade: SA-387, Grade 91, Cl. 2 to SA-387, Grade 91, Cl. 2 P-No. 5B Group No. 2 to P-No. 5B Group No. 2 Thickness (in.): 1.5	
		<b>Preheat (QW-406)</b> Minimum Preheat Temperature: 400 °F Preheat Maintenance: Electric Ceramic Heaters Maximum Interpass Temperature: 600 °F Once welding starts, preheat must be maintained until welding is completed. Once welding is complete, slow cool under blankets to ambient.	
		<b>Postweld Heat Treatment (QW-407)</b> Type: PWHT performed below lower transformation temp. PWHT Temperature: 1400 °F PWHT Holding Time: 2 hr. Rise and cooling rate over 600 F to be 250 F/hr max. PWHT Hold between 1375 and 1425 F. Hold time 2 hrs min for thickness less than 2", 1hr/in thickness over 2", then 2 hrs/in over 5" thk.	
<b>First Process: SMAW</b> <b>Filler Metals (QW-404)</b> AWS Classification: E9015-B9H4 SFA Specification: 5.5 F-No.: 4 A-No. or Chemical Composition: 5 Filler Metal Trade Name: N/R Weld Deposit 't' (in.): 3/4 Pass Greater Than 1/2": No <b>Positions (QW-405)</b> Position of Joint: 1G - Flat Weld Progression: N/A		<b>Type: Manual</b> <b>Electrical Characteristics (QW-409)</b> Current Type and Polarity: DCEP (reverse) <b>Welding Details</b> Filler Metal Size (in.): 5/32   -   - Amperage Used: 130-220   -   - Voltage Used: 20-23   -   - Travel Speed (in/min): 6-8   -   - Max. Heat Input (J/in): N/R <b>Technique (QW-410)</b> Thermal Processes: No Stringer or Weave Bead: Stringer and weave bead Multiple / Single Pass (per side): Multipass	
Covered electrode Ms/S ratio shall be greater than 50. Covered electrode to be low hydrogen and have Manganese and Nickel content <= 1.5%.			
<b>Second Process: GMAW</b> <b>Filler Metals (QW-404)</b> AWS Classification: ER90S-B9 SFA Specification: 5.28 F-No.: 6 A-No. or Chemical Composition: 5 Filler Metal Trade Name: N/R Filler Metal Product Form: Bare (Solid) Supplemental Filler Metal: None Weld Deposit 't' (in.): 0.75 Pass Greater Than 1/2": No <b>Positions (QW-405)</b> Position of Joint: 1G - Flat Weld Progression: N/A <b>Gas (QW-408)</b> Shielding: 98% Argon, 2% CO2 / 35 CFH Backing: N/A / - CFH Trailing: None / - CFH		<b>Type: Semiautomatic</b> <b>Electrical Characteristics (QW-409)</b> Current Type and Polarity: DCEP (reverse) Transfer Mode: Spray arc <b>Welding Details</b> Filler Metal Size (in.): 0.045   -   - Amperage Used: 225-250   -   - Wire Feed Speed (in/min): 410   -   - Voltage Used: 26-28   -   - Travel Speed (in/min): 6-15   -   - Max. Heat Input (J/in): N/R <b>Technique (QW-410)</b> Thermal Processes: No Stringer or Weave Bead: Stringer and weave bead Nozzle / Gas Cup Size: 1/2" Contact Tube to Work Distance: 1/2" Multiple / Single Pass (per side): Multipass	

Procedure Qualification Record (PQR)

PQR No.: 211 Page 2 of 2

Tensile Test (QW-150)

Specimen No.	Width (in.)	Thickness (in.)	Area (in <sup>2</sup> )	Ultimate Total Load (lb)	Ultimate Unit Stress (PSI)	Failure Type and Location
T-1	0.749	1.41	1.056	103500	98000	Ductile - BM
T-2	0.749	1.41	1.056	105400	99800	Ductile - BM

Guided Bend Tests (QW-160)

Type and Figure No.	Result	Type and Figure No.	Result
QW-462.2 Side bend	Satisfactory	QW-462.2 Side bend	Satisfactory
QW-462.2 Side bend	Satisfactory	QW-462.2 Side bend	Satisfactory

Visual Examination: Per Qw194 Satisfactory

Welder's Name: Small, David ID: 6 Stamp No.: 6  
 PQR was done and welding of coupon was witnessed by: Artisan Industries, Inc.  
 Test conducted by: Triangle Engineering Inc. Lab Test No.: ST-6866

We certify that the statements in this record are correct and that the test welds were prepared, welded, and tested in accordance with the requirements of Section IX of the ASME Code.

Prepared By:  Arthur Hunt Date: 12/6/07 QC Manager



## **Appendix D**

**C Code and Input File Used to  
Calculate Silicon Diffusion  
Constants in Alloy F91**

```

#include <stdio.h>
#include <stdlib.h>
#include <math.h>

char Alloy[20];           // The alloy in question
char Element[20];       // The element in question
double D0_Min, D0_Max;  // Bounds for the infinite diffusivity (D0)
double Ac_Min, Ac_Max;  // Bounds for the activation energy (Ac) in kcal/mol
double D0_Step;         // The step change for infinite diffusivity
double Ac_Step;         // The step change for activation energy in kcal/mol
unsigned int D0_Dimension; // The number of D0 values to use, calculated from the bounds and
                        // the step size of D0
unsigned int Ac_Dimension; // The number of Ac values to use, calculated from the bounds and
                        // the step size of Ac
double Conc_Min, Conc_Max; // The minimum and maximum (bounding) concentrations for the element
                        // in question in atomic percent
double delta_C, Cavg;    // Values used in the diffusion equation
unsigned int NumDatasets; // The number of data sets to analyze
unsigned char LastControlSet; // The index of the last dataset that was not aged - used for
                        // constructing the Effective Starting Times

struct DataSet
{
    unsigned long Seconds; // The number of seconds for which the
                        // diffusion couple was heated
    unsigned int Temperature; // The temperature at which the diffusion couple was heated
                        // in Kelvin
    unsigned int NumberOfDataPoints; // The number of data points in this data set
    double Cmin;
    double Cmax;
    double Cavg;
    double DeltaC;
    double X_Values[255]; // The distances from the interface in microns
    double Y_Values[255]; // The point concentration of the element
                        // in question in atomic percent
};

struct DataSet CurrentData[10];

```

```

const double R = 0.001986;           // Gas constant in kcal/K-mol

void GetGlobalParameters(void);      // Get the global parameters (value bounds) for the current
                                     // diffusion problem
void LoadDataIntoMemory(void);      // Load the data set from the input file
                                     // into memory for processing
double DC(double, double, unsigned int); // Calculate diffusion constant (D) from a given D0,
                                     // Ac and temperature
double PointConc(double, double, unsigned long, unsigned char);
                                     // Calculate the theoretical element concentration from
                                     // a given D, distance and time

int main (void)
{
    unsigned int i, j, l, m, n;      // Dummy variables for loops
    unsigned long k;
    double Local_D0, Local_Ac, Local_D;
                                     // Local values of D0 and Ac, used for computing each step
    unsigned long Local_Time;        // Local copy of the time in seconds. Used in computations
    double RMS_Sum;                 // The total RMS value for matching the theory with
                                     // the current experiment
    double Min_RMS;                 // Keeps track of the minimum RMS value, used to find the best time
    unsigned long MinimumTime;      // Keeps track of the minimum time value reached in the
                                     // first step
    double D_Scale;                 // Temporary diffusion constant multiplied by a power of ten
                                     // specified below
    double SinglePointMSE;          // The result of a single MSE calculation for one point
    unsigned char AbortLoopFlag;    // If this flag is set, it will stop going through the
                                     // EffectiveStartingTime loop
    double AbsoluteMinimumRMS;      // This is the absolute minimum value of the total RMS
    double AbsoluteMinimumX, AbsoluteMinimumY;
                                     // These are the coordinates (in D0-Ac space) of the minimum point
    unsigned long AbsoluteMinimumTime;

    FILE *fp = fopen("output-time.csv", "w");
    FILE *fp_results = fopen("output_results.csv", "w");
    FILE *fp_gnuplot = fopen("output_gnuplot.dat", "w");

    LoadDataIntoMemory();

```

```

GetGlobalParameters();

unsigned long EffectiveStartingTimes[D0_Dimension+1] [Ac_Dimension+1][NumDatasets];
    // Effective starting times
double RMS_Map[D0_Dimension+1][Ac_Dimension+1];
    // This is the final output map of RMS values, in D0 / Ac space.
    // This will be output to a file to help the user figure out
    // where the best fit values are for the entire problem.

// First generate an "effective control aging time" for each combination
// of D0 and Ac for each data set. This generates a three dimensional
// array of "effective control aging times", with the X Y and Z axes
// being D0, Ac and Dataset Number. Each of these values (in seconds)
// will then be added to the recorded time to get an effective aging
// time. This is because making the diffusion couples causes some
// diffusion to happen, so that the initial concentration profile is
// not a perfect step function.

printf("\n\nReady to run simulation with Cmin = %f, Cmax = %f", Conc_Min, Conc_Max);
printf("\nYou have %u datasets.\n", NumDatasets);
printf("\nD0_Dimension = %u, Ac_Dimension = %u\n", D0_Dimension, Ac_Dimension);
getchar();

for (l=0; l<NumDatasets; l++)
{
    if (CurrentData[l].Seconds == 0) LastControlSet = l;

    for (i=0; i<=D0_Dimension; i++)          // Loop over specified values of D0
    {
        for (j=0; j<=Ac_Dimension; j++) // Loop over specified values of Ac
        {
            AbortLoopFlag = 0;

            Local_D0 = D0_Min + ((double)i * D0_Step);
            Local_Ac = Ac_Min + ((double)j * Ac_Step);

            Local_D = DC(Local_D0, Local_Ac, CurrentData[l].Temperature);
            D_Scale = Local_D * pow(10, 13);
        }
    }
}

```

```

//          printf("\nD0 = %.3lf, Ac = %.3lf, D = %.3lf * 10^-13, #points = %u,\
=>          ", Local_D0, Local_Ac, D_Scale, CurrentData[l].NumberOfDataPoints);

          EffectiveStartingTimes[i][j][l] = 0;

          if (CurrentData[l].Seconds == 0)
// Only compute effective starting times if this dataset is a control (no aging)
          {

              for (k=3600; k<=3600000000; k+=3600)
// Step through in units of 0.01 hours, start at 0.01 hours to avoid divide by zero errors
              {

                  RMS_Sum = 0;

                  if (AbortLoopFlag == 0)
                  {

                      for (m=0; \
                          m<CurrentData[l].NumberOfDataPoints; m++)
// Computes the RMS for the curve at the specified time. Loops through data points.
                      {

// printf("X = %lf cm, ", CurrentData[l].X_Values[m]);
// (DEBUG) Shows the current X-coordinate
                          SinglePointMSE = sqrt(pow((CurrentData[l].Y_Values[m] - \
                              PointConc(Local_D, CurrentData[l].X_Values[m], k, l)), 2));
// printf("X_Ex = %lf, X_Th = %lf, time = %lu seconds, MSE = %lf\n", CurrentData[l].Y_Values[m], \
                              PointConc(Local_D, CurrentData[l].X_Values[m], k), k, SinglePointMSE);
// printf("%f\n", SinglePointMSE);

                              RMS_Sum += SinglePointMSE;

                      }

// getchar();

// getchar();

// printf("when time = %lu seconds, MSE_Sum = %f\n", k, RMS_Sum);

                              if ((k == 3600) || (RMS_Sum < Min_RMS))

```

```

// Tag this time and keep its RMS if it's at a minimum - finds the best fit
// for the "effective aging time" from making the diffusion couple
//
// {
//     Min_RMS = RMS_Sum;
//     printf("%lf\n", RMS_Sum);
//     MinimumTime = k;
// }
// if (RMS_Sum > (1.1 * Min_RMS)) \
//     AbortLoopFlag = 1;
// }
}
}
if (l == LastControlSet)
{
    EffectiveStartingTimes[i][j][l] = MinimumTime;
// Locks the effective starting time in for this combination of D0, Ac and DataSet
}
else
// Use the control dataset's effective aging time to add to the experiment's time
{
    EffectiveStartingTimes[i][j][l] = \
        EffectiveStartingTimes[i][j][LastControlSet];
// Locks the effective starting time in for this combination
// of D0, Ac and DataSet. Uses the control dataset.
}
// printf("Minimum Time = %lu seconds.", MinimumTime);
// getchar();
    }
// getchar();
    if (CurrentData[l].Seconds == 0) printf("\nEnd D0=%f Step\n", Local_D0);
    }
    if (CurrentData[l].Seconds == 0) printf("\nEnd %uC Control Dataset\n", \
        CurrentData[l].Temperature);
// getchar();
}

printf("\n\nEnd Starting Time Calculation\n\n");

```

```

for (l=0; l<NumDatasets; l++)
{
    fprintf(fp, "/=====");
    for (m=0; m<=Ac_Dimension; m++) fprintf(fp, "=====");
    fprintf(fp, "\\n");
    fprintf(fp, "|          | Dataset %u has %u points at %u degrees C\n", l, \
    CurrentData[l].NumberOfDataPoints, CurrentData[l].Temperature);
    fprintf(fp, "|=====");
    for (m=0; m<Ac_Dimension; m++) fprintf(fp, "=====");
    fprintf(fp, "=====\n");
    fprintf(fp, "| D0 / Ac |");
    for (m=0; m<=Ac_Dimension; m++) fprintf(fp, " %5.2f |", Ac_Min + \
    ((double)m * Ac_Step));
    fprintf(fp, "\n");
    fprintf(fp, "|=====");
    for (m=0; m<Ac_Dimension; m++) fprintf(fp, "=====");
    fprintf(fp, "=====\n");
    for (i=0; i<=D0_Dimension; i++)
    {
        fprintf(fp, "| %6.3f |", D0_Min + ((double)i * D0_Step));
        for (j=0; j<=Ac_Dimension; j++)
        {
            fprintf(fp, "%8lu |", EffectiveStartingTimes[i][j][l]);
        }
        fprintf(fp, "\n");
    }
    // printf("%lu, ", EffectiveStartingTimes[i][j][l]);

    // printf("\n");
}

    fprintf(fp, "\\=====");
    for (m=0; m<=Ac_Dimension; m++) fprintf(fp, "=====");
    fprintf(fp, "/\n\n");
// printf("\n\n");
// getchar();

}

```

```

fclose(fp);

AbsoluteMinimumRMS = 1000;

for (i=0; i<=D0_Dimension; i++)          // Loop over specified values of D0
{
    for (j=0; j<=Ac_Dimension; j++) // Loop over specified values of Ac
    {
        Local_D0 = D0_Min + ((double)i * D0_Step);
        Local_Ac = Ac_Min + ((double)j * Ac_Step);

        RMS_Sum = 0;
        // Reset the RMS sum before testing each combination of D0 and Ac
        RMS_Map[i][j] = 0;

        for (l=0; l<NumDatasets; l++)
        // Computes the total RMS sum for each combination of D0 and Ac over all datasets. This
        // makes it so the fit is universal to the whole set of data, and not just to one experiment.
        {
            Local_D = DC(Local_D0, Local_Ac, CurrentData[l].Temperature);
            // Compute the diffusion constant for this combination of D0 and Ac

            if (CurrentData[l].Seconds == 0)
            // Only compute an RMS value for non-control datasets (aged samples only)
            {
                Local_Time = EffectiveStartingTimes[i][j][l];
            }

            else
            // Only compute an RMS value for non-control datasets (aged samples only)
            {
                for (m=0; m<CurrentData[l].NumberOfDataPoints; m++)
                // Loop over the individual datapoints
                {
                    RMS_Sum += sqrt(pow((CurrentData[l].Y_Values[m] - \
                    PointConc(Local_D, CurrentData[l].X_Values[m], \
                    (CurrentData[l].Seconds + Local_Time), l)), 2));
                }
            }
        }
    }
}

// printf("%f\n", RMS_Sum);

```



```

    }
}
// printf("When D0 = %f and Ac = %f and T = %u, RMS_Sum = %f\n", Local_D0, Local_Ac, CurrentData
[l].Temperature, RMS_Sum);
}

RMS_Map[i][j] = RMS_Sum;
// Locks the total RMS (summed over all datasets) for this combination of D0 and Ac
if (RMS_Sum < AbsoluteMinimumRMS)
{
    AbsoluteMinimumRMS = RMS_Sum;
    AbsoluteMinimumX = Local_D0;
    AbsoluteMinimumY = Local_Ac;
    AbsoluteMinimumTime = EffectiveStartingTimes[i][j][0];
}
}
// printf("\n");
// getchar();
}

fprintf(fp_results, "RMS = %f at D0 = %f and Ac = %f,\nTime = %lu seconds.\n\n", \
AbsoluteMinimumRMS, AbsoluteMinimumX, AbsoluteMinimumY, AbsoluteMinimumTime);

for (i=0; i<=D0_Dimension; i++)
{
    for (j=0; j<=Ac_Dimension; j++)
    {
        fprintf(fp_results, "%f,", RMS_Map[i][j]);
        if (RMS_Map[i][j] < (1.1 * AbsoluteMinimumRMS)) fprintf(fp_gnuplot, \
"%f %f %f\n", (D0_Min + (i * D0_Step)), (Ac_Min + (j * Ac_Step)), \
RMS_Map[i][j]);
// The above line only prints values close to the minimum,
// used for making the plot more dramatic
}
}

// printf("%f, ", RMS_Map[i][j]);
}

fprintf(fp_results, "\n");
fprintf(fp_gnuplot, "\n");

```

```

// printf("\n");
}

    fprintf(fp_results, "\n\n\n");
    printf("\n\nFinished\n\n");

    fclose(fp_results);
    fclose(fp_gnuplot);

    return 0;
}

void GetGlobalParameters(void)
{
    system("clear");

    printf("\n\nMike's Diffusion Data Fitting Program");
    printf("\n\nYou have %d datasets for %s in %s", NumDatasets, Element, Alloy);

    printf("\n\nPlease enter the following parameters for the infinite diffusivity (D0)\n");
    printf("\nMinimum value of D0: ");
    scanf("%lf", &D0_Min);
    printf("\nMaximum value of D0: ");
    scanf("%lf", &D0_Max);
    printf("\nStep size for D0: ");
    scanf("%lf", &D0_Step);

    D0_Dimension = ceil((D0_Max - D0_Min) / D0_Step);

    printf("\nMinimum value of Ac: ");
    scanf("%lf", &Ac_Min);
    printf("\nMaximum value of Ac: ");
    scanf("%lf", &Ac_Max);
    printf("\nStep Size for Ac: ");
    scanf("%lf", &Ac_Step);

    Ac_Dimension = ceil((Ac_Max - Ac_Min) / Ac_Step);
}

```

```

void LoadDataIntoMemory(void)
{
    printf("\n\nLoading files (debug)\n\n");

    FILE *fp = fopen("input-Si-T91-700.csv", "r");
    double TempData[10];
    unsigned int l, j;
    double dummy;
    unsigned long hours;
    printf("\nStill loading");

    if (fp == 0)
    {
        printf("Could not open input file. Possible problems:\n\n");
        printf("-Did you make an input file called \"input.csv\"?\n");
        printf("-Is it in the same directory as this program?\n\n");
    }

    else // Start parsing the input file
    {
        fscanf(fp, "%u,,\n", &NumDatasets);
        fscanf(fp, "%s,,\n", Alloy);
        fscanf(fp, "%s,,\n", Element);
        fscanf(fp, ",,\n");

        for (l=0; l<NumDatasets; l++)
        {
            fscanf(fp, "%u,%u,%lu", &CurrentData[l].NumberOfDataPoints, \
                &CurrentData[l].Temperature, &CurrentData[l].Seconds);
            fscanf(fp, "%lf,%lf,", &CurrentData[l].Cmin, &CurrentData[l].Cmax);
            CurrentData[l].Cavg = (CurrentData[l].Cmin + CurrentData[l].Cmax) / 2;
            CurrentData[l].DeltaC = CurrentData[l].Cmax - CurrentData[l].Cmin;

            for (j=0; j<CurrentData[l].NumberOfDataPoints; j++)
            {
                fscanf(fp, "%lf,%lf,\n", &CurrentData[l].X_Values[j], \
                    &CurrentData[l].Y_Values[j]);
                CurrentData[l].X_Values[j] /= 10000;
            }
        }
    }
}

```

```

        fscanf(fp, ",,\n");
    }

    fclose(fp);

    printf("Your alloy is %s\n", Alloy);
    printf("Your element is %s\n", Element);
    printf("You have %d datasets\n", NumDatasets);

/*
    for (l=0; l<NumDatasets; l++)
    {
// This function displays the file contents to ensure they made it to memory.
// It's usually only executed in DEBUG mode.
        hours = CurrentData[l].Seconds / 3600;
        printf("\n\nThis dataset was run at %d degrees Celsius for %lu hours\n", \
            CurrentData[l].Temperature, hours);
        printf("This dataset contains %d points\n", \
            CurrentData[l].NumberOfDataPoints);
        for (j=0; j<CurrentData[l].NumberOfDataPoints; j++) printf("%f microns, \
            %f wt percent Si\n", CurrentData[l].X_Values[j], \
            CurrentData[l].Y_Values[j]);
        getchar();
    }
*/
}

double DC(double Current_D0, double Current_Ac, unsigned int Current_Temperature)
{
    double Current_D;

    Current_D = Current_D0;
    Current_D *= exp((( -Current_Ac) / (R * (Current_Temperature + 273.15))));

    return Current_D;
}

double PointConc(double Current_D, double Current_X, unsigned long Current_Time, unsigned char l)
{

```

```

double Concentration;

Concentration = (CurrentData[l].DeltaC / 2);
Concentration *= erf(Current_X / sqrt(4*Current_D*Current_Time));
Concentration += CurrentData[l].Cavg;

return Concentration;
}

```

#### Example Input File

```

6           Number of Datasets (positive integer)
T91        Name of alloy (string)
Silicon    Name of diffusing species (string)
           Blank line required
31,700,0   (# of datapoints),(Temperature in C),(Aging time in hours)
0.6846,3.8980, (Min concentration in at. %),(max concentration in at. %),
-244.59,0.67, (distance in microns),(concentration in atomic percent),
-232.59,0.69, (distance in microns),(concentration in atomic percent),
-220.59,0.68, (distance in microns),(concentration in atomic percent),
...        Continue value pairs here. Note that you need a comma
More Values... at the end of each pair before the next line. If you are
...        having trouble, check the Windows/Linux line feed
-10.59,0.92, character issue (0x0a vs. 0x0d)
-3.59,1.31,

           Datasets separated by blank line
Next dataset... Continue exactly as above, separating datasets by blank lines.
           Note that the data must be presented with the minimum
           concentration on the left. Reverse your data ahead of time.

```